

Modeling Pattern Formation in Biopolymer Systems induced by Reaction Kinetics and Molecular Motors

Von der Universität Bayreuth
zur Erlangung des Grades eines
Doktors der Naturwissenschaften (Dr. rer. nat.)
genehmigte Abhandlung

von
Falko Ziebert
aus Illingen (Saar)

1. Gutachter : Prof. Dr. W. Zimmermann
2. Gutachter : Prof. Dr. H. Brand

Tag der Einreichung : 27.06.2006
Tag des Kolloquiums : 12.09.2006

Contents

1	Introduction and Overview	1
2	Biological components	7
2.1	Cytoskeletal polymers	8
2.1.1	Structure	8
2.1.2	Polymerization	11
2.2	Motor proteins	14
2.2.1	Structure and properties	15
2.2.2	Processivity and duty ratio	17
2.2.3	The motor cycle: chemistry vs. mechanics	19
3	Prerequisites	21
3.1	Liquid crystals (LCs)	22
3.2	The rod liquid as a model for lyotropic LCs	24
3.2.1	The model of Onsager	24
3.2.2	The Doi equation	27
3.2.3	Physical motivation of the Doi equation	30
3.2.4	Analyzing the Doi equation	33
3.2.5	Moment equations	34
3.3	Phase separation and Cahn-Hilliard theory	37
I	Pattern formation in self-assembling nematic biopolymers	41
4	A minimal model for the I-N phase separation	43
4.1	The I-N part of the model	44
4.1.1	Derivation of an order parameter equation	44
4.1.2	The closure relation method	46
4.1.3	Homogeneous bifurcation analysis	47
4.2	The phenomenological model	50
4.2.1	Linear stability analysis	51
4.2.2	Phase separated solutions	57
4.3	Conclusions	60

5	Reaction kinetics drives pattern formation	61
5.1	The underlying idea	62
5.2	Simple reaction kinetics in the model	63
5.3	Analysis of the reactive model	64
5.3.1	The spatially homogeneous case	64
5.3.2	Linear stability analysis of the nematic state	65
5.3.3	Numerical analysis	68
5.3.4	Robustness of the pattern forming mechanism	71
5.4	Conclusions	73
II	Pattern formation in filament-motor solutions	75
6	Introduction	77
6.1	The experiments we want to describe	77
6.2	Modeling	79
7	The filament-motor model	81
7.1	Motivation	81
7.2	The model	83
7.3	Symmetries of the motor-mediated velocities	85
8	Derivation of continuum equations	89
8.1	Two approximations on the way to a continuum model	89
8.1.1	The continuum model	91
8.2	Details of the derivation	93
8.2.1	The gradient expansion of the interaction integrals	93
8.2.2	The moment expansion method	95
8.2.3	Structure of the equations	96
9	Linear analysis	101
9.1	Linear operator and general discussion	102
9.2	Without polarity sorting	105
9.3	Separation of longitudinal and transverse modes	109
9.4	With polarity sorting	110
9.5	Discussion	114
9.5.1	Influence of polarity sorting	114
9.5.2	Influence of the diffusion ratio	118
10	Stationary patterns	119
10.1	Weakly nonlinear analysis	120
10.1.1	Amplitude equations	120
10.1.2	Derivation of the amplitude equations	122
10.2	Existence and stability of stripes and squares	127

10.2.1	Scaling of the diffusion coefficients	129
10.3	Results of numerical simulations	130
10.4	Comparison to experiments	132
11	Oscillatory patterns	135
11.1	Weakly nonlinear analysis in one dimension	136
11.1.1	Amplitude equations	136
11.1.2	Derivation of the amplitude equations	137
11.1.3	Existence and stability of the nonlinear waves	142
11.2	Higher order excluded volume effects	144
11.3	Nonlinear influence of the polarity sorting	147
11.4	Results of numerical simulations	148
11.5	Weakly nonlinear analysis in two dimensions	149
11.5.1	Amplitude equations	149
11.5.2	Existence and stability of two-dimensional waves	150
11.5.3	Numerical simulations	154
11.6	Discussion and conclusions	157
12	Density instability	159
12.1	Linear properties	159
12.2	Numerical simulations	160
12.3	Discussion	163
13	Patterns in actomyosin	165
13.1	ATP depletion and filament clustering	168
13.2	Permanent crosslinkers introduce disorder	171
13.3	Discussion	174
14	Summary/Zusammenfassung	175
14.1	Summary	175
14.2	Zusammenfassung	180
A	Isotropic averages	187
A.1	Isotropic averages in three dimensions	187
A.2	Isotropic averages in two dimensions	188

Chapter 1

Introduction and Overview

Biological cells are apart from highly specialized biological units like the cell nucleus, mitochondria and other organelles made of a complex fluid, the so-called cytosol. Its main constituents are the cytoskeletal proteins which are met mainly in its polymerized form as actin filaments and microtubules. These are major parts of the cytoskeleton building the scaffold of most eukaryotic cells, stabilizing the cell morphology and thus determining predominantly the mechanical properties of the cell [1, 2, 3, 4]. Apart from this obvious importance for the overall cell structure the cell is organized vastly by an efficient machinery which involves in addition to the cytoskeletal proteins also different kinds of filament-associated proteins like motor proteins [5], crosslinkers [1], capping proteins etc.. Motors are specialized proteins that can move on the cytoskeletal polymer scaffold either to perform intracellular transport or to reorganize the cytoskeleton itself if in contact with several filaments. Vesicles for instance are transported across a cell by motors moving along the tracks defined by microtubules, or – which is the scope of part II of this work – oligomeric motor proteins that attach to two or more filaments induce relative motion between neighboring filaments and cause dynamical networks. The latter process is vitally important in cells, since the cytoskeleton constituted of the filaments has to be self-organized and even actively reorganized during cell locomotion [6, 7] and in order to react to outer stimuli. During mitosis, microtubules attach to the chromosomes, which are then divided and the two halves finally are transported by the motor-induced filament sliding into the two evolving daughter cells [8, 9].

The detailed regulation of the above mentioned processes naturally is rather complex and still a huge field of research in molecular cell biology. However, many properties of the cytoskeleton are based on purely physical mechanisms [10]. Looking at such diverse fields like cell mechanics and cell rheology, complex fluid behavior and the statistical physics of polymer solutions or nonequilibrium states and pattern forming processes, all of these are fields of growing interest among physicists.

To apply a physical description to such a complex problem as cytoskeletal dynamics, one is obliged to first identify smaller subproblems that can be easier investigated. In the present work I will study two inherent aspects of the cytoskeleton, inherent meaning that these processes are caused by the nonequilibrium state of the cell and therefore are not met

in systems that might look similar but are in equilibrium like usual polymers or colloids. Both the polymerization and depolymerization process of the cytoskeletal filaments and the motor-mediated transport need a chemical fuel which is delivered abundantly by the cell's metabolism keeping the cell in a highly nonequilibrium state. In most cases, this biological fuel is Adenosine-triphosphate (ATP) and for both the polymerization of one monomer onto a filament and for one step of a motor protein on such a filament, one molecule of ATP is needed.

The constituents of the cytoskeletal system will be introduced and their properties, as far as they are relevant to my work, will be discussed in chapter 2.

Pattern formation in self-assembling nematic biopolymers

The ongoing polymerization and depolymerization of actin filaments and microtubules are important for many different purposes, such as cell motility [7, 11, 12], cell division [8, 13] or morphogenesis [14]. Due to the nonequilibrium character of the polymerization both cytoskeletal filaments show new states like oscillatory polymerization [15, 16] and active phenomena like treadmilling [17]. On the other hand, being quite stiff polymers like the famous example for rod-like particles, the Tobacco Mosaic Virus [18], also actin and microtubule filaments undergo with increasing density a transition to an orientational order [19, 20, 21, 22, 23, 24]. This so-called nematic order [25] has been traced back to the excluded volume interaction between the filaments [26, 27], which is lowered by the ordering and compensates the loss of entropy due to the ordering. This remains to be true for semiflexible polymers, albeit at a slightly higher filament density [28], as has been observed for actin *in vitro* [21].

Part I of this work is devoted to investigate the interplay of the above processes, namely the influence of the self-assembly of the cytoskeletal filaments on the nematic order. We predict a new pattern forming mechanism which is based on the following idea: Onsager's theory [26] of the isotropic-nematic (I-N) transition, which is valid for long filaments of fixed shape and infinite lifetime τ , predicts near the I-N ordering transition a phase separation into domains of isotropically oriented rods at low density and nematic domains of higher rod density, a process which has been observed also for actin filaments with an almost vanishing kinetics [24]. For a finite lifetime τ of actin and microtubule filaments however, as usually the case due to the nonequilibrium polymerization kinetics, Onsager's equilibrium theory for the nematic order does not apply. Moreover, this finite τ limits the diffusive transport distance and the coarsening during the phase separation close to the orientational transition to a length scale of about $l_D = \sqrt{D\tau}$, with the filament diffusion coefficient D . Accordingly we expect a kinetically induced periodic pattern of alternating isotropic and nematic regions, with a wavelength that can be estimated to be in the order of $10\mu\text{m}$.

The generic scenario near the ordering transition is investigated in chapter 4 in terms of a phenomenological model which is minimal in the sense that it catches all the features of the Onsager theory. The model is introduced and analyzed at first without the polymerization kinetics of the filaments and compared extensively with the predictions of Onsager's theory. In chapter 5 it is extended by the essential reaction steps as motivated by actin

and microtubule polymerization and the predicted pattern formation is investigated. Part of these results have been published in Ref. [29]. Before, in chapter 3, I will introduce how the I-N transition can be described and quantified and review the Onsager theory and the Doi equation for rigid rods which will also be the starting point of the investigations in part II of this work.

Pattern formation in filament-motor solutions

In the second part of this work, I consider the nonequilibrium motor-mediated interaction of the cytoskeletal filaments. To circumvent having to deal with two dissipative processes simultaneously, in contrast to the first part we will consider a state without polymerization. This can be achieved both *in vivo* and *in vitro* by the use of capping proteins, which attach to the filament ends and by this way hinder further polymerization and stabilize the filaments. The interaction of filaments with motors as well as motor-mediated filament-filament interactions play a crucial role in eukaryotic cells. Most prominently, microtubules and associated motors like kinesin are involved in highly connected dynamical structures, such as the mitotic spindle in cell division [14, 8], while the motility of the cell as a whole is also partly governed by acto-myosin complexes [7, 30]. Due to the nonequilibrium state of high ATP supply, filament-motor solutions may display dissipative patterns and self-organized structures like asters, bundles and vortices, [31, 32, 33] and active phenomena like active response to stresses [34, 35] and fluidization [36].

Since the situation again is very complex in a living cell, well designed *in vitro* experiments are the agent of choice for controlled explorations of prominent aspects of cellular systems. Recent experimental progress yielded indeed important insights into organization and dynamical properties of the cell, which in turn call for modeling activities to foster their deeper understanding. These experiments comprise investigations of self-organization in filament-motor mixtures of microtubules in the presence of a single type of motor protein [37, 31, 32] and more recently also in actin-myosin networks [36, 38] as well as assays where two types of motors interact with microtubules [33]. Even in such model systems, simple compared to a living cell, there has been found a great variety of different two-dimensional patterns, such as stripe patterns, asters, vortices and irregular arrangements. I shortly review the experiments we want to describe in section 6.1.

To model pattern formation in filament-motor systems, in part II we follow a mesoscopic approach starting from the Smoluchowski equation for rigid rods or Doi equation [39] introduced in section 3.2.2. This is an equation for the spatial and angular distribution of rigid rods, the latter approximating the stiff microtubules and with limitations also the actin filaments. Such an approach is widely used in polymer and colloidal science and recently has been supplemented by active currents to describe filament-motor systems [40] in a way inspired by a model for filament bundling in one spatial dimension [41]. In this approach one makes use of the fact that the small motor proteins diffuse much faster than the filaments. Hence the density of the motors can be assumed to be homogeneous and – as well as properties like the mean velocity and the duty ratio of the motors – enters into the model only via the coefficients. The phenomenological description of the active currents

can be derived by symmetry considerations. The filament-filament interactions induced by the motors as well as by excluded volume effects are generically nonlocal, but they can be approximated by a gradient expansion. Most of the experimental assays are quasi two-dimensional, thus we restrict our analysis also to two spatial dimensions. Moreover, since *in vitro* aster-like patterns evolve at much lower filament density than the isotropic-nematic transition, a moment expansion of the probability density function can be truncated to derive a closed set of equations for the physical observables, which are the density and the orientation field of the filaments. The details of the mesoscopic model and the derivation of the coarse-grained equations for the density and the orientation field can be found in chapters 7 and 8.

In the framework of the derived coarse-grained model, a detailed linear stability analysis of the homogeneous and isotropic filament distribution as carried out in chapter 9 reveals a rich variety of instabilities in an infinite two-dimensional system: homogeneous isotropic-nematic, stationary and oscillatory finite wavelength instabilities as well as a motor-mediated demixing instability. It follows a detailed characterization of the weakly nonlinear behavior of the patterns beyond their threshold. For this purpose we employ on the one hand numerical simulations of the coupled equations for the filament density and the orientational field. On the other hand we use the method of amplitude expansion, where equations of motion for the amplitudes of the spatially periodic pattern are derived close to the pattern forming instability [42, 43, 44]. By a linear analysis of the stationary solutions of the amplitude equations one can also calculate the stability regions of the respective patterns.

Chapter 10 is devoted to the stationary finite wavelength instability, which near the threshold of pattern formation allows for stripes, squares or hexagonal patterns in a two-dimensional system. However, hexagons can be ruled out both analytically and numerically. The remaining square and stripe patterns can be related to the aster-like and bundle-like patterns observed in experiments. The linear analysis and the investigation of the stationary finite wavelength instability have been published in [45]. Since the filament-filament interactions are nonlocal, a gradient expansion of the interaction kernel has to be used, which has to be continued up to fourth order to describe the pattern forming instabilities in a reasonable manner, cf. Ref. [46]. Chapter 11 is devoted to the oscillatory finite wavelength instability, which is first investigated in one dimension yielding coupled density-orientation waves, either traveling or standing ones. In two dimensions one can derive four coupled amplitude equations for right- and left-traveling waves in the two orthogonal directions of a square. From the diverse solution space however, only traveling and alternating waves are found to be stable. An alternating wave is a four mode solution which is composed of two standing waves in perpendicular directions with a $\pi/2$ phase shift in time. The demixing instability is investigated in chapter 12. Here the linearly most unstable mode determines the initial stage of the patterns, followed by a coarsening process that involves aster-like patterns whose wavelengths are growing in time.

Eventually, in chapter 13 an interpretation of the model to account for actomyosin is proposed, which tries to explain and has triggered recent experimental results [38]. In contrast to the dissipative patterns in microtubule-motor solutions, the myosin motors

maintain disorder in solutions of actin filaments when active and induce patterns when the ATP concentration is depleted. We propose that these patterns are caused by a crosslinking process due to motors running out of ATP, which are known to attach rigidly to the actin filaments. These clusters can be still transported and may drive the system into the unstable region of phase space, where patterns form quickly through one of the linear instabilities discussed above. Ultimately the patterns are frozen in due to total ATP depletion. Second, the influence of permanent crosslinking proteins like streptavidin is discussed and exemplified within the existing model. We argue that the permanent crosslinkers can be interpreted as a disorder in the pattern forming problem, which reduces the instability threshold. Thus a filament-motor system shows a higher propensity for pattern formation in the presence of a small fraction of crosslinkers, in agreement with the experimental results [38].

Chapter 2

Biological components: filaments and motors

Presumably, everybody knows the pictures of a biological cell from schoolbooks, where the cell membrane separates the inside containing the nucleus and specialized organelles like the endoplasmatic reticulum or the mitochondria from the cells' surroundings. In recent times, after the functions of these organelles - which for obvious reasons attracted the interest of biologists since their discovery by light microscopy - have been to some extent understood, also the complex fluid in which these are embedded has become a growing field of research.

The main constituent of this so-called cytosol are the *cytoskeletal proteins*. These proteins in their polymerized form build up the *cytoskeleton* which is the scaffold used in most eukaryotic cells to stabilize the cell morphology and determines to a major part the cell mechanics. Apart from this obvious importance for the overall cell structure already clear from the notion "skeleton", also the inside of the cell is vastly organized by a clever machinery which involves the cytoskeletal polymers, as well as different proteins associated to these like motor proteins, crosslinkers, capping proteins etc. *Motor proteins*, often also called *molecular motors*, are specialized proteins that can walk on the polymer scaffold either to perform intracellular transport or to organize actively the cytoskeleton if in contact with several filaments.

What makes the cytoskeleton and their associated proteins not only interesting for biologists but also for physicists is the fact that a living cell inherently is a nonequilibrium system. Indeed, in both fundamental processes mentioned above, the polymerization of the cytoskeletal filaments and the motor-mediated transport, a chemical fuel is needed that is delivered by the cell metabolism. Nonequilibrium polymer physics as well as irreversible transport processes in a complex fluid are answers physics should give in the future to the above biological questions, both topics being also of a more general interest.

Since physicists usually are not familiar with cell biology, I introduce in the following section the constituents of the cytoskeletal system and discuss their nonequilibrium properties. This chapter is a synopsis mainly from the textbook [5], but also from [1, 2, 6, 3] as well as from several review articles [47, 48, 8, 7, 49, 50, 51].

2.1 Cytoskeletal polymers

To distinguish the nonequilibrium cytoskeletal polymers from usual equilibrium polymers, they are often called *biopolymers*. There are three main types, *actin filaments*, *microtubules* and so-called intermediate filaments, the latter ones being not well understood (even their structure is still subject to discussions) and therefore not considered in this work.

2.1.1 Structure

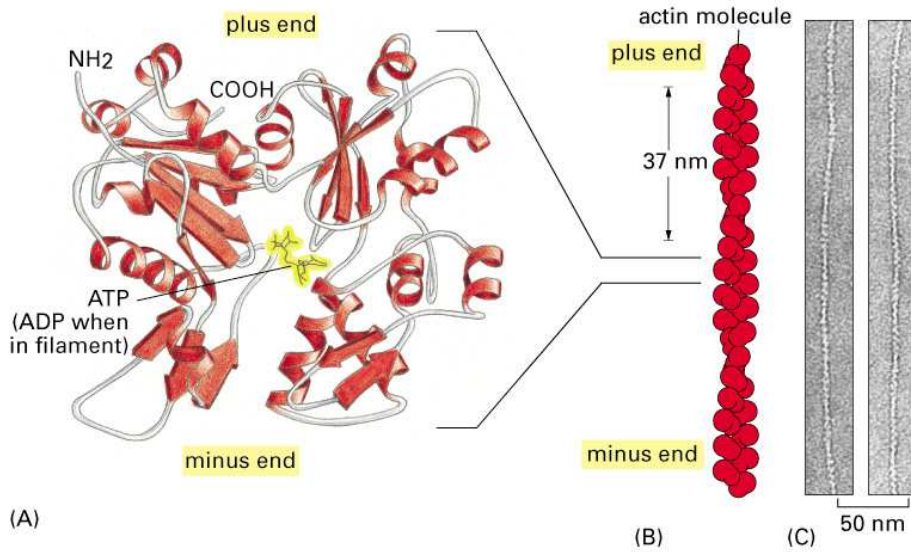


Figure 16-7. Molecular Biology of the Cell, 4th Edition.

Figure 2.1: A) The structure of an actin monomer. B) The structure of filamentous actin. C) Electron micrographs of actin filaments. The picture is taken from [2].

Let's look at first at the biopolymers from a polymer physicists point of view. Actin filaments, which are also called *microfilaments*, a notion which is not used here to prevent confusion with the microtubules, are shown in Fig. 2.1C. They have a diameter of 6nm and a persistence length¹ of about $L_p = 15\mu\text{m}$. In total length they range from very short aggregates of $\sim 35\text{nm}$ in the cortex just underneath the cell membrane of erythrocytes (red blood cells) to very long structures of $10 - 100\mu\text{m}$ in stereocilia, the sensory receptors of the vertebrate inner ear [5]. The usual length in the cytosol however is several μm meaning that cytoskeletal actin is a so-called *semiflexible* polymer since the filament length is of the order of the persistence length.

¹The persistence length of a polymer can be defined as the decay length of the tangent-tangent correlation function, i.e. if s is the contour parameter and \mathbf{t} the tangent on the filament, the relation $\langle \mathbf{t}(x+s) \cdot \mathbf{t}(x) \rangle \sim e^{-s/L_p}$ holds.

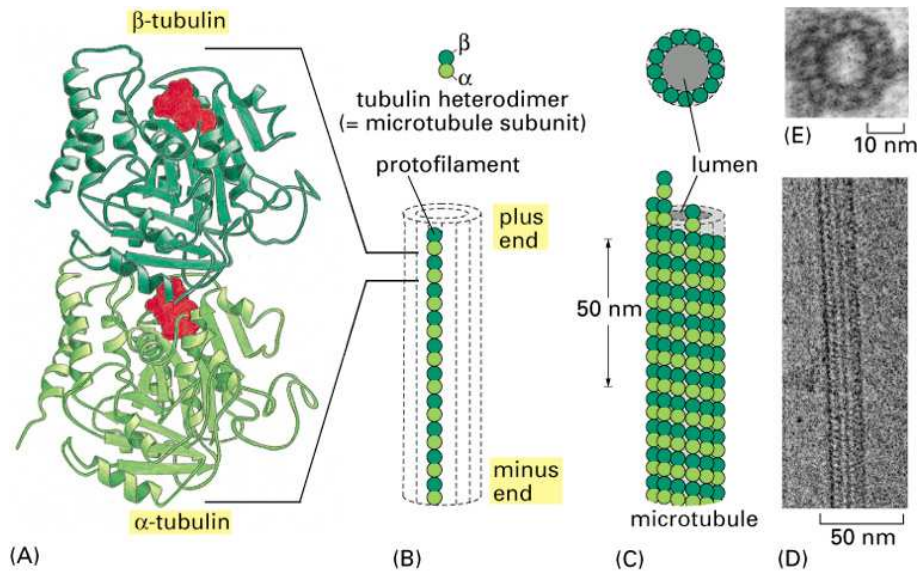


Figure 16-6. Molecular Biology of the Cell, 4th Edition.

Figure 2.2: A) The structure of a tubulin dimer comprising one α - and one β -tubulin. B) The dimers form a linear protofilament. C) The structure of a microtubule containing thirteen protofilaments. D) An electron micrograph of a microtubule. The picture is taken from [2].

Microtubules (MTs) as shown in Fig. 2.2D have a diameter of 25nm and a persistence length of about $L_p = 6\mu\text{m}$, implying that they are much stiffer than actin filaments. In the cytoskeleton, likewise the actin filaments MTs have lengths of the order of μm and thus are nearly rigid rods since their length is small compared to the persistence length. Nevertheless, lengths can reach up to 1mm in insect sperm [5] then implying semiflexibility.

Structure of the subunits

Both biopolymers are build up of subunits, namely actin monomers in the case of actin filaments and tubulin dimers in the case of microtubules. The protein structures² of both

²Some words on protein families [5]: the proteins which we refer to as just actin or tubulin however can differ (since their aminoacid sequences differ) due to the following reasons: first by genetic polymorphism inside a species (where different proteins in most cases are functionally identical, if not this often leads to genetic diseases). Second by genetic variations between species, where however both actin and tubulin are very conserved protein structures: as examples, skeletal muscle actin of humans is identical with that of mice and chickens and even the β -tubulin of the beer yeast has 72% identity to that of humans. A third possibility of protein diversity is the fact that in higher animals proteins are encoded in the genes more often than once, which is supposed to be used to generate slightly different proteins for differentiated tasks. For our purposes however, since actin and tubulin are such conserved structures we discard these variations and treat different actins as identical, as well as different MTs.

has been resolved by X-ray diffraction on crystallized proteins and they are displayed in Figs. 2.1A and 2.2A respectively. Both subunit proteins have in common that they exhibit a cleft where a nucleotide and a Mg^{2+} ion is bound. In the case of actin, the nucleotide is ATP or ADP (*Adenosine triphosphate* or *adenosine diphosphate* respectively) while for microtubules it is GTP or GDP (*Guanosine triphosphate* or *guanosine diphosphate* respectively). These bound nucleotides are essential for the nonequilibrium polymerization process as explained in section 2.1.2 below.

The tubulin dimer consists of two similar structured tubulin monomers, called α - and β -tubulin, which are joined together in a head-to-tail fashion, the nucleotide of the α -tubulin being trapped in between, cf. Fig. 2.2A. Thus the α -tubulin can almost not exchange its nucleotide (it is also called N site for nonexchangeable), while the nucleotide of the β -tubulin is in contact with the solvent and can be more easily exchanged (E site for exchangeable). When I refer in the following to the hydrolysis of the subunits' nucleotides, in the case of tubulin this means the one of the β -tubulin. To summarize, although the subunits of MTs are dimers, for our purposes they can be treated in quite the same way as the actin monomers.

Filament structure and polarity

The structures of the polymerized forms of actin and tubulin differ largely and can easily explain the differences in their rigidity. As can be seen in Fig. 2.1B, the actin filament is a two-stranded and right-handed helix with a period of 72nm. Because the actin monomers are asymmetrical (most importantly the cleft, which is crucial for the nucleotide exchange during polymerization is showing in a specified direction) the whole actin filament is *polar* with structurally different ends, which are therefore called *plus end* and *minus end*.

The structure of a microtubule is even more complex: the dimers are polymerized head-to-tail to form a so-called *protofilament* displayed in Fig. 2.2B, which are themselves associated laterally to form a hollow cylinder as can be seen in Fig. 2.2C. Since there is a small offset of $\sim 0.92\text{nm}$ between dimers in neighboring protofilaments the most common number of protofilaments in a microtubule is 13, leading to a total offset of 12nm meaning exactly three monomer sizes³. The most common MT can therefore be seen as a so-called three-start helix. From the stiff hollow cylindrical structure of MTs and their larger diameter as compared to the two-stranded actin filament, the difference in the rigidities is quite obvious. From the helical structure and the head-to-tail arrangement of the dimers, the MT is again a *polar* structure and one can define a *plus end* (being the direction of the β -tubulins) and a *minus end*.

Properties from the structure

Three key features are important for the processes under consideration in this work: First, the fact that both actin filaments and microtubules are multistranded with extensive con-

³There exist also MTs with protofilament numbers ranging from 9 – 17, which however have in common that they require the protofilaments not to be parallel to the MT axis.

tacts between the strands lead to a high stability of the filamentous structure. Therefore the polymerization and depolymerization processes occur by monomer addition and subtraction on the filament ends, while addition and subtraction of short filaments as well as filament breaking effects are negligible [5]. Experiments verify this both *in vitro* and *in vivo* [52, 53]. Breaking events have only finite probability when catalyzed by so-called *severing proteins*, gelsolin for actin and katanin for MTs [54, 55].

Second, the polarity of both filaments has important consequences: the polymerization and depolymerization rates are different on both ends, the faster polymerizing one defining the plus end. In addition, also the surfaces of both filaments are asymmetrical which is important for the interaction of proteins with the filaments, especially for the motor protein interaction modelled in part II of this work. As will be discussed in Section 2.2, a species of motor proteins can move on a filament only in a specified direction. Therefore one can discriminate plus and minus end-directed motor species.

Third, both filaments are stiff objects (for actin filaments this is only true for not too long filament lengths, cf. above) and they can therefore be approximated for our purposes by rigid rods, a fact that simplifies theory considerably. An additional consequence of the rod-like shape is that biopolymer solutions can display orientational i.e. liquid crystalline order, which is a main topic of part I of this work and also involved in part II where polar orientational order in the presence of motor proteins is investigated. An introduction to liquid crystals and their statistical description follows in chapter 3.

2.1.2 Polymerization

Evidences for nonequilibrium

There are many evidences for polymerization and depolymerization of the cytoskeletal filaments being a nonequilibrium process: First, the time scales are much faster than for processes at or close to thermal equilibrium. Both actin monomers and tubulin dimers can be fluorescently labeled and followed to build up filaments in a microscope. For actin in stress fibers this happens in several minutes and for MTs in interphase cells the time scale is about an hour [56, 57]. For an equilibrium polymer however, where one has approximately an exponential length distribution and diffusive growth, one can estimate the standard deviation for length changes to be in the order of only a few tens of nanometers per minute [5], far too slow to account for the above processes.

Second, a state called *dynamic instability* has been observed in microtubules both *in vivo* and *in vitro* [15, 16], which takes place only in the presence of the biological fuel GTP. In this state, there are random transitions of individual MTs between a growing and a shrinking state with different rates ($1\mu\text{m}/\text{min}$ and $10\mu\text{m}/\text{min}$ respectively). The switching happens on a time scale of minutes and the fact that nearby MTs can be in opposite states indicates that it cannot be explained just by fluctuations in the monomer density. This nonequilibrium state has attracted already several physical modeling efforts [13, 58, 59].

Third, in specialized cells, filaments can be generated with well defined lengths, e.g. the actin filaments in muscle cells have fixed lengths with a deviation in the nanometer

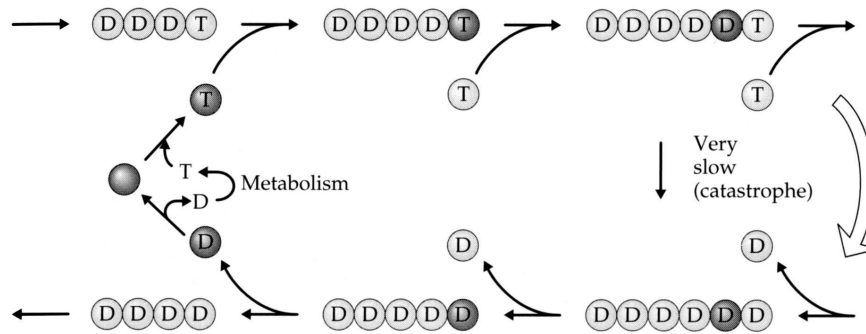


Figure 2.3: The involvement of the hydrolysis cycle in the nonequilibrium polymerization process is sketched. The top row applies to the growing state due to polymerization and the bottom row to the shrinking due to depolymerization. Subunits carrying an ATP (actin) or a GTP (MTs) are marked with T and those with ADP and GDP respectively are marked with D. While becoming a part of the filaments' interior by subsequent polymerization, T becomes hydrolyzed to D. If the T-'cap', here sketched only as a single T unit, gets lost, the growing state switches to the shrinking one. The picture is taken from [5].

(i.e. monomer) range, and this state is maintained over the half-life time of actin, which is about a week. This is also a state which is hard to maintain in an equilibrium situation.

Coupling to hydrolysis

These unexpected properties are made possible, as will be explained below, by the coupling of nucleotide hydrolysis to the polymerization process. Actin is called a polymerization-catalyzed ATPase, i.e. while actin monomers carry ATP, in the polymerized state they carry ADP, implying that *ATP hydrolysis*,



with P_i a phosphate ion, has happened in the course of the polymerization of each subunit. If depolymerizing however, the process does not run backwards: only ADP-monomers are released and the "recycling" of ADP to ATP happens on the free monomers driven by metabolic processes through ATP-synthase. So depolymerization is not the chemical reverse of polymerization anymore as is the case in an equilibrium situation. Apart from its involvement in actin polymerization, ATP hydrolysis is even more important as it is used to drive many reactions including the motion of molecular motors, and it is discussed in more detail in section 2.2.3. For microtubules the hydrolysis scenario is similar, but with ATP and ADP being replaced by GTP and GDP.

The detailed structure of a polymerizing filament is as follows, cf. also Fig. 2.3. During polymerization, a monomer carrying a nucleotide triphosphate (NTP, i.e. either ATP or GTP for actin and MTs respectively) is added to the filament. While becoming a part

of the filaments' interior by subsequent polymerization, its NTP becomes hydrolyzed to NDP. However, there is a certain time lag between polymerization and hydrolysis, leading to a *cap structure* at the filament end containing some NTP subunits, while the interior filament only comprises NDP subunits. The hydrolysis of the NTPs in this cap leads to a destabilization of the whole filament, which switches then to the shrinking state. This is (in short words) the dynamic instability mentioned above. Whilst well established for MTs, since the rate difference at the two ends for actin are smaller than for MTs, a dynamic instability has not been found for actin so far.

A novel nonequilibrium state is the so-called *treadmilling* state [17], where one of the filament ends has a cap while the other has not, thus the one polymerizes and the other depolymerizes. It can be achieved that the total filament length is nearly a constant and thus the filament appears to move in space into the plus end direction. This state is not yet fully understood since it exists *in vivo* in a much wider concentration regime than in *in vitro* (implying that additional regulatory proteins are involved). However it may be of high relevance since it is a quite fast (some $\mu\text{m}/\text{min}$) and directed motion compared to the slow and undirected filament diffusion.

Simplified kinetics; critical monomer concentration

As already mentioned in section 2.1.1, a multistranded filament like actin and MT elongates by addition and subtraction of subunits at the filament ends, implying

$$\frac{dn}{dt} = k_{on}m_0 - k_{off} \quad (2.2)$$

for the temporal change of the mean number of subunits per filament. Here m_0 means the monomer (or dimer in the case of MTs) concentration and k_{on} , k_{off} are the on- and off-rates, here assumed equal on both ends for simplicity. From Eq. (2.2) follows the existence of a *critical monomer concentration*, $m_c = \frac{k_{off}}{k_{on}}$, for which the elongation rate equals zero. From a simple model of a two-stranded polymer [5], it follows that for concentrations larger than m_c , the polymers grow and at steady state the polymerized monomer concentration equals the total monomer (or dimer in the case of MTs) concentration minus m_c , while for concentrations less than m_c polymers will shrink and finally disappear. Second, the mean filament length increases very steeply for concentrations larger than m_c . Thus slight changes in monomer concentration, e.g. regulated by proteins, can have large effects on the filament length and therefore on the cytoskeletal structure⁴.

Due to the polarity of the filaments, the rates k_{on} and k_{off} are usually different for the two distinct filament ends (the plus end has been defined as the faster growing one). Moreover, also the critical concentrations can differ since the nonequilibrium character of the polymerization (due to the coupling to the hydrolysis) breaks the requirement of

⁴A second consequence of the multistrandedness being beneficial for the cell is that the number of spontaneous nuclei is smaller than in the singlestranded case, it can be estimated to be in the nM range. If the cell can supply more nuclei than this, by regulatory proteins like e.g. the Arp2/3 complex, it can govern efficiently where the filament growth should start.

microscopic reversibility,⁵ making the treadmilling state with ends in different states possible. For example, for actin *in vivo*, the critical concentrations are $m_c^{A+} = 0.1\mu\text{M}$ and $m_c^{A-} = 0.8\text{M}$ [1] for the plus and the minus end respectively.

Some words on concentrations⁶: Total densities (i.e. polymerized and free monomers together) range for actin from $200\mu\text{M}$ for non-muscle cells to 0.5mM in blood platelets and 5mM in microvilli, total tubulin concentrations in cells are about $20\mu\text{M}$. ATP and GTP have typical cytoplasmic concentrations of 1mM , while ADP and GDP concentrations are about $10\mu\text{M}$. Since the affinities of the polymer subunits to the tri- and diphosphate nucleotides are similar, this leads to the fact that most free subunits carry ATP or GTP in the case of actin and MTs respectively. Inside the cell, there is thus strong tendency to filament polymerization, since the free subunit concentrations carrying ATP/GTP and thus being able to polymerize exceed the critical concentrations by orders of magnitude: the cytoplasmic ATP-actin-monomer concentration is about $30\mu\text{M} \gg m_c^{A+} = 0.1\mu\text{M}$ while for MTs the GTP-tubulin-dimer concentration is about $10\mu\text{M} \gg m_c^{M+} = 0.03\mu\text{M}$.

Functional aspects

The biological advantage of the nonequilibrium polymerization is quite obvious: The cell can reorganize its cytoskeleton more quickly and more well defined without having to synthesize new or degrade old protein. The dynamic instability is used as an efficient way to search in space during mitosis [13]. In addition, the polymerization can even be used to do mechanical work (with forces in the pN range, i.e. comparable to molecular motors), if the monomer concentration differs from the stationary concentration. This is again faster and more effective using the hydrolysis energy as compared to the equilibrium case. It is used in cells during mitosis and also as a mechanism for locomotion e.g. in the bacterium *Listeria monocytogenes* [60].

2.2 Motor proteins

Motor proteins, also referred to as *molecular motors*, convert the chemical energy delivered by the cell in the form of ATP into mechanical work. This is again done by the hydrolysis reaction, Eq. (2.1), we have already encountered in the nonequilibrium polymerization process. The mechanical work is most often a translation of the motor protein relative to a filament, which is used for many purposes: in cell locomotion, in intracellular transport like the movement of organelles or the segregation of chromosomes, in force generation and

⁵In an equilibrium system, if going from a n -mer to a $(n + 1)$ -mer by polymerization, it is indistinguishable on which end the monomer has been added, Boltzmann's law thus implying equal equilibrium constants and therefore equal critical concentrations. The on- and off-rates can however differ if only m_c does not change [17].

⁶It should be mentioned that critical concentrations depend highly on ionic strength and also on temperature, the given numbers being measured at physiological conditions: a higher temperature enhances the polymerization as does a higher cation concentration.

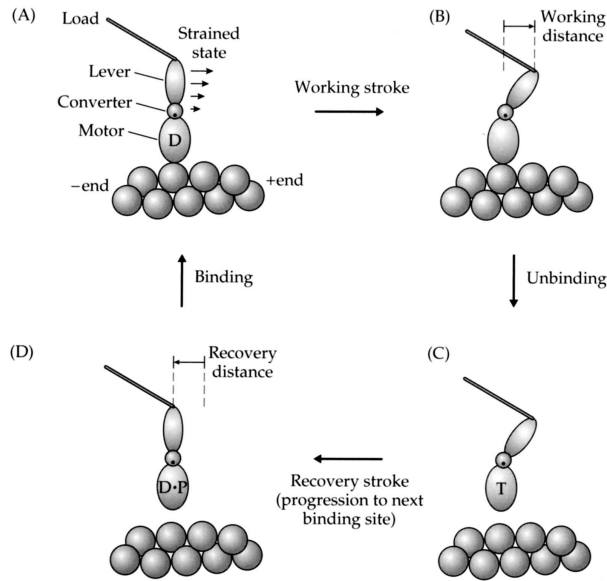


Figure 2.4: Sketch of the motor cycle for myosin. A) If the motor binds to the actin, the phosphate is released and the motor is strained. B) The strain drives a conformational change which is amplified by the lever region and moves the load. C) After release of ADP and binding of ATP, the motor leaves the filament. D) Being unbound the motor recovers its initial conformation which leads to a movement of the motor towards the next binding site on the filament. D, T and P indicate that the motor carries ADP, ATP or P_i respectively. The picture is taken from [5].

in the beating of cilia and flagella. The first motor protein, myosin, has been discovered by Huxley in 1957 during investigations of muscle contraction [61].

2.2.1 Structure and properties

The most widely accepted model that accounts for the structural, biochemical and mechanical properties of motor proteins is the *rotating crossbridge model* which involves three main steps: first, the nucleotide carried by the motor regulates the affinity of the motor to the filament. Thus the motor cycles between attached and detached states. Second, small changes in the order of angstroms in the nucleotide binding pocket of the motor must be amplified to changes of the whole protein domain in the order of nm which is called the *swinging lever arm hypothesis*. Third, an elastic element is assumed in the motor which is strained upon the conformational change and moves the load-bearing region of the motor along the filament, which is called *powerstroke* model. A cartoon of the rotating crossbridge model is shown in Fig. 2.4. Accordingly in a motor protein one should be able to discriminate three distinct regions: a motor region with a nucleotide binding pocket that creates the conformational change, a converter region that converts this change to directional motion and a lever region that amplifies it.

Myosin and Kinesin

The *myosin II* motors are associated to the actin filaments with which they build the sarcomere structure being the force generators of muscle cells. Apart from being responsible for macroscopic movement, myosins are also present in many non-muscle eukaryotic cells to organize actin networks. The structure of an individual motor as shown in Fig. 2.5 can be investigated by electron microscopy and stepwise proteolysis of the protein: by cutting

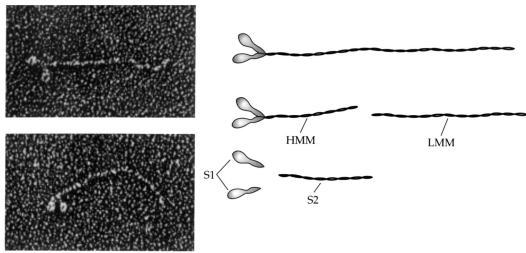


Figure 2.5: Micrographs and sketched structure of myosin II. Picture from [5].

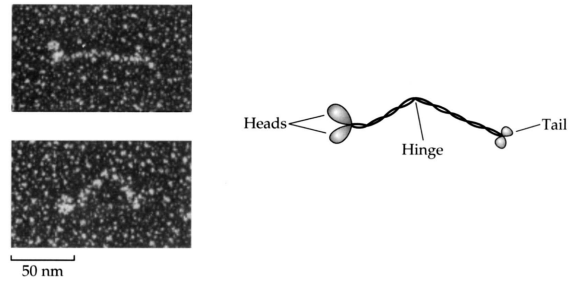


Figure 2.6: Micrographs and sketched structure of kinesin. Picture from [5].

the protein down to the *head domain* it has been shown that only this globular domain of $16.5 \times 6.5 \times 4$ nm binds to the actin filament. The head domain is an actin-activated ATPase, i.e. the ATP hydrolysis rate is accelerated in the presence of actin.

The microtubule associated motor protein *kinesin*, shown in Fig. 2.6, is used in the intracellular transport of vesicles and involved in the chromosome separation during cell mitosis. It has a size of $7 \times 4.5 \times 4.5$ nm and binds specifically to MTs. Analogously as in the actin-myosin case, here the presence of a MT catalyzes the ATPase activity, so in both cases, myosin and kinesin, the presence of the associated filament accelerates the ATP hydrolysis and therefore switches between attachment and detachment of the motor to the filament. For all motors studied so far, removing the nucleotides from the solution results in a very strong and rigid attachment of the motor to the filament.

In a so-called *motility assay* experiment [62, 63], where motor heads are attached to a substrate and exposed to a filament solution, one can watch fluorescently marked filaments being transported in specific directions. It has been established that due to the interplay of the polar structure of the filament with the molecular structure of the motor - motors are said to bind stereospecifically to their associated filaments, i.e. at a unique location on the filament and in a specific orientation - motors can walk on their associated filaments only in one direction. Skeletal muscle myosin and conventional kinesin both proceed towards the plus end⁷.

Besides the head domain, both myosin and kinesin also have a tail region consisting of a coiled-coil structure which acts as an association domain. In muscle cells, thousands of myosins are oligomerized at the tails to form the so-called thick filament, which can be μ m long and moves along the actin (thin) filament. In contrast, kinesin "works alone" with its tail attaching to the desired cargo, e.g. a vesicle. Thus in spite of structural similarities, there however is a crucial difference between the two motors: While skeletal muscle myosin acts as a one-headed motor and therefore forms oligomers to transport actin

⁷The polarity can also be shown in so-called *decoration experiments*, where the myosin motors are fluorescently labeled and attach to the actin filament in such way that the filament looks like an arrow. Therefore one defines a *barbed* and a *pointed* end, the barbed end being identical with the fast-polymerizing plus end. Recently, fluorescence techniques improved so much, especially by better removing the background light, that one can even watch single motors moving on a filament [64].

filaments, for kinesin a cooperative effect of the two heads of a single motor, cf. Fig. 2.6, leads to a continuous motion on a MT. This will become clear in sections 2.2.2 and 2.2.3. Additionally, there are also differences inside the protein families⁸.

Step sizes and forces

Step sizes and forces can be measured in single-molecule experiments using AFM or laser tweezers. For conventional kinesin, the step size is 8nm which fits nicely the distance between two tubulin dimers on the same protofilament. That kinesin follows the paths parallel to the protofilaments has been established in motility assay experiments where 13 protofilament MTs transported by a kinesin-coated surface did not rotate while MTs consisting of 12 and 14 protofilaments did [65]. The maximum force that kinesin can work against is 6pN, which can be measured with an optical tweezer where a kinesin is allowed to walk away from the center of the trap: as the distance increases, the load increases and finally the motor stalls.

Myosin only interacts transiently with an actin filament and does not step continuously along it, cf. section 2.2.2. As for kinesin, myosin II follows a path that is parallel to the axis of the filament, since the latter does not rotate in a gliding assay, demonstrating that the motor does not follow the two-stranded actin helix which would imply one rotation per pitch. In an experiment where an actin filament was "bowed" quickly past a fixed myosin head, so that there was not enough time for the bead and the filament to rotate, binding was only observed at multiples of 36nm, which is interpreted as the step size [66]. The force per head at zero velocity is about 1.5pN for myosin.

2.2.2 Processivity and duty ratio

While myosin in a muscle oligomerizes in huge arrays, kinesin "walks alone". The speeds are also very different, velocities vary from nm/s to $\mu\text{m/s}$ depending on motor type and external conditions, e.g. the load. This can be understood using the concept of *duty ratio*.

One distinguishes between *processive* and *nonprocessive* motors. Conventional kinesin is processive, i.e. a single motor moves continuously on the surface of a MT for up to several microns, corresponding to hundreds of steps with the step size of 8nm. Biochemical experiments showed that kinesin hydrolyzes more than 100 ATP molecules before dissociating, consistent with one step per ATP molecule.

In contrast, muscle myosin II is nonprocessive and a threshold density of myosin attached to the substrate surface is needed for a continuous transport of actin filaments.

⁸Apart from myosin II and conventional kinesin, there are many motors related to these two families. Interestingly, there exist proteins, namely myosin VI and the kinesin-related Ncd, which have similar protein sequences as compared to myosin II and kinesin respectively, but are both minus end-directed. This led to the assumption of the converter domain between motor and lever domain which directs the motion like a gearbox. Also the motor velocities range from 0.1 – 60 $\mu\text{m/s}$ for different myosin-related proteins and from 0.02 – 2 $\mu\text{m/s}$ for kinesin-related proteins. Additionally there are other families of motors, e.g. the MT-associated dynein, which however are poorly understood up to now.

Below this threshold, myosins attach to the filaments too short a time to produce efficient filament sliding. The threshold density varies with the length of the filaments from some hundreds to thousands of motor molecules/ μm^2 corresponding to about 50 myosins interacting in average with one actin filament to get continuous sliding.

Motor proteins move along their filaments through distances large compared to molecular dimensions, (a thick filament in a muscle can slide up to $0.7\mu\text{m}$ as the muscle contracts and a MT can slide over a kinesin-coated surface for microns) therefore the motor is supposed to work in a cyclic fashion, cf. section 2.2.3. Actually there are two cycles: a mechanical cycle, i.e. alternating attached and detached states, and a chemical cycle related to the ATP hydrolysis. During each cycle, a motor domain spends an average time τ_{on} attached to the filament and performing its working stroke and an average time τ_{off} detached from the filament in which it makes the recovery stroke returning to the initial conformation, cf. the scheme in Fig. 2.4. One therefore defines the *duty ratio* as the fraction of time a head domain spends in the attached phase,

$$r = \frac{\tau_{on}}{\tau_{on} + \tau_{off}} = \frac{\tau_{on}}{\tau_{total}} \simeq \frac{1}{N_{min}} , \quad (2.3)$$

which is related to one over the minimum number of motors N_{min} needed for a continuous sliding as this guarantees that there will be on average at least one head bound to the filament. Because the two-headed kinesin is processive, its duty ratio is $r \geq 0.5$, while for muscle myosin being able to perform continuous motion only in large aggregates of at least 50 to 100 motors, the duty ratio is small, about 0.01-0.02.

If there is a one-to-one coupling between the mechanical cycle (binding, working stroke, unbinding, recovery stroke) and the chemical cycle (ATP hydrolysis) one expects the motor speed to be equal to

$$v = k_{ATPase}\Delta , \quad (2.4)$$

with Δ as the distance traveled by each head relative to the filament per mechanical cycle and k_{ATPase} as the rate at which each head hydrolyzes a molecule of ATP. Such a coupling of the chemical to the mechanical cycle is clear⁹ from the fact that the presence of the associated filaments increases the ATPase rate. Conversely, the speed of movement increases with the ATP concentration, showing that the mechanics couples back to chemistry. The ATPase rate saturates as a function of the filament density and the maximum value k_{max}

⁹A somehow unexpected finding from the point of view of strong coupling is the fact that in a thick filament myosin can move a very large distance during the time it takes to hydrolyze a molecule of ATP. Dividing the speed by the ATPase rate gives a distance of about 400nm per myosin. This was called the step-size paradox and it was argued that myosin performs many steps with only one molecule of ATP. It can however be explained by the low duty ratio of myosin: each of the hundred or so motors needed to perform a continuous motion contributes only one step size 5nm to the distance the filament moves and hydrolyzes one ATP molecule. While this motor is detached, the other myosins sweep the filament along the rest of the way. Additionally single-molecule experiments recently confirmed that there is a one-to-one coupling between the mechanical and chemical cycle, i.e. one ATP is needed for one step.

is assumed to correspond to the ATPase rate during motility. Values are $k_{max} = 20s^{-1}$ for fast skeletal muscle myosin, $1s^{-1}$ for smooth muscle myosin and $44s^{-1}$ for kinesin.

The biological reasons for an organism having motors with low and others with high duty ratios are quite obvious: the low duty ratio, nonprocessive motor myosin is fast, since many motors act collectively while the ATPase rate has not to be very high. In contrast, the high-duty ratio, processive motor kinesin acts alone and is quite slow, since for each single step an ATP is needed meaning only very high ATPase rates would speed up the motor. But nevertheless, the motion is continuous for a single motor, important for secure transportation of loads through the cell. So while the first kind of motor can be used for fast motion and reaction, the second kind can perform slow but reliable transport.

2.2.3 The motor cycle: chemistry vs. mechanics

ATP hydrolysis and nonequilibrium

Hydrolysis of nucleotides, ATP or GTP for actin and MTs respectively, is not only responsible for the nonequilibrium polymerization discussed in section 2.1.2. The much more central role of ATP as the dominant energy currency of cells was realized first in 1941 by Lipmann [67]. ATP is involved in many biochemical reactions including the motion of motor proteins.

The hydrolysis reaction, Eq. (2.1), which can be summarized by $ATP \rightleftharpoons ADP + P_i$ has an equilibrium constant of

$$K_{eq} = \frac{[ADP]_{eq}[P_i]_{eq}}{[ATP]_{eq}} = 4.9 \times 10^5 M \quad (2.5)$$

at cytoplasmic conditions of vertebrate cells, i.e. $[Mg^{2+}]_{free} = 1mM$, $pH = 7$, ionic strength $250mM$ and temperature $25^\circ C$. Although the products, ADP and P_i , are highly favored, equilibration is extremely slow, the time scale being weeks. This stability is the reason that the gamma phosphate bond is such an ideal high-energy intermediate. The free energy of the hydrolysis reaction reads

$$\Delta G = \Delta G_0 - k_B T \ln \frac{[ATP]_{cell}}{[ADP]_{cell}[P_i]_{cell}}, \quad (2.6)$$

with the standard free energy $\Delta G_0 = -54 \times 10^{-21} J = -k_B T \ln(4.9 \times 10^5)$ leading to $\Delta G = 0$ at equilibrium and $\Delta G = \Delta G_0$ at standard chemical state, i.e. all reagents at $1M$.

In cells, the concentrations of ATP, ADP and phosphates are $\simeq 1mM$, $\simeq 10\mu M$ and $\simeq 1mM$ respectively. Thus the cellular free energy is about $-100 \times 10^{-21} J$, corresponding to $-25k_B T$, and much higher in absolute value than the standard free energy. So the metabolic processes within the cell maintain the concentrations *very far from equilibrium*.

The mechano-chemical cycle

In the case of myosin, the main features of the chemical cycle, i.e. of the hydrolysis, follow from the fact that myosin binds strongly to actin and to the gamma phosphate, but not

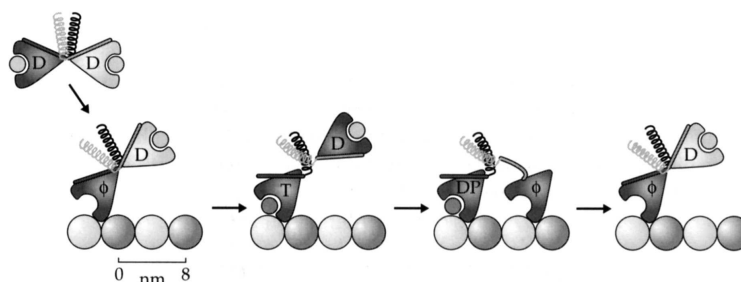


Figure 2.7: The mechanochemical cycle of kinesin and the hand-over-hand mechanism, cf. the text below. The picture is taken from [5].

to both simultaneously. By measuring rates, one can establish the following connection: The release of phosphate is catalyzed by the binding of myosin to the actin filament, i.e. actin accelerates the ATPase rate, whereas the release of myosin from the actin filament is catalyzed by the binding of ATP. Thus a mechanical step (the binding of myosin to the actin filament) is required to catalyze a chemical step (the release of phosphate), then a second chemical step (the binding of ATP) is required to catalyze a second mechanical step (dissociation of myosin from the filament). The release of phosphate in the attached state is thought to produce a highly strained state, the relaxation of this strain being the driving force for the working stroke and the sliding of the filaments. The interconnected mechano-chemical cycle for myosin has already been sketched in Fig. 2.4.

Kinesin's hydrolysis reaction is also tightly coupled to the binding and unbinding of kinesin to the MT. However, the phases between the mechanical and the chemical cycle are sort of shifted by 90 degrees: in the presence of ATP, kinesin binds tightly to the MT - in the case of myosin, ATP was needed for the unbinding - and in the absence of the associated filament, kinesin releases phosphate quickly while myosin releases it slowly. Moreover, the hydrolysis cycles of the two heads of kinesin are highly coordinated, leading to the picture of a hand-over-hand mechanism [68] as depicted in Fig. 2.7: a chemical step (ATP binds to head 1) catalyzes a mechanical step (head 2 attaches to the MT), which in turn catalyzes a chemical step (head 2 releases ADP), which in turn catalyzes a mechanical step (head 1 detaches from the MT). The release of phosphate from head 1 then completes the cycle.

Chapter 3

Prerequisites

The aim of this work is to better understand the physical aspects of the biopolymers that build up the cytoskeleton. One of these purely physical aspects is the excluded volume interaction of polymers which can lead to orientational ordering accompanied by demixing phenomena. Indeed, in the beginning of the nineties it has been found that both microtubules [19] and actin filaments [20, 21, 22, 23, 24], when extracted from cells, purified and concentrated display *in vitro* lyotropic liquid crystalline phases, i.e. the polymer solution gains orientational order if the filament density exceeds a certain threshold. This was not so surprising, because since the observations for Tobacco Mosaic Viruses [18] and the theoretical work of Onsager [26], it was clear that for long rod-like objects which cannot overlap, i.e. which interact by excluded volume or steric effects, it is favorable to order if the density is high enough. Nevertheless the polymers are not always in stable conditions, and the interplay between the polymerization process, which is the usual state inside a living cell, and the ordering may lead to something new, namely to a pattern of alternating isotropic and nematic ranges which is the topic of part I of this work.

In this chapter, after a summary of a few elementary notions for liquid crystals in section 3.1, the statistical model of Onsager is reviewed in section 3.2.1, which acts as a reference model for the model proposed in part I. Then the Doi equation is derived and shortly discussed in sections 3.2.2 to 3.2.4, which will be used to formulate a minimal model for the isotropic-nematic transition in part I and which is the starting point for the investigation of filament-motor systems in part II. Section 3.2.5 is devoted to the moment expansion technique, which will be used to derive equations for observable physical quantities, namely the moments with respect to the orientation, from the Doi equation, which is an equation for the probability distribution function. Finally, section 3.3 introduces the phenomenon of phase separation and its phenomenological description by the Cahn-Hilliard model, which is the second ingredient to formulate the model proposed in part I.

3.1 Liquid crystals (LCs)

Liquid crystalline (LC) phases are also called mesophases, after the greek word for middle, because they lie in a certain sense in the middle between a homogeneous isotropic liquid and a perfect crystalline solid. On the one side, the homogeneous isotropic liquid is invariant under arbitrary translations and rotations, so it is the state of matter with the highest symmetry, and it has only short-range but no long-range order. On the other side, a perfect crystal is the opposite limit, where there is long-range positional and orientational order but the symmetry is reduced to discrete translations and point group operations depending on the structure of the bravais lattice. Liquid crystals have orientational long-range order, not perfectly as in a crystal but nevertheless present, and no positional order (nematic phase) or positional order in one (smectic phases) or two dimensions (hexatic phases). According to the relevant control parameter which drives the liquid crystalline order, one distinguishes *thermotropic* LCs that undergo transitions by varying the temperature, i.e. by cooling, and *lyotropic* LCs which display the LC phases due to excluded volume and as a function of the density. In the cell biology context investigated here, for physiological reasons (e.g. protein stability) the temperature is not a relevant parameter. However, the cytoskeletal polymers display lyotropic LC order.

Although also cholesteric, i.e. nematic phases with an internal twist, and smectic phases have been observed in actin filaments [69], they appear at such high filament densities, that we restrict ourselves to the *nematic* phase. This is the simplest LC phase with orientational order but no long-range positional order. In the case of the cytoskeletal filaments actin and microtubules, the constituents have rod-like shape. In the nematic phase these rods point on average in a preferred direction, while the centers of mass of the molecules show liquid-like behavior, i.e. only some short-range order exists which decays rapidly after a few filament lengths.

The preferred direction in the nematic phase can be described by a unit vector $\hat{\mathbf{n}}(\mathbf{r})$, which has a $\pm\hat{\mathbf{n}}$ -symmetry and is thus called director [25]. This symmetry is due to the fact that the two ends of a rod can in general not be distinguished¹. The *scalar* order parameter describing the amount of ordering in the preferred direction specified by $\hat{\mathbf{n}}(\mathbf{r})$ is usually defined as

$$S = \langle P_2(\mathbf{u} \cdot \hat{\mathbf{n}}) \rangle = \frac{1}{2} \langle 3(\mathbf{u} \cdot \hat{\mathbf{n}})^2 - 1 \rangle , \quad (3.1)$$

which is the orientational average of the second Legendre polynomial, or more formally the second moment of the orientational distribution with respect to the orientational degree of freedom \mathbf{u} . The second polynomial or moment has to be used, since the first moment vanishes due to the $\pm\hat{\mathbf{n}}$ -symmetry. By the same symmetry reason, the full order parameter

¹In part II of this work, it is a crucial point that for cytoskeletal polymers this symmetry is broken due to the presence of molecular motors, which walk on the filaments in a specified direction and thus making the filament's head and tail distinguishable, cf. chapter 2. A consequence of this is the possibility of a finite first moment with respect to orientation. Such a phase could be called a *polar nematic*.

is not a vector, but a symmetric traceless tensor, which can be defined microscopically as

$$Q_{ij} = \frac{V}{N} \sum_{n=1}^N (u_i^n u_j^n - \frac{1}{3} \delta_{ij}) \delta(\mathbf{r} - \mathbf{r}^n) , \quad (3.2)$$

in a situation where in a certain volume V one has N rod-like particles at places \mathbf{r}^n and in orientation \mathbf{u}^n . The mean value $\langle Q_{ij} \rangle$ is zero in the isotropic, i.e. non-ordered, phase and

$$\langle Q_{ij} \rangle = S(\hat{n}_i \hat{n}_j - \frac{1}{3} \delta_{ij}) = \frac{S}{3} \begin{pmatrix} -1 & 0 & 0 \\ 0 & -1 & 0 \\ 0 & 0 & 2 \end{pmatrix} \quad (3.3)$$

in the nematic phase, where in the last expression we have chosen $\hat{\mathbf{n}} \parallel \hat{z}$.

The Onsager model of the lyotropic isotropic-nematic (I-N) transition will be reviewed in the next section in some detail since cytoskeletal polymers display this transition and we want to investigate it in the presence of polymerization kinetics in part I of this work. Here I only shortly describe the Landau-DeGennes theory [25] usually applied to thermotropics. This theory gives the important insight that the I-N transition must be first order in three dimensions and can be second order in two dimensions, simply due to the fact that the order parameter is a symmetric traceless tensor. As usual for a Landau theory of phase transitions, the free energy of the considered system is expanded formally with respect to powers of the order parameter. For a nematic liquid crystal, in the spatially homogeneous case one gets

$$\mathcal{F} = \tilde{r} \text{Tr} \langle \underline{Q} \rangle^2 - \tilde{w} \text{Tr} \langle \underline{Q} \rangle^3 + \tilde{u} (\text{Tr} \langle \underline{Q} \rangle^2)^2 . \quad (3.4)$$

Since the free energy must be rotationally invariant but the order parameter transforms like a tensor, only the scalar contributions $\text{Tr} \langle \underline{Q} \rangle^n$ can occur and as furthermore $\langle Q_{ij} \rangle$ is traceless, $n \geq 2$ holds. Inserting Eq. (3.3) into the free energy yields a simple expression in terms of the scalar order parameter,

$$\mathcal{F} = \frac{r}{2} S^2 - w S^3 + u S^4 , \quad (3.5)$$

with some renormalized coefficients r, w, u . Assuming for a thermotropic LC a temperature dependent $r = r(T - T^*)$ and constant w, u clearly leads to a temperature-driven phase transition which is of first order, i.e. discontinuous, due to the non-vanishing cubic term.

In two dimensions however, the order parameter tensor, defined in Eq. (3.3), has to be adapted to

$$\langle Q_{ij} \rangle = S(\hat{n}_i \hat{n}_j - \frac{1}{2} \delta_{ij}) = \frac{S}{2} \begin{pmatrix} -1 & 0 \\ 0 & 1 \end{pmatrix} . \quad (3.6)$$

This implies that $\text{Tr} \langle \underline{Q} \rangle^n$ vanishes for all odd n and the free energy, Eq. (3.5), is changed to

$$\mathcal{F} = \frac{r}{2} S^2 + u S^4 , \quad (3.7)$$

which describes a phase transition of second order for $r = r(T - T^*)$.

Since this argument is based solely on the tensor character of the order parameter in a nematic liquid crystal, it also holds in the lyotropic case, which is reviewed in some detail in the next section. For more information on LC phases and their theoretical description I refer to the literature [25, 70].

3.2 The rod liquid as a model for lyotropic LCs

3.2.1 The model of Onsager

In 1949 Lars Onsager introduced a model for a lyotropic liquid crystal [26]. He wrote down the free energy for a solution of infinite long rods which is in the spirit of a virial expansion with respect to the filament density. This free energy is functionally dependent on the probability distribution function (pdf) $\Psi(\mathbf{u})$ of the rods with respect to the orientation \mathbf{u} .

To have a reference, for a dilute gas of N hard spheres of density $\rho = N/V$, the virial expansion can be found in textbooks [71] and reads

$$\frac{\mathcal{F}}{Nk_B T} = \frac{\mu^0(T, \mu_0)}{k_B T} - 1 + \ln \rho + \frac{1}{2}\rho B_2 + O(\rho^2) . \quad (3.8)$$

There is an entropic contribution $\ln \rho$ and an excluded volume contribution proportional to the second virial coefficient which for spheres is just $B_2 = \frac{4}{3}\pi (2r)^3$. $\mu^0(T, \mu_0)$ is the chemical potential of the spheres at the temperature T in a solvent with the chemical potential μ_0 .

Onsager generalized this expansion for a liquid of rod-like particles to

$$\frac{\mathcal{F}}{Nk_B T} = \frac{\mu^0(T, \mu_0)}{k_B T} - 1 + \ln \rho - S_{or} + \frac{1}{2}\rho B_2 + O(\rho^2) , \quad (3.9)$$

where an additional entropic contribution occurs due to the orientational degree of freedom, namely the ordering entropy

$$S_{or} = - \int d\mathbf{u} \Psi(\mathbf{u}) \ln (4\pi \Psi(\mathbf{u})) = -\sigma . \quad (3.10)$$

The second virial coefficient is now also orientation dependent and reads

$$B_2 = \int d\mathbf{u} \int d\mathbf{u}' \beta(\mathbf{u}, \mathbf{u}') \Psi(\mathbf{u}) \Psi(\mathbf{u}') \quad (3.11)$$

with

$$\beta(\mathbf{u}, \mathbf{u}') = 2L^2 b |\mathbf{u} \times \mathbf{u}'| = 2L^2 b |\sin \gamma| \quad (3.12)$$

reflecting the excluded volume, namely the volume spanned by two rods of length L and diameter b that have directions \mathbf{u} and \mathbf{u}' respectively.

Defining the excluded volume integral

$$\omega = \frac{4}{\pi} \int d\mathbf{u} \int d\mathbf{u}' |\mathbf{u} \times \mathbf{u}'| \Psi(\mathbf{u}) \Psi(\mathbf{u}') \quad (3.13)$$

and scaling the density by

$$\rho' = v\rho = \frac{\pi}{4} L^2 b \frac{N}{V} \quad , \quad v = \frac{\pi}{4} L^2 b \quad , \quad (3.14)$$

one gets (omitting the primes) the compact formulation

$$\frac{\mathcal{F}[\Psi]}{Nk_B T} = f(T, \mu_0, \rho) + \sigma[\Psi] + \rho\omega[\Psi] \quad . \quad (3.15)$$

Minimizing this free energy functional with respect to the orientational pdf, i.e. performing $\frac{\delta \mathcal{F}[\Psi]}{\delta \Psi}$, leads to the following nonlinear integral equation

$$\ln(4\pi\Psi(\mathbf{u})) = C - \frac{8\rho}{\pi} \int d\mathbf{u}' |\mathbf{u} \times \mathbf{u}'| \Psi(\mathbf{u}') \quad , \quad (3.16)$$

where C is a constant determined by the normalization condition

$$\int d\mathbf{u} \Psi(\mathbf{u}) = 1 \quad . \quad (3.17)$$

Eq. (3.16) can be analyzed by means of approximative methods [72] or numerically [73] and yields a first-order transition to a nematic state at a critical density $\rho > \rho_c = 4$ in scaled units or

$$\rho_c = \frac{16}{\pi b L^2} \quad (3.18)$$

in unscaled units. This threshold can also be calculated from the Doi equation, cf. section 3.2.5. Onsager attacked the problem with a symmetry adopted test function, namely

$$\Psi(\mathbf{u}, \alpha) = \Psi(\theta, \alpha) = \frac{\alpha}{4\pi \sinh \alpha} \cosh(\alpha \cos \theta) \quad , \quad (3.19)$$

which allows for capturing all the physics qualitatively. It makes use of the uniaxial symmetry around the axis of preferred orientation, i.e. if \mathbf{u} is expressed in spherical coordinates there is no dependence on φ and $\cos \theta = \mathbf{u} \cdot \hat{\mathbf{n}}$ is the angle with respect to the director $\hat{\mathbf{n}}$. Additionally it interpolates between the isotropic state, $\Psi(\mathbf{u}, \alpha \rightarrow 0) = \Psi^{iso}(\mathbf{u}) = \frac{1}{4\pi}$, and the nematic state as $\Psi(\mathbf{u}, \alpha \gg 1)$ is sharply peaked around $\theta = 0$.

Phase separation near the I-N transition

Since the lyotropic I-N transition described by the Onsager model is of first order in three dimensions, cf. section 3.1, there is a density range where the nematic and the isotropic phase coexist and where the system thus phase separates into nematic and isotropic regions. For solutions of rod-like particles this was discovered first by Zocher in 1925 [74], whose experiments inspired Onsager to his theoretical work. However, phase separation takes place in many systems either when a first order transition occurs or when an interacting mixture is present. It has been investigated extensively since decades, mainly due to its broad industrial relevance, e.g. in alloys, emulsions etc.. The temporal evolution of phase separation towards a thermal equilibrium state will be reviewed in section 3.3.

The equilibrium densities of the isotropic and nematic phases in coexistence near the I-N transition can be determined by the *coexistence conditions*, i.e. the equality of osmotic pressure and chemical potential in the two coexisting phases at equilibrium. The osmotic pressure and the chemical potential are easily calculated with Eq. (3.15) to be

$$\begin{aligned}\Pi &= -\frac{\partial \mathcal{F}}{\partial V} = -Nk_B T \left(\frac{1}{\rho} \frac{\partial \rho}{\partial V} + \frac{\partial \rho}{\partial V} \omega \right) , \\ \mu &= \frac{\partial \mathcal{F}}{\partial N} = \mu^0 - k_B T + k_B T (\ln \rho + \sigma + \rho \omega) + Nk_B T \left(\frac{1}{\rho} \frac{\partial \rho}{\partial N} + \frac{\partial \rho}{\partial N} \omega \right) ,\end{aligned}$$

and eventually yield

$$\Pi = k_B T \rho (1 + \rho \omega) , \quad (3.20a)$$

$$\mu = \mu^0 + k_B T (\ln \rho + \sigma + 2\rho \omega) . \quad (3.20b)$$

In the isotropic phase, by using $\Psi(\mathbf{u}) = \Psi^{iso}(\mathbf{u}) = \frac{1}{4\pi}$, one can easily calculate that $\sigma = 0$ and $\omega = 1$. Finally, the *coexistence conditions* of equal osmotic pressure and chemical potential in both phases read

$$\rho^i (1 + \rho^i) = \rho^n (1 + \rho^n \omega) , \quad (3.21a)$$

$$\ln \rho^i + 2\rho^i = \ln \rho^n + \sigma + 2\rho^n \omega , \quad (3.21b)$$

which can be solved numerically² to determine the density ρ^i in the isotropic and ρ^n in the nematic phase [72]. We will use the argument of coexistence equations as an additional test for the model proposed in part I.

Polydispersity

An additional complication in lyotropic LC systems is polydispersity. While most thermotropic LCs are made of small identical molecules which are mesogenic (i.e. able to display

² σ and ω are functionals of ρ^n since via the minimization of the free energy the distribution $\Psi(\mathbf{u})$ depends now on ρ^n . One can make again use of Eq. (3.19) to approximate these functionals [72] and then calculate ρ^i and ρ^n .

LC phases) due to rigid subunits like aromatic rings, lyotropic LCs like the cytoskeletal polymers, Tobacco Mosaic Viruses (TMV) [18, 75] or other colloidal systems often have a distribution of rod lengths. For a recent general review we refer to [76], whereas for rod systems the problem has been investigated e.g. in Refs. [72, 77]. What happens in brief is that first the phase diagram becomes richer and richer with the appearance of various different nematic phases and second that the longer rods enrich in the nematic phases and the smaller ones in the isotropic phase, which was already guessed by Onsager in his original work [26]. For our modeling in part I we neglect polydispersity, as discussed and partly justified in section 5.2.

Onsager model in two dimensions

The rod liquid and the Onsager model can also be investigated in two dimensions (2D), meaning that the orientation \mathbf{u} of the rods is now restricted to the unit circle instead of the unit sphere. From the Landau-DeGennes argument of section 3.1 it is already clear that the I-N transition is usually of second order, i.e. continuous, in 2D so there is no phase coexistence and no phase separation anymore.

In part II we investigate a filament-motor system in two dimensions. Since the filament densities in the experiments are far below the density of the I-N transition, we will neglect the nematic order parameter in our description. To have an upper bound for the density, the critical density of the I-N transition is calculated in the framework of the Doi equation in section 3.2.5 yielding $\rho_c = \frac{3\pi}{2}$ or $\frac{3\pi}{2L^2}$ in scaled and unscaled units respectively.

LCs in two dimensions however are a subtle topic: Although the 2D-Onsager model predicts a I-N transition [78], numerical simulations yield long-range [79] or only quasi-long-range orientational order (i.e. algebraically decaying correlation functions) [80], depending on the detailed system. Additionally, the Onsager approximation of considering only the second virial coefficient is problematic in 2D. While in 3D the third virial term $\rho^2 B_3$ is of the order b/L , the ratio between the diameter and the length of the rods, and therefore small in the limit of long rods, in 2D this is no longer the case [78, 81]. The reason for this is simply that the third order virial term only contributes if the three rods are nearly in the same plane, which has a very tiny probability in 3D but is guaranteed in 2D. Since the third virial coefficient for rods is a highly complicated object, cf. Ref. [27], an analytical treatment in the framework of the Onsager theory has not been done yet. Simulations as reported in Refs. [79, 80] however imply that the I-N transition should occur at a higher density of about $\rho_c \simeq 7 > \frac{3\pi}{2}$.

3.2.2 The Doi equation

In part II of this work, the starting point of our description of a filament-motor system is the Doi theory of a rigid rod liquid [39]. It is a well studied approach in polymer and colloid science and is based on the Smoluchowski equation for rigid rods interacting by excluded volume. In the long time limit and for a system assumed spatially homogeneous one recovers the Onsager model as the stationary solution of the Doi equation. Thus the

latter can be considered as a generalization of the equilibrium Onsager theory to situations out of equilibrium. In addition, it comprises also the spatial dependence during that evolution and a microscopic treatment of the phase separation near the I-N transition in the framework of the Doi model is still ongoing research, cf. e.g. Ref. [82]. In this chapter I will motivate the Doi equation and review some useful results needed later on.

As in Onsager theory, in the Doi model one investigates a solution of rigid rods of fixed length L which are described by a probability distribution function (pdf). The probability of finding a rod at the position \mathbf{r} with the orientation \mathbf{u} (which is the unit vector along the rod, $|\mathbf{u}| = 1$) at time t is described now by the pdf $\Psi(\mathbf{r}, \mathbf{u}, t)$ ³, instead of a time- and space-independent $\Psi(\mathbf{u})$. Its temporal evolution is governed by a Smoluchowski equation [39] which is basically just the continuity equation for the probability

$$\partial_t \Psi + \nabla \cdot \mathbf{J}_t + \mathcal{R} \cdot \mathbf{J}_r = 0 . \quad (3.22)$$

For a rod, there are two kinds of (Brownian) motion, translational and rotational. Therefore not only the divergence of the translational current \mathbf{J}_t is entering Eq. (3.22), as one is familiar with from the description of Brownian point-like particles, but also the rotational degrees of freedom of the rods have to be accounted for. The orientation vector \mathbf{u} also undergoes a Brownian motion restricted to the unit sphere spanned by $|\mathbf{u}| = 1$, which can be described by the rotational current \mathbf{J}_r entering Eq. (3.22) through the dot product with the so-called rotational operator

$$\mathcal{R} = \mathbf{u} \times \partial_{\mathbf{u}} . \quad (3.23)$$

In section 3.2.3, I will motivate and explain the rotational contributions as well as the detailed form of the translational and rotational currents which read

$$J_{t,i} = -D_{ij} [\partial_j \Psi + \Psi \partial_j V_{ex}] , \quad (3.24a)$$

$$J_{r,i} = -D_r [\mathcal{R}_i \Psi + \Psi \mathcal{R}_i V_{ex}] . \quad (3.24b)$$

The first term of the translational contribution is just diffusion, which is anisotropic since in the surrounding fluid a rod can diffuse easier parallel to its orientation than perpendicular. The translational diffusion matrix therefore reads

$$D_{ij} = D_{\parallel} u_i u_j + D_{\perp} (\delta_{ij} - u_i u_j) , \quad (3.25)$$

with two different diffusion coefficients, D_{\parallel} and D_{\perp} , for parallel and perpendicular diffusion with respect to the rod axis respectively. The second term in Eq. (3.24a) is due to the excluded volume interaction

$$V_{ex}(\mathbf{r}, \mathbf{u}) = \int d\mathbf{u}' \int d\mathbf{r}' W(\mathbf{r}-\mathbf{r}', \mathbf{u}, \mathbf{u}') \Psi(\mathbf{r}', \mathbf{u}') \quad (3.26)$$

³In the following I will write $\Psi(\mathbf{r}, \mathbf{u})$ for reasons of brevity and $\Psi(\mathbf{r}, \mathbf{u}, t)$ only if we want to emphasize the time dependence.

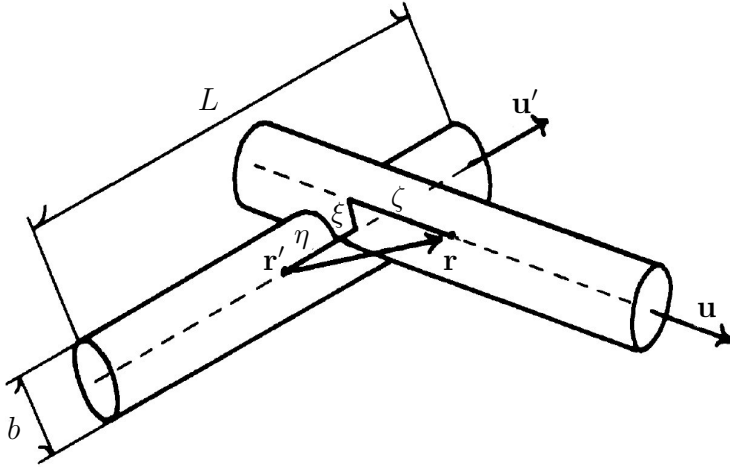


Figure 3.1: The geometry of intersecting rods in three spatial dimensions. As expressed by Eq. (3.27), an overlap corresponds to the connection vector $\mathbf{r} - \mathbf{r}'$ of the mass centers of the rods being constructable by a linear combination $\mathbf{u}\zeta + \mathbf{u}'\eta + (\mathbf{u} \times \mathbf{u}') |\mathbf{u} \times \mathbf{u}'|^{-1}\xi$. The picture has been taken from Ref. [83].

between two rods. The interaction kernel $W(\mathbf{r}-\mathbf{r}', \mathbf{u}, \mathbf{u}')$ is defined as 1 if there is overlap of the rods at (\mathbf{r}, \mathbf{u}) and $(\mathbf{r}', \mathbf{u}')$ and zero if there is no overlap.

The rotational current, Eq. (3.24b), has the same structure as the translational one, but with the spatial derivative replaced by the rotational operator \mathcal{R} and with D_r as the rotational diffusion coefficient.

The excluded volume overlap function

The excluded volume interaction, Eq. (3.26), is expressed most conveniently in terms of the so-called Straley coordinates [83] shown in Fig. 3.1. In three spatial dimensions they read

$$\mathbf{r} - \mathbf{r}' = \mathbf{u}\zeta + \mathbf{u}'\eta + \frac{\mathbf{u} \times \mathbf{u}'}{|\mathbf{u} \times \mathbf{u}'|} \xi, \quad (3.27)$$

with the volume element $d\mathbf{r}' = |\mathbf{u} \times \mathbf{u}'| d\zeta d\eta d\xi$. Overlap happens in the range $|\zeta| < \frac{L}{2}$, $|\eta| < \frac{L}{2}$ and $|\xi| < b$, where L is the length and b the diameter of the rods. In a coarse-grained model, it is only sensible to take into account spatial modulations of wavelengths much longer than the rod diameter, i.e. $|\mathbf{k}b| \ll 1$. In this limit one can suppress the term proportional to ξ in Eq. (3.27) and the ξ -integration trivially yields a factor of $2b$ leaving us with

$$W(\mathbf{r}-\mathbf{r}', \mathbf{u}, \mathbf{u}') = 2b |\mathbf{u} \times \mathbf{u}'| \int_{-L/2}^{L/2} d\zeta \int_{-L/2}^{L/2} d\eta \delta(\mathbf{r}-\mathbf{r}'+\mathbf{u}\zeta+\mathbf{u}'\eta). \quad (3.28)$$

In two spatial dimensions where the coordinates read

$$\mathbf{r} - \mathbf{r}' = \mathbf{u}\zeta + \mathbf{u}'\eta \quad (3.29)$$

one gets directly

$$W(\mathbf{r}-\mathbf{r}', \mathbf{u}, \mathbf{u}') = |\mathbf{u} \times \mathbf{u}'| \int_{-L/2}^{L/2} d\zeta \int_{-L/2}^{L/2} d\eta \delta(\mathbf{r}-\mathbf{r}'+\mathbf{u}\zeta+\mathbf{u}'\eta) . \quad (3.30)$$

The meaning of the Straley coordinates can be easier seen in the 2D version: an overlap of the rods at (\mathbf{r}, \mathbf{u}) and $(\mathbf{r}', \mathbf{u}')$ is equal to the possibility that the connection vector $\mathbf{r} - \mathbf{r}'$ of the mass centers can be constructed by a linear combination $\mathbf{u}\zeta + \mathbf{u}'\eta$ of the rod orientations with $-L/2 < \zeta, \eta < L/2$, which is nothing but Eq. (3.29). In 3D, one has also to take into account the dimension orthogonal to both filament orientations leading to Eq. (3.27). The prefactor $|\mathbf{u} \times \mathbf{u}'|$, which reflected the excluded volume in the second virial coefficient of the Onsager model, cf. Eq. (3.12), here comes into play automatically as the Jacobian of the transformation.

3.2.3 Physical motivation of the Doi equation

Point-like particles in a potential

To motivate Eqs. (3.22) and (3.24), we follow [39] and start with the well known diffusion of point-like particles with density $\rho(\mathbf{r}, t)$, where Fick's law relating the current to density gradients, $\mathbf{j}(\mathbf{r}, t) = -D\nabla\rho(\mathbf{r}, t)$, together with the continuity equation (or mass conservation) yields the diffusion equation $\partial_t\rho = -\nabla \cdot \mathbf{j} = D\Delta\rho$. Considering an external potential $V(\mathbf{r})$ exerting a force $\mathbf{F}(\mathbf{r}) = -\nabla V(\mathbf{r})$ on the particles, leads for the overdamped motion in a surrounding fluid to an average velocity \mathbf{v} , which for small forces is linear in \mathbf{F} , so

$$\mathbf{v}(\mathbf{r}) = \frac{1}{\zeta}\mathbf{F} = -\frac{1}{\zeta}\nabla V(\mathbf{r}) \quad (3.31)$$

holds, with the friction coefficient ζ of the surrounding fluid. This average velocity gives an additional current $\rho\mathbf{v}$, so that Fick's law has to be generalized to $\mathbf{j} = -D\nabla\rho - \frac{\rho}{\zeta}\nabla V$.

The friction coefficient ζ and the diffusion coefficient D are related through the famous Einstein relation

$$D = \frac{k_B T}{\zeta} . \quad (3.32)$$

In the context of the Smoluchowski equation, it can be easily derived by the demand that in equilibrium, the density should be given by the Boltzmann distribution $\rho = \rho_{eq} \sim \exp\left(-\frac{V}{k_B T}\right)$ and that the current has to vanish.

Since the particle density $\rho(\mathbf{r}, t)$ and the pdf $\Psi(\mathbf{r}, t)$ differ only by a normalization factor, with the help of Eq. (3.32) the current in Fick's law can be cast in the equivalent

forms (with \mathbf{J} now describing a probability current)

$$\begin{aligned}\mathbf{J}(\mathbf{r}, t) &= -D \left(\nabla \Psi + \frac{\Psi}{k_B T} \nabla V \right) \\ &= -\frac{1}{\zeta} \left(k_B T \nabla \Psi + \Psi \nabla V \right) \\ &= -\Psi(\mathbf{r}, t) \frac{1}{\zeta} \nabla \left(k_B T \ln \Psi + V \right) .\end{aligned}\tag{3.33}$$

Via $\mathbf{J}(\mathbf{r}, t) = \Psi(\mathbf{r}, t) \mathbf{v}(\mathbf{r}, t)$, the latter form defines the total velocity for the motion of a particle in the *effective* potential

$$V_{eff}(\mathbf{r}, t) = k_B T \ln \Psi(\mathbf{r}, t) + V(\mathbf{r}) .\tag{3.34}$$

This identification allows for the following formal argument: If one wants to describe Brownian motion in a potential $V(\mathbf{r})$, to get the probability current one has just to add the so-called *Brownian potential*, $k_B T \ln \Psi(\mathbf{r}, t)$, to the external potential $V(\mathbf{r})$, use the linear force-velocity relation Eq. (3.31) to get the velocity and multiply by the pdf, $\Psi(\mathbf{r}, t)$. We will benefit from this reasoning in the next two sections where we derive the translational and rotational currents for the diffusion of a rod-shaped particle.

Using the continuity equation of probability,

$$\partial_t \Psi + \nabla \cdot \mathbf{J} = 0 ,\tag{3.35}$$

together with the probability current in its first version of Eq. (3.33),

$$\mathbf{J}(\mathbf{r}, t) = -D \left(\nabla \Psi + \frac{\Psi}{k_B T} \nabla V \right) ,\tag{3.36}$$

one gets the Smoluchowski equation for point-like particles, which has exactly the structure of Eqs. (3.22) and (3.24a)⁴.

Translational motion of rod-like particles

In the limit of overdamped motion, or hydrodynamically speaking in the Stokes limit, the friction force on a moving particle is parallel to the velocity and linear. So for a rod-like particle one can decompose the velocity parallel and perpendicular to the rod orientation \mathbf{u} by writing

$$\mathbf{F} = \zeta_{\parallel} \mathbf{v}_{\parallel} + \zeta_{\perp} \mathbf{v}_{\perp} ,\tag{3.37}$$

⁴In the definition of the Doi model, Eqs. (3.22) and (3.24), we have set $k_B T = 1$ for convenience. The temperature window is rather small for most biological systems. Especially for the lyotropic or motor-induced ordering mechanisms under consideration, the system can be regarded as athermal.

with two generally different friction coefficients ζ_{\parallel} and ζ_{\perp} . Solving for \mathbf{v} by introducing $\mathbf{v}_{\parallel} = \mathbf{u}(\mathbf{u} \cdot \mathbf{v})$ and $\mathbf{v}_{\perp} = \mathbf{v} - \mathbf{v}_{\parallel} = (\mathbf{I} - \mathbf{u}\mathbf{u}) \cdot \mathbf{v}$ yields

$$\mathbf{v} = \left[\frac{1}{\zeta_{\parallel}} \mathbf{u}\mathbf{u} + \frac{1}{\zeta_{\perp}} (\mathbf{I} - \mathbf{u}\mathbf{u}) \right] \mathbf{F} . \quad (3.38)$$

This is the velocity that defines the translational probability current for a rod-like particle, $\mathbf{J}_t = \Psi \mathbf{v}$.

Rotational motion of rod-like particles

A torque \mathbf{M} acting on a rod in a surrounding quiescent liquid leads to an angular velocity $\boldsymbol{\omega}$. Neglecting rotations around the rod axis \mathbf{u} , one can assume that both \mathbf{M} and $\boldsymbol{\omega}$ are perpendicular to \mathbf{u} . If the motion is again overdamped and the torque is small, analogously to Eq. (3.31), there should be a linear relation

$$\boldsymbol{\omega} = \frac{1}{\zeta_r} \mathbf{M} , \quad (3.39)$$

with a rotational friction coefficient ζ_r . In formal equivalence to the translational case, we want now to express the torque in terms of a potential which is now orientationally dependent, $V(\mathbf{u})$. Considering a small rotation $\delta\boldsymbol{\phi}$, which leads to a change in orientation from \mathbf{u} to $\mathbf{u} + \delta\boldsymbol{\phi} \times \mathbf{u}$, then the work needed for this change has to equal the change in the potential, namely

$$-\mathbf{M} \cdot \delta\boldsymbol{\phi} = V(\mathbf{u} + \delta\boldsymbol{\phi} \times \mathbf{u}) - V(\mathbf{u}) = (\partial_{\mathbf{u}} V) \cdot (\delta\boldsymbol{\phi} \times \mathbf{u}) = (\mathbf{u} \times \partial_{\mathbf{u}} V) \cdot \delta\boldsymbol{\phi} \quad (3.40)$$

has to hold. Together with the rotational operator already introduced in Eq. (3.23), $\mathcal{R} = \mathbf{u} \times \partial_{\mathbf{u}}$, we have found the torque as a formal derivative of a potential, $\mathbf{M} = -\mathcal{R}V$, and Eq. (3.39) becomes

$$\boldsymbol{\omega} = -\frac{1}{\zeta_r} \mathcal{R}V . \quad (3.41)$$

Conservation of probability demands $\partial_t \Psi = -\partial_{\mathbf{u}} \cdot (\Psi \dot{\mathbf{u}})$, which can be rewritten in terms of the angular velocity by using $\dot{\mathbf{u}} = \boldsymbol{\omega} \times \mathbf{u}$ and $\partial_{\mathbf{u}} \cdot (\Psi \boldsymbol{\omega} \times \mathbf{u}) = (\mathbf{u} \times \partial_{\mathbf{u}}) \cdot (\Psi \boldsymbol{\omega})$ leading to

$$\partial_t \Psi = -\mathcal{R} \cdot \mathbf{J}_r = -\mathcal{R} \cdot (\Psi \boldsymbol{\omega}) , \quad (3.42)$$

which defines the rotational probability current \mathbf{J}_r .

Smoluchowski equation for rod-like particles - the Doi equation

Considering now both translational and orientational degrees of freedom, the continuity of probability can be written as

$$\partial_t \Psi + \nabla \cdot \mathbf{J}_t + \mathcal{R} \cdot \mathbf{J}_r = 0 , \quad (3.43)$$

with the translational current

$$\mathbf{J}_t = \Psi \mathbf{v}, \quad \mathbf{v} = - \left[\frac{1}{\zeta_{\parallel}} \mathbf{u} \mathbf{u} + \frac{1}{\zeta_{\perp}} (\mathbf{I} - \mathbf{u} \mathbf{u}) \right] \nabla V \quad (3.44)$$

and the rotational current

$$\mathbf{J}_r = \Psi \boldsymbol{\omega}, \quad \boldsymbol{\omega} = - \frac{1}{\zeta_r} \mathcal{R} V . \quad (3.45)$$

Using the formal argument of the effective potential introduced above, the potential we have to consider to describe a solution of rod-like particles is the sum of the Brownian potential and the excluded volume potential $V_{ex}(\mathbf{r}, \mathbf{u})$ defined in Eq. (3.26), namely

$$V_{eff}(\mathbf{r}, \mathbf{u}, t) = k_B T \ln \Psi(\mathbf{r}, \mathbf{u}, t) + V_{ex}(\mathbf{r}, \mathbf{u}) . \quad (3.46)$$

Implying $k_B T = 1$ again, the Einstein relation leads to $D_* = \frac{1}{\zeta_*}$ for $* = \parallel, \perp, r$, where I have introduced the rotational diffusion coefficient D_r . Finally we have arrived at the Doi model, Eqs. (3.22), (3.24) and (3.26).

3.2.4 Analyzing the Doi equation

Inserting the currents given by Eqs. (3.24) into the conservation of probability, Eq. (3.22), one explicitly gets the following partial differential equation

$$\partial_t \Psi = \partial_i D_{ij} [\partial_j \Psi + \Psi \partial_j V_{ex}] + D_r \mathcal{R}_i [\mathcal{R}_i \Psi + \Psi \mathcal{R}_i V_{ex}] \quad (3.47)$$

for the pdf $\Psi(\mathbf{r}, \mathbf{u}, t)$. The latter pdf additionally has to fulfill the normalization condition

$$\int d\mathbf{r} \int d\mathbf{u} \Psi(\mathbf{r}, \mathbf{u}) = \int d\mathbf{r} \rho(\mathbf{r}) = N = \rho V , \quad (3.48)$$

where N is the number of rods, V the sample volume and ρ the mean rod density. Due to the excluded volume interaction V_{ex} defined in Eq. (3.26), the Doi equation is both nonlinear and nonlocal in Ψ and therefore hard to deal with in the most general case. However, a stationary solution can simply be found and identified with the Onsager solution, as shown in this section. In the subsequent section I exemplify how equations for the moments of a pdf can be derived from an equation for the pdf like Eq. (3.47), which often are sufficient to describe the qualitative physics. Especially in part II of this work, such a moment expansion method is applied to derive a continuum model from Eq. (3.47), which can then be analyzed in more detail than the underlying pdf equation. As an example I also calculate the threshold densities of the I-N transition in 2D, which we need in part II as an upper density bound, from the moment equation for the nematic order parameter.

From Doi back to Onsager

Both $\partial_{\mathbf{r}}$ and \mathcal{R} being differential operators, from the structure of both the translational and the rotational part of Eq. (3.47) one can read the stationary solution $\Psi \sim \exp[-V_{ex}]$, or explicitly

$$\Psi(\mathbf{r}, \mathbf{u}) \sim \exp \left[- \int d\mathbf{u}' \int d\mathbf{r}' W(\mathbf{r}-\mathbf{r}', \mathbf{u}, \mathbf{u}') \Psi(\mathbf{r}', \mathbf{u}') \right] . \quad (3.49)$$

Redefining the normalization by introducing $\Psi = \rho \tilde{\Psi}$, multiplying by 4π and taking the logarithm yields

$$\ln(4\pi \tilde{\Psi}(\mathbf{r}, \mathbf{u})) = \text{const} - \rho \int d\mathbf{u}' \int d\mathbf{r}' W(\mathbf{r} - \mathbf{r}', \mathbf{u}, \mathbf{u}') \tilde{\Psi}(\mathbf{r}', \mathbf{u}') . \quad (3.50)$$

After transforming to the Straley coordinates, cf. Eq. (3.27), and assuming spatial homogeneity one finally gets

$$\ln(4\pi \tilde{\Psi}(\mathbf{u})) = \text{const} - 2bL^2 \rho \int d\mathbf{u}' |\mathbf{u} \times \mathbf{u}'| \tilde{\Psi}(\mathbf{u}') , \quad (3.51)$$

which is nothing but Eq. (3.16) in unscaled units. So one can conclude that the stationary solution of the Doi equation is the equilibrium distribution minimizing the free energy of the Onsager model.

3.2.5 Moment equations

Moments of a pdf

It is a well known fact from statistical mechanics, that the entire pdf is not needed for a qualitative or semi-quantitative description and that often the first few moments of the pdf catch the essential physics. As an example, we have already made use of this in the definition of the nematic order parameter as the second moment of the orientational distribution in Eq. (3.1) - higher moments are not needed to describe the I-N transition qualitatively.

Having the pdf $\Psi(\mathbf{r}, \mathbf{u}, t)$, one can define the moments with respect to the orientation vector \mathbf{u} . The zeroth moment integrates out the orientational degree of freedom and is therefore just the rod density

$$\rho(\mathbf{r}, t) = \int d\mathbf{u} \Psi(\mathbf{r}, \mathbf{u}, t) . \quad (3.52)$$

The first moment vanishes in the framework of the Doi equation, since from the $\pm\mathbf{u}$ -symmetry directly follows $\int d\mathbf{u} \mathbf{u} \Psi(\mathbf{r}, \mathbf{u}, t) = 0$. However, this is no longer the case in a filament solution interacting with motors, as investigated in part II of this work. The second moment with respect to the orientation contains the information of the nematic

order parameter tensor, which can be defined in 3D either by⁵

$$\tilde{S}_{ij}(\mathbf{r}, t) = \int d\mathbf{u} \left(u_i u_j - \frac{1}{3} \delta_{ij} \right) \Psi(\mathbf{r}, \mathbf{u}, t) \quad (3.54)$$

or by

$$S_{ij}(\mathbf{r}, t) = \int d\mathbf{u} u_i u_j \Psi(\mathbf{r}, \mathbf{u}, t) . \quad (3.55)$$

The former definition is analogous to Eq. (3.2) and has the advantage of being traceless, $\tilde{S}_{ii} = 0$, while the latter, for which $S_{ii} = \rho$ holds, is sometimes more convenient for expansions and therefore used in section 4.1.1 of part I.

Moment expansion technique

Since the moment expansion technique is extensively used in part II for a 2D system, I restrict myself here to the 2D versions of the moment expansion and the isotropic averages needed therein. The 3D case is fully analogous and has been investigated in the framework of the I-N phase separation e.g. in [84, 85]. We will also need some 3D averages in part I, where a different kind of moment expansion based on a closure relation is applied. Useful formulas for the isotropic averages can be found in appendix A.

The simple idea behind a moment expansion is to write the pdf in terms of the moments in a self-consistent way. For a 2D system with $\pm\mathbf{u}$ -symmetry, this expansion reads

$$\Psi(\mathbf{r}, \mathbf{u}, t) \simeq \frac{1}{2\pi} \left\{ \rho(\mathbf{r}, t) + 4u_\mu u_\nu \tilde{S}_{\mu\nu}(\mathbf{r}, t) \right\} , \quad (3.56)$$

while in a 2D system lacking this symmetry the first moment comes into play, as shown in detail in chapter 8 of part II. The validity of the representation, Eq. (3.56), can be checked immediately by using it to evaluate the moments again. For subsequent calculations it is convenient to define the two-dimensional orientational average, cf. Eq. (A.7), by

$$\langle A(\mathbf{u}) \rangle = \int \frac{d\mathbf{u}}{2\pi} A(\mathbf{u}) = \int_0^{2\pi} \frac{d\theta}{2\pi} A(\theta) , \quad (3.57)$$

where θ parameterizes the unit vector \mathbf{u} in two dimensions. Using some of the isotropic averaging formulas collected in appendix A.2, Eq. (3.56) correctly yields

$$\int d\mathbf{u} \Psi = \int \frac{d\mathbf{u}}{2\pi} \left\{ \rho + 4u_\mu u_\nu \tilde{S}_{\mu\nu} \right\} = \rho + 4\langle u_\mu u_\nu \rangle \tilde{S}_{\mu\nu} = \rho , \quad (3.58)$$

⁵In two spatial dimensions, instead of Eq. (3.54) one has to use the definition

$$\tilde{S}_{ij}(\mathbf{r}, t) = \int d\mathbf{u} \left(u_i u_j - \frac{1}{2} \delta_{ij} \right) \Psi(\mathbf{r}, \mathbf{u}, t) \quad (3.53)$$

for the nematic order parameter to ensure the tracelessness.

due to $\langle u_\mu u_\nu \rangle = \delta_{\mu\nu}/2$ and $\tilde{S}_{\nu\nu} = 0$. Analogously

$$\int d\mathbf{u} \left(u_\alpha u_\beta - \frac{1}{2} \delta_{\alpha\beta} \right) \Psi = \int \frac{d\mathbf{u}}{2\pi} \left(u_\alpha u_\beta - \frac{1}{2} \delta_{\alpha\beta} \right) \left\{ \rho + 4u_\mu u_\nu \tilde{S}_{\mu\nu} \right\} = \tilde{S}_{\mu\nu} \quad (3.59)$$

holds, since the term $\propto \rho$ vanishes due to $\langle u_\alpha u_\beta \rangle = \delta_{\alpha\beta}/2$ and the prefactor of $\tilde{S}_{\mu\nu}$ evaluates to one, using the above properties as well as Eq. (A.9).

Homogeneous I-N transition - 2D and 3D thresholds

Since the Onsager model is contained in the Doi equation, both models should have the same threshold density for the homogeneous I-N transition, namely $\rho_c = \frac{16}{\pi b L^2}$ in 3D. Here we determine the threshold for a 2D system by starting from the homogeneous part of the Doi equation,

$$\partial_t \Psi = -D_r \mathcal{R} [\mathcal{R} \Psi + \Psi \mathcal{R} V_{ex}], \quad (3.60)$$

and investigating the linear stability of the homogeneous and isotropic solution $\rho = \rho_0$ and $\tilde{S} = 0$. Integrating Eq. (3.60) over $\int d\mathbf{u} (u_\alpha u_\beta - \frac{1}{2} \delta_{\alpha\beta})$ yields the following equation for the nematic order parameter tensor

$$\partial_t \tilde{S}_{\alpha\beta} = -D_r \int d\mathbf{u} \left(u_\alpha u_\beta - \frac{1}{2} \delta_{\alpha\beta} \right) \mathcal{R} [\mathcal{R} \Psi + \Psi \mathcal{R} V_{ex}]. \quad (3.61)$$

Using the moment approximation, Eq. (3.56), for the pdf's on the right hand side, one can linearize the equation by writing $\mathcal{R} [\Psi \mathcal{R} V_{ex}] = \rho_0 \mathcal{R}^2 V_{ex}$. Twofold integration by parts with respect to \mathbf{u} , cf. Eq. (A.15), leads to

$$\partial_t \tilde{S}_{\alpha\beta} = -D_r \langle \mathcal{R}^2 (u_\alpha u_\beta) \Psi \rangle - D_r \langle \mathcal{R}^2 (u_\alpha u_\beta) \rho_0 V_{ex} \rangle. \quad (3.62)$$

The rotational operator terms can be evaluated by use of Eq. (A.14),

$$\mathcal{R}^2 u_\alpha u_\beta = -4 \left(u_\alpha u_\beta - \frac{1}{2} \delta_{\alpha\beta} \right), \quad (3.63)$$

and the remaining isotropic averages from Eqs. (A.12) and (A.9). Making again use of $\tilde{S}_{ii} = 0$, one ends up with

$$\partial_t \tilde{S}_{\alpha\beta} = -4D_r \left(1 - \frac{2}{3\pi} \rho_0 L^2 \right) \tilde{S}_{\alpha\beta}, \quad (3.64)$$

leading to an instability of $\tilde{S}_{\alpha\beta} = 0$ at $(1 - \frac{2}{3\pi} \rho_0 L^2) < 0$ or

$$\rho_0 > \rho_{IN}^{2D} = \frac{3\pi}{2L^2}. \quad (3.65)$$

The factor L^2 comes in from the explicit form of V_{ex} . For completeness, in the 3D case where the isotropic averages are slightly different, cf. appendix A.1, the analog of Eq. (3.64) reads

$$\partial_t \tilde{S}_{\alpha\beta} = -6D_r \left(1 - \frac{\pi}{32} \rho_0 2bL^2\right) \tilde{S}_{\alpha\beta} , \quad (3.66)$$

yielding

$$\rho_0 > \rho_{IN}^{3D} = \frac{16}{\pi b L^2} , \quad (3.67)$$

in agreement with the Onsager result [26, 73].

3.3 Phase separation and Cahn-Hilliard theory

As we have already encountered in section 3.2.1 in the context of the I-N transition, near first order transitions a region of coexistence appears. If one *quenches* the system into that region, i.e. if one suddenly changes the external conditions like the mean density in the lyotropic case or the temperature in the thermotropic case, then the system will evolve towards the equilibrium state, i.e. to the density and order parameter values given by the coexistence conditions.

The simplest system illustrating the phenomenon of phase separation is a A-B binary mixture, where the free energy density can be written as

$$f = x_A \mu_A + x_B \mu_B + k_B T x_A \ln x_A + k_B T x_B \ln x_B + u x_A x_B , \quad (3.68)$$

with the volume fractions x_A, x_B , the chemical potentials μ_A, μ_B and an interaction potential u . Due to mass conservation, $x_A + x_B = 1$ holds, and thus one can express Eq. (3.68) in terms of the volume fraction of a single species, e.g. x_A . By a simple calculation one can show that for u positive (meaning repelling interaction) and large enough, the free energy density has a double well form as shown in Fig. 3.2. The minima reflect that the repelling interaction is stronger than the thermal mixing and the system favors a separation in a phase that is rich in A and in one that is rich in B.

In principle there are two mechanisms for the homogeneous state to develop into the inhomogeneous phase separated state, *nucleation and growth* and *spinodal decomposition*. I give a short introduction to this topic here, based loosely on Refs. [70, 86], to establish technical terms like spinodal decomposition and coarsening and to motivate the Cahn-Hilliard equation used in the phenomenological model in part I of this work.

Nucleation and growth

Nucleation and growth appears for points in the phase diagram that correspond to metastable states which lie inside but not too far from the boundary of the two-phase region. To be more exact, these points lie between the *coexistence curve*, given by the minima of

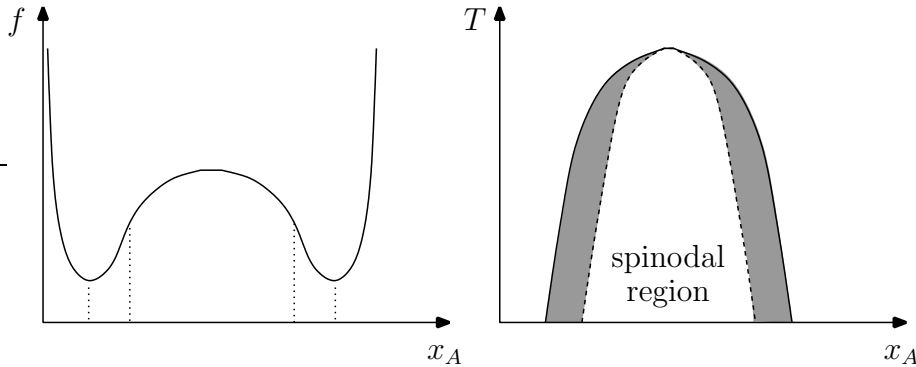


Figure 3.2: Free energy density and phase diagram of a binary mixture. The coexistence or binodal curve is defined by the minima of the free energy and shown as the solid line in the phase diagram. The spinodal line defined by the inflection points of the free energy is the dashed line. In the shaded regions between these two curves, the mixture is metastable and nucleation occurs for large enough fluctuations. In the spinodal region, spinodal decomposition takes place.

the free energy, and the *spinodal curve*, given by the inflection points of the free energy, as shown as the shaded region in the phase diagram in Fig. 3.2. Although the state is metastable, thermal fluctuations will create small droplets of the lower energy equilibrium phase inside the initially dominating metastable phase. One can show that there exists a critical droplet radius, which governs the behavior. It is given by

$$R_c = \frac{2\sigma}{\Delta f} , \quad (3.69)$$

where $\Delta f > 0$ is the free energy density difference of the metastable and equilibrium phases and σ is the energy (per area) it costs the system to create a phase boundary between the two phases. For $R < R_c$ it is too costly for the system to generate a boundary wall and the droplet shrinks. Only for $R > R_c$ the total energy can be lowered by creating an inhomogeneity, droplets spontaneously grow and create the favored equilibrium phase.

One should note that Eq. (3.69) is the most simple case that holds for a nonconserved order parameter with discrete symmetry (as in the Ising model). For a continuous symmetry, like in the I-N transition case, there are additional, e.g. elastic, contributions. For a *conserved* order parameter Φ , the conservation restriction $\int d\mathbf{r} \Phi = \text{const}$ has to be accounted for via a Lagrangian multiplier and Δf in Eq. (3.69) is no more the usual Free energy. In addition, the conservation restriction limits the accessible points in the phase diagram.

To characterize phase separation processes, the temporal behavior of the typical domain size $R(t)$ is an important measure. If one considers for simplicity a symmetric quench from $\Phi = 0$ to a parameter range where $\pm\Phi_0$ are coexisting and unstable (e.g. in an Ising model without magnetic field), then both phases are equally probable and initially will

arise on short length scales separated by long domain walls. As the system evolves the characteristic domain size will grow with time, a process which is called *coarsening* and is inherent to phase separation processes. For a symmetric quench, one can derive a simple scaling behavior, the Allen-Cahn-Equation

$$\partial_t R \propto \frac{1}{R}, \quad (3.70)$$

which implies $R(t) \sim t^{\frac{1}{2}}$.

Spinodal decomposition

As already mentioned above, spinodal decomposition appears below the spinodal curve, where the system is globally unstable due to the curvature of the free energy. However, one should not take this curve as a sharp border since it is based on a mean field concept and in real, i.e. fluctuating, systems it can become quite blurred. For a A-B mixture, the order parameter can be defined by the difference in the volume fractions of the two species, $\Phi = x_B - x_A$, which in total has to be conserved, i.e. $\int dx(\Phi(x) - \Phi_0) = 0$ with Φ_0 the homogeneous value in the one-phase region. Expanding the free energy around Φ_0

$$f = f(\Phi_0) + \frac{1}{2} \frac{\partial^2 f}{\partial \Phi^2} \Big|_{\Phi_0} (\Phi - \Phi_0)^2 + \dots, \quad (3.71)$$

where the first derivative term vanishes since Φ_0 has to be an extremum, and adding a term $\frac{c}{2}(\nabla\Phi)^2$ that accounts for the fact that variations in composition cost energy due to the formation of interfaces, one ends up with the Cahn-Hilliard (CH) model [87]

$$\partial_t \Phi = \lambda \nabla^2 \frac{\delta f}{\delta \Phi} = \lambda \nabla^2 \left[\frac{\partial^2 f}{\partial \Phi^2} \Big|_{\Phi_0} \Phi - c \nabla^2 \Phi \right]. \quad (3.72)$$

The term $\lambda \nabla^2$ (with λ being a mobility coefficient) in front of the variational derivative guarantees the conservation of the overall composition.

The simplest form of the Cahn-Hilliard model is gained using a symmetric free energy quartic in Φ and reads

$$\partial_t \Phi = \lambda \nabla^2 [D\Phi - c\nabla^2\Phi + g\Phi^3]. \quad (3.73)$$

Performing a linear stability analysis and calculating the growth rate $\sigma(q)$ of inhomogeneous modes with wave number q by the ansatz $\Phi \sim e^{\sigma t + i q x}$ one gets

$$\sigma(q) = \lambda [-Dq^2 - cq^4]. \quad (3.74)$$

Thus the homogeneous state $\Phi = 0$ is unstable for $D < 0$ (reflecting that one is in the region of spinodal decomposition, where $\frac{\partial^2 f}{\partial \Phi^2} < 0$ holds) in a wavenumber range $[0, q_{max}]$ with $q_{max} = \sqrt{\frac{-D}{c}}$. The fastest growing mode q_{fg} will dominate the early stage, thus in

contrast to the nucleation and growth process where localized droplets of inhomogeneities appeared, spinodal decomposition leads to a composition modulation throughout the sample. However, due to the nonlinearity in Eq. (3.73), q_{fg} will not prevail and the system coarsens to larger length scales in the late stages of spinodal decomposition.

To conclude, the various terms in Eq. (3.73) can be interpreted as follows: first a linear term $\propto D$ which destabilizes long wavelength modes if one is in the region of spinodal instability, i.e. for $D < 0$, second a fourth derivative term $\propto c$ which restricts the unstable modes and is motivated by the energy costs of interfaces and third a nonlinear term $\propto g$ which limits the amplitudes of the unstable modes and is responsible for the coarsening process. These ingredients will be used in the phenomenological modeling in part I of this work.

Langer has shown [86] that Eq. (3.73) can also be derived from a microscopic Fokker-Planck equation approach, and that the coarsening process can be described by a mapping of Eq. (3.73) to the "motion" not in time but in the space variable x in a double well potential. By this procedure one can describe the late stage evolution of the phase domains by a scaling law for the size of these domains. For a review of phase ordering dynamics we refer to [88].

From the viewpoint of pattern formation, the Cahn-Hilliard dynamics is not a real pattern forming instability, since there is only a fastest growing mode but not a preferred q_c at finite amplitude modulation. However, as shown in part I of this work, due to the polymerization kinetics of biopolymers during the I-N spinodal decomposition, long wavelength modulations are suppressed transforming the unstable wavenumber range $[0, q_{max}]$ of the linear Cahn-Hilliard dynamics into a window $[q_1, q_2]$ with only finite wavelengths. This mechanism has been recognized recently in a model system with a simple A-B reaction kinetics in Refs. [89, 90]. In the nonlinear regime, a wavenumber within this finite window prevails, and in the biopolymer model a critical wavenumber q_c can also be defined, cf. chapter 5.

Part I

Pattern formation in self-assembling nematic biopolymers

Chapter 4

A minimal model for the I-N phase separation

This part of my work is devoted to studying the interplay of the phase separation during the lyotropic isotropic-nematic (I-N) transition in biopolymers like actin and microtubules [19, 20, 21, 22, 23, 24] with the polymerization and depolymerization kinetics which these polymers can undergo.

The phase separation process taking place at the I-N transition is an interesting phenomenon. Previously, appropriate microscopic models have been investigated in the linear regime, e.g. in [84, 82], which however only capture the early stages of the temporal evolution. Other models are based on free energy arguments, e.g. [91], which can not unambiguously be generalized to nonequilibrium situations as for instance the polymerization kinetics present in the biopolymer systems. Therefore the aim of this chapter is to formulate a minimal nonlinear model with as few parameters as possible that describes both the I-N transition and the phase separation near that transition, which will then be generalized to take also reaction kinetics into account. The homogeneous I-N part of the model is derived from the Smoluchowski equation for rigid rods or Doi equation [39] as introduced in section 3.2.2, and the phase separation is modeled in a phenomenological way by partial differential equations similar to the Cahn-Hilliard model [87], cf. section 3.3. To secure that the model is not oversimplified, we test and compare it quite extensively to the known results from Onsager theory [26, 27, 25, 92], as reviewed in section 3.2.1.

In the following chapter we will analyze this minimal model in the presence of a very simple reaction kinetics that mimics the polymerization kinetics of the cytoskeletal biopolymers. The model presented here should however also be able to be generalized to account for other nonequilibrium situations like e.g. shear flow or molecular motors.

4.1 The I-N part of the model

4.1.1 Derivation of an order parameter equation

In this section a minimal model for the lyotropic isotropic-nematic (I-N) transition in a system of rod-like particles is presented and analyzed, which can be derived from the Doi equation reviewed in Sec. 3.2.2. The resulting evolution equation for the nematic order parameter resembles that derived by a Landau-DeGennes expansion of the free energy in terms of the order parameter. Nevertheless, our derivation has the conceptual advantage that it does not rely on arguments needing the assumption of thermal equilibrium. So in spite of similarities in the resulting equations, the derivation based on a kinetic equation like the Smoluchowski equation for rigid rods is better justified in the face of nonequilibrium situations than formulating a free energy functional, adding nonequilibrium processes and assuming that the free energy still gives a good description. In addition, by the mesoscopic treatment as used here no extra parameters in front of the nonlinear terms have to be introduced, as would be the case for the Landau-deGennes approach.

Our starting point is the Doi equation for a spatially homogeneous situation, so from Eqs. (3.22) and (3.24b) we can read

$$\partial_t \Psi = D_r \mathcal{R}_i [\mathcal{R}_i \Psi + \Psi \mathcal{R}_i \bar{V}_{ex}] \quad (4.1)$$

with $\mathcal{R} = \mathbf{u} \times \partial_{\mathbf{u}}$. The excluded volume contribution, cf. Eq. (3.26),

$$V_{ex}(\mathbf{r}, \mathbf{u}) = \int d\mathbf{u}' \int d\mathbf{r}' W(\mathbf{r}-\mathbf{r}', \mathbf{u}, \mathbf{u}') \Psi(\mathbf{r}', \mathbf{u}') \quad (4.2)$$

with the overlap kernel

$$W(\mathbf{r}-\mathbf{r}', \mathbf{u}, \mathbf{u}') = 2b|\mathbf{u} \times \mathbf{u}'| \int_{-L/2}^{L/2} d\zeta \int_{-L/2}^{L/2} d\eta \delta(\mathbf{r}-\mathbf{r}'+\mathbf{u}\zeta+\mathbf{u}'\eta) \quad (4.3)$$

can be simplified in the spatially homogenous case to Onsager's excluded volume, cf. Eq. (3.12),

$$\bar{V}_{ex}(\mathbf{r}, \mathbf{u}) = 2bL^2 \int d\mathbf{u}' |\mathbf{u} \times \mathbf{u}'| \Psi(\mathbf{u}') . \quad (4.4)$$

Thus Eq. (4.1) becomes explicitly

$$\partial_t \Psi = D_r \mathcal{R}_i \left[\mathcal{R}_i \Psi + 2bL^2 \Psi \mathcal{R}_i \int d\mathbf{u}' |\mathbf{u} \times \mathbf{u}'| \Psi(\mathbf{u}') \right], \quad (4.5)$$

whose stationary solution is identical with the one predicted by the Onsager model, as has been shown in Sec. 3.2.4.

Since we are interested in a simple model, we should extract from Eq. (4.5), which governs the evolution of the whole pdf, an equation for the nematic order parameter which describes the I-N transition. For this purpose the moments of the pdf are used, as already exemplified in section 3.2.5. We define the orientational moment of order p as the following tensorial quantity of rank p

$$S_{n_1..n_p}^{(p)}(t) = \int d\mathbf{u} u_{n_1}..u_{n_p} \Psi(\mathbf{u}, t) . \quad (4.6)$$

Due to the $\pm\mathbf{u}$ -symmetry of the rods, all odd moments of Ψ vanish. Normalization implies that the zeroth moment is the number of particles or the homogeneous particle density, depending on the chosen normalization¹

$$S^{(0)} = \int d\mathbf{u} \Psi(\mathbf{u}) = \rho . \quad (4.7)$$

The second moment describes the degree of orientation, cf. Eq. (3.55),

$$S_{nm}^{(2)} = \int d\mathbf{u} u_n u_m \Psi(\mathbf{u}) =: S_{nm} . \quad (4.8)$$

This definition differs slightly from the standard version given in Ref. [25] and by Eq. (3.54). However both variants obviously provide the same information and can be transformed into each other. The definition of Eq. (4.8) is just more convenient here as will become clear later on.

To make the orientational integral feasible in Eq. (4.5), the Jacobi determinant in the overlap integral is approximated as follows

$$|\mathbf{u} \times \mathbf{u}'| \simeq \frac{5\pi}{16} \left[1 - \frac{3}{5}(\mathbf{u} \cdot \mathbf{u}')^2 \right] . \quad (4.9)$$

This approximation, as given in Refs. [93, 94], is similar to the Taylor expansion of $|\mathbf{u} \times \mathbf{u}'|$ in terms of bilinear products of \mathbf{u} and \mathbf{u}' , $|\mathbf{u} \times \mathbf{u}'| = 1 - \frac{1}{2}(\mathbf{u} \cdot \mathbf{u}')^2$, which we could have also used yielding slightly more complicated prefactors. With the use of this approximation, an integration $\int d\mathbf{u} u_n u_m$ on both sides of Eq. (4.5) finally yields an equation for the order parameter S_{nm} ² (summation convention is implied)

$$\partial_t S_{nm} = -6D_r \left(S_{nm} - \frac{1}{3}\rho\delta_{nm} \right) + D_r \frac{3}{2}\pi bL^2 \left(S_{ni}S_{im} - S_{nmij}^{(4)}S_{ij} \right) . \quad (4.11)$$

¹In the inhomogeneous case $\int d\mathbf{r} S^{(0)}(\mathbf{r}, t) = \int d\mathbf{r} \int d\mathbf{u} \Psi(\mathbf{r}, \mathbf{u}, t) = \int d\mathbf{r} \rho(\mathbf{r}, t) = N$, with N the number of particles, holds. Thus the zeroth moment with respect to orientation is the density $\rho(\mathbf{r}, t)$, cf. Eq. (3.52). Therefore I have chosen here also for the homogeneous case the normalization to the density.

²It should be mentioned that by performing the integration $\int d\mathbf{u}'$, the excluded volume term can be cast into an effective potential of the Maier-Saupe form [95] with no parameters to be adjusted (as it is the case in Doi theory cf. [39, 96])

$$V_{eff} = \frac{5\pi}{8} bL^2 \left[1 - \frac{3}{5} S_{ij} u_i u_j \right] . \quad (4.10)$$

Here we have made use of the integration by parts rule, cf. Eq. (A.5),

$$\int d\mathbf{u} A(\mathbf{u}) \mathcal{R}[B(\mathbf{u})] = - \int d\mathbf{u} \mathcal{R}[A(\mathbf{u})] B(\mathbf{u}) \quad (4.12)$$

and of Eq. (A.6),

$$\mathcal{R}^2 u_\alpha u_\beta = -6 \left(u_\alpha u_\beta - \frac{1}{3} \delta_{\alpha\beta} \right) , \quad (4.13)$$

for the action of the rotational operator \mathcal{R} defined in Eq. (3.23).

The appearance of an unknown higher moment in Eq. (4.11), here of the fourth moment $S_{nmij}^{(4)}$, is a problem typical for procedures trying to extract equations for the moments from an equation of the respective pdf. One could derive by the same procedure an equation for $S^{(4)}$, but this will contain the unknown moment $S^{(6)}$, and so on. A similar problem appears in deriving correlation functions from pdf equations, e.g. in the BBGKY hierarchy in statistical mechanics or Ornstein-Zernike theory, cf. e.g. Ref. [97].

What has to be done to solve the dilemma is to use a suitable "closure relation". This is an empirical or physically sensible relation that approximately expresses the unknown higher moment by means of the known moments. Such procedures have been studied e.g. for a hydrodynamic theory of colloids in Ref. [98]. If one does not know better, one can apply the so-called "decoupling approximation", i.e.

$$S_{nmij}^{(4)} = S_{nm} S_{ij}. \quad (4.14)$$

This is already enough for a qualitative description of the I-N transition, cf. Ref. [39], but it is an unnecessarily bad approximation. For the investigation of phase separation during I-N transition in shear flow, in Ref. [94] there has been proposed a more accurate approximation of the fourth order moment, as described in the next section, which will lead us to the following evolution equation for the order parameter

$$\partial_t S_{nm} = -6D_r \left(S_{nm} - \frac{1}{3} \rho \delta_{nm} \right) + D_r \frac{18}{20} \pi b L^2 \left(S_{ni} S_{im} - \frac{1}{\rho} S_{nm} S_{ij} S_{ji} \right) . \quad (4.15)$$

4.1.2 The closure relation method

For evaluating Eq. (4.11), we do not really need an approximation for $S_{nmij}^{(4)}$, but rather one for $S_{nmij}^{(4)} S_{ij}$ (with summation), in terms of S_{ij} . In a work on the influence of shear flow on the phase separation near the I-N transition [94], a rather accurate closure relation was presented which expresses the contraction of the fourth order orientational moment $S^{(4)}$ with a second rank tensor M in terms of powers of the second moment S and this tensor M by interpolating between the perfectly isotropic and the perfectly aligned state.

First we introduce the three-dimensional isotropic orientational average, cf. Eq. (A.1),

$$\langle A(\mathbf{u}) \rangle = \int \frac{d\mathbf{u}}{4\pi} A(\mathbf{u}) = \int_0^{2\pi} \frac{d\varphi}{2\pi} \int_0^\pi \frac{d\theta}{2} \sin(\theta) A(\theta, \varphi) , \quad (4.16)$$

where in the second step spherical coordinates (θ, φ) have been introduced.

In the isotropic state, all moments can be calculated exactly, since they are just isotropic averages. For the fourth moment one gets

$$S_{ijkl}^{(4)} = \langle u_i u_j u_k u_l \rangle = \frac{1}{15} (\delta_{ij} \delta_{kl} + \delta_{ik} \delta_{jl} + \delta_{il} \delta_{jk}) . \quad (4.17)$$

In the opposite limit, in the perfectly aligned state, one can express $S^{(4)}$ simply by the nematic director $\hat{\mathbf{n}}$,

$$S_{ijkl}^{(4)} = \hat{n}_i \hat{n}_j \hat{n}_k \hat{n}_l . \quad (4.18)$$

For the product $S_{nmij}^{(4)} M_{ij}$ of the fourth order moment with a symmetric tensor M , one can make an ansatz which is linear in M and up to second order in powers of the nematic order parameter tensor S ,

$$\begin{aligned} S_{ijkl}^{(4)} M_{kl} = & c_1 S_{in} M_{nj} + c_2 M_{in} S_{nj} + c_3 \delta_{ij} S_{nm} M_{mn} + c_4 S_{ij} M_{nn} \\ & + c_5 S_{in} S_{nm} M_{mj} + c_6 S_{in} M_{nm} S_{mj} + c_7 M_{in} S_{nm} S_{mj} \\ & + c_8 S_{ij} S_{nm} M_{mn} + c_9 M_{ij} S_{nm} S_{mn} . \end{aligned} \quad (4.19)$$

By using the symmetries of $S^{(4)}$ and S , the consistency condition

$$S_{ikl}^{(4)} M_{kl} = \langle u_i u_j u_k u_l \rangle M_{kl} = \langle u_k u_l \rangle M_{kl} = S_{kl} M_{kl} \quad (4.20)$$

and the two analytically known values for the fully isotropic and nematic states one obtains exactly the number of conditions to fix all expansion coefficients. By this procedure one has interpolated the desired contraction of the fourth moment between the isotropic and the fully nematic state, yielding

$$\begin{aligned} S_{ijkl}^{(4)} M_{kl} = & \frac{1}{5} \left[S_{ik} M_{kj} + M_{ik} S_{kj} - S_{ik} S_{kl} M_{lj} - M_{ik} S_{kl} S_{lj} \right. \\ & \left. + 2S_{ik} M_{kl} S_{lj} + 3S_{ij} S_{kl} S_{kl} \right] . \end{aligned} \quad (4.21)$$

If we use explicitly S_{ij} in place of M_{ij} , one gets

$$S_{ijkl}^{(4)} S_{kl} = \frac{1}{5} \left[2S_{ik} S_{kj} + 3S_{ij} S_{kl} S_{kl} \right] , \quad (4.22)$$

which has been used in the last section en route from Eq. (4.11) to Eq. (4.15).

4.1.3 Homogeneous bifurcation analysis

In the last two sections we have derived an evolution equation for the order parameter tensor, Eq. (4.15),

$$\partial_t S_{nm} = -6D_r \left(S_{nm} - \frac{1}{3} \rho \delta_{nm} \right) + D_r \frac{18}{20} \pi b L^2 \left(S_{ni} S_{im} - \frac{1}{\rho} S_{nm} S_{ij} S_{ji} \right) . \quad (4.23)$$

In a uniaxial nematic phase, the orientational order can be more easily described by a scalar order parameter, which accounts for the degree of orientation, and by the director, which specifies the direction of the preferred orientation. If one chooses this mean orientation of the rods to be the x -axis of the cartesian coordinate system³, the order parameter tensor as defined in Eq. (4.8) becomes diagonal,

$$S_{nm} = \rho \operatorname{diag} \left(\bar{\lambda}, \frac{1}{2}(1 - \bar{\lambda}), \frac{1}{2}(1 - \bar{\lambda}) \right) , \quad (4.24)$$

with $\bar{\lambda}$ being the largest eigenvalue. The two other eigenvalues must be equal due to the cylindrical symmetry around the director. Their values as well as the fact that $S \propto \rho$ are due to the following relation for the trace of S (remember that \mathbf{u} is a unit vector)

$$S_{nn} = \int d\mathbf{u} u_n u_n \Psi(\mathbf{u}) = \int d\mathbf{u} \Psi(\mathbf{u}) = \rho . \quad (4.25)$$

From Eq. (4.24) one can read that in the perfectly nematic phase $\bar{\lambda} = 1$ holds, while in the isotropic phase $S_{nm}^{iso} = \frac{1}{3}\rho\delta_{nm}$ implies that $\bar{\lambda} = 1/3$. It is convenient to separate the isotropic contribution to the order parameter from the orientational contribution via $\bar{\lambda} = \frac{1}{3} + \lambda$ and to introduce a dimensionless rod density

$$\tilde{\rho} = \rho \frac{\pi b L^2}{20} , \quad (4.26)$$

with L and b the length and the diameter of the rods respectively. Then one gets from Eq. (4.23) the following nonlinear equation for λ (omitting the tilde on the density)

$$\dot{\lambda} = -6D_r \left[(1 - \rho)\lambda - \frac{3}{2}\rho\lambda^2 + \frac{9}{2}\rho\lambda^3 \right] . \quad (4.27)$$

Linearizing Eq. (4.27) around $\lambda = 0$, one obtains

$$\dot{\lambda} = -6D_r(1 - \rho)\lambda , \quad (4.28)$$

and by a Fourier ansatz $\lambda \sim e^{\sigma t}$ one finds that beyond a critical density⁴ of

$$\rho_c = 1 , \quad (4.29)$$

the growth rate σ of the homogeneous orientation mode becomes positive, the homogeneous isotropic state $\lambda = 0$ loses its stability and the nematic phase starts to form. This

³In the nematic state this is of course legitimate but since we are dealing with the I-N transition this is only an approximation. In the isotropic phase, the preferred direction of orientation is not yet given and one should use the full order parameter tensor instead, cf. [99]. Nevertheless we are looking for a minimal model and neglect these complications here.

⁴The critical value $\rho_c = 1$ corresponds to the critical rod density $\frac{20}{\pi b L^2}$ in unscaled units. This deviation from the critical density $\frac{16}{\pi b L^2}$ as calculated by the Onsager theory is a result of the expansion in Eq. (4.9).

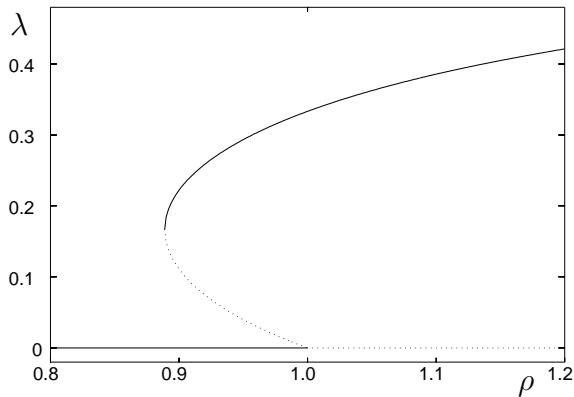


Figure 4.1: The bifurcation diagram according to Eq. (4.32) as a minimal description of the homogeneous lyotropic I-N transition. The largest eigenvalue λ of the orientational order parameter S_{nm} is shown as a function of the rod density ρ in units of $\frac{20}{\pi b L^2}$. Stable branches are drawn as solid lines, while unstable branches are dotted. At $\rho = \rho_c = 1$ a first order transition to the nematic state takes place. The unstable branch λ_- and the stable branch λ_+ meet at a saddle node at $\rho_{sn} = 8/9$.

bifurcation to a homogeneous nematic state with $\lambda \neq 0$ is discontinuous (subcritical) and the stationary values of the largest eigenvalue of the nematic order parameter tensor can be determined by the stationary solutions of Eq. (4.27) to be

$$\lambda_{\pm}(\rho) = \frac{1}{6} \pm \frac{1}{6} \sqrt{9 - \frac{8}{\rho}}. \quad (4.30)$$

Both solution branches emerge as a saddle node at $\rho_{sn} = 8/9$. The λ_+ -branch exists for all values larger than ρ_{sn} and tends in the limit $\rho \rightarrow \infty$ to $2/3$ ($\bar{\lambda}_+$ tends to 1), whilst the λ_- -branch ceases to exist at $\rho = \rho_c = 1$, the threshold of the I-N transition. λ_+ is a stable and λ_- an unstable branch, as is easily established: linearizing Eq. (4.27) around a homogeneous λ_0 by writing $\lambda = \lambda_0 + \tilde{\lambda}$ with a small homogeneous deviation $\tilde{\lambda}$ one gets

$$\dot{\tilde{\lambda}} = -6D_r \left[1 - \rho \left(1 + 3\lambda_0 - \frac{27}{2}\lambda_0^2 \right) \right] \tilde{\lambda} \quad (4.31)$$

Inserting λ_+ one calculates that this branch is marginally stable at ρ_{sn} and stable for $\rho > \rho_{sn}$. λ_- however is unstable in its whole existence region, which is also clear from the topology of a backward bifurcation. The full homogeneous bifurcation diagram⁵ is shown in Fig. 4.1.

For our qualitative considerations we can absorb the factor 6 in Eq. (4.27) into the rotational diffusion coefficient, which is the only free model parameter. Thus as the description of the I-N transition, in the following we will use

$$\dot{\lambda} = -D_r \left[(1 - \rho)\lambda - \frac{3}{2}\rho\lambda^2 + \frac{9}{2}\rho\lambda^3 \right]. \quad (4.32)$$

with λ the largest eigenvalue of the order parameter tensor and ρ the dimensionless rod density in units of $\frac{20}{\pi b L^2}$.

⁵One should note that, the model having only a third order polynomial in λ , the detailed structure of the unstable branch near the bifurcation point is wrong. However, here we are mainly interested in the influence of the reaction kinetics on the stable nematic branch.

4.2 The phenomenological model

After the preparations of the last sections, we are now able to formulate our minimal model that describes both the lyotropic isotropic-nematic (I-N) transition and the phase separation into isotropic and nematic domains in the coexistence region of the both phases. To keep in mind our aim again, the model described here will be generalized in the next chapter to the nonequilibrium state of polymerization kinetics in biopolymers and thus we will not rely on arguments based on equilibrium statistical physics.

As we have seen in the last section, the largest eigenvalue λ of the nematic order parameter tensor is sufficient to describe the strength of the orientational order. For a constant director orientation $\hat{\mathbf{n}}$ throughout the sample, which neglects director distortions and defects, spatial variations of ρ and λ however allow for spatially alternating isotropic and nematic ranges. Since it is known for long rods that the preferred director orientation is parallel to the isotropic–nematic interface [91], we assume spatial variations only in the direction perpendicular to $\hat{\mathbf{n}}$, which we will call the x -direction. Therefore in a first approach we can concentrate on an effectively one-dimensional model.

For the I-N transition, with Eq. (4.32) we have already a homogeneous equation for the order parameter. However, the phase separation of the order parameter is reflected also in the density, as can be seen from the coexistence equations (3.21) in the framework of the Onsager model. Therefore we need in total two equations, one for the rod density and one for the largest eigenvalue of the order parameter. The phase separation should be accounted for by Cahn-Hilliard terms, cf. section 3.3, in both the density and the order parameter equation, which are driven, i.e. acquire a positive effective diffusion coefficient, in a mutual way: in case of the density equation by the order parameter, reflecting the starting of phase separation for the density if the I-N transition starts and λ becomes nonzero, and in case of the order parameter equation by the density, since the I-N transition for lyotropic systems is driven by the density, this transition and the phase separation occurring at the same threshold density ρ_c [84].

In summary, we choose the following phenomenological model for the conserved rod density $\rho(x, t)$ and for the nonconserved order parameter field $\lambda(x, t)$

$$\partial_t \rho = D_\rho \partial_x^2 [-\lambda \rho - \delta_\rho \partial_x^2 \rho + a_\rho \rho^3] , \quad (4.33a)$$

$$\begin{aligned} \partial_t \lambda = & -D_r \left[(1 - \rho) \lambda - \frac{3}{2} \rho \lambda^2 + \frac{9}{2} \rho \lambda^3 \right] \\ & + D_\lambda \partial_x^2 [(1 - \rho) \lambda - \delta_\lambda \partial_x^2 \lambda + a_\lambda \lambda^3] . \end{aligned} \quad (4.33b)$$

The spatially homogeneous part of the order parameter equation (4.33b) is just Eq. (4.32) which has been derived in the last section, with ρ the filament density. The factor ρ in front of the nonlinear terms reflects the fact that the orientational order is driven by excluded volume interaction. Since the rod density is a conserved quantity, the homogeneous solution of Eq. (4.33a) is just $\rho = \rho_0 = \text{const}$, while the homogeneous solutions of Eq. (4.33b) are

given as in the last section by

$$\lambda_0 = 0, \quad \lambda_{\pm} = \frac{1}{6} \pm \frac{1}{6} \sqrt{9 - \frac{8}{\rho_0}}. \quad (4.34)$$

As before $\lambda_0 = 0$ corresponds to the isotropic rod distribution that becomes linearly unstable with respect to homogeneous nematic fluctuations beyond the critical density $\rho > \rho_c = 1$. The homogeneous orientational order fluctuations grow up to the homogeneously stable upper nematic branch λ_+ . Since the I-N transition is of first order, both the isotropic and the nematic state coexist in a range $\frac{8}{9} \leq \rho \leq 1$ where additionally a second but unstable nematic branch λ_- exists. This has already been displayed in Fig. 4.1.

Eq. (4.33a) is of the Cahn-Hilliard type [87] as introduced in Section 3.3. Expressing its right hand side by the divergence of a current density

$$j_{\rho}(x) = -D_{\rho} \partial_x \mu(x) \quad \text{with} \quad \mu(x) = -\lambda \rho - \delta_{\rho} \partial_x^2 \rho + a_{\rho} \rho^3, \quad (4.35)$$

it takes the form of a conservation law for the density of the rod-like particles. The first term in Eq. (4.33a), i.e. $-D_{\rho} \partial_x^2 (\lambda \rho)$, destabilizes the spatially homogeneous particle density for any finite value of λ (λ is always positive). This mimics Onsagers prediction [26, 92] that the free energy can be reduced by separating the system into isotropic ranges of low rod density ρ_i and nematic regions of high density ρ_n . The second term describes an isotropic-nematic interface energy that suppresses high wavenumber modes and the third term limits the modulation amplitudes of the density. So the density equation (4.33a) is a straightforward application of Cahn-Hilliard theory, where the effective diffusion is governed by the nematic order parameter λ as implied by empiricism.

As can be seen in the framework of the Doi equation [84], beyond a critical density, which coincides with the threshold for the I-N transition, i.e. $\rho_c = 1$, an instability of the isotropic distribution against *inhomogeneous* order parameter fluctuations occurs. In the order parameter equation (4.33b) this is taken into account by the term $\partial_x^2 ((1 - \rho)\lambda)$, which leads to a negative effective diffusion coefficient for $\rho > \rho_c = 1$. The successional two terms again limit the high wavenumbers and the amplitudes of the nonlinear modulations of λ as usual in Cahn-Hilliard theory.

It should be noted that Eqs. (4.33) are intended to be a minimal model. Additional nonlinearities which cannot be ruled out, e.g. by symmetry reasons, are not crucial for our qualitative reasoning, neither for the I-N transition nor for the occurrence of phase separation. Nevertheless, the details of the nonlinear dynamics would of course be changed by additional terms.

4.2.1 Linear stability analysis

In this section we answer the question how the model defined by Eqs. (4.33) allows for instabilities of the homogeneous solutions ρ_0 and $\lambda_0 = 0, \lambda_-, \lambda_+$, cf. Eq. (4.34), towards inhomogeneous solutions as should be expected from the phase separation within the co-existence region.

With the ansatz $\rho(x, t) = \rho_0 + \tilde{\rho}(x, t)$ and $\lambda(x, t) = \lambda_0 + \tilde{\lambda}(x, t)$ we separate the homogeneous parts of the filament density and the order parameter from the spatially inhomogeneous parts and linearize Eqs. (4.33) with respect to the assumed small inhomogeneous contributions $\tilde{\rho}(x, t)$ and $\tilde{\lambda}(x, t)$. By this procedure, a set of two coupled linear equations is obtained that can be written in matrix form

$$\partial_t \mathbf{w}(x, t) = \mathcal{L}_0 \mathbf{w}(x, t) = \begin{pmatrix} \mathcal{L}_{11}^{(0)} & \mathcal{L}_{12}^{(0)} \\ \mathcal{L}_{21}^{(0)} & \mathcal{L}_{22}^{(0)} \end{pmatrix} \mathbf{w}(x, t), \quad (4.36)$$

for the two-component vector

$$\mathbf{w}(x, t) = \begin{pmatrix} \rho(x, t) \\ \lambda(x, t) \end{pmatrix}, \quad (4.37)$$

where the tildes have been omitted once again. The components of the linear operator \mathcal{L}_0 read explicitly

$$\begin{aligned} \mathcal{L}_{11}^{(0)} &= D_\rho [-\lambda_0 - \delta_\rho \partial_x^2 + 3a_\rho \rho_0^2] \partial_x^2, \\ \mathcal{L}_{12}^{(0)} &= -D_\rho \rho_0 \partial_x^2, \\ \mathcal{L}_{21}^{(0)} &= -D_r \left[-\lambda_0 - \frac{3}{2} \lambda_0^2 + \frac{9}{2} \lambda_0^3 \right] - D_\lambda \lambda_0 \partial_x^2, \\ \mathcal{L}_{22}^{(0)} &= -D_r \left[1 - \rho_0 \left(1 + 3\lambda_0 - \frac{27}{2} \lambda_0^2 \right) \right] + D_\lambda [1 - \rho_0 - \delta_\lambda \partial_x^2 + 3a_\lambda \lambda_0^2] \partial_x^2. \end{aligned} \quad (4.38)$$

Since only linearizations performed around homogeneously stationary states make sense, the entry $\mathcal{L}_{21}^{(0)}$ can be simplified by using the stationary solutions of Eq. (4.32),

$$\dot{\lambda} = 0 = -D_r \left[(1 - \rho) \lambda - \frac{3}{2} \rho \lambda^2 + \frac{9}{2} \rho \lambda^3 \right], \quad (4.39)$$

implying

$$\lambda_0 = \rho_0 \left(\lambda_0 + \frac{3}{2} \lambda_0^2 - \frac{9}{2} \lambda_0^3 \right). \quad (4.40)$$

One therefore gets

$$\mathcal{L}_{21}^{(0)} = D_r \frac{\lambda_0}{\rho_0} - D_\lambda \lambda_0 \partial_x^2 \quad (4.41)$$

for linearizations around ρ_0 and λ_0 that are stationary concerning homogeneous fluctuations.

Linear analysis, isotropic state

Let's at first consider the homogeneous isotropic state, i.e. ρ_0 is finite and $\lambda_0 = 0$. By Fourier transforming the linear operator by the ansatz $e^{\sigma t + i q x}$, \mathcal{L}_0 becomes

$$\mathcal{L}_0 = \begin{pmatrix} -D_\rho (\delta_\rho q^2 + 3a_\rho \rho_0^2) q^2 & D_\rho \rho_0 q^2 \\ 0 & -D_r (1 - \rho_0) - D_\lambda (1 - \rho_0 + \delta_\lambda q^2) q^2 \end{pmatrix}. \quad (4.42)$$

The eigenvalues can be read directly from the diagonal elements to be

$$\begin{aligned} \sigma_\rho(q) &= -D_\rho (\delta_\rho q^2 + 3a_\rho \rho_0^2) q^2, \\ \sigma_\lambda(q) &= -D_r (1 - \rho_0) - D_\lambda (1 - \rho_0 + \delta_\lambda q^2) q^2. \end{aligned} \quad (4.43)$$

The homogeneous density is conserved, $\sigma_\rho(0) = 0$, and stable since $\sigma_\rho < 0$ holds for all finite wavenumbers ($\delta_\rho, a_\rho > 0$ are assumed). Thus inhomogeneous density fluctuations are always damped if there is no nematic order. In contrast, orientational fluctuations grow for $\rho_0 > \rho_c = 1$ both homogeneously through the term $\propto D_r$ and inhomogeneously through the contribution $\propto D_\lambda$. Thus an initially homogeneous nematic state is built up by the D_r -contribution and simultaneously the phase separation starts due to the Cahn-Hilliard term $\propto D_\lambda$. Orientational fluctuations grow in the range $[0, q_{max}[$ wherein $\sigma_\lambda > 0$ holds. The upper border of the unstable wavenumbers can be calculated to be

$$q_{max} = \sqrt{\frac{\varepsilon}{2\delta_\lambda} \left(1 + \sqrt{1 + 4 \frac{D_r \delta_\lambda}{D_\lambda \varepsilon}} \right)}, \quad (4.44)$$

with ε being the relative distance from the threshold

$$\varepsilon = \frac{\rho_0 - \rho_c}{\rho_c} = \rho_0 - 1 > 0. \quad (4.45)$$

The fastest growing rate defined by the maximum of the growth rate σ_λ reads

$$q_{fg} = \sqrt{\frac{\varepsilon}{2\delta_\lambda}}. \quad (4.46)$$

As established above, for vanishing nematic order the two modes are decoupled and the density mode is stable. For the slightest finite value of λ_0 however, the modes become coupled and a coupled density-orientation mode arises which is unstable against inhomogeneous perturbations. This can be seen in the next section, when the linear stability around the homogeneous nematic state is calculated.

The wavenumber dependent growth rates are shown for a typical set of parameters in Fig. 4.2a). The shape of $\sigma_\lambda(q)$ (solid line) around the isotropic state is in good agreement with calculations from the linearized Doi equation [84]: the positive value at $q = 0$ is due to the building up of the homogeneous nematic phase. However simultaneously phase separation occurs, the finite wavenumber modes having a larger growth rate than the $q = 0$ mode, and therefore inhomogeneous solutions will develop which are dominated by q_{fg} .

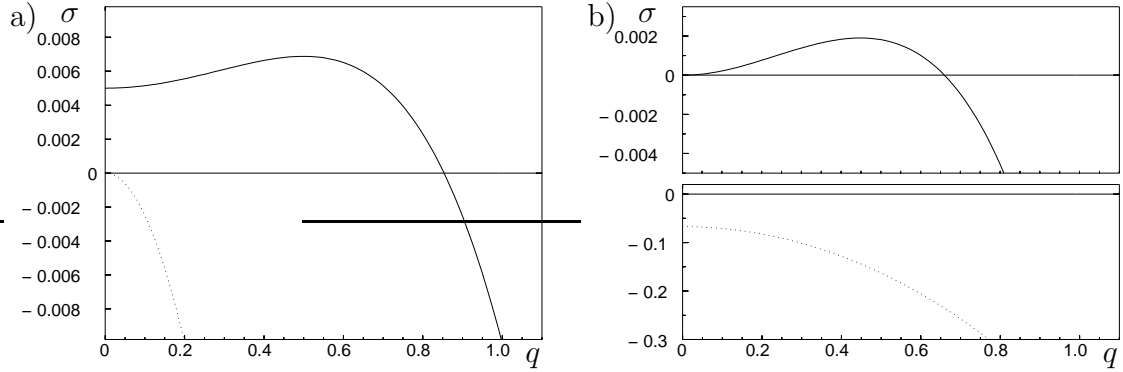


Figure 4.2: In part a) the growth rates $\sigma(q)$ are shown for periodic perturbations of the isotropic state with $\rho_0 > \rho_c = 1$. The damped mode (dotted line) is the conserved density mode and the solid line is the unstable orientational mode, which reflects the build-up of the nematic state by the finite value at $q = 0$ and the phase separation by the maximum at the finite wavenumber q_{fg} . Part b) displays the growth rates for perturbations of the homogeneously stable nematic state at the inhomogeneously unstable branch in Fig. 4.6b). Now the dotted line is a damped orientation mode and the solid line displays a coupled density-orientation mode with a Cahn-Hilliard-like behavior. Besides $\rho_0 = 1.05$ we chose the parameters of the model to be $D_r = 0.1$, $D_\rho = D_\lambda = 0.3$, $a_\rho = 0.25$, $a_\lambda = 2.0$, $\delta_\rho = \delta_\lambda = 0.1$.

Nevertheless I should mention that the presented linearization around the homogeneous isotropic state has limitations for the following reasons: In general, both the scalar order parameter (related to λ in our formulation) *and* the director $\hat{\mathbf{n}}$ are fluctuating at the I-N transition, the latter being neglected in our treatment to get a simple, one-dimensional model. Moreover, if one wants to calculate the instability of the isotropic state, usually there is not yet a predefined director. Thus one has to consider the full order parameter tensor Q_{ij} , as defined in Eq. (3.2), which can be rather intricate. However, we constructed our model mainly to address the question of how reaction kinetics can interplay with the I-N phase separation and how the homogeneous nematic state is changed in the presence of polymerization kinetics. For these questions our simplifications are appropriate.

Linear analysis, nematic state

A linear stability analysis of the homogeneously stable nematic state (λ_+ in our model) in terms of microscopic models is rather involved, since already the exact homogeneous nematic state can only be obtained numerically [73]. For our phenomenological model however, the determination of $\sigma(q)$ on the homogeneous nematic branch is a straightforward task.

We now have to deal with the full linear operator \mathcal{L}_0 with the matrix elements as defined in Eqs. (4.38) and $\lambda = \lambda_+$ from Eq. (4.34). One gets two real eigenvalues σ_1 and σ_2 as the

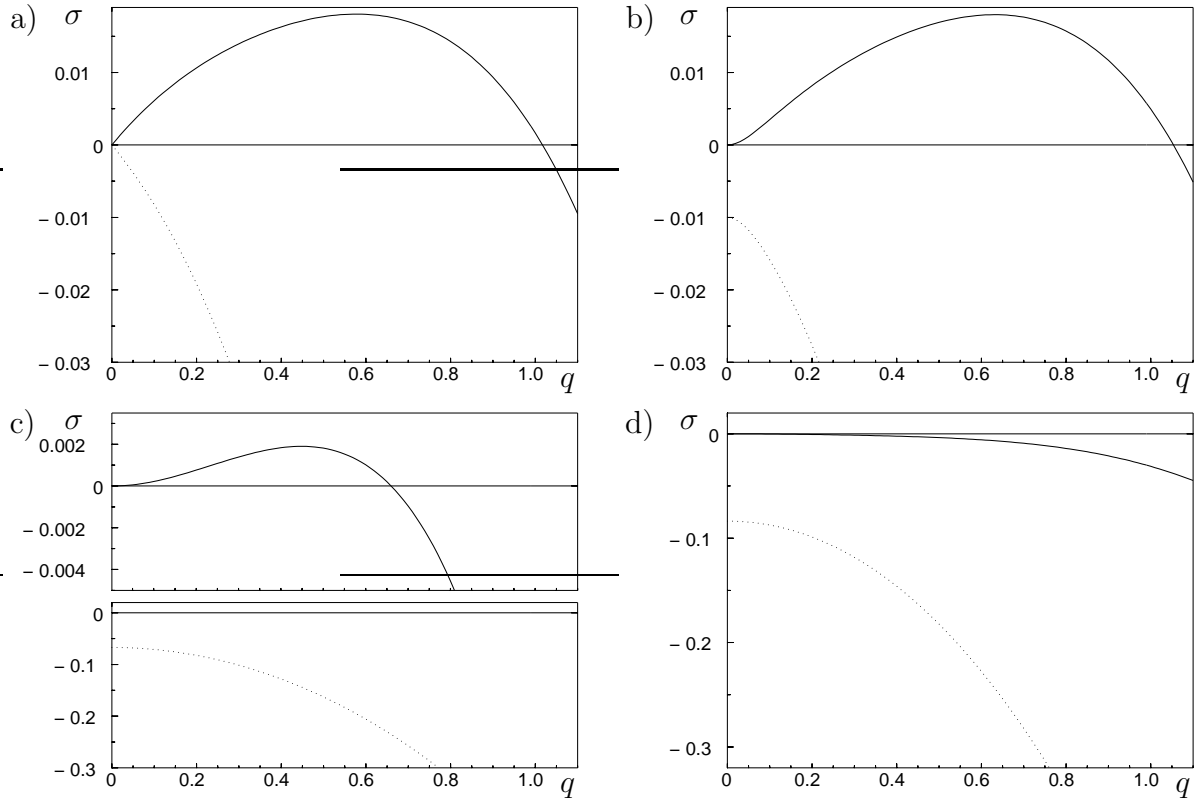


Figure 4.3: The growth rates $\sigma(q)$ along the branch λ_+ for different values of the mean density: at the saddle node, $\rho_0 = \rho_{sn} = 8/9$, where a nematic state is possible for the first time, and at $\rho_0 = 0.9, 1.05, 1.1$ from a) to d). From a) to d) one can see that the dotted mode becomes more and more damped while the mean density is increased. In d) $\rho_0 > \rho_h$ holds for the parameters used here and therefore the homogeneous nematic state is linearly stable. The parameters are as in Fig. 4.2.

solutions of the determinant equation

$$\sigma^2 - \left(\mathcal{L}_{11}^{(0)} + \mathcal{L}_{22}^{(0)} \right) \sigma + \mathcal{L}_{11}^{(0)} \mathcal{L}_{22}^{(0)} - \mathcal{L}_{12}^{(0)} \mathcal{L}_{21}^{(0)} = 0 , \quad (4.47)$$

with $\mathcal{L}_{ij}^{(0)} = \mathcal{L}_{ij}^{(0)}(q)$ in Fourier space.

By applying $q = 0$ to the eigenvalues, one can identify a conserved coupled density-orientation mode with $\sigma_c(q = 0) = 0$ and a pure orientation mode $\sigma_o(q = 0) < 0$ that is damped. While explicit formulas are quite lengthy, the typical shape of $\sigma_c(q)$ and $\sigma_o(q)$ near the I-N transition density and on the homogeneously stable nematic branch are shown in Fig. 4.2b) as the solid and dotted lines respectively. σ_o is damped for all wavenumbers, while σ_c is of the typical Cahn-Hilliard form.

In Fig. 4.3, the growth rates are shown along the homogeneously stable branch λ_+ for different values of the mean density ρ_0 . At the saddle node, the growth rate is for small

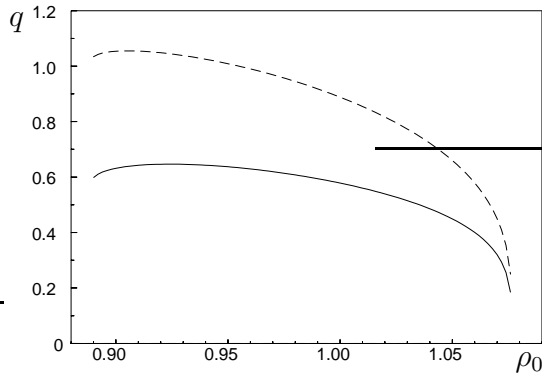


Figure 4.4: The wavenumber of the fastest growing mode q_{fg} (solid line) and the maximal unstable wavenumber q_{max} (dashed line) are shown as a function of the mean density ρ_0 on the homogeneously stable but inhomogeneously unstable nematic branch λ_+ . The range of existence of unstable modes starts at the saddle node $\rho_0 = \rho_{sn} = 8/9$ and ends at $\rho_0 = \rho_h$. Parameters as in Fig. 4.2.

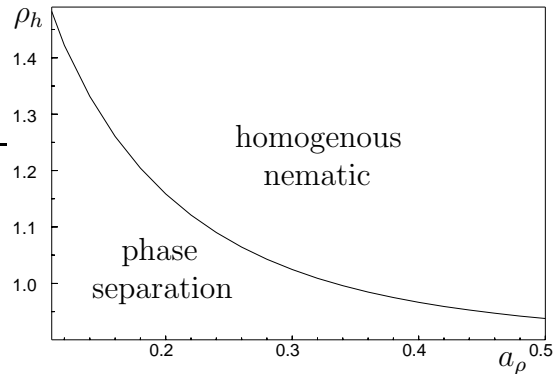


Figure 4.5: The threshold density ρ_h between the region on the nematic branch that is unstable against inhomogeneous perturbations (for $\rho < \rho_h$) and the linearly stable homogeneous nematic state (for $\rho > \rho_h$) is solely determined by the parameter a_ρ . The dependence is shown in this figure. In the test simulations we have chosen $a_\rho = 0.25$ leading to $\rho_h \simeq 1.0768 > \rho_c$.

q linear in q , which is somewhat singular. For all other densities it goes like q^2 : either with a positive coefficient in the density range $]\rho_{sn}, \rho_h[$, reflecting the instability towards phase separation, or with a negative coefficient for $\rho_0 > \rho_h$, reflecting the linear stability of the nematic state. One can conclude from this that for high enough mean densities, the homogeneous nematic state should again be preferred at least in the linear regime, in agreement with the predictions from Onsager theory.

From the growth rates on the homogeneously stable nematic branch one can also obtain the fastest growing wavenumber q_{fg} and the maximal unstable wavenumber q_{max} as a function of the mean density ρ_0 , which are displayed in Fig. 4.4.

The upper border ρ_h , where the nematic λ_+ -branch becomes linearly stable again against inhomogeneous fluctuations, is solely determined by a_ρ in the way as displayed in Fig. 4.5. For $a_\rho = 1/3$, ρ_h coincides with the density of the I-N transition, $\rho_c = 1 = \rho_h$. Because of experimental evidence - the I-N transition and the phase separation take place simultaneously while increasing the density on the homogeneous and isotropic branch above $\rho_c = 1$ - in our model one should choose a_ρ in such a way that $\rho_h > \rho_c$ holds.

Comparing this overall analysis to Fig. 4.1, where the homogeneous nematic branch λ_+ was displayed as stable against homogeneous fluctuations, we are now able to draw a more detailed picture. Along the dashed part of the curve in Fig. 4.6b) the homogeneous nematic state is - from the saddle node up to the upper border ρ_h - linearly unstable against inhomogeneous fluctuations. This is in agreement with the prediction of phase separation

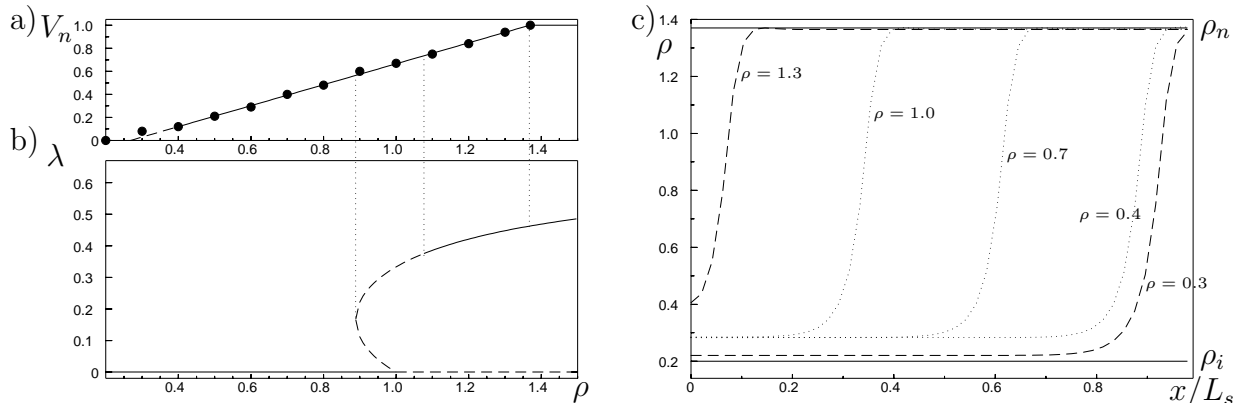


Figure 4.6: Part b) shows the stable (solid) and the unstable branch (dashed) of the nematic order parameter λ_{\pm} as a function of the rod density ρ , cf. Eq. (4.34). Part c) shows stable kink solutions of Eqs. (4.33) interpolating between the nematic ($\rho = \rho_n$) and the isotropic range ($\rho = \rho_i$). The x -axis has been scaled with the system length L_s . The nematic volume fraction V_n as a function of ρ is given in a). For the used parameter set (as in Fig. 4.2), the whole system is in the homogeneous nematic state (i.e. $V_n = 1$) for $\rho_0 > 1.367$.

in the region of coexistence, e.g. from Onsager theory, so ρ_h should be compared to ρ_n , the nematic density derived from the coexistence equations.

4.2.2 Phase separated solutions

Apart from the linear stability of the nematic branch being easily to establish, our model gives a second insight as compared to calculations based on the entire Doi equation, e.g. the linear stability analysis around the isotropic state as described in [84]: In both the Doi equation and our minimal model, the growth rate $\sigma(q)$ for perturbations of the isotropic state takes its maximum at a finite value of q and has positive values for *any* $\rho > \rho_c$. This has to be contrasted to Onsager's statistical theory, where inhomogeneous phase separated states are only energetically preferred for a rod density below a maximum value $\rho < \rho_n$ determined by the coexistence equations (3.21). The mere linear analysis around the homogeneous isotropic state thus gives a misleading picture, since the nonlinearities are responsible for the stabilization of the homogeneous nematic state for high densities. In our model - without having this explicitly implemented - the homogeneous nematic state (whose linear stability already involves nonlinearities of course) is linearly unstable against inhomogeneous fluctuations only up to a mean density ρ_h , as established in the last section. The question is now what happens in the nonlinear regime.

In order to check in which density range phase separated states are stable - we are not interested in the detailed dynamics - we performed the most simple numerical simulation of our model with an Euler step in time and a finite difference scheme with a discretization

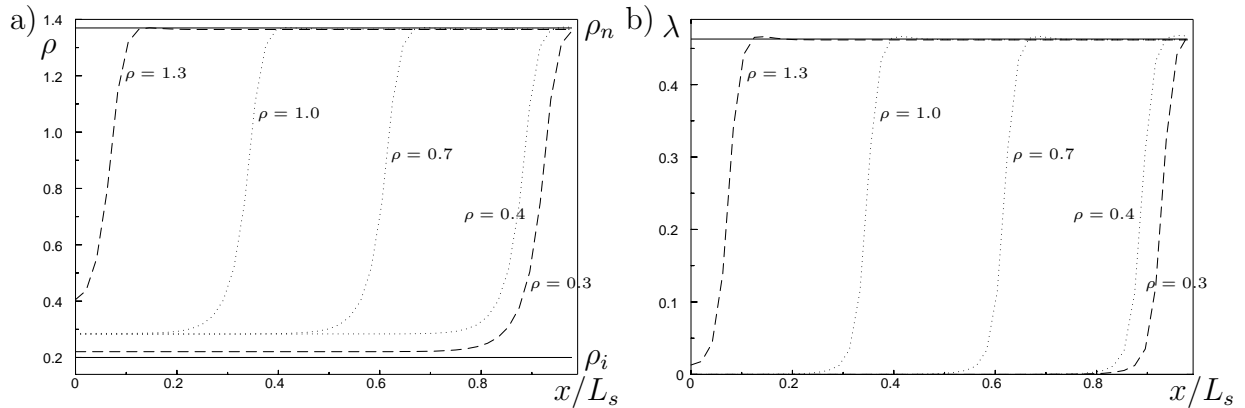


Figure 4.7: Numerically obtained kink solutions of $\rho(x)$ and $\lambda(x)$ are displayed in a) and b) respectively. Away from the interface, the density and order parameter values in the isotropic and nematic regions are almost perfectly constant. The x -axis has been scaled with the system length L_s . Parameters as in Fig. 4.2.

of 128 in space. As boundary conditions we chose that both ρ and λ have vanishing first and third order derivatives at the boundaries, to allow for states with different density and orientation on both sides but still allowing for periodic states.

Such simulations of Eqs. (4.33) confirm that inhomogeneous solutions $\lambda(x)$ and $\rho(x)$ only occur for a mean density ρ_0 below a value $\rho_n > \rho_h$ as shown in Fig. 4.6b). The inhomogeneous solutions for $\rho(x)$ and the volume fraction of the nematic region, which depends linearly on the mean density ρ_0 , are displayed in Fig. 4.6c) and a) respectively and discussed in the next section.

The behavior on the homogenous nematic branch can thus be summarized: for mean densities ρ_0 from ρ_{sn} (first vertical dotted line in Fig. 4.6b)) to ρ_h (second vertical dotted line), the homogeneously stable nematic branch is linearly unstable against inhomogeneous perturbations. From ρ_h up to ρ_n (third vertical dotted line) it is linearly stable but inhomogeneous states are still possible in the nonlinear regime and could be excited by large fluctuations. For $\rho > \rho_n$ the nonlinear terms stabilize the uniform nematic state.

Comparison to the Onsager model

Here we want to investigate if one can interpret the numerically obtained inhomogeneous solutions as phase separated states. Then we will compare features of these inhomogeneous solutions to the predictions from Onsager theory, which again confirms that the model is sound and also allows us to fix some free model parameters.

In a certain density interval $\rho_1 < \rho < \rho_2$ around the critical density $\rho_c = 1$ of the I-N transition, Eqs. (4.33) have stationary kink solutions that can be obtained numerically and are displayed in Fig. 4.7a) and b) for $\rho(x)$ and $\lambda(x)$ respectively. These solutions interpolate between a region of high density ρ_n and order parameter λ_n and a region with low density ρ_i and zero order parameter. Since in addition both the densities and the order parameters in

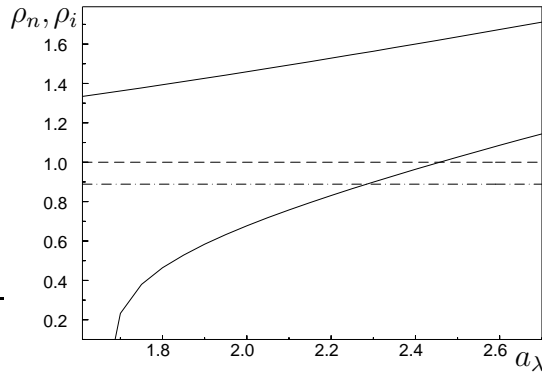


Figure 4.8: The solutions ρ_n, ρ_i (solid lines, $\rho_n > \rho_i$) of the "coexistence equations", Eqs. (4.48) and (4.50), are shown in dependence of a_λ and for fixed parameter $a_\rho = 0.25$. For the chosen parameters, since ρ_i should be positive and smaller than ρ_{sn} (dash-dotted line), the range of sensible values for a_λ is about $[1.68, 2.29]$. The dashed line marks ρ_c .

the two regions are almost perfectly constant, these regions can unambiguously be identified as the nematic and isotropic domains and the respective inhomogeneous solutions as the late stages of phase separation. The existence region of these solutions, $[\rho_1, \rho_2]$, should therefore be regarded as the I-N coexistence region $[\rho_i, \rho_n]$.

The densities ρ_i and ρ_n , in the isotropic and the nematic regions respectively, can be determined for an infinitely large system by the two nonlinear coefficients a_ρ and a_λ , as described in the following. For stationary kinks as in Fig. 4.7, the system can be assumed to be totally phase separated and therefore to be in equilibrium. Thus the total particle current introduced in Eq. (4.35) vanishes, $j_\rho(x) = 0$, implying that $\mu(x) = \mu_i = \mu_n$ is a constant. Sufficiently far away from the kink, the density is constant too, ρ_i or ρ_n respectively, and one obtains the equation

$$a_\rho \rho_i^3 = -\lambda_n \rho_n + a_\rho \rho_n^3, \quad (4.48)$$

where $\lambda_n = \lambda_+(\rho_n) = 1/6 + 1/6\sqrt{9 - 8/\rho_n}$ is the order parameter in the nematic region of homogeneous density ρ_n , which we have chosen as the usual homogeneous value, cf. Eq. (4.34). The rotational contribution to the order parameter equation, i.e. the term $\propto D_r$ in Eq. (4.33b), vanishes in the nematic range for λ_n as well as trivially in the isotropic range. By inspection of the remaining inhomogeneous part of Eq. (4.33b), we define analogously as was done for j_ρ in Eq. (4.35) a translational current for the orientational order

$$j_\lambda(x) = -D_\lambda \partial_x \nu(x), \quad \nu(x) = (1 - \rho)\lambda - \delta_\lambda \partial_x^2 \lambda + a_\lambda \lambda^3. \quad (4.49)$$

Since λ_i vanishes in the isotropic range, ν_i is zero as well. To prevent a current through the interface, the total current j_λ in the nematic region has to vanish as well and it follows $\nu_n = \nu_i = 0$ leading to a second equation

$$(1 - \rho_n)\lambda_n + a_\lambda \lambda_n^3 = 0. \quad (4.50)$$

As λ_n is known, or approximated in a finite system by $\lambda_0(\rho_n)$, from Eq. (4.50) the anisotropic density ρ_n follows as a function of a_λ (or vice versa). ρ_i can then be calculated for ρ_n with Eq. (4.48) as a function of a_ρ (or vice versa). In this spirit, Eqs. (4.48) and (4.50) may be considered as the "coexistence equations" within the framework of our

minimal model, since they uniquely determine the homogeneous densities ρ_i and ρ_n in the isotropic and nematic domains respectively. The other way round, the two densities ρ_i and ρ_n may also be considered as input parameters that are obtained from different approaches as for instance from coexistence equations or possibly also from experiments, and the two parameters a_ρ and a_λ of our phenomenological model could thus be fixed. The region of sensible values of these two parameters is not large, as can be seen in Fig. 4.8. There the values of ρ_i and ρ_n are shown in dependence of a_λ for a fixed value of $a_\rho = 0.25$ (which was chosen to respect $\rho_h > \rho_c = 1$). Since $0 < \rho_i < \rho_{sn}$ should hold, a_λ should evaluate to about $a_\lambda \simeq 2$ as chosen by us throughout this chapter.

Since ρ_i and ρ_n do not depend on the system size L_s , the position of the kink-like interface is determined by the mean density ρ_0 as can be seen from Fig. 4.7. If one measures the fraction of the system that is nematic, V_n , one gets an almost perfectly linear dependence from the mean density ρ_0 , as shown in Fig. 4.6a) and again in agreement with the results expected from Onsager theory.

4.3 Conclusions

So we can conclude that our model reflects all the properties known from the Onsager model: first, it describes the homogeneous I-N transition for $\rho > \rho_c = 1$ via the spatially homogeneous part of Eq. (4.33b). Second, the late stage phase separation into an isotropic phase with a density ρ_i and a nematic phase with a different and higher density ρ_n and an order parameter λ_n is contained in the model. Both densities are independent of the system size (or volume) thus leading to the correct linear behavior of the fraction of the nematic volume as shown in Fig. 4.6a). Moreover, with ρ_i and ρ_n as input from a free energy approach or from experiments, the two nonlinear parameter a_ρ and a_λ can be fixed to reduce the parameter space of the model. It is also straightforward to perform a linear stability analysis on the homogeneously stable nematic branch. This branch is unstable against inhomogeneous perturbations, i.e. against phase separation, from the saddle node up to a density ρ_h . Suitable parameters can be found for whom $\rho_h > \rho_c$ and $\rho_h < \rho_n$ hold. In addition, our model not only reformulates the predictions of Onsager but is also able to repair the ostensible contradiction discussed in the last section, that the isotropic state is unstable against phase separation for all densities $\rho > \rho_c$, while phase separation should only occur for $\rho < \rho_n$.

Nevertheless there are still things to improve: first, simulations around the isotropic state cannot be taken too seriously, as already mentioned above. Second, in a naive deterministic implementation of the model, the simulation can become stuck in a situation with small parts of the simulated region remaining in a different state. These should, however, be destabilized if fluctuations are taken into account, i.e. if noise is added in a way that the density equation is still conserved. This is called model C dynamics, cf. [100], where one has a nonconserved order parameter coupled to a conserved field.

Chapter 5

Reaction kinetics drives pattern formation

In a living cell, the cytoskeletal polymers, namely actin filaments and microtubules, are usually met in a nonequilibrium state with a finite lifetime. If the filaments are not stabilized by additional proteins, they are continuously assembled and disassembled, where the polymerization process is coupled to the hydrolysis of ATP as discussed in section 2.1.2. Such a state can also be reproduced *in vitro*, cf. e.g. Ref. [53].

Such a nonequilibrium state enables the cell to reorganize its cytoskeleton quickly and effectively for many vital purposes, predominantly during cell movement, but also e.g. in vesicle transport, cell division, etc.. There are at least two ways the cell can actively regulate its cytoskeleton: by delivering nucleation sites it can polymerize the filaments where it needs them, e.g. during cell locomotion at the moving front, and depolymerize them where they are no more useful - a state which sounds simple but of course is a very complex and highly biochemically regulated one. It is also rather costly, i.e. energy consuming, since huge amounts of ATP are needed for the polymerization. Nevertheless there is strong evidence for this state [1, 7]. A second way of reorganization is to transport the existing filaments to places where they are needed. This can be done by motor proteins, and this process is investigated in part II of this work. Both states are supposed to be of high importance for bacteria propulsion and cell locomotion [60, 101, 7, 102, 51, 11], different cell types using both of them simultaneously or only one of them.

As has been shortly reviewed in section 2.1.2, the polymerization processes can be rather complex. The polymerization and depolymerization rates on the two distinct filament ends are different and additionally there can be statistical switching between catastrophe and rescue in the case of microtubules. Apart from leading to a stationary length distribution of the filaments [24, 103] as may be expected, the reaction kinetics can also introduce states of polymerization that are not possible in usual, i.e. equilibrium, polymers and which are inherent to the nonequilibrium character of the assembly, like the treadmilling state [17], or the state called dynamic instability where oscillatory polymerization arises [15, 58, 59].

In this part of my work, I am interested in the interplay between the nematic ordering and the accompanied phase separation, as modeled and investigated in the last chapter,

with a simple polymerization kinetics. We predict here that this interplay results in a new pattern forming process, leading to a pattern of alternating isotropic and nematic regions. For this pattern forming process, we want to consider a quite simple state of polymerization, as compared to the possible complex processes mentioned above, where the main consequence of the ongoing polymerization and depolymerization process is that the filaments have only a finite lifetime τ . Such a state is surely possible for actin and presumably also for microtubules if the probability of the rescue phenomenon is small.

The aim of this chapter is therefore to exemplify by means of the addition of a very simple reaction kinetics to the phenomenological model of the last chapter, how a finite lifetime of the rods can introduce a pattern forming process in the vicinity of the isotropic-nematic transition.

5.1 The underlying idea

As we have reviewed in Section 3.2.1, the phase separation at the I-N transition leads in the ideal case and in the long time limit to the building up of a nematic region with high density ρ_n and an isotropic region with a low density ρ_i . This long time limit of course assumes that the idealized rod liquid comprises filaments with infinite lifetime. In the state considered here however, where the filaments have only a finite (mean) lifetime τ , they can still phase separate, but not throughout the whole sample but only over a lifetime-dependent maximum distance which is in the order of

$$l_D = \sqrt{D_\rho \tau} , \quad (5.1)$$

where D_ρ is the effective diffusion coefficient of the filaments. What one should therefore expect is a stationary and approximately periodic pattern with alternating isotropic and nematic regions. Using a typical diffusion coefficient for actin filaments with a length of some microns, $D_\rho \simeq 10^{-13} \text{m}^2 \text{s}^{-1}$ [24], and a typical lifetime of tens of minutes, $\tau = 1000 \text{s}$, one expects the wavelength of the pattern to be around $10 \mu\text{m}$, meaning a few filament lengths.

Apart from this scaling argument, one can also consider the following more illustrative picture: Since the lifetime of the filaments is approximately a constant, much more polymer subunits (monomers in the case of actin and dimers in the case of microtubules) are released in the nematic range, where the density ρ_n is high, than in the isotropic range with a low density ρ_i . However, due to the much larger diffusion coefficient of the subunits as compared to the filaments (two to three orders of magnitude), the former are redistributed quickly, leading to a nearly homogeneous subunit density $m(x)$. Thus the number of nucleated filaments per unit time, which depends only on $m(x)$ and not on the filament density $\rho(x)$, is weakly varying too. By this qualitative reasoning one expects a steady net transport of subunits from the nematic to the isotropic range and in the opposite direction a transport of filaments, whereby the latter one is limited to distances of the order of l_D or smaller. This length restriction causes, instead of a large scale phase separation, a spatially periodic pattern with a wavelength in the order of l_D as already argued above.

5.2 Simple reaction kinetics in the model

Since we are looking for a simple model to exemplify that the pattern forming process proposed above is possible, one should identify the most important consequence of the reaction kinetics for the problem we want to describe. The simple qualitative picture of the finite lifetime of the filaments interplaying with the phase separation process and introducing a length scale into the system shows that the complexity of the biochemical reaction steps, involved during the assembly and disassembly of actin or microtubules, should not be crucial. Let's consider for example the polydispersity of the filaments - as already mentioned above, actin and microtubules are usually met with a distribution of lengths. As the slowest kinetic step and the smallest diffusion coefficient - since diffusion scales with mass namely the one of the longest filaments - will govern the length scale limitation, one can in a first approach discard polydispersity and assume for the sake of simplicity that all filaments are of the same length.

Therefore we can use just the model introduced in the last chapter, with $\rho(x)$ and $\lambda(x)$ interpreted as the density and orientation of the longest filaments. Additionally the minimal model, Eqs. (4.33), has to be adjusted to account for the reaction kinetics process: at first we have to add a new balance equation for the subunit density $m(x)$. m stands here for 'monomers' as would be the case in an actin solution. However, regarding the level of simplicity of our model, it likewise refers to the tubulin dimers in the case of polymerizing microtubules. The subunits are able to diffuse with a diffusion coefficient for which $D_m \gg D_\rho$ should hold. Since the polymerization and depolymerization process is fast compared to filament diffusion (timescales are minutes versus several hours), the complex filament assembly is mimicked just by transitions between the subunits and the (longest) filaments. Thus we introduce a decay rate $\Sigma = \tau^{-1}$ and a nucleation rate s of the filaments. The total amount of free subunits and subunits contained in the filaments being a conserved quantity, the reaction terms in the filament density equations have to appear also in the subunit density equation but with opposite sign. Additionally a factor γ has to be introduced which is a measure for the number of subunits in one filament of fixed length.

Finally we end up with the following model equations

$$\partial_t \rho = D_\rho \partial_x^2 [-\lambda \rho - \delta_\rho \partial_x^2 \rho + a_\rho \rho^3] + sm - \Sigma \rho, \quad (5.2a)$$

$$\begin{aligned} \partial_t \lambda = & -D_r \left[(1 - \rho) \lambda - \frac{3}{2} \rho \lambda^2 + \frac{9}{2} \rho \lambda^3 \right] \\ & + D_\lambda \partial_x^2 [(1 - \rho) \lambda - \delta_\lambda \partial_x^2 \lambda + a_\lambda \lambda^3] - \Sigma \lambda, \end{aligned} \quad (5.2b)$$

$$\partial_t m = D_m \partial_x^2 m - \gamma sm + \gamma \Sigma \rho. \quad (5.2c)$$

In Eq. (5.2a) the subunit density comes in with positive sign, implying that subunits are a source of filaments, while the filament density is a sink since they depolymerize to monomers (Σ and s are assumed positive). As already mentioned above, in the subunit equation (5.2c), the same terms enter but with opposite sign and with the factor γ counting the amount of subunits in one filament. One can directly check that the total amount of

subunits m_{tot} , i.e. both polymerized and free subunits, is conserved: it is sufficient to look at the homogeneous equations, implying

$$\partial_t m_{tot} = \partial_t (\gamma\rho + m) = 0 . \quad (5.3)$$

In the order parameter equation, Eq. (5.2b), there is a decay term $-\Sigma\lambda$, since in the nematic range oriented filaments are lost. However, new ones are nucleated everywhere with an arbitrary orientation¹ and have to relax to the local mean orientation by rotational diffusion, i.e. the homogeneous part of Eq. (5.2b) proportional to D_r . Accordingly, there is no source term in Eq. (5.2b), the orientational order has to form just as in the nonreactive case.

5.3 Analysis of the reactive model

We can now look if our prediction is correct and periodic patterns can be found within this simple model. First we have to check whether an isotropic-nematic transition is still possible. If so we can investigate the effect of the reaction kinetics on the linear stability of the nematic branch and search for periodic density and orientation states.

5.3.1 The spatially homogeneous case

At first we investigate again the spatially homogeneous case to answer the question whether the I-N transition is still possible in a system undergoing reaction kinetics. In the presence of the reactive steps the nucleation and decay rates s and Σ determine the mean filament density ρ_0 in terms of the mean monomer density m_0 in the following way

$$\rho_0 = s\Sigma^{-1}m_0 . \quad (5.4)$$

Assuming that one is in the state where this homogeneous filament density is already established, we linearize the spatially homogeneous part of Eq. (5.2b) and arrive at

$$\dot{\lambda} = -D_r \left(1 + \frac{\Sigma}{D_r} - \rho_c \right) \lambda. \quad (5.5)$$

One can thus conclude that a I-N transition remains possible and that the reaction kinetically caused partial loss of the orientational order, i.e. the existence of a sink $-\Sigma\lambda$ but the absence of a source term in Eq. (5.2b), leads to an increase of the critical density for the transition,

$$\rho_c = 1 + \Sigma/D_r , \quad (5.6)$$

¹This should be true if the filament density is not as high that polymerization in the nematic phase is only possible parallel to the mean orientation. For such high densities however, there should be no phase separation anymore, so this case is irrelevant for the problem under consideration.

as compared to the equilibrium case, where $\rho_c = 1$ held. This is physically intuitive, since the decay of filaments should hinder the build-up of the nematic state, thus a higher mean filament density should be needed for the nematic phase to be formed. Second, that the effect is smaller if the effective rotational diffusion constant is larger also fits the intuition, since then the nematic phase is formed more effectively. One should however take in mind that we are dealing with a mean field theory, and that if fluctuations (which could be important in a reaction kinetics) dominate, our model will break down.

The spatially homogeneous part of Eq. (5.2b) can again be solved for stationary values of the order parameter,

$$0 = -D_r \left[(1 - \rho_0)\lambda_0 - \frac{3}{2}\rho_0\lambda_0^2 + \frac{9}{2}\rho_0\lambda_0^3 \right] - \Sigma\lambda_0 , \quad (5.7)$$

and the spatially homogeneous stationary solutions of Eqs. (5.2) accordingly are

$$\begin{aligned} \rho &= \rho_0 , \quad m = m_0 , \\ \lambda_0 &= 0 , \quad \lambda_{\pm} = \frac{1}{6} \pm \frac{1}{6} \sqrt{9 - \frac{8}{\rho_0} \left(1 + \frac{\Sigma}{D_r} \right)} , \end{aligned} \quad (5.8)$$

I will not show the homogeneous bifurcation diagram here, since it is just Fig. 4.1 again with the threshold shifted by Σ/D_r to the right. It can also be seen from Fig. 5.5d), which contains already the stability against inhomogeneous perturbations.

5.3.2 Linear stability analysis of the nematic state

We perform again a linear stability analysis by the ansatz $\rho(x, t) = \rho_0 + \tilde{\rho}(x, t)$, $\lambda(x, t) = \lambda_0 + \tilde{\lambda}(x, t)$ and additionally $m(x, t) = m_0 + \tilde{m}(x, t)$ for the monomer density, yielding the linear system

$$\partial_t \mathbf{w}(x, t) = \mathcal{L}_0 \mathbf{w}(x, t) = \begin{pmatrix} \mathcal{L}_{11}^{(0)} & \mathcal{L}_{12}^{(0)} & \mathcal{L}_{13}^{(0)} \\ \mathcal{L}_{21}^{(0)} & \mathcal{L}_{22}^{(0)} & \mathcal{L}_{23}^{(0)} \\ \mathcal{L}_{31}^{(0)} & \mathcal{L}_{32}^{(0)} & \mathcal{L}_{33}^{(0)} \end{pmatrix} \mathbf{w}(x, t) , \quad (5.9)$$

for the three-component vector

$$\mathbf{w}(x, t) = \begin{pmatrix} \rho(x, t) \\ \lambda(x, t) \\ m(x, t) \end{pmatrix} , \quad (5.10)$$

where the tildes have been omitted again. The components of the linear operator \mathcal{L}_0 can be read directly from Eq. (4.38) with the addition of the homogeneous reaction kinetics

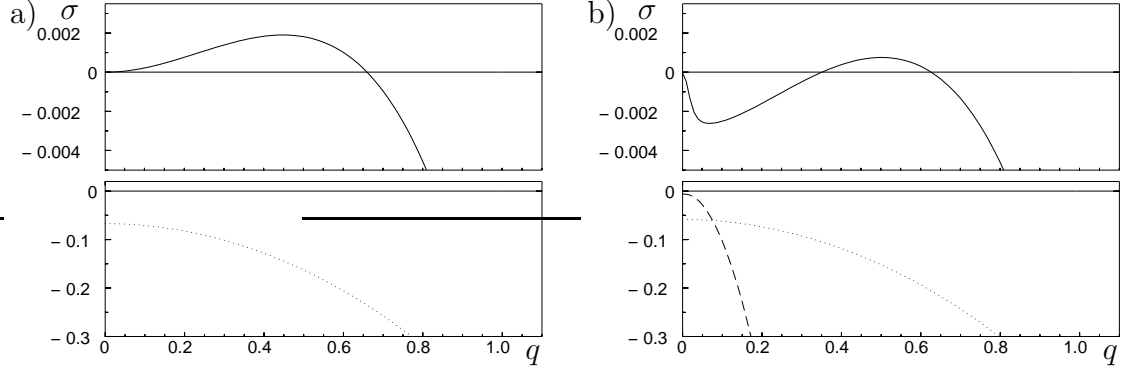


Figure 5.1: The growth rates $\sigma(q)$ for spatial perturbations of the nematic state are shown. The left part again displays the case without reaction kinetics, cf. Fig. 4.2b), with a damped orientation mode and an unstable and conserved Cahn-Hilliard-like mode. To the right are the modes in the presence of reaction kinetics and in the region where the homogeneously stable λ_+ branch is inhomogeneously unstable, cf. Fig. 5.5d). Now one can distinguish three modes: a damped orientational mode (dotted line) and two coupled modes, one damped (dashed line) and a pattern forming mode (solid line) which is linked to the total density, but also coupled to the orientation. Parameters are $\rho_0 = 1.05$, $\Sigma = 0.003$, $s = 0.01\Sigma$, $D_m = 100$, $\gamma = 100$ and the others as in Fig. 4.2.

terms and the diffusive term in the monomer density. One gets

$$\begin{aligned}
\mathcal{L}_{11}^{(0)} &= -\Sigma + D_\rho \left[-\lambda_0 - \delta_\rho \partial_x^2 + 3a_\rho \rho_0^2 \right] \partial_x^2, \\
\mathcal{L}_{12}^{(0)} &= -D_\rho \rho_0 \partial_x^2, \\
\mathcal{L}_{13}^{(0)} &= s, \\
\mathcal{L}_{21}^{(0)} &= -D_r \left[-\lambda_0 - \frac{3}{2} \lambda_0^2 + \frac{9}{2} \lambda_0^3 \right] - D_\lambda \lambda_0 \partial_x^2 = D_r \frac{\lambda_0}{\rho_0} - D_\lambda \lambda_0 \partial_x^2, \\
\mathcal{L}_{22}^{(0)} &= -D_r \left[1 - \rho_0 \left(1 + 3\lambda_0 - \frac{27}{2} \lambda_0^2 \right) \right] - \Sigma + D_\lambda \left[1 - \rho_0 - \delta_\lambda \partial_x^2 + 3a_\lambda \lambda_0^2 \right] \partial_x^2, \\
\mathcal{L}_{23}^{(0)} &= 0, \\
\mathcal{L}_{31}^{(0)} &= \gamma \Sigma, \\
\mathcal{L}_{32}^{(0)} &= 0, \\
\mathcal{L}_{33}^{(0)} &= -\gamma s - D_m \partial_x^2.
\end{aligned} \tag{5.11}$$

Determining the growth rates $\sigma(q)$ of modes with wavenumber q on the homogeneously stable nematic branch λ_+ from Eq. (5.8) by the ansatz $\lambda_1, \rho_1, m_1 \propto \exp(\sigma t \pm i q x)$, the eigenvalues of \mathcal{L}_0 have the typical form as depicted in Fig. 5.1b). The modes can be

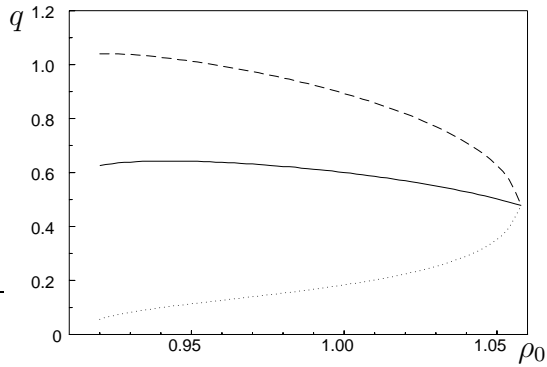


Figure 5.2: The wavenumber of the fastest growing mode q_{fg} (solid line) and the minimum and maximum wavenumbers, q_{min} (dotted) and q_{max} (dashed), are shown as a function of the mean density ρ_0 on the homogeneously stable nematic branch λ_+ . The existence range of unstable modes starts at the saddle node $\rho_{sn} = 8/9(1 + \Sigma/D_r)$ and ends at ρ_p , defining the threshold of pattern formation. Parameters are as in Fig. 4.2, and $\Sigma = 0.003$, $s = 0.01\Sigma$, $D_m = 100 = \gamma$.

identified by setting $q = 0$. Eqs. (5.9) then yield three eigenvalues

$$\sigma_1 = 0, \quad \sigma_2 = -\Sigma - \gamma s, \quad \sigma_3 = -D_r \left[1 - \rho_0 \left(1 + 3\lambda_0 - \frac{27}{2}\lambda_0^2 \right) \right] - \Sigma. \quad (5.12)$$

σ_1 is connected to the conserved mode of the total monomer density $m_{tot} = \gamma\rho + m$, since $\sigma_1(q = 0) = 0$ holds. The eigenvector contains all three fields meaning that the orientation is coupling to the total density. σ_3 is at $q = 0$ a pure orientational mode and σ_2 again a mode coupling the three fields, both however are dampened since $\sigma_2, \sigma_3 < 0$ holds.

This behavior of the modes, as displayed in Fig. 5.1b), has now to be compared to the case without reaction kinetics as shown again for comparison in Fig. 5.1a). In both cases, one can identify a damped orientational mode starting at $q = 0$ from $\sigma_o = -D_r \left[1 - \rho_0 \left(1 + 3\lambda_0 - \frac{27}{2}\lambda_0^2 \right) \right]$ or from $\sigma_3 = \sigma_o - \Sigma$ respectively. In the non-reactive case, if the homogeneous nematic branch is inhomogeneously unstable, the second conserved mode displays a Cahn-Hilliard-like behavior, meaning it starts from $q = 0$ like $\propto q^2$ with a positive coefficient and then decays with higher powers of the wavenumber, displaying a fastest growing mode q_{fg} and instability in a range $q \in [0, q_{max}]$ that contains the long wavelength modes. In the presence of reaction kinetics however, a third mode naturally emerges due to the additional equation for the monomer density and the interaction of the filament density with the monomers by the homogeneous reaction kinetics together with the conservation of the total monomer density m_{tot} is reflected in the modes by a long wavelength coupling of the new mode with the unstable conserved mode. By this mechanism, the long wavelength part of the conserved mode is damped and instead of an unstable range $q \in [0, q_{max}]$, the system displays a pattern forming instability in a finite wavenumber window $[q_{min}, q_{max}]$ *not* containing the long wavelength modes.

Fig. 5.2 displays the fastest growing wavenumber q_{fg} and the minimal and maximal unstable wavenumbers q_{min} and q_{max} in dependence of the mean density ρ_0 . The critical wavenumber q_c of the pattern forming instability can be identified at the point where these three wavenumbers coincide, the density at this point defining also the threshold density ρ_p . From the viewpoint of pattern formation, we have found a *stationary finite wavelength instability* if one moves on the homogeneous nematic branch in the direction of decreasing density and crosses ρ_p . If one walks on the homogeneous isotropic state towards higher densities, the I-N transition starts at $\rho_c = 1 + \Sigma/D_r$, as discussed in the last section.

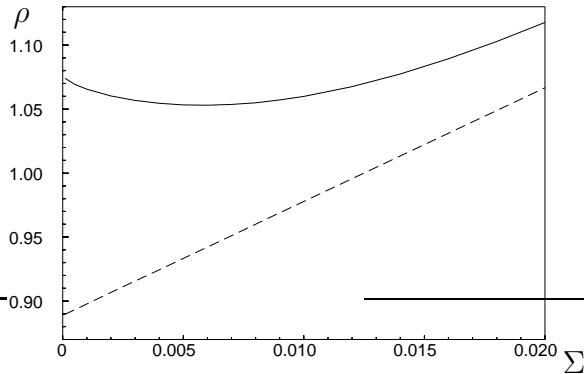


Figure 5.3: The threshold density ρ_p and the density ρ_{sn} at the saddle node are shown in dependence of the decay rate Σ as the solid and the dashed line respectively. Parameters are as in Fig. 5.4.

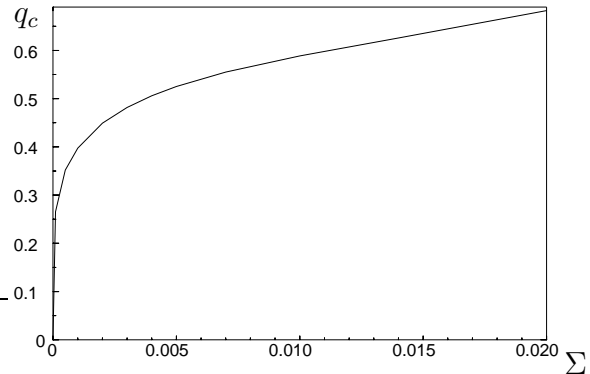


Figure 5.4: The critical wavenumber q_c is shown as a function of the decay rate Σ . Parameters are $s = 0.01\Sigma$, $D_m = 100$, $\gamma = 100$ and the others as in Fig. 4.2.

However, since $\rho_p > \rho_c$ holds, at ρ_c one is already in the highly nonlinear regime of pattern formation, namely a distance $\rho_p - \rho_c$ away from the threshold, and things already can be complicated. Fig. 5.2 should also be compared to the case without reaction kinetics, namely Fig. 4.4, where the fastest growing mode tends to zero at ρ_h .

The density range where the homogeneous branch λ_+ is unstable against the stationary finite wavelength instability, i.e. $[\rho_{sn}, \rho_p]$, is indicated by the dashed line in the bifurcation diagram Fig. 5.5d). For $\rho_0 > \rho_p$ the nematic branch is linearly stable. The dependence of the pattern formation threshold density ρ_p on the decay rate Σ (with a nucleation rate $s = 0.01\Sigma$) is shown in Fig. 5.3. Surprisingly, the behavior of $\rho_p(\Sigma)$ is nonmonotonous with a minimum threshold at approximately $\Sigma = 0.006$. However, since the density ρ_{sn} of the saddle node increases with Σ , cf. Eq. (5.8), the density range of the pattern forming instability is largest for small values of Σ . Fig. 5.4 shows the critical wavenumber q_c at $\rho_0 = \rho_p$ in dependence of Σ . The wavenumber increases with the decay rate, since a higher value of Σ broadens the wavenumber region where the mode interaction through the reaction kinetics leads to a damping of the modes, cf. the discussion of the growth rates and Fig. 5.1.

5.3.3 Numerical analysis

We performed again some numerical simulations of the model in the presence of the reaction kinetics. We used both the finite difference scheme mentioned already above and a Fourier Galerkin spectral code, both with periodic boundary conditions. It turns out that periodic patterns bifurcate subcritically at ρ_p , i.e. at ρ_p there is already a finite amplitude of the pattern. Additionally, the periodic states have a broad existence region, persisting even to densities smaller than ρ_{sn} . The inhomogeneous bifurcation diagram is displayed in Fig. 5.5:

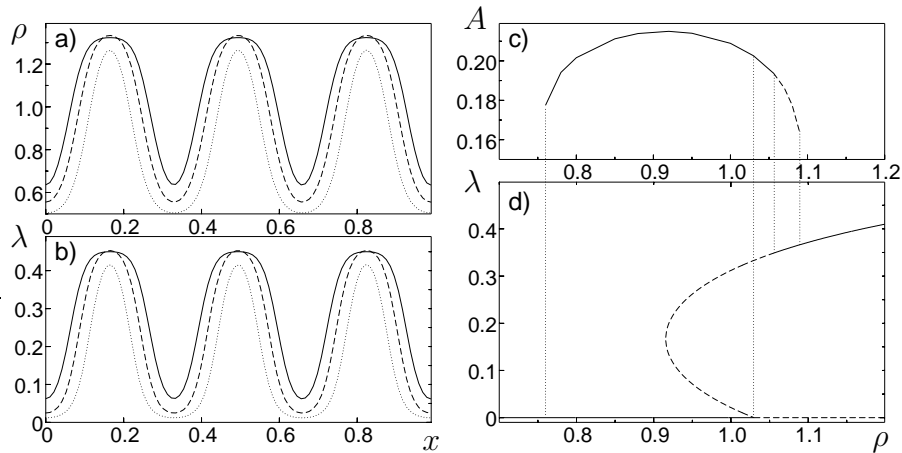


Figure 5.5: Part a) and b) show periodic solutions $\rho(x)$ and $\lambda(x)$ of Eqs. (5.2) for $\rho_0 = 0.8$ (dotted), $\rho_0 = 0.95$ (dashed) and $\rho_0 = 1.056$ (solid), respectively. Part d) displays the stable homogeneous nematic branch (solid) and the unstable ones (dashed). In part c) the existence range of the stable (solid) and unstable (dashed) periodic patterns with the modulation amplitude A of $\lambda(x)$ are given. Parameters are as in Fig. 4.6 with $D_m = 10$, $\gamma = 100$, $\Sigma = 0.003$, $s = 0.01\Sigma$.

part d) shows the homogeneously stable nematic branch and its region of linear instability towards the pattern forming instability as the dashed region on the upper branch. Part c) displays the amplitude A of the orientation field $\lambda(x)$ of the periodic solutions in the range where the nonlinear periodic state is in coexistence with the homogeneous states. One can clearly see that A is already finite at $\rho_0 = \rho_p$ and persists nearly down to $\rho_0 \simeq 0.76 < \rho_{sn}$.

Numerically obtained periodic states at the unstable nematic branch are shown in Figs. 5.6-5.8 for three different mean densities: at $\rho_0 = 0.8 < \rho_{sn}$, $\rho_0 = 0.95$ and $\rho_0 = 1.056$, the latter being very close to ρ_p . The figures display the rod density $\rho(x)$, the orientation field $\lambda(x)$ and the deviation of the subunit density from the homogeneous value $\delta m(x) = m(x) - m_0$ to make these visible since $\delta m \ll m_0$. As compared to the case without reaction kinetics, where the coexistence conditions determine the isotropic and nematic densities ρ_i and ρ_n , cf. Fig. 4.6, the maxima of $\rho(x)$ come now close to ρ_n while the minima of $\rho(x)$ are considerably larger than ρ_i . However, the anharmonic shape of Fig. 5.6 as compared to Fig. 5.8 seems to imply that in the former case the system tends to the isotropic state, as can be judged from the narrow maxima of the periodic solutions, while in the latter case the maxima are pronounced implying a tendency to the nematic state.

In the region of Fig. 5.5c), where the amplitude A is drawn as the dashed line, the periodic patterns become increasingly anharmonic, plateaus $\rho \sim \rho_n$ spread out and the valleys of low filament density in between become less and narrower by approaching the upper end of the dashed curve in Fig. 5.5c), a behavior implying that in this density region, the reaction kinetics is not sufficiently effective to prevent the system from coarsening. At

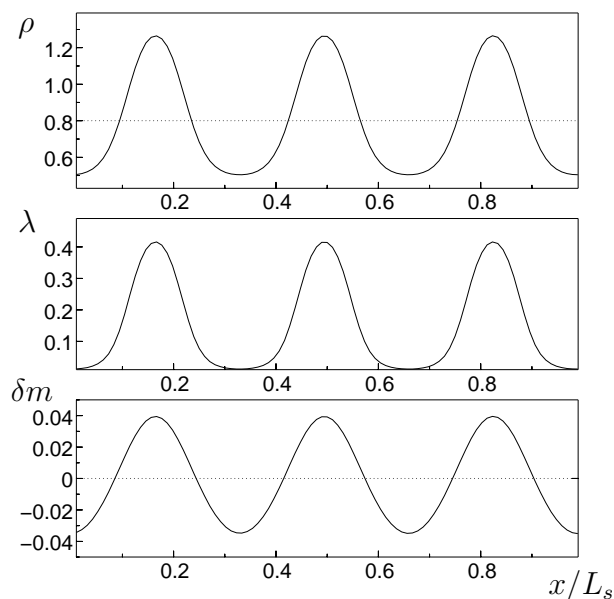


Figure 5.6: Periodic patterns for a mean density $\rho_0 = 0.8$. Displayed are the rod density $\rho(x)$, the orientation field $\lambda(x)$ and the deviation of the subunit density from the homogeneous value $\delta m(x) = m(x) - m_0$ respectively. The system size L_s has been chosen so that three pattern wavelengths fit into the system at $\rho_0 = \rho_p$. Apart from the mean density, parameters are as in Fig. 5.1.

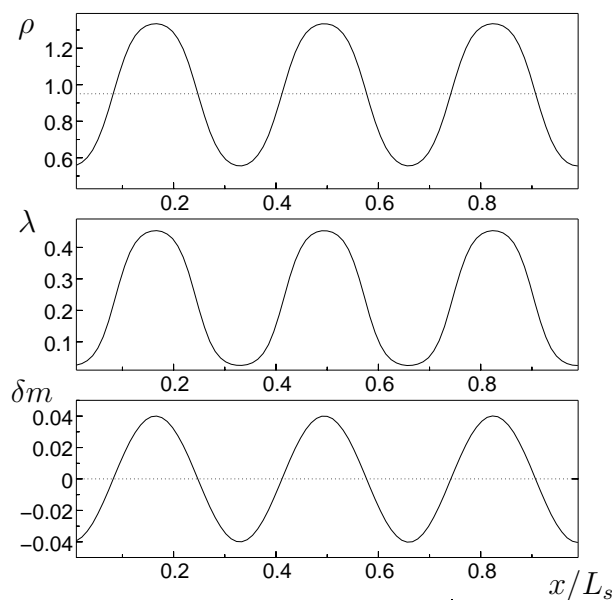


Figure 5.7: Periodic patterns for a mean density $\rho_0 = 0.95$. For details cf. Fig. 5.6.

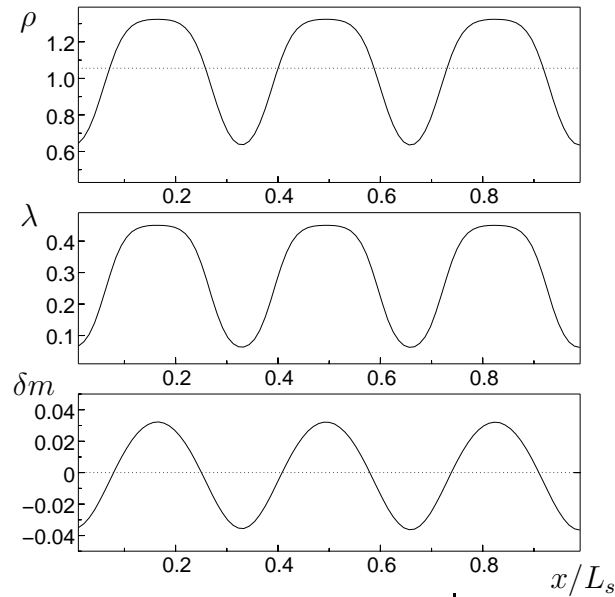


Figure 5.8: Periodic patterns for a mean density $\rho_0 = 1.056$. For details cf. Fig. 5.6.

the left end of this curve, as can be seen e.g. in Fig. 5.6, the state remains periodic without a tendency to coarsen, until for a too small mean density the valleys spread out and the system becomes homogeneous.

5.3.4 Robustness of the pattern forming mechanism

One can now ask the question, how much the emergence of periodic patterns depends on parameter variations. As was already mentioned in the investigation of the model without reaction kinetics, some of the parameters must be chosen in a sensible way. So a_ρ and a_λ should be chosen such that the isotropic and nematic densities are sensible. If one adds the reaction kinetics, it makes not much sense to investigate the patterns as a function of these two parameters, since they do not allow for large variations and determine the behavior of a nonreactive system. In the case without reaction kinetics, δ_ρ and δ_λ only determine the maximum unstable wavenumbers and can more or less be chosen ad lib. In the presence of reaction kinetics however, since the growth rates of modes on the homogeneously stable nematic branch are first damped for small wavenumbers and then have to become positive again, δ_ρ and δ_λ are now also involved in determining the instability threshold ρ_p . However, the influence is not surprising, as shown in Figs. 5.9 and 5.10. The threshold density ρ_p is lowered with increasing $\delta_\rho = \delta_\lambda$, since then I-N interfaces are energetically more costly, while the critical wavenumber q_c decreases for the same reason. The diffusion coefficients D_ρ, D_λ and D_m are not very important, however $D_m \gg D_\rho \simeq D_\lambda$ should be fulfilled. The rotational diffusion coefficient D_r determines the time scale of the formation of the homogeneous nematic phase and more important, in the reactive case, its ratio with the

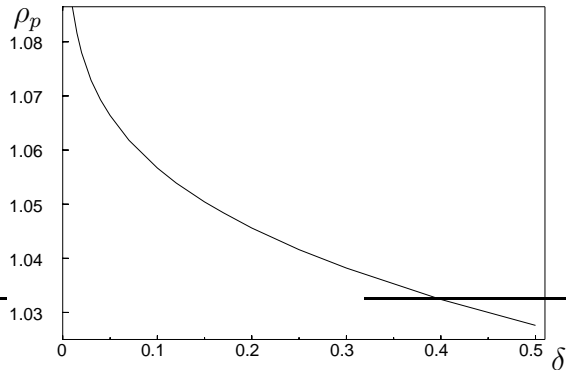


Figure 5.9: The threshold density ρ_p is shown in dependence of the interfacial energy parameter $\delta = \delta_\rho = \delta_\lambda$. Parameters are as in Fig. 5.2.

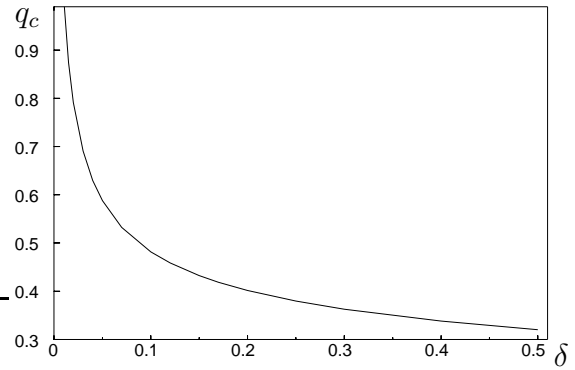


Figure 5.10: The critical wavenumber q_c is shown as a function of the interfacial energy parameter $\delta = \delta_\rho = \delta_\lambda$. Parameters are as in Fig. 5.2.

decay rate Σ fixes the threshold of the I-N transition.

The influence of the decay rate Σ has already been discussed in Sec. 5.3.2 for a fixed ratio of $\Sigma : s$. In all the figures shown up to now we used the following parameter set for the reaction kinetics: γ , the number of subunits that build up one filament, has been chosen to be 100. In reality this value should be higher, but we wanted to avoid numerical difficulties because of too different time scales and suppose that $D_m = 100 \gg 0.3 = D_\rho, D_\lambda$ should already lead to sufficiently different scales. In addition, we used $\Sigma = 0.003$ and $s = 0.01\Sigma$, leading according to Eq. (5.4) to

$$\rho_0 = s\Sigma^{-1}m_0 = 0.01m_0 = \gamma^{-1}m_0. \quad (5.13)$$

Together with $\gamma = 100$ this implies that the amount of polymerized monomers $\gamma\rho_0$ equals the amount of free monomers. This means that one is near the critical monomer concentration for the polymerization, cf. section 2.1.2. In a real self-assembling biopolymer system, the filament density at the critical monomer density is lower than the one needed for the I-N transition. However, using $s = 0.1\Sigma$, meaning the ratio of polymerized monomers to free monomers is 10 : 1, does not lead to a qualitative change for the pattern formation, as can be seen from Fig. 5.11. The damping of the small wavenumbers is not so pronounced, but one has still a pattern forming instability instead of a Cahn-Hilliard-like instability without the reaction kinetics, and the wavenumber window of unstable modes is only slightly changed. The case with a polymerized monomer number smaller than the free monomer number seems not sensible with respect to actin and microtubule polymerization. To conclude, the pattern forming mechanism proposed by us is very robust.

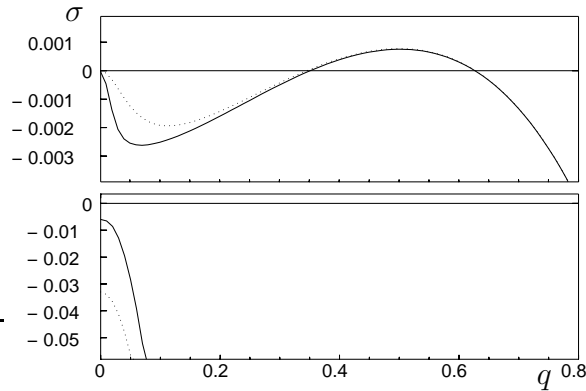


Figure 5.11: The growth rates $\sigma_1(q)$ and $\sigma_2(q)$ of the reactive modes are shown for two parameter sets. The solid lines correspond to the parameters already used in Fig. 5.2, especially $s = 0.01\Sigma$ and $\gamma = 100$ leading to a 1 : 1 ratio of monomers in polymerized and nonpolymerized form. The dotted lines correspond to the same parameters apart from $s = 0.1\Sigma$, together with $\gamma = 100$ implying a state where this ratio is 10 : 1, i.e. most subunits are polymerized. In the latter case, since $\sigma_2(q = 0)$ decreases with increasing s , cf. Eq. (5.12), the coupling is less pronounced but nevertheless, the long wavelength modes are damped and nothing changes qualitatively.

5.4 Conclusions

In part I of my work, a reaction kinetically driven pattern forming process has been predicted near the isotropic–nematic (I-N) transition of biopolymers like actin and microtubules. In Chapter 4, a phenomenological continuum model has been introduced and motivated that reproduces the first order I-N transition in lyotropic liquid crystals, including the phase separation in its neighborhood and being in agreement with the statistical theory of Onsager. As compared to prior formulations in the literature, it enables to investigate quite easily the linear stability of the homogeneously stable nematic branch and it establishes that the nonlinearities suppress the phase separation for high filament densities.

The pattern forming mechanism proposed in this chapter uses only one main ingredient of the polymerization kinetics of biopolymers, namely the occurrence of a finite lifetime $\tau = \Sigma^{-1}$ and a nucleation rate of the filaments. Beyond the critical density ρ_c for the I-N transition the isotropic orientation of the filaments and below a certain density ρ_p the uniform nematic state become unstable against inhomogeneous perturbations. Hence, moving on the homogeneous nematic branch in the direction of decreasing mean density, one crosses at ρ_p a *stationary finite wavelength instability* with critical wavenumber q_c , while coming along on the isotropic branch, one usually is already in the nonlinear regime of pattern formation. The bifurcation diagram in the presence of reaction kinetics is summarized in Fig. 5.5.

The pattern formation process investigated here has been established to be robust and

is expected to be quite generic. The correlation between a finite lifetime τ of a unstable field and the occurrence of periodic patterns is quite independent of details. It has been investigated for the first time in a simple reactive A-B mixture [89, 90] and should apply to all kind of systems that are both unstable against long wavelength inhomogeneous perturbations and reactive. A further biological example is the interplay between a different transport and filament accumulation mechanism, namely motor-induced filament bundling [104, 105], with the polymerization kinetics. It has been investigated recently after this work, [106].

Even though our description is very simplified we expect that the basic physical mechanism survives in situations with broad polydisperse filament distributions [15, 24, 76], including living cells. Polydispersity favors periodic patterns and together with a formulation of our model in more than one dimension, this should give rise to a larger variety of phenomena. As an example it should be expected that having a polydisperse filament distribution, the longer filaments will gather in the nematic regions while the shorter filaments enrich in the isotropic regions.

Recently, there has also been experimental effort to discover the periodic patterns in a solution of polymerizing actin. Periodic patterns with a wavelength of about $10\mu\text{m}$ have indeed been found [107], although their interpretation remains doubtful. Their formation may be due to our mechanism, but they remain stable if the chemical fuel needed for the active polymerization, namely ATP, is used up. Probably this is due to contaminations with inactive motors or crosslinkers, which stabilize bundle-like structures, since in the mechanism proposed by us, if the kinetics is switched off again one expects a coarsening of the small wavelength pattern to larger domains of isotropic and nematic regions again. As far as our mechanism is concerned, the ideal experimental realization would be the preparation of a quite homogeneous nematic phase of actin with fixed filament lengths, which could be obtained using the stabilization effects of capping proteins, followed by a washing out of the capping proteins and the addition of ATP. This situation would most easily compare to the investigation of the stability of the homogeneous nematic branch as calculated in the framework of the phenomenological model.

Part II

Pattern formation in filament-motor solutions

per aspera ad astra, proverb

Chapter 6

Introduction

6.1 The experiments we want to describe

As shortly reviewed in chapter 2, the combined dynamics of cytoskeletal filaments and motor proteins is of crucial importance for the cell. As a prominent example, microtubules and molecular motors participate in the formation of the mitotic spindle [14]. Such a spindle has two organizing centers, the so-called centrosomes, from where MTs are nucleating and radially growing towards the chromosomes. Both polymerization and active transport by motors are used to segregate the duplicated chromosomes during the cell division process. In such microbiological studies *in vivo*, hitherto one is yet far from understanding the complicated processes and it is often unknown which regulatory proteins and even more which signal and regulation pathways are present and of importance.

However, well designed *in vitro* experiments were carried out recently: it has been reported [37] that in a simple model system, namely a solution of purified MTs and motors, in the presence of ATP aster patterns very similar to the dynamic aster structure in the spindle apparatus can be found *in vitro*, i.e. without the organizing centrosomes and without the extensive regulation by the cell. Also, in experiments with *Xenopus laevis* egg extract, asters and even a stable bipolar spindle have been reported to form in the absence of centrosomes [108]. In Ref. [31], experiments either with stabilized MTs (i.e. MTs with fixed length) or with a certain amount of tubulin able to polymerize dynamically, together with artificial multi-headed constructs of kinesin showed patterns in both cases. The time scale of the formation are several minutes, the steady states then being stable for about one hour, and the length scale of an aster is about $50\mu\text{m}$. In addition, a rough description of the phase space of a filament-motor system could be given. As a function of the kinesin concentration, varying from $15\mu\text{g/ml}$ to $55\mu\text{g/ml}$, and for a tubulin concentration of 5mg/ml in the case of polymerizing MTs or $0.2\text{-}0.3\text{ mg/ml}$ in the case of stabilized MTs, the following sequence of patterns appeared with increasing motor concentration: a lattice of vortices, a mixture of asters and vortices, a lattice of asters and finally bundle-like structures.

In subsequent experiments and molecular dynamics (MD) simulations, cf. Ref. [33] from which Fig 6.1 gives an example of the aster formation, the influence of various variables on

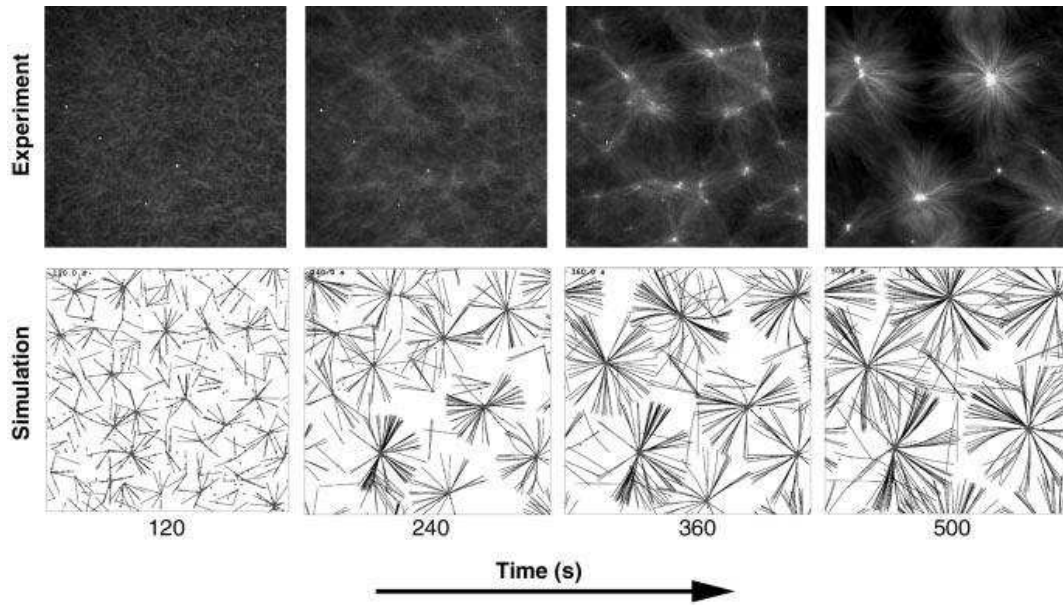


Figure 6.1: Patterns formed upon ATP and GTP consumption in a solution of tubulin and artificial multimeric kinesin complexes. Upper row: dark-field microscopy pictures. Lower row: Molecular dynamics simulation: MTs treated as flexible, polar rods, motors are treated as highly processive with a linear force-velocity relation. The picture is taken from [33].

the patterns has been addressed: there a multimeric minus end-directed motor based on Ncd has been constructed which allowed to study the cooperation of plus and minus end-directed motors together. While a system with kinesin alone showed isotropic to vortex to aster transitions as a function of motor concentration, Ncd yielded a transition from the isotropic filament distribution directly to the aster patterns, i.e. without the intermediate formation of vortices. This could be explained in the MD simulations by means of the time motors spend bound at the MTs end: upon reaching a MT end, motors detach with a finite off-rate $p_{off,end}$. Usually only asters formed, but if $p_{off,end}$ is increased (implying a smaller residence time of the motors on a MT) this induced the formation of vortices. This established that the residence time at MTs ends is important with regard to the capacity of motors to focus MTs to a pole. Also the importance of processivity was established in the MD simulation, since decreasing the processivity did destroy the patterns or led to less pronounced asters, a tendency that could however be compensated partly upon increasing the motor density. Furthermore, the MT's orientations are opposite for the two motor species: kinesin-asters have MTs with the plus end directing to the center, while Ncd-asters point with the minus-end to the center. In both cases motors accumulate in the aster centers. Mixing both kinds of motors together led to Ncd-asters and kinesin-vortices becoming a network of interconnected poles for increasing motor-tubulin ratio and with a fixed and moderate Ncd-kinesin ratio. Changing the Ncd-kinesin concentration ratio led

to the winning of one kind of motors and to the formation of the respective kind of asters.

In Ref. [31], the authors for the first time made a comparison to classical pattern forming systems, arguing that the dissipation in their system should be due to the consumption of ATP by the motors and of GTP by the MT's polymerization. They called for the determination of the "out-of-equilibrium phase diagram" of such a system, to which I want to contribute in this second part of my work. However, to what extent such an *in vitro* phase diagram can be related to situations *in vivo* is an open question, since inside a cell variables like motor and tubulin densities are not absolute values and instead of changing these concentrations, their activity could be changed by regulatory proteins. Hence the understanding of the *in vitro* systems can only be considered as a first step in a reasonable direction.

Recently also patterns in actin-myosin mixtures have been reported [38], which however are not dissipative ones. They emerge upon ATP depletion and are frozen-in patterns. We review the experiments and propose a possible mechanism of how these patterns form in chapter 13.

6.2 Modeling

In the two original works [31, 33], the experiments have been supplemented by molecular dynamics simulations which displayed asters and vortex patterns and also gave insight to the importance of processivity and residence time at the ends of the filaments for the pattern formation process. Nevertheless in the simulations about 20 parameters had to be specified, luckily most of them being known for kinesin from measurements, however implying a high-dimensional parameter space. A continuum formulation with fewer parameters is thus desirable and would also have the advantage that the whole repertoire of nonlinear pattern formation theory as developed since decades from hydrodynamic instabilities and other model systems, cf. Ref. [42] for a review, could then be used to explore such a model.

As a first trial of a continuum description, mean field approximations for spin models have been investigated which displayed stripe-like patterns [109]. More recently a phenomenological model of a motor density interacting with a phenomenological vector field has been considered, which is able to reproduce asters and vortex-like solutions [110] and has been generalized to account for two distinct states of the motors, either bound to the filament and performing directed movement or unbound and diffusing freely [111, 112]. A second class of more microscopic models are inspired by experiments on filament-motor bundle contraction [104, 113] and are formulated in one spatial dimension [114, 41, 105, 115, 116]. They are able to display bundling instabilities and self-propagating patterns. A further approach is a formulation coming from theories for flocking birds and bacterial colonies which describes active or self-propelled particles [117, 118]. However, it has never been applied directly to filament-motor systems and only linear investigations have been carried out so far since such an approach has to account for all nonlinearities allowed by symmetry which makes an analysis very intricate. Very recently a model has been proposed where the motor-mediated filament-filament interaction is described by collision rules [119].

I have chosen here an approach based on the Smoluchowski equation for rigid rods, namely the Doi equation already introduced in section 3.2.2. It accounts for the spatial and angular distribution of the filaments which are approximated by rigid rods and assumes that the motors are practically homogeneously distributed and come into the model only via active currents in the filaments' equation. The latter approximation has been proposed in a one-dimensional theory for filament bundling [41] and has been generalized for a two- and three-dimensional filament-motor solution in [40]. The detailed structure of the active currents can be obtained in two-particle approximation by considering the symmetries of the system and imposing vanishing momentum and angular momentum of a filament pair in the absence of external forces and torques [40]. In part II of this work I will review the model for a two-dimensional filament-motor solution and perform a corrected linear analysis [46] as compared to [40]. Subsequently I study all the instabilities in the weakly nonlinear regime. Here the above mentioned techniques from nonlinear pattern formation theory can be effectively used, namely I will derive amplitude equations for stationary [45] and oscillatory patterns and establish their ranges of stability, part of the "out-of-equilibrium phase diagram" as demanded in Ref. [31].

The filament-motor model in part II of this work applies more directly to processive motors, cf. section 2.2.2, as is however the case for the systems investigated in [31, 33], namely mixtures of microtubules and kinesin or Ncd. In chapter 13 I propose how the model should be interpreted and modified to account also for the nonprocessive myosin-actin system [38].

Chapter 7

The filament-motor model

7.1 Motivation

The cytoskeletal filaments being rather stiff and elongated objects - at least in the case of microtubules - the Smoluchowski equation for rigid rods or Doi equation, cf. section 3.2.2 and [39], should be apt to describe their passive behavior, i.e. in the absence of polymerization and motors. Then the probability distribution function (pdf) $\Psi(\mathbf{r}, \mathbf{u}, t)$ of finding a microtubule of fixed length L at position \mathbf{r} with orientation \mathbf{u} at time t obeys, cf. Eq. (3.22), just the conservation of probability,

$$\partial_t \Psi + \nabla \cdot \mathbf{J}_t + \mathcal{R} \cdot \mathbf{J}_r = 0 \quad , \quad (7.1)$$

with a translational current \mathbf{J}_t and a rotational current \mathbf{J}_r . Recently, it has been proposed [40] that the influence of the motors could be enclosed by additional active currents \mathbf{J}_t^a and \mathbf{J}_r^a . These are supposed to be caused by relative translations and rotations of a filament pair through the movement of a motor attached to both filaments, cf. the sketch in Fig. 7.1. A similar approach has been applied to the one-dimensional situation of a filament bundle in the presence of motors in Ref. [41]. Although the motor density could be treated as an additional field in both models, it was suggested to assume that the motors are homogeneously distributed with a sufficiently high concentration in order to an overlap of two filaments immediately leading to an active transport. This can be motivated by the much higher diffusion coefficient of a motor protein as compared to microtubules, namely by 2 to 3 orders of magnitude. It has proven to be a sufficiently good approximation and instabilities have been found in both models. In subsequent publications of both groups [120, 116], the motor density has been accounted for in more detail, but to keep the modeling simple I refrain here from treating the motors explicitly.

Hence the density of the (active and attached) motors as well as properties like the mean velocity on a filament and the duty ratio of the motors enter into the model only via coefficients of the additional active currents. The phenomenological part of these currents can be derived in two-particle approximation by symmetry considerations of a filament pair and includes three leading order contributions, two active translational and one active rotational ones, as discussed in section 7.3.

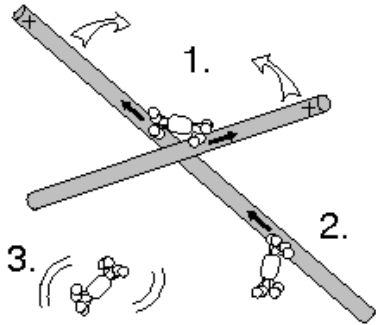


Figure 7.1: Sketch of motor oligomers interacting with filaments. The most important process is (1.) where an oligomer of motors attaches to a filament pair (overlap $W = 1$) exerting a force that results in relative translations \mathbf{v} and rotations $\boldsymbol{\omega}$ of the filament pair. In our approach we assume that the motors are homogeneously distributed due to their very fast diffusion (3.) compared to the filaments. Second, the motor density is assumed to be sufficiently high that if an overlap of filaments happens, there is a motor nearby leading immediately to the process described in (1.). A motor oligomer moving on a single filament as depicted in (2.) does not have an effect. The picture has been taken from Ref. [121].

To motivate the active currents for the motor-induced relative filament displacements and for the change in the relative orientations as sketched in Fig. 7.1, we start with a closer look at the excluded volume interaction. Since both the excluded volume and the motor-induced transport need an overlap of at least two filaments¹ the resulting currents should be of second order in the pdf Ψ and are nonlocal functions of it. The currents resulting from the excluded volume defined already in section 3.2.2 can be read from Eqs. (3.24) to be

$$J_{t,i}^{ex} = -D_{ij}\Psi(\mathbf{r}, \mathbf{u})\partial_j V_{ex}(\mathbf{r}, \mathbf{u}) , \quad (7.2)$$

$$J_{r,i}^{ex} = -D_r\Psi(\mathbf{r}, \mathbf{u})\mathcal{R}_i V_{ex}(\mathbf{r}, \mathbf{u}) , \quad (7.3)$$

having the form Ψ times the derivative of a Ψ -dependent potential, namely the excluded volume potential

$$V_{ex}(\mathbf{r}, \mathbf{u}) = \int d\mathbf{u}' \int d\mathbf{r}' W(\mathbf{r}-\mathbf{r}', \mathbf{u}, \mathbf{u}')\Psi(\mathbf{r}', \mathbf{u}') . \quad (7.4)$$

In case of the motor-mediated current, the process is an active, dissipative one, thus there does not exist a potential. Instead of a force expressed by the derivative of a potential as in the passive, excluded volume case, there should be an actively generated force provided there is an overlap. Since the motion is overdamped in a filament-motor solution, this force can be represented by a velocity. Considering the translational current, in contrast to the passive contribution where

$$\mathbf{J}_t^{ex} \sim \Psi(\mathbf{r}, \mathbf{u}) \partial_{\mathbf{r}} \int d\mathbf{u}' \int d\mathbf{r}' W(\mathbf{r}-\mathbf{r}', \mathbf{u}, \mathbf{u}')\Psi(\mathbf{r}', \mathbf{u}') \quad (7.5)$$

¹For reasons of feasibility we restrict our model to the overlap of exactly two filaments. In principle one should investigate a virial or cluster expansion of Ψ . While in three spatial dimensions higher order terms are quickly decreasing due to the scaling with b/L , the ratio of rod diameter and rod length, this is not the case in two dimensions, cf. Ref. [81]. The effects of the passive excluded volume interaction is considered in third order in Ψ in section 11.2.

holds, for the additional active contribution one can write

$$\mathbf{J}_t^a \sim \Psi(\mathbf{r}, \mathbf{u}) \int d\mathbf{u}' \int d\mathbf{r}' \mathbf{v}(\mathbf{r}-\mathbf{r}', \mathbf{u}, \mathbf{u}') W(\mathbf{r}-\mathbf{r}', \mathbf{u}, \mathbf{u}') \Psi(\mathbf{r}', \mathbf{u}') . \quad (7.6)$$

The actively generated relative translational velocity in principle depends on both the relative separation of the rods' centers of masses as well as on the rod orientations,

$$\mathbf{v} = \mathbf{v}(\mathbf{r}-\mathbf{r}', \mathbf{u}, \mathbf{u}') . \quad (7.7)$$

Analogously one can introduce an active relative angular velocity

$$\boldsymbol{\omega} = \boldsymbol{\omega}(\mathbf{r}-\mathbf{r}', \mathbf{u}, \mathbf{u}') , \quad (7.8)$$

which enters into the active rotational current

$$\mathbf{J}_r^a \sim \Psi(\mathbf{r}, \mathbf{u}) \int d\mathbf{u}' \int d\mathbf{r}' \boldsymbol{\omega}(\mathbf{r}-\mathbf{r}', \mathbf{u}, \mathbf{u}') W(\mathbf{r}-\mathbf{r}', \mathbf{u}, \mathbf{u}') \Psi(\mathbf{r}', \mathbf{u}') . \quad (7.9)$$

Now one has to specify the detailed structure of the velocity \mathbf{v} and the angular velocity $\boldsymbol{\omega}$. In Ref. [40] this has been achieved in leading order by considering the symmetries and conservation laws of a filament pair. This will be critically reviewed in section 7.3. At first I will write down the entire model for the active filament-motor solution, i.e. with the velocities resulting from [40], in the next section.

7.2 The model

We can now formulate the generalization of the Doi model to active filament-motor solutions: the total translational and rotational currents entering the conservation of probability,

$$\partial_t \Psi + \nabla \cdot \mathbf{J}_t + \mathcal{R} \cdot \mathbf{J}_r = 0 , \quad (7.10)$$

can be written as

$$J_{t,i} = -D_{ij} [\partial_j \Psi + \Psi \partial_j V_{ex}] + J_{t,i}^a , \quad (7.11a)$$

$$J_{r,i} = -D_r [\mathcal{R}_i \Psi + \Psi \mathcal{R}_i V_{ex}] + J_{r,i}^a , \quad (7.11b)$$

the terms with an upper index a being the motor-mediated active currents. As already introduced in section 3.2.2 for a solution of passive rods, translational diffusion is anisotropic, namely uniaxial with two coefficients D_{\parallel} and D_{\perp} ,

$$D_{ij} = D_{\parallel} u_i u_j + D_{\perp} (\delta_{ij} - u_i u_j) , \quad (7.12)$$

and the rotational diffusion, proportional to the rotational diffusion coefficient D_r , is mediated by the rotational operator

$$\mathcal{R} = \mathbf{u} \times \partial_{\mathbf{u}} . \quad (7.13)$$

The active currents induced by the motors are of the form

$$\mathbf{J}_t^a = \Psi(\mathbf{r}, \mathbf{u}) \int d\mathbf{u}' \int d\mathbf{r}' \mathbf{v}(\mathbf{r}-\mathbf{r}', \mathbf{u}, \mathbf{u}') W(\mathbf{r}-\mathbf{r}', \mathbf{u}, \mathbf{u}') \Psi(\mathbf{r}', \mathbf{u}') , \quad (7.14)$$

$$\mathbf{J}_r^a = \Psi(\mathbf{r}, \mathbf{u}) \int d\mathbf{u}' \int d\mathbf{r}' \boldsymbol{\omega}(\mathbf{r}-\mathbf{r}', \mathbf{u}, \mathbf{u}') W(\mathbf{r}-\mathbf{r}', \mathbf{u}, \mathbf{u}') \Psi(\mathbf{r}', \mathbf{u}') . \quad (7.15)$$

The interaction kernel W is the same as in the excluded volume potential already introduced in section 3.2.2,

$$V_{ex}(\mathbf{r}, \mathbf{u}) = \int d\mathbf{u}' \int d\mathbf{r}' W(\mathbf{r}-\mathbf{r}', \mathbf{u}, \mathbf{u}') \Psi(\mathbf{r}', \mathbf{u}') , \quad (7.16)$$

with $W = 1$ in the case of an overlap and $W = 0$ else, guaranteeing that active transport is only possible for overlapping filaments. Since our assumed homogeneously distributed motor density is also supposed to be sufficiently high, at any position of overlap there will always be a motor complex nearby inducing active transport, i.e. a relative velocity \mathbf{v} and an angular velocity $\boldsymbol{\omega}$.

Following Ref. [40] and as will be explained in the next section, the translational and rotational velocities, \mathbf{v} and $\boldsymbol{\omega}$ respectively, can be written in leading order as

$$\mathbf{v}(\mathbf{r}-\mathbf{r}', \mathbf{u}, \mathbf{u}') = \frac{\alpha}{2} \frac{\mathbf{r}' - \mathbf{r}}{L} \frac{1 + \mathbf{u} \cdot \mathbf{u}'}{|\mathbf{u} \times \mathbf{u}'|} + \frac{\beta}{2} \frac{\mathbf{u}' - \mathbf{u}}{|\mathbf{u} \times \mathbf{u}'|} , \quad (7.17)$$

$$\boldsymbol{\omega}(\mathbf{u}, \mathbf{u}') = \gamma (\mathbf{u} \cdot \mathbf{u}') \frac{\mathbf{u} \times \mathbf{u}'}{|\mathbf{u} \times \mathbf{u}'|} . \quad (7.18)$$

The active currents have been normalized to the excluded volume $|\mathbf{u} \times \mathbf{u}'|$ and they fulfill both the conservation of translational and rotational momentum in the absence of external forces and torques, as well as translational and rotational invariance, cf. the next section. The coefficients α and β have the units of a velocity, while γ has like the rotational diffusion coefficient D_r the unit s^{-1} .

To get a first impression for the active translational velocity, let's consider a one-dimensional arrangement of filaments², like in a bundle. Then the term proportional to α takes its maximum, namely $1 + \mathbf{u} \cdot \mathbf{u}' = 2$, for parallel filaments and vanishes for antiparallel filaments where $\mathbf{u} \cdot \mathbf{u}' = -1$ holds. Conversely, the contribution proportional to β is maximum for antiparallel alignment and vanishes in the parallel case. Thus in one dimension, the two terms perfectly separate, the α -contribution describing interaction of parallel filaments and the β -contribution interaction of antiparallel filaments. In two dimensions, this separation does not hold anymore and the interaction becomes more involved. In this sense, the two-dimensional model is a generalization of the one considered by Kruse et al. to describe filament bundling in Ref. [41].

One may ask how the interaction of parallel filaments via motors leads to a relative filament displacement, since the motor then should proceed on both filaments with the

²The factor $|\mathbf{u} \times \mathbf{u}'|^{-1}$ cancels upon performing the orientational integrals and is not a problem here.

same speed. However, it is known that there is a difference in motor activity along the filament. Moreover, motors stall at the endpoints for some finite time, which has been recognized as a crucial condition for aster formation [122]. Thus if a motor interacting with two parallel filaments reaches the end of one filament before the one of the other, it stalls there and pulls the second filament. This happens until the end of this second filament is reached or the motor detaches. The need for the difference in the places where the motor attaches to the two filaments is reflected by the $(\mathbf{r}' - \mathbf{r})$ -dependence of the α -contribution.

The angular velocity $\boldsymbol{\omega}$ is proportional to $\mathbf{u} \times \mathbf{u}'$ and therefore associated to a rotation in the plane defined by the two orientation vectors \mathbf{u} and \mathbf{u}' .

7.3 Symmetries of the motor-mediated velocities

The explicit form of the motor-mediated translational and angular velocities, namely Eqs. (7.17) and (7.18), can be obtained by writing down the simplest terms fulfilling the conservation laws and symmetries of the system.

First of all, only relative positions of the rods play a role. Translational invariance therefore implies

$$f(\mathbf{r}, \mathbf{r}', \mathbf{u}, \mathbf{u}') = f(\mathbf{r} - \mathbf{r}', \mathbf{u}, \mathbf{u}') \quad (7.19)$$

for $f = \mathbf{v}, \boldsymbol{\omega}$. If one considers an interacting filament pair in the absence of external forces and torques, both momentum and angular momentum of the pair have to be conserved. Hence the motor-mediated translational and angular velocities have to be odd under exchange of particles $(\mathbf{r}, \mathbf{u}; \mathbf{r}', \mathbf{u}') \rightarrow (\mathbf{r}', \mathbf{u}'; \mathbf{r}, \mathbf{u})$, or together with Eq. (7.19) under the transformation $(\mathbf{r} - \mathbf{r}'; \mathbf{u}, \mathbf{u}') \rightarrow (\mathbf{r}' - \mathbf{r}; \mathbf{u}', \mathbf{u})$, leading to the conditions

$$\mathbf{v}(\mathbf{r} - \mathbf{r}', \mathbf{u}, \mathbf{u}') = -\mathbf{v}(\mathbf{r}' - \mathbf{r}, \mathbf{u}', \mathbf{u}) \quad , \quad (7.20)$$

$$\boldsymbol{\omega}(\mathbf{r} - \mathbf{r}', \mathbf{u}, \mathbf{u}') = -\boldsymbol{\omega}(\mathbf{r}' - \mathbf{r}, \mathbf{u}', \mathbf{u}) \quad . \quad (7.21)$$

Finally, due to rotational invariance, \mathbf{v} has to be odd and $\boldsymbol{\omega}$ even under the transformation $(\mathbf{r} - \mathbf{r}'; \mathbf{u}, \mathbf{u}') \rightarrow (\mathbf{r}' - \mathbf{r}; -\mathbf{u}, -\mathbf{u}')$, or explicitly

$$\mathbf{v}(\mathbf{r} - \mathbf{r}', \mathbf{u}, \mathbf{u}') = -\mathbf{v}(\mathbf{r}' - \mathbf{r}, -\mathbf{u}, -\mathbf{u}') \quad , \quad (7.22)$$

$$\boldsymbol{\omega}(\mathbf{r} - \mathbf{r}', \mathbf{u}, \mathbf{u}') = \boldsymbol{\omega}(\mathbf{r}' - \mathbf{r}, -\mathbf{u}, -\mathbf{u}') \quad . \quad (7.23)$$

Let's at first have a look at the active translational velocity \mathbf{v} . It has to fulfill

$$\mathbf{v}(\mathbf{r} - \mathbf{r}', \mathbf{u}, \mathbf{u}') = -\mathbf{v}(\mathbf{r}' - \mathbf{r}, \mathbf{u}', \mathbf{u}) \quad , \quad (7.24)$$

$$\mathbf{v}(\mathbf{r} - \mathbf{r}', \mathbf{u}, \mathbf{u}') = -\mathbf{v}(\mathbf{r}' - \mathbf{r}, -\mathbf{u}, -\mathbf{u}') \quad . \quad (7.25)$$

The simplest terms fulfilling both conditions are $\boldsymbol{\xi} = \mathbf{r}' - \mathbf{r}$ and $\mathbf{u}' - \mathbf{u}$. On the other hand, both ξ^2 and $\mathbf{u} \cdot \mathbf{u}'$ are even under the transformations $(\mathbf{r} - \mathbf{r}'; \mathbf{u}, \mathbf{u}') \rightarrow (\mathbf{r}' - \mathbf{r}; \mathbf{u}', \mathbf{u})$ and

$(\mathbf{r} - \mathbf{r}'; \mathbf{u}, \mathbf{u}') \rightarrow (\mathbf{r}' - \mathbf{r}; -\mathbf{u}, -\mathbf{u}')$, namely fulfilling both conservation of momentum and angular momentum as well as rotational invariance. Thus one can write

$$\mathbf{v}(\boldsymbol{\xi}, \mathbf{u}, \mathbf{u}') = \boldsymbol{\xi} (v_{\xi 1} + v_{\xi 2} \mathbf{u} \cdot \mathbf{u}' + v_{\xi 3} \xi^2 + v_{\xi 4} (\mathbf{u} \cdot \mathbf{u}')^2 + \dots) \quad (7.26)$$

$$+ (\mathbf{u}' - \mathbf{u}) (v_{u 1} + v_{u 2} \mathbf{u} \cdot \mathbf{u}' + v_{u 3} \xi^2 + v_{u 4} (\mathbf{u} \cdot \mathbf{u}')^2 + \dots) \quad , \quad (7.27)$$

with some coefficients $v_{\xi i}$ and $v_{u i}$, $i = 1, 2$, etc..

Since $\xi = |\boldsymbol{\xi}| < 1$ holds in units of the rod length L due to the overlap condition, an expansion in powers of ξ seems adequate. Additionally, upon deriving continuum equations isotropic averaging has to be applied to the model equations as worked out in some detail in chapter 8. As can be seen already from appendix A, formulas (A.8)-(A.10), isotropic averages of powers of \mathbf{u} decrease quite rapidly with the powers. Consequently, one can assume that leading order terms in $\boldsymbol{\xi}$ and $\mathbf{u}' - \mathbf{u}$ already describe the qualitative features of the motor-induced relative displacement. Liverpool et al. proposed in Ref. [40] the following simplified form

$$\mathbf{v}(\mathbf{r} - \mathbf{r}', \mathbf{u}, \mathbf{u}') = \frac{\alpha}{2} \frac{\mathbf{r}' - \mathbf{r}}{L} \frac{1 + \mathbf{u} \cdot \mathbf{u}'}{|\mathbf{u} \times \mathbf{u}'|} + \frac{\beta}{2} \frac{\mathbf{u}' - \mathbf{u}}{|\mathbf{u} \times \mathbf{u}'|} \quad , \quad (7.28)$$

i.e. with $v_{\xi 1} = \frac{\alpha}{2L} |\mathbf{u} \times \mathbf{u}'|^{-1} = v_{\xi 2}$ and $v_{u 1} = \frac{\beta}{2} |\mathbf{u} \times \mathbf{u}'|^{-1}$. In principle, $v_{\xi 1}$ and $v_{\xi 2}$ could be chosen differently. However, with the above choice, especially with $v_{\xi 1} = v_{\xi 2}$, one regains the one-dimensional model of Ref. [41], where the α -contribution corresponds to the interaction of parallel filaments and the β -contribution to the interaction of antiparallel filaments, cf. the discussion in the last section. Thus this choice is sensible and additionally it guarantees that the orientational part of the α -term always has a positive sign. The common factor $|\mathbf{u} \times \mathbf{u}'|^{-1}$ is just a normalization to the excluded volume and vanishes upon orientational integration.

In the case of the angular velocity $\boldsymbol{\omega}$, the symmetry requirements are

$$\boldsymbol{\omega}(\mathbf{r} - \mathbf{r}', \mathbf{u}, \mathbf{u}') = -\boldsymbol{\omega}(\mathbf{r}' - \mathbf{r}, \mathbf{u}', \mathbf{u}) \quad , \quad (7.29)$$

$$\boldsymbol{\omega}(\mathbf{r} - \mathbf{r}', \mathbf{u}, \mathbf{u}') = \boldsymbol{\omega}(\mathbf{r}' - \mathbf{r}, -\mathbf{u}, -\mathbf{u}') \quad . \quad (7.30)$$

Both conditions can be fulfilled by a term $\mathbf{u} \times \mathbf{u}'$ and analogously to the translational case one can write

$$\boldsymbol{\omega}(\boldsymbol{\xi}, \mathbf{u}, \mathbf{u}') = (\mathbf{u} \times \mathbf{u}') (\omega_1 + \omega_2 \mathbf{u} \cdot \mathbf{u}' + \omega_3 \xi^2 + \omega_4 (\mathbf{u} \cdot \mathbf{u}')^2 + \dots) \quad . \quad (7.31)$$

Liverpool et al. chose $\omega_1 = 0$ and $\omega_2 = \gamma |\mathbf{u} \times \mathbf{u}'|^{-1}$, namely

$$\boldsymbol{\omega}(\mathbf{u}, \mathbf{u}') = \gamma (\mathbf{u} \cdot \mathbf{u}') \frac{\mathbf{u} \times \mathbf{u}'}{|\mathbf{u} \times \mathbf{u}'|} \quad . \quad (7.32)$$

The first order term is neglected compared to the second order term, since the factor $\mathbf{u} \cdot \mathbf{u}'$ in the latter accounts for the tendency of motors to bind on two filaments sharing an angle

smaller than $\frac{\pi}{2}$ [40]. As will become clearer in the next chapter, a consequence of the above choice is that the active rotational contribution is purely nonlinear and inhomogeneous.

One can also consider the model with nonzero ω_1 . Then a linear and homogeneous contribution from the active rotations makes a homogeneously polarized state possible, as has been started to be investigated recently [123, 124].

As an additional remark, the above choices fulfill the symmetries and conservation laws of a filament pair in the absence of external forces and torques. This however does not imply that all these contributions that fulfill the symmetry conditions are obligatorily present in a filament-motor solution, a point which is discussed in Ref. [120].

Chapter 8

Derivation of continuum equations

8.1 Two approximations on the way to a continuum model

The model defined in section 7.2 is a nonlinear and nonlocal integro-differential equation for the probability distribution function (pdf) $\Psi(\mathbf{r}, \mathbf{u}, t)$. Both the excluded volume interaction defined by Eq. (7.16) and the filament-filament interactions induced by the motors, Eqs. (7.14), (7.15), (7.17) and (7.18), are nonlocal, which makes the model hard to solve both analytically and numerically. However, if one is interested in the formation of patterns whose wavelength is large in comparison to the filament length L , a gradient expansion of the interaction kernel is a suitable approximation. Integrations $\int d\mathbf{r}$ can then be carried out, but the model still remains a nonlinear integro-differential equation with respect to the orientation variable \mathbf{u} .

As already discussed in section 3.2.5, the complete information provided by the pdf $\Psi(\mathbf{r}, \mathbf{u}, t)$, which in two spatial dimensions is a four-dimensional function (two spatial coordinates, one orientational¹ coordinate and time), is often not needed to describe the basic physics of a system. In a usual liquid crystal for example, cf. section 3.1 and [26, 25], since the first moment with respect to the orientational degree of freedom vanishes due to the $\pm\mathbf{u}$ -symmetry of the molecules, one can describe the isotropic-nematic (I-N) transition in such a system in good approximation by the second moment with respect to orientation, $S_{ij} = \int d\mathbf{u} u_i u_j \Psi(\mathbf{u})$, which defines the nematic order parameter tensor. As has already been exemplified in section 3.2.5, where the threshold of the I-N transition has been calculated by performing a moment expansion, one can derive an equation of motion for the nematic order parameter, which is much easier to analyze than the pdf equation. In a similar manner, to investigate the filament-motor model one should extract from the pdf equation equations of motion for the moments that are relevant for the description of the basic physics.

In part I of this work, there has been already discussed that both kind of filaments under

¹The unit vector \mathbf{u} can be expressed in two spatial dimensions by a single angle variable θ . In three dimensions one needs two angles (θ, φ) , the problem then being even $3 + 2 + 1 = 6$ -dimensional.

consideration here, namely microtubules and actin, can display lyotropic liquid crystalline phases, i.e. S_{ij} can become relevant for densities near or above the I-N threshold density ρ_{IN} . In filament-motor systems however, an important difference to usual liquid crystalline behavior arises: the molecular motors interacting with the filaments and influencing their order when in contact with more than one of them walk on the filaments only in a specified direction, which is defined by the underlying protein structures of both the motor and the helical filaments. By this mechanism the presence of the motors breaks the $\pm\mathbf{u}$ -symmetry of the rod liquid. Thus the first moment of the pdf, namely the vectorial quantity $\int d\mathbf{u} \mathbf{u} \Psi(\mathbf{u})$, may become nonvanishing in a filament-motor solution and has to be accounted for.

In the model defined in section 7.2, one has assumed that the motor density is homogeneous, whereas the filaments are allowed to become inhomogeneously distributed. The relevant moments with respect to the orientation are thus the zeroth, first and second moment of the pdf describing the filaments, corresponding to the filament density $\rho(\mathbf{r}, t)$, the polar orientation $\mathbf{t}(\mathbf{r}, t)$ and the nematic order parameter $S_{ij}(\mathbf{r}, t)$ respectively. These are defined by the following expressions, cf. also section 3.2.5,

$$\begin{aligned}\rho(\mathbf{r}, t) &= \int d\mathbf{u} \Psi(\mathbf{r}, \mathbf{u}, t) , \\ \mathbf{t}(\mathbf{r}, t) &= \int d\mathbf{u} \mathbf{u} \Psi(\mathbf{r}, \mathbf{u}, t) , \\ S_{ij}(\mathbf{r}, t) &= \int d\mathbf{u} u_i u_j \Psi(\mathbf{r}, \mathbf{u}, t) .\end{aligned}\tag{8.1}$$

The density for the isotropic-nematic transition in the framework of the Doi model has already been obtained in section 3.2.5 and evaluates for a two-dimensional system to $3\pi/2$ in dimensionless units. However, in the experiments of Refs. [31, 33] we want to describe, the aster patterns evolve at a much lower filament density than the critical density of the isotropic-nematic transition, namely at concentrations of about 0.2-0.3 mg/ml as compared to the experimental value of the transition density for microtubules of 2.5 mg/ml [19]. Thus it appears to be a suitable approximation to truncate the moment expansion for the pdf already at the first moment to derive a closed set of equations. Instead of Eq. (3.56), which has to be used in a usual nematic, now the distribution function should be represented in terms of $\rho(\mathbf{r}, t)$ and $\mathbf{t}(\mathbf{r}, t)$ (for more details we refer to section 8.2.2)

$$\Psi(\mathbf{r}, \mathbf{u}, t) \simeq \frac{1}{2\pi} \left\{ \rho(\mathbf{r}, t) + 2\mathbf{u} \cdot \mathbf{t}(\mathbf{r}, t) \right\} .\tag{8.2}$$

If we consider now the filament-motor model, governed by Eq. (7.10),

$$\partial_t \Psi + \nabla \cdot \mathbf{J}_t + \mathcal{R} \cdot \mathbf{J}_r = 0 ,\tag{8.3}$$

an integration of this equation over $\int d\mathbf{u}$ leads to an evolution equation for the macroscopic density $\rho(\mathbf{r}, t)$, while integration over $\int d\mathbf{u} \mathbf{u}$ yields a dynamical equation for the macroscopic filament orientation field $\mathbf{t}(\mathbf{r}, t)$. The integrals on the right hand sides of the evolution equations can be carried out analytically if the currents are gradient expanded,

as mentioned above and described in more detail in section 8.2.1, and the pdfs in the currents are replaced by the moment approximation of Eq. (8.2). One finally gets a system of nonlinear partial differential equations that can now be dealt with, at least to some extent, both analytically and numerically.

8.1.1 The continuum model

In two spatial dimensions, the equations for the filament density and the two components of the filament orientation field t_i ($i = 1, 2$ or x, y) read as follows:

$$\begin{aligned} \partial_t \rho &= \frac{1+D}{2} \Delta \rho + \left(\frac{1+D}{\pi} - \frac{\alpha}{24} \right) \partial_j (\rho \partial_j \rho) - \frac{\alpha}{48} \partial_i \left[t_i \partial_j t_j + t_j \partial_i t_j + t_j \partial_j t_i \right] \\ &- \frac{\alpha}{C_1} \left[38 \partial_j (\rho \partial_j \Delta \rho) + 11 \partial_i (t_j \partial_i \Delta t_j) + 16 \partial_i \left(t_i \Delta \partial_j t_j + 2 t_j \partial_j \partial_i \partial_l t_l + t_j \partial_j \Delta t_i \right) \right] \\ &- \frac{\beta}{96} \partial_i \left[\rho \partial_i \partial_j t_j - t_j \partial_j \partial_i \rho + \frac{3}{2} (\rho \Delta t_i - t_i \Delta \rho) \right], \end{aligned} \quad (8.4a)$$

$$\begin{aligned} \partial_t t_i &= -D_r t_i + \frac{3D+1}{4} \Delta t_i + \frac{1-D}{2} \partial_i \partial_j t_j \\ &+ \frac{3D+1}{2\pi} \partial_j (t_i \partial_j \rho) + \frac{1-D}{2\pi} \left[\partial_j (t_j \partial_i \rho) + \partial_i (t_j \partial_j \rho) \right] \\ &- \frac{\alpha}{96} \partial_j \left[3 t_i \partial_j \rho + t_j \partial_i \rho + \delta_{ij} t_l \partial_l \rho + \rho (\partial_i t_j + \partial_j t_i + \delta_{ij} \partial_l t_l) \right] \\ &- \frac{\alpha}{2C_1} \partial_j \left[\rho \left(11 \partial_j \Delta t_i + 16 \partial_i \Delta t_j + 32 \partial_j \partial_i \partial_l t_l + 16 \delta_{ij} \Delta \partial_l t_l \right) \right. \\ &\quad \left. + 16 t_j \partial_i \Delta \rho + 32 t_l \partial_l \partial_i \partial_j \rho + 44 t_i \partial_j \Delta \rho + 16 \delta_{ij} t_l \partial_l \Delta \rho \right] \\ &+ \frac{\beta}{2} \partial_j \left[\frac{1}{2} \delta_{ij} \rho^2 - t_i t_j \right] + \frac{\beta}{96} \partial_j \left[\frac{3}{4} \delta_{ij} \rho \Delta \rho + \frac{1}{2} \rho \partial_i \partial_j \rho - t_l \partial_l \partial_i t_j - t_i \partial_j \partial_l t_l - t_i \Delta t_j \right] \\ &+ \frac{1}{48} \left(\frac{\gamma}{4} - \frac{4}{\pi} D_r \right) \left[t_j \partial_j \partial_i \rho - \frac{1}{2} t_i \Delta \rho \right], \end{aligned} \quad (8.4b)$$

with the abbreviation $C_1 = 23040$. The equations have been made dimensionless by the following rescaling of variables

$$\begin{aligned} t' &= \frac{D_{\parallel}}{L^2} t, \quad x' = \frac{1}{L} x, \quad \rho' = L^2 \rho, \quad \mathbf{t}' = L^2 \mathbf{t}, \\ D'_r &= \frac{L^2}{D_{\parallel}} D_r, \quad D = \frac{D_{\perp}}{D_{\parallel}}, \quad \alpha' = \frac{L}{D_{\parallel}} \alpha, \quad \beta' = \frac{L}{D_{\parallel}} \beta, \quad \gamma' = \frac{L^2}{D_{\parallel}} \gamma. \end{aligned} \quad (8.5)$$

Here the ratio D of the translational diffusion coefficients in perpendicular and parallel direction has been introduced. One can again see by the rescaling that while α and β

have the units of a velocity, γ has the same unit as the rotational diffusion coefficient D_r , namely s^{-1} .

Details of the derivation are postponed to the next sections: in section 8.2.1 the gradient expansion of the nonlocal integrals is carried out and in sections 8.2.2 and 8.2.3 the moment expansion and the structure of the resulting equations is shown and discussed in some detail.

One can see from Eqs. (8.4) that the contributions from the diffusion as well as the terms proportional to α and γ have $\pm\mathbf{t}$ symmetry, whereas the β -contributions break this symmetry. Additionally, Eqs. (8.4) are unchanged by the transformations $(\mathbf{t}, \mathbf{r}) \rightarrow (-\mathbf{t}, -\mathbf{r})$, $(\mathbf{t}, \beta) \rightarrow (-\mathbf{t}, -\beta)$ and $(\mathbf{r}, \beta) \rightarrow (-\mathbf{r}, -\beta)$. This emphasizes that the β -contributions play a special role². Consequently, the linear analysis carried out in chapter 9 predicts, apart from a long wavelength demixing instability, a finite wavenumber instability which is stationary in the case $\beta = 0$ but becomes oscillatory in the case $\beta \neq 0$. The symmetries $(\mathbf{t}, \beta) \rightarrow (-\mathbf{t}, -\beta)$ and $(\mathbf{r}, \beta) \rightarrow (-\mathbf{r}, -\beta)$ then imply that waves traveling to the right and left can be transformed into each other by a change of sign in β .

Nevertheless the α -contribution has to be considered the most important one, since it is responsible for inducing the instabilities in the system, while the β -contribution changes the quality of the instability from stationary to oscillatory. Consequently, I first investigate the stationary instability in detail in chapter 10, followed by the oscillatory instability in chapter 11. The active rotational current proportional to γ is purely nonlinear and therefore influences only the pattern selection beyond threshold, as will also be addressed briefly in chapter 10.

Considering the demixing instability mentioned above, while the density and the orientation are decoupled in the linear regime in the case $\beta = 0$, the presence of the β -contributions leads to a linear coupling. This allows for the aster-like structures formed during the demixing to discriminate asters with the filaments pointing outwards from those with the filaments pointing inwards. This instability is investigated in chapter 12.

The contributions to Eqs. (8.4) that have fourth order derivatives are indispensable for the determination of the instabilities evolving from the homogeneous filament distribution, as will become clear during the linear stability analysis in chapter 9. They were not taken into account in the original work, Ref. [40], which has been criticized by us and their importance pointed out in Ref. [46]. Contributions with fourth order derivatives caused by excluded volume induced translational diffusion have however been neglected in Eqs. (8.4). First they are overcompensated by the included fourth derivative terms resulting from the active current and therefore influence the presented results only quantitatively by a small amount (but considerably complicate the equations). Second they have the same symmetries as the terms discussed above and therefore should not lead to additional insight.

²One should keep in mind that we have allowed \mathbf{t} to become nonzero, i.e. we have allowed the breaking of the $\pm\mathbf{u}$ -symmetry of the microscopic model, Eq. (3.22). The continuum equations (8.4) nevertheless have a $\pm\mathbf{t}$ -symmetry in the case $\beta = 0$.

8.2 Details of the derivation

8.2.1 The gradient expansion of the interaction integrals

The excluded volume interaction, Eq. (7.16), as well as the motor induced filament-filament interactions, Eqs. (7.14), (7.15), (7.17) and (7.18), are defined by overlap integrals. Hence the equation of motion (7.10) for the pdf $\Psi(\mathbf{r}, \mathbf{u}, t)$ is nonlocal and its solution is exceedingly difficult. Assuming that spatial variations are small on the length scale L of a filament, in order to get a local equation one performs a systematic expansion of the integrals with respect to gradients of the pdf.

The potential of the excluded volume interaction, Eq. (7.16), is defined by

$$V_{ex}(\mathbf{r}, \mathbf{u}) = \int d\mathbf{u}' \int d\mathbf{r}' W(\mathbf{r}-\mathbf{r}', \mathbf{u}, \mathbf{u}') \Psi(\mathbf{r}', \mathbf{u}') , \quad (8.6)$$

wherein $W(\mathbf{r}-\mathbf{r}', \mathbf{u}, \mathbf{u}') = 1$ if there is overlap of two rods at (\mathbf{r}, \mathbf{u}) and $(\mathbf{r}', \mathbf{u}')$ and $W = 0$ else. As already discussed in section 3.2.2, this overlap integral is best expressed in (two-dimensional) Straley coordinates, cf. Eq. (3.29), which are defined by

$$\mathbf{r} - \mathbf{r}' = \mathbf{u}\zeta + \mathbf{u}'\eta , \quad (8.7)$$

with the parameter constraint $-L/2 < \zeta, \eta < L/2$ and the Jacobian $|\mathbf{u} \times \mathbf{u}'|$. In these coordinates overlap is conveniently described by the possibility that a linear combination $\mathbf{u}\zeta + \mathbf{u}'\eta$ of the rod orientations with $-L/2 < \zeta, \eta < L/2$ yields the difference vector of the center of masses of the two rods $\mathbf{r} - \mathbf{r}'$. The integral kernel expressed in these coordinates reads, cf. Eq. (3.30),

$$W(\mathbf{r}-\mathbf{r}', \mathbf{u}, \mathbf{u}') = |\mathbf{u} \times \mathbf{u}'| \int_{-L/2}^{L/2} d\zeta \int_{-L/2}^{L/2} d\eta \delta(\mathbf{r}-\mathbf{r}'+\mathbf{u}\zeta+\mathbf{u}'\eta) \quad (8.8)$$

and the excluded volume interaction explicitly becomes the multidimensional integral

$$V_{ex}(\mathbf{r}, \mathbf{u}) = \int d\mathbf{u}' \int d\mathbf{r}' \int_{-L/2}^{L/2} d\zeta \int_{-L/2}^{L/2} d\eta |\mathbf{u} \times \mathbf{u}'| \delta(\mathbf{r}-\mathbf{r}'+\mathbf{u}\zeta+\mathbf{u}'\eta) \Psi(\mathbf{r}', \mathbf{u}') . \quad (8.9)$$

Performing now the \mathbf{r}' -integration and expanding the obtained pdf, $\Psi(\mathbf{r} + \mathbf{u}\zeta + \mathbf{u}'\eta)$, in powers of $\tilde{\mathbf{u}} = \mathbf{u}\zeta + \mathbf{u}'\eta$ one gets

$$V_{ex}(\mathbf{r}, \mathbf{u}) = \int d\mathbf{u}' |\mathbf{u} \times \mathbf{u}'| \int_{-L/2}^{L/2} d\zeta \int_{-L/2}^{L/2} d\eta \left[1 + (\tilde{\mathbf{u}} \cdot \partial_{\mathbf{r}}) + \frac{1}{2} (\tilde{\mathbf{u}} \cdot \partial_{\mathbf{r}})^2 + \dots \right] \Psi(\mathbf{r}, \mathbf{u}') . \quad (8.10)$$

As the η - and ζ -integrations are on a symmetric interval, $[-L/2, L/2]$, odd powers in one of the two variables vanish. So does the term linear in $\tilde{\mathbf{u}}$, as well as the mixed term $\propto \eta\zeta$

from the quadratic contribution. The purely quadratic terms being trivially integrable, e.g.

$$\int_{-L/2}^{L/2} d\eta \int_{-L/2}^{L/2} d\zeta \zeta^2 (\mathbf{u} \cdot \partial_{\mathbf{r}})^2 = \frac{L^4}{12} (\mathbf{u} \cdot \partial_{\mathbf{r}})^2,$$

one finally obtains

$$V_{ex}(\mathbf{r}, \mathbf{u}) = L^2 \int d\mathbf{u}' |\mathbf{u} \times \mathbf{u}'| \left[1 + \frac{L^2}{24} \left\{ (\mathbf{u} \cdot \partial_{\mathbf{r}})^2 + (\mathbf{u}' \cdot \partial_{\mathbf{r}})^2 \right\} \right] \Psi(\mathbf{r}, \mathbf{u}') , \quad (8.11)$$

which holds up to an error of $\mathcal{O}(\partial_{\mathbf{r}}^4)$. The prefactor L^2 in this expression reflects the two-dimensional excluded volume.

By the same procedure, we have to evaluate the contributions of the active translational and rotational currents, following from Eqs. (7.14), (7.15), (7.17) and (7.18),

$$\mathbf{J}_t^a = \Psi(\mathbf{r}, \mathbf{u}) \int d\mathbf{u}' \int d\mathbf{r}' \mathbf{v}(\mathbf{r}-\mathbf{r}', \mathbf{u}, \mathbf{u}') W(\mathbf{r}-\mathbf{r}', \mathbf{u}, \mathbf{u}') \Psi(\mathbf{r}', \mathbf{u}') , \quad (8.12)$$

$$\mathbf{J}_r^a = \Psi(\mathbf{r}, \mathbf{u}) \int d\mathbf{u}' \int d\mathbf{r}' \boldsymbol{\omega}(\mathbf{r}-\mathbf{r}', \mathbf{u}, \mathbf{u}') W(\mathbf{r}-\mathbf{r}', \mathbf{u}, \mathbf{u}') \Psi(\mathbf{r}', \mathbf{u}') , \quad (8.13)$$

with the relative translational and angular velocities

$$\mathbf{v}(\mathbf{r}-\mathbf{r}', \mathbf{u}, \mathbf{u}') = \frac{\alpha}{2} \frac{\mathbf{r}' - \mathbf{r}}{L} \frac{1 + \mathbf{u} \cdot \mathbf{u}'}{|\mathbf{u} \times \mathbf{u}'|} + \frac{\beta}{2} \frac{\mathbf{u}' - \mathbf{u}}{|\mathbf{u} \times \mathbf{u}'|} , \quad (8.14)$$

$$\boldsymbol{\omega}(\mathbf{u}, \mathbf{u}') = \gamma (\mathbf{u} \cdot \mathbf{u}') \frac{\mathbf{u} \times \mathbf{u}'}{|\mathbf{u} \times \mathbf{u}'|} . \quad (8.15)$$

Let's at first consider the active translational term proportional to α , which explicitly reads

$$\mathbf{J}_t^\alpha = \frac{\alpha}{2L} \Psi(\mathbf{r}, \mathbf{u}) \int d\mathbf{u}' \int d\mathbf{r}' (\mathbf{r}' - \mathbf{r}) (1 + \mathbf{u} \cdot \mathbf{u}') \delta(\mathbf{r} - \mathbf{r}' + \mathbf{u}\zeta + \mathbf{u}'\eta) \Psi(\mathbf{r}', \mathbf{u}') , \quad (8.16)$$

where we have used Eq. (8.8) to express W . The Jacobian $|\mathbf{u} \times \mathbf{u}'|$ cancels due to the normalization of the velocities to the excluded volume. Performing again the \mathbf{r}' -integration transforms the factor $(\mathbf{r}' - \mathbf{r})$ into $\tilde{\mathbf{u}}$ and the pdf can again be expanded. Due to the additional factor $\tilde{\mathbf{u}}$ from the velocity, now the linear and cubic powers in the expansion survive the symmetric integrations. In total one gets

$$\begin{aligned} J_t^\alpha &= \frac{\alpha L^3}{24} \Psi(\mathbf{r}, \mathbf{u}) \int d\mathbf{u}' (1 + \mathbf{u} \cdot \mathbf{u}') \\ &\cdot \left\{ \mathbf{u} (\mathbf{u} \cdot \partial_{\mathbf{r}}) \left[1 + \frac{L^2}{8} \left(\frac{1}{5} (\mathbf{u} \cdot \partial_{\mathbf{r}})^2 + \frac{1}{3} (\mathbf{u}' \cdot \partial_{\mathbf{r}})^2 \right) \right] \right. \\ &\quad \left. + \mathbf{u}' (\mathbf{u}' \cdot \partial_{\mathbf{r}}) \left[1 + \frac{L^2}{8} \left(\frac{1}{5} (\mathbf{u}' \cdot \partial_{\mathbf{r}})^2 + \frac{1}{3} (\mathbf{u} \cdot \partial_{\mathbf{r}})^2 \right) \right] \right\} \Psi(\mathbf{r}, \mathbf{u}') . \end{aligned} \quad (8.17)$$

Since there is no factor $(\mathbf{r}' - \mathbf{r})$ and consequently no additional ζ, η -dependence in the translational velocity $\propto \beta$, as well as in the angular velocity contribution $\propto \gamma$, the procedure is entirely analogous to the evaluation of the excluded volume contribution and yields

$$J_t^\beta = \frac{\beta L^2}{2} \Psi(\mathbf{r}, \mathbf{u}) \int d\mathbf{u}' (\mathbf{u}' - \mathbf{u}) \left[1 + \frac{L^2}{24} \left\{ (\mathbf{u} \cdot \partial_{\mathbf{r}})^2 + (\mathbf{u}' \cdot \partial_{\mathbf{r}})^2 \right\} \right] \Psi(\mathbf{r}, \mathbf{u}') \quad (8.18)$$

and

$$J_r^\gamma = \gamma L^2 \Psi(\mathbf{r}, \mathbf{u}) \int d\mathbf{u}' (\mathbf{u} \cdot \mathbf{u}') (\mathbf{u} \times \mathbf{u}') \left[1 + \frac{L^2}{24} \left\{ (\mathbf{u} \cdot \partial_{\mathbf{r}})^2 + (\mathbf{u}' \cdot \partial_{\mathbf{r}})^2 \right\} \right] \Psi(\mathbf{r}, \mathbf{u}') \quad , \quad (8.19)$$

respectively.

One should note that due to the ζ, η -integrations, odd powers of $\partial_{\mathbf{r}}$ vanish in the expressions for the excluded volume and the α - and γ -contributions, which is the mathematical reason underlying the rotational symmetry of Eqs. (8.4) for $\beta = 0$.

The gradient expanded expressions are still integrals over the orientational degree of freedom \mathbf{u}' , which can be carried out analytically after having performed the moment expansion described in the next section.

8.2.2 The moment expansion method

As already discussed in section 8.1, we use a moment expansion to extract from the model equation for the pdf, Eq. (7.10), equations of motion for the relevant moments of the pdf with respect to orientation. These have already been identified as the density $\rho(\mathbf{r}, t)$ and the orientation field $\mathbf{t}(\mathbf{r}, t)$, cf. Eqs. (8.1). Due to the low filament densities both in cells and in *in vitro* experiments, we opt for neglecting the second moment, i.e. the nematic order parameter. Therefore one can write

$$\Psi(\mathbf{r}, \mathbf{u}, t) \simeq \frac{1}{2\pi} \left\{ \rho(\mathbf{r}, t) + 2\mathbf{u} \cdot \mathbf{t}(\mathbf{r}, t) \right\} \quad . \quad (8.20)$$

The validity of this representation can be seen immediately by using it to evaluate the first moments, analogously to the procedure in section 3.2.5. Defining the two-dimensional orientational average, cf. Eq. (A.7), by

$$\langle A(\mathbf{u}) \rangle = \int \frac{d\mathbf{u}}{2\pi} A(\mathbf{u}) = \int_0^{2\pi} \frac{d\theta}{2\pi} A(\theta) \quad , \quad (8.21)$$

with θ parameterizing the unit vector \mathbf{u} , making use of Eq. (8.20) correctly yields

$$\begin{aligned} \int d\mathbf{u} \Psi(\mathbf{r}, \mathbf{u}, t) &= \int \frac{d\mathbf{u}}{2\pi} \left\{ \rho(\mathbf{r}, t) + 2\mathbf{u} \cdot \mathbf{t}(\mathbf{r}, t) \right\} \\ &= \rho(\mathbf{r}, t) + 2\langle u_j \rangle t_j(\mathbf{r}, t) = \rho(\mathbf{r}, t) \quad , \end{aligned} \quad (8.22)$$

since odd powers of \mathbf{u} vanish upon orientational averaging. Analogously,

$$\begin{aligned} \int d\mathbf{u} u_i \Psi(\mathbf{r}, \mathbf{u}, t) &= \int \frac{d\mathbf{u}}{2\pi} u_i \left\{ \rho(\mathbf{r}, t) + 2\mathbf{u} \cdot \mathbf{t}(\mathbf{r}, t) \right\} \\ &= \langle u_i \rangle \rho(\mathbf{r}, t) + 2\langle u_i u_j \rangle t_j(\mathbf{r}, t) = t_i(\mathbf{r}, t) \end{aligned} \quad (8.23)$$

holds, since again $\langle u_i \rangle = 0$ and $\langle u_i u_j \rangle = \delta_{ij}/2$.

The way of deriving Eqs. (8.4) is now the following: Integration of Eq. (7.10),

$$\partial_t \Psi + \nabla \cdot \mathbf{J}_t + \mathcal{R} \cdot \mathbf{J}_r = 0, \quad (8.24)$$

by $\int d\mathbf{u}$ and $\int d\mathbf{u} \mathbf{u}$ yields evolution equations for $\rho(\mathbf{r}, t)$ and $\mathbf{t}(\mathbf{r}, t)$ respectively,

$$\begin{aligned} \partial_t \rho &= - \int d\mathbf{u} \left(\nabla \cdot \mathbf{J}_t + \mathcal{R} \cdot \mathbf{J}_r \right), \\ \partial_t t_i &= - \int d\mathbf{u} u_i \left(\nabla \cdot \mathbf{J}_t + \mathcal{R} \cdot \mathbf{J}_r \right). \end{aligned} \quad (8.25)$$

Inserting the gradient expanded expressions for the excluded volume, Eq. (8.11), and the active translational, Eqs. (8.17), (8.18), and rotational currents, Eq. (8.19), on the right hand sides of Eqs. (8.25) leads to integrals $\int d\mathbf{u} \int d\mathbf{u}'$ over $\Psi(\mathbf{u})$ and $\Psi(\mathbf{u}')$. However, if we now express the pdfs by its moments using Eq. (8.20), the integrands are reduced to powers in both \mathbf{u} and \mathbf{u}' and the integrals can be carried out analytically using the averaging formulas given in appendix A.2.

The detailed structure and symmetries of Eqs. (8.4) can be traced back to the different structures concerning powers of \mathbf{u} and \mathbf{u}' of the nonlinear filament-filament interactions. The structure of the different contributions will be derived in the next section, neglecting however the detailed numerical coefficients. The derivation of the latter is quite cumbersome and gives no additional insight.

8.2.3 Structure of the equations

The specific prefactors of the continuum equations, Eqs. (8.4), need the correct evaluation of quite elaborate isotropic averages. Simple characteristics of these averages however give already deep insight into the structure and symmetry of the equations. Inserting the gradient expanded expressions for the excluded volume and the active currents, cf. section 8.2.1, into the conservation law for the probability, Eq. (7.10), one gets the following contributions for the evolution of $\Psi(\mathbf{r}, \mathbf{u}, t)$:

$$\partial_t \Psi = D_{ij} \partial_i \partial_j \Psi \quad \text{translational diffusion} \quad (8.26a)$$

$$+ D_{ij} \partial_i (\Psi \partial_j V_{ex}) \quad \text{translational excluded volume interaction} \quad (8.26b)$$

$$- \partial_i J_{t,i}^\alpha - \partial_i J_{t,i}^\beta \quad \text{active translations by the motors} \quad (8.26c)$$

$$+ D_r \mathcal{R}^2 \Psi \quad \text{rotational diffusion} \quad (8.26d)$$

$$+ D_r \mathcal{R}_i (\Psi \mathcal{R}_i V_{ex}) \quad \text{rotational excluded volume interaction} \quad (8.26e)$$

$$- \mathcal{R}_i J_{r,i}^\gamma \quad \text{active rotations by the motors} \quad (8.26f)$$

As can be seen, the contributions taken into account in the model are translational and rotational diffusion, (8.26a) and (8.26d), translational and rotational excluded volume contributions, (8.26b) and (8.26e), and active translational and rotational motor transport, (8.26c) and (8.26f), respectively. As already explained in the last section, continuum equations for the filament density $\rho(\mathbf{r}, t)$ and the filament orientation field $\mathbf{t}(\mathbf{r}, t)$ are obtained by expressing the pdfs on the right hand side of Eq. (8.26) by its first two moments, cf. Eq. (8.20),

$$\Psi(\mathbf{r}, \mathbf{u}, t) \simeq \frac{1}{2\pi} \left\{ \rho(\mathbf{r}, t) + 2\mathbf{u} \cdot \mathbf{t}(\mathbf{r}, t) \right\}, \quad (8.27)$$

and performing integrations $\int d\mathbf{u}$ and $\int d\mathbf{u} \mathbf{u}$.

The structure of these continuum equations can already be determined by using a simple property of the isotropic averages, namely the fact that isotropic averages of odd powers of \mathbf{u} or \mathbf{u}' vanish. For simplicity we do not care about prefactors here and will not write down all indices. The aim of this section is just to establish where density and orientation or gradients thereof couple and in which powers. Thus when I write e.g. a term $\partial(t\partial t)$ this should be read as some components or contractions of $\partial_i(t_j\partial_k t_l)$.

The equation for the density

Let's first have a look at the density equation, i.e. which contributions the right hand side of Eq. (8.26) yields to $\int d\mathbf{u} \partial_i \Psi = \partial_i \rho$. The translational diffusion contribution, (8.26a), reads

$$\int d\mathbf{u} D_{ij} \partial_i \partial_j \frac{1}{2\pi} \left\{ \rho + 2\mathbf{u} \cdot \mathbf{t} \right\} = \left\langle D_{ij} \partial_i \partial_j \left\{ \rho + 2\mathbf{u} \cdot \mathbf{t} \right\} \right\rangle. \quad (8.28)$$

Since the anisotropic diffusion coefficient $D_{ij} = D_{\parallel} u_i u_j + D_{\perp} (\delta_{ij} - u_i u_j)$ is even in \mathbf{u} and odd powers vanish upon isotropic averaging, the term $\propto \mathbf{t}$ vanishes. Thus one gets just an anisotropic diffusion term in the density $\sim \langle D_{ij} \rangle \partial_i \partial_j \rho$ and no linear coupling to the orientation.

The translational excluded volume contribution, (8.26b), reads explicitly

$$\left\langle D_{ij} \partial_i \left(\left\{ \rho + 2\mathbf{u} \cdot \mathbf{t} \right\} \partial_j \left\langle |\mathbf{u} \times \mathbf{u}'| \left[1 + \frac{L^2}{24} \left\{ (\mathbf{u} \cdot \partial_{\mathbf{r}})^2 + (\mathbf{u}' \cdot \partial_{\mathbf{r}})^2 \right\} \right] \left\{ \rho + 2\mathbf{u}' \cdot \mathbf{t} \right\} \right) \right) \right\rangle, \quad (8.29)$$

where the primed averaging brackets imply averaging upon \mathbf{u}' . Since D_{ij} , $|\mathbf{u} \times \mathbf{u}'|$ and the gradient expansion term in the squared brackets are even in \mathbf{u} and \mathbf{u}' , the orientation field \mathbf{t} entering with an odd factor of \mathbf{u} or \mathbf{u}' respectively does not survive. I have calculated the excluded volume contribution up to the order $\mathcal{O}(\partial_{\mathbf{r}}^4)$. However, the active motor contribution $\propto \alpha$ wins over the excluded volume and leads to the needed high wavenumber restriction, cf. chapter 9. For this reason and to make the coarse grained equations not unnecessarily complicated, we omit the $\mathcal{O}(\partial_{\mathbf{r}}^4)$ -term in the excluded volume and end up with a diffusion term that is nonlinear in the density and $\propto \partial_i (\rho \partial_j \rho)$.

From the last calculation we have learned that terms even in \mathbf{u} and \mathbf{u}' play not a decisive role for the structure of the equations (they determine however which vectorial components of $\partial_{\mathbf{r}}$ and \mathbf{t} enter into the equations). Therefore we will abbreviate such terms in the following. For the active translational motor transport, (8.26c), we have to deal with the term $\propto \alpha$,

$$-\alpha \partial_i \left\langle \left\{ \rho + 2\mathbf{u} \cdot \mathbf{t} \right\} \left\langle (1 + \mathbf{u} \cdot \mathbf{u}') [\partial_{\mathbf{r}} + \partial_{\mathbf{r}}^3]_i \left\{ \rho + 2\mathbf{u}' \cdot \mathbf{t} \right\} \right\rangle \right\rangle , \quad (8.30)$$

where the abbreviation $[\partial_{\mathbf{r}} + \partial_{\mathbf{r}}^3]_i$ has been introduced for the squared bracketed term in Eq. (8.17) resulting from the gradient expansion and containing only even powers of \mathbf{u} and \mathbf{u}' . The decisive factor in the α -contribution is $(1 + \mathbf{u} \cdot \mathbf{u}')$, leading to contributions $-\alpha \partial(\rho \partial \rho)$ and $-\alpha \partial(\rho \partial^3 \rho)$ from the constant term and to contributions $-\alpha \partial(t \partial t)$ and $-\alpha \partial(t \partial^3 t)$ from the part $\mathbf{u} \cdot \mathbf{u}'$. Here the orientation field enters for the first time into the evolution equation for the density.

The contribution $\propto \beta$ reads

$$-\beta \partial_i \left\langle \left\{ \rho + 2\mathbf{u} \cdot \mathbf{t} \right\} \left\langle (u'_i - u_i) [1 + \partial_{\mathbf{r}}^2] \left\{ \rho + 2\mathbf{u}' \cdot \mathbf{t} \right\} \right\rangle \right\rangle , \quad (8.31)$$

where $[1 + \partial_{\mathbf{r}}^2]$ abbreviates the gradient expanded excluded volume, having only even powers of \mathbf{u} and \mathbf{u}' . From the factor $(u'_i - u_i)$ one would expect coupled terms like $-\beta \partial(\rho t - t \rho)$ and $-\beta \partial(\rho \partial^2 t - t \partial^2 \rho)$. However, while the third order derivative term is present, the term linear in $\partial_{\mathbf{r}}$ vanishes from

$$\begin{aligned} & -\beta \partial_i \left\langle \left\{ \rho + 2\mathbf{u} \cdot \mathbf{t} \right\} \left\langle (u'_i - u_i) \left\{ \rho + 2\mathbf{u}' \cdot \mathbf{t} \right\} \right\rangle \right\rangle \\ &= -\beta \partial_i \left(\rho \langle u'_i u'_k \rangle' 2t_k - 2t_k \langle u_k u_i \rangle \rho \right) = 0 , \end{aligned} \quad (8.32)$$

where the bracket cancels due to $\langle u_i u_k \rangle = \delta_{ik}/2$.

In the density equation, the rotational diffusion, (8.26d), the rotational excluded volume contributions, (8.26e), as well as the rotational motor transport term, (8.26f), all vanish. This is clear from intuition, since the density (as the zeroth order moment of the orientation) should not depend on rotational degrees of freedom. The mathematical reason is that in the density equation, i.e. upon integration over $\int d\mathbf{u}$, all these contributions have the form $\int d\mathbf{u} \mathcal{R} \cdot (\dots)$, which is zero due to the Stokes's theorem on the unit sphere³.

³Stokes's theorem for a vector field $\mathbf{f}(\mathbf{r})$ with a surface A and ∂A its boundary, reads $\int_A d\mathbf{A} \cdot \nabla_{\mathbf{r}} \times \mathbf{f}(\mathbf{r}) = \int_{\partial A} d\mathbf{l} \cdot \mathbf{f}(\mathbf{r})$. Considering now a vector field $\mathbf{f}(\mathbf{u})$, the unit sphere defined by $|\mathbf{u}| = 1$ is a closed surface, thus there is no boundary and the left hand side is zero in this case. The surface element can be parameterized by $d\mathbf{A} = \mathbf{u} d\mathbf{u}$ and together with the identity $\mathbf{u} \cdot (\nabla_{\mathbf{u}} \times \mathbf{f}(\mathbf{u})) = (\mathbf{u} \times \nabla_{\mathbf{u}}) \cdot \mathbf{f}(\mathbf{u}) = \mathcal{R} \cdot \mathbf{f}(\mathbf{u})$ one obtains $\int d\mathbf{u} \mathcal{R} \cdot \mathbf{f}(\mathbf{u}) = 0$. From Ref. [93].

The equation for the orientation field

The equation for the orientation field, i.e. the contributions from the right hand side of Eq. (8.26) to $\int d\mathbf{u} u_i \partial_t \Psi = \partial_t t_i$, can be discussed analogously.

In the translational contributions, (8.26a) again yields a diffusive contribution, $\partial_i \partial_j t$, but no linear coupling to the density. The excluded volume contribution however, (8.26b), now leads to a coupling $\partial_i(t \partial_j \rho)$, in contrary to the case of the density equation, where only a self-coupling arose. Concerning the active motor transport, (8.26c) yields $-\alpha \partial(\rho \partial t)$ and $-\alpha \partial(\rho \partial^3 t)$, as well as $-\alpha \partial(t \partial \rho)$ and $-\alpha \partial(t \partial^3 \rho)$, and for the β -term $-\beta \partial(-\rho^2 + t^2)$ and $-\beta \partial(-\rho \partial^2 \rho + t \partial^2 t)$. Here the terms of order $\mathcal{O}(\partial_{\mathbf{r}})$ obviously do not cancel.

The rotational contributions, (8.26d), (8.26e) and (8.26f), are a bit more involved to evaluate because the rotational operator, defined as $\mathcal{R} = \mathbf{u} \times \partial_{\mathbf{u}}$ or explicitly as

$$\mathcal{R}_i = [\mathbf{u} \times \partial_{\mathbf{u}}]_i = \delta_{i3} (u_1 \partial_{u_2} - u_2 \partial_{u_1}) \quad (8.33)$$

in two dimensions, comes into play upon averaging. For the rotational diffusion term, (8.26d), we have to calculate

$$D_r \left\langle u_i \mathcal{R}^2 \left\{ \rho + 2\mathbf{u} \cdot \mathbf{t} \right\} \right\rangle = D_r \left\langle u_i (\mathcal{R}^2 u_j) 2t_j \right\rangle = -D_r \langle u_i u_j \rangle 2t_j = -D_r t_i, \quad (8.34)$$

where in the second step we have made use of

$$\begin{aligned} \mathcal{R}^2 u_j &= (u_1 \partial_{u_2} - u_2 \partial_{u_1}) (u_1 \partial_{u_2} - u_2 \partial_{u_1}) u_j \\ &= u_1^2 \partial_{u_2}^2 u_j - u_1 \partial_{u_2} (u_2 \partial_{u_1} u_j) - u_2 \partial_{u_1} (u_1 \partial_{u_2} u_j) + u_2^2 \partial_{u_1}^2 u_j \\ &= -u_1 \partial_{u_2} (u_2 \delta_{j1}) - u_2 \partial_{u_1} (u_1 \delta_{j2}) = -u_1 \delta_{j1} - u_2 \delta_{j2} = -u_l \delta_{jl} = -u_j. \end{aligned} \quad (8.35)$$

For the rotational excluded volume contribution, (8.26e), which reads explicitly

$$D_r \left\langle u_i \mathcal{R}_j \left(\left\{ \rho + 2\mathbf{u} \cdot \mathbf{t} \right\} \mathcal{R}_j \left\langle |\mathbf{u} \times \mathbf{u}'| [1 + \partial_{\mathbf{r}}^2] \left\{ \rho + 2\mathbf{u}' \cdot \mathbf{t} \right\} \right\rangle \right) \right\rangle, \quad (8.36)$$

the homogeneous contribution from $[1 + \partial_{\mathbf{r}}^2]$ vanishes, since $\langle |\mathbf{u} \times \mathbf{u}'| \{ \rho + 2\mathbf{u}' \cdot \mathbf{t} \} \rangle' \propto \rho$ vanishes when the rotational operator is applied on it. Twofold integration by part yields for the inhomogeneous part

$$D_r \left\langle \mathcal{R}_j \left[(\mathcal{R}_j u_i) \left\{ \rho + 2\mathbf{u} \cdot \mathbf{t} \right\} \right] \left\langle |\mathbf{u} \times \mathbf{u}'| \left\{ (\mathbf{u} \cdot \partial_{\mathbf{r}})^2 + (\mathbf{u}' \cdot \partial_{\mathbf{r}})^2 \right\} \left\{ \rho + 2\mathbf{u}' \cdot \mathbf{t} \right\} \right\rangle \right\rangle. \quad (8.37)$$

One can calculate

$$\begin{aligned} \mathcal{R}_j \left[(\mathcal{R}_j u_i) \left\{ \rho + 2\mathbf{u} \cdot \mathbf{t} \right\} \right] &= \mathcal{R}^2 u_i \rho + 2\mathcal{R}_j \left[(\mathcal{R}_j u_i) u_l \right] t_l \\ &= -u_i \rho + 2 \left[(u_1 \partial_{u_2} - u_2 \partial_{u_1}) (u_1 \delta_{i2} - u_2 \delta_{i1}) u_l \right] t_l \\ &= -u_i \rho + 2 \left[u_1^2 \delta_{i2} t_2 + u_2^2 \delta_{i1} t_1 - u_1 u_2 (t_1 \delta_{i2} + t_2 \delta_{i1}) - u_i u_l t_l \right] \\ &= -u_i \rho + 2 (t_i - 2u_i u_l t_l), \end{aligned} \quad (8.38)$$

where in the last step we have used $u_1^2 = 1 - u_2^2$ twice to rearrange the first two terms in the squared brackets. Neglecting the vanishing odd contributions one gets

$$D_r \left\langle (2t_i - 4u_i u_l t_l) \left\langle |\mathbf{u} \times \mathbf{u}'| \left\{ (\mathbf{u} \cdot \partial_{\mathbf{r}})^2 + (\mathbf{u}' \cdot \partial_{\mathbf{r}})^2 \right\} \rho \right\rangle' \right\rangle. \quad (8.39)$$

which leads to a term $\propto D_r t \partial^2 \rho$ in the continuum equations.

In the active rotational current, (8.26f), one has to deal with

$$\begin{aligned} & \gamma \left\langle u_i \mathcal{R}_j \left(\left\{ \rho + 2\mathbf{u} \cdot \mathbf{t} \right\} \left\langle (\mathbf{u} \cdot \mathbf{u}') [\mathbf{u} \times \mathbf{u}']_j [1 + \partial_{\mathbf{r}}^2] \left\{ \rho + 2\mathbf{u}' \cdot \mathbf{t} \right\} \right\rangle' \right) \right\rangle \\ = & -\gamma \left\langle (\mathcal{R}_j u_i) \left\{ \rho + 2\mathbf{u} \cdot \mathbf{t} \right\} \left\langle (\mathbf{u} \cdot \mathbf{u}') [\mathbf{u} \times \mathbf{u}']_j [1 + \partial_{\mathbf{r}}^2] \left\{ \rho + 2\mathbf{u}' \cdot \mathbf{t} \right\} \right\rangle' \right\rangle, \end{aligned} \quad (8.40)$$

where we have used the integration by parts rule Eq. (A.15). Since the orientation dependence coming from the active angular velocity, namely $(\mathbf{u} \cdot \mathbf{u}') [\mathbf{u} \times \mathbf{u}']_j$, is even in both \mathbf{u} and \mathbf{u}' while $\mathcal{R}_j u_i$ is odd, only the following contribution survives

$$-\gamma \left\langle (\mathcal{R}_j u_i) 2\mathbf{u} \cdot \mathbf{t} \left\langle (\mathbf{u} \cdot \mathbf{u}') [\mathbf{u} \times \mathbf{u}']_j [1 + \partial_{\mathbf{r}}^2] \rho \right\rangle' \right\rangle. \quad (8.41)$$

Having again a look at the homogeneous contribution from $[1 + \partial_{\mathbf{r}}^2]$, one calculates

$$\begin{aligned} & -\gamma 2t_k \left\langle (u_1 \delta_{i2} - u_2 \delta_{i1}) u_k \left\langle u_l u'_l [u_1 u'_2 - u_2 u'_1] \right\rangle' \right\rangle \rho \\ = & -\gamma 2t_k \epsilon_{3ji} \epsilon_{3mn} \left\langle u_j u_k u_l u_m \langle u'_l u'_n \rangle' \right\rangle \rho \\ = & -\gamma t_k \epsilon_{3ji} \epsilon_{3mn} \langle u_j u_k u_n u_m \rangle \rho = 0, \end{aligned} \quad (8.42)$$

where $\langle u'_l u'_n \rangle' = \frac{1}{2} \delta_{ln}$ has been used again and the last term vanishes since the Levi-Civita tensor ϵ_{3mn} is antisymmetric in (n, m) while $\langle u_j u_k u_l u_m \rangle$ is symmetric in (n, m) . Thus, as has been the case for the rotational excluded volume interaction, the homogeneous contribution of the active rotations vanishes and only an inhomogeneous contribution of the form $\propto \gamma t \partial^2 \rho$ does exist.

To conclude, we have established the form of Eqs. (8.4) whereby the differences between the structure of the equation for the filament density and the one for the filament orientation field have been traced back to the different coupling of the nonlinear interactions with the additional power of \mathbf{u} which is present in the equation for the orientation field. The rotational contributions are quite complicated to evaluate, but apart from the trivial (but important) linear rotational diffusion, $-D_r t_i$, they play only a minor role. Due to their structure $\propto t \partial^2 \rho$, they vanish upon linearization with respect to the homogeneous and isotropic basic state $\rho = \rho_0$ and $\mathbf{t} = 0$, cf. chapter 9. Thus they are purely nonlinear contributions not involved in the instability mechanisms and only contribute to pattern selection processes.

Chapter 9

Linear analysis and possible instabilities

In this chapter we want to start our analysis of the continuum equations, Eqs. (8.4), that have been extracted in chapter 8 from the underlying microscopic filament-motor model, Eq. (7.10), introduced in chapter 7. In total we have to deal with three coupled nonlinear equations, one for the filament density ρ and two for the components of the polar orientation field t_i ($i = 1, 2$ or x, y) of the filaments in two spatial dimensions,

$$\begin{aligned}
 \partial_t \rho &= \frac{1+D}{2} \Delta \rho + \left(\frac{1+D}{\pi} - \frac{\alpha}{24} \right) \partial_j (\rho \partial_j \rho) - \frac{\alpha}{48} \partial_i \left[t_i \partial_j t_j + t_j \partial_i t_j + t_j \partial_j t_i \right] \\
 &- \frac{\alpha}{C_1} \left[38 \partial_j (\rho \partial_j \Delta \rho) + 11 \partial_i (t_j \partial_i \Delta t_j) + 16 \partial_i (t_i \Delta \partial_j t_j + 2 t_j \partial_j \partial_i \partial_l t_l + t_j \partial_j \Delta t_i) \right] \\
 &- \frac{\beta}{96} \partial_i \left[\rho \partial_i \partial_j t_j - t_j \partial_j \partial_i \rho + \frac{3}{2} (\rho \Delta t_i - t_i \Delta \rho) \right], \tag{9.1a}
 \end{aligned}$$

$$\begin{aligned}
 \partial_t t_i &= -D_r t_i + \frac{3D+1}{4} \Delta t_i + \frac{1-D}{2} \partial_i \partial_j t_j \\
 &+ \frac{3D+1}{2\pi} \partial_j (t_i \partial_j \rho) + \frac{1-D}{2\pi} \left[\partial_j (t_j \partial_i \rho) + \partial_i (t_j \partial_j \rho) \right] \\
 &- \frac{\alpha}{96} \partial_j \left[3 t_i \partial_j \rho + t_j \partial_i \rho + \delta_{ij} t_l \partial_l \rho + \rho (\partial_i t_j + \partial_j t_i + \delta_{ij} \partial_l t_l) \right] \\
 &- \frac{\alpha}{2C_1} \partial_j \left[\rho \left(11 \partial_j \Delta t_i + 16 \partial_i \Delta t_j + 32 \partial_j \partial_i \partial_l t_l + 16 \delta_{ij} \Delta \partial_l t_l \right) \right. \\
 &\quad \left. + 16 t_j \partial_i \Delta \rho + 32 t_l \partial_l \partial_i \partial_j \rho + 44 t_i \partial_j \Delta \rho + 16 \delta_{ij} t_l \partial_l \Delta \rho \right] \\
 &+ \frac{\beta}{2} \partial_j \left[\frac{1}{2} \delta_{ij} \rho^2 - t_i t_j \right] + \frac{\beta}{96} \partial_j \left[\frac{3}{4} \delta_{ij} \rho \Delta \rho + \frac{1}{2} \rho \partial_i \partial_j \rho - t_l \partial_l \partial_i t_j - t_i \partial_j \partial_l t_l - t_i \Delta t_j \right] \\
 &+ \frac{1}{48} \left(\frac{\gamma}{4} - \frac{4}{\pi} D_r \right) \left[t_j \partial_j \partial_i \rho - \frac{1}{2} t_i \Delta \rho \right]. \tag{9.1b}
 \end{aligned}$$

Again the abbreviation $C_1 = 23040$ is used and we have introduced the ratio of perpendicular to parallel diffusion $D = D_\perp/D_\parallel$, which we will choose later on to be $1/2$, a value suitable for dilute solutions of rigid rods as can be derived from hydrodynamic calculations [39, 125, 126], cf. the discussion in section 9.5.2.

The only free parameters of the above model are the rescaled rotational diffusion coefficient D_r , and the coefficients α and β of the leading order translational and γ of the rotational motor contributions. Naturally, the mean filament density ρ_0 is an additional free variable. As compared to purely phenomenological models inherently having many parameters, e.g. the ones proposed in [115, 127, 128], to analyze our model we have to explore only a quite decent parameter space.

In this chapter, I perform a thorough linear analysis correcting the predictions from the original reference, Ref. [40], that were based on insufficient conditions [46]. The analysis reveals three different instabilities which will be investigated subsequently in the weakly nonlinear regime in the following three chapters. This work is the first investigation of a filament-motor model in two dimensions that comprises the whole parameter space in the linear and weakly nonlinear regime.

9.1 Linear operator and general discussion

Having defined the model, the first issue in the field of pattern formation is the determination of possible instabilities. From the experiments we want to describe, we are interested especially in instabilities of the orientational field \mathbf{t} that lead to spatially inhomogeneous orientation patterns like the asters displayed in Fig. 6.1.

As already encountered in part I of this work, the possible linear instabilities can be determined by a linear stability analysis of the homogeneously stationary basic state. The latter one can be obtained trivially from the homogeneous limit of Eqs. (9.1), namely

$$\partial_t \rho = 0 \quad , \quad \partial_t \mathbf{t} = -D_r \mathbf{t} \quad . \quad (9.2)$$

This implies a constant filament density ρ_0 and a vanishing polar orientation $\mathbf{t}_0 = 0$ as the homogeneous basic state.

To investigate the stability of this state with respect to inhomogeneous perturbations $\tilde{\rho}(\mathbf{r}, t)$ and $\mathbf{t}(\mathbf{r}, t)$, by the ansatz $\rho(\mathbf{r}, t) = \rho_0 + \tilde{\rho}(\mathbf{r}, t)$ we separate the constant part ρ_0 of the filament density from the spatially inhomogeneous one, $\tilde{\rho}(\mathbf{r}, t)$. Linearizing Eqs. (9.1) with respect to small inhomogeneous contributions $\tilde{\rho}(\mathbf{r}, t)$ and $\mathbf{t}(\mathbf{r}, t)$, one obtains a set of three coupled linear equations which by use of the three component vector

$$\mathbf{w}(\mathbf{r}, t) = \begin{pmatrix} \tilde{\rho}(\mathbf{r}, t) \\ t_x(\mathbf{r}, t) \\ t_y(\mathbf{r}, t) \end{pmatrix} \quad (9.3)$$

can be conveniently written in the form

$$\partial_t \mathbf{w}(\mathbf{r}, t) = \mathcal{L}_0 \mathbf{w}(\mathbf{r}, t) = \begin{pmatrix} \mathcal{L}_{11}^{(0)} & \mathcal{L}_{12}^{(0)} & \mathcal{L}_{13}^{(0)} \\ \mathcal{L}_{21}^{(0)} & \mathcal{L}_{22}^{(0)} & \mathcal{L}_{23}^{(0)} \\ \mathcal{L}_{31}^{(0)} & \mathcal{L}_{32}^{(0)} & \mathcal{L}_{33}^{(0)} \end{pmatrix} \mathbf{w}(\mathbf{r}, t) . \quad (9.4)$$

The components of the linear operator \mathcal{L}_0 are given by the expressions

$$\begin{aligned} \mathcal{L}_{11}^{(0)} &= \left[\frac{1+D}{2} \left(1 + \frac{2}{\pi} \rho_0 \right) - \frac{\alpha \rho_0}{24} \right] \Delta - \frac{19 \alpha \rho_0}{11520} \Delta^2 , \\ \mathcal{L}_{12}^{(0)} &= -\frac{\beta}{96} \frac{5}{2} \rho_0 \Delta \partial_x , \\ \mathcal{L}_{13}^{(0)} &= -\frac{\beta}{96} \frac{5}{2} \rho_0 \Delta \partial_y , \\ \mathcal{L}_{21}^{(0)} &= \left\{ \frac{\beta \rho_0}{2} + \frac{\beta}{96} \frac{5}{4} \rho_0 \Delta \right\} \partial_x , \\ \mathcal{L}_{22}^{(0)} &= -D_r + \frac{3D+1}{4} \Delta + \frac{1-D}{2} \partial_x^2 - \frac{\alpha \rho_0}{96} (\Delta + 2\partial_x^2) \\ &\quad - \frac{\alpha \rho_0}{46080} (11\Delta^2 + 64\Delta \partial_x^2) , \\ \mathcal{L}_{23}^{(0)} &= \left(\frac{1-D}{2} - \frac{\alpha \rho_0}{48} \right) \partial_x \partial_y - \frac{\alpha \rho_0}{720} \Delta \partial_x \partial_y , \\ \mathcal{L}_{31}^{(0)} &= \left\{ \frac{\beta \rho_0}{2} + \frac{\beta}{96} \frac{5}{4} \rho_0 \Delta \right\} \partial_y , \\ \mathcal{L}_{32}^{(0)} &= \mathcal{L}_{23}^{(0)} , \\ \mathcal{L}_{33}^{(0)} &= -D_r + \frac{3D+1}{4} \Delta + \frac{1-D}{2} \partial_y^2 - \frac{\alpha \rho_0}{96} (\Delta + 2\partial_y^2) \\ &\quad - \frac{\alpha \rho_0}{46080} (11\Delta^2 + 64\Delta \partial_y^2) . \end{aligned} \quad (9.5)$$

First of all one can directly see the following symmetry: the components $\mathcal{L}_{13}^{(0)}$, $\mathcal{L}_{31}^{(0)}$, $\mathcal{L}_{32}^{(0)}$ and $\mathcal{L}_{33}^{(0)}$ can be obtained by permuting ∂_x and ∂_y in $\mathcal{L}_{12}^{(0)}$, $\mathcal{L}_{21}^{(0)}$, $\mathcal{L}_{23}^{(0)}$ and $\mathcal{L}_{22}^{(0)}$, respectively. This is due to the $(t_x, x) \leftrightarrow (t_y, y)$ -symmetry of Eqs. (9.1).

Second, \mathcal{L}_0 is independent of rotational contributions apart from the (important) linear contribution $-D_r$ in $\mathcal{L}_{22}^{(0)}$ and $\mathcal{L}_{33}^{(0)}$, respectively. As already discussed in the last chapter, the rotational excluded volume contributions as well as the active rotational contributions proportional to γ are purely nonlinear and thus are only relevant for the issue of pattern selection, i.e. stability of patterns, but not for the emergence of patterns through linear instabilities.

Now let's determine which active motor-induced contribution is the most important one. As has already been used extensively in part I of this work, an instability is equivalent to an eigenvalue $\sigma = \lambda + i\omega$ of the linear operator \mathcal{L}_0 with a positive real part $\lambda > 0$.

In the inactive case, i.e. for $\alpha = 0 = \beta$, the homogeneous solution $\rho = \rho_0$ and $\mathbf{t} = 0$ should be stable, since only diffusive, i.e. damping, terms are present. The growth rates for this case can be obtained most easily by letting the motor terms vanish in the growth rates calculated in the next two sections. As expected, one gets three real growth rates $\sigma(k)$ that are damped, namely

$$\begin{aligned}\sigma_1 &= -\frac{1+D}{2} \left(1 + \frac{2}{\pi}\rho_0\right) k^2, \\ \sigma_2 &= -D_r - \frac{D+3}{4}k^2, \\ \sigma_3 &= -D_r - \frac{3D+1}{4}k^2.\end{aligned}\tag{9.6}$$

If we consider next the case $\alpha = 0$, $\beta \neq 0$, the mode structure is similar to the one depicted in Fig. 9.3a): while σ_3 is unchanged, the two other modes are coupled implying

$$\sigma_{1,2} = \frac{1}{2} \left(\bar{\mathcal{L}}_{11}^{(0)} + \bar{\mathcal{L}}_{22}^{(0)} \pm \sqrt{(\bar{\mathcal{L}}_{11}^{(0)} - \bar{\mathcal{L}}_{22}^{(0)})^2 + 4\bar{\mathcal{L}}_{12}^{(0)}\bar{\mathcal{L}}_{21}^{(0)}} \right)\tag{9.7}$$

in the notation for $\bar{\mathcal{L}}_0$ of section 9.3. Both growth rates start as real modes, σ_1 from zero and $\propto -k^2$ while σ_2 from $-D_r$ and $\propto +k^2$ and meet at a certain k^* , cf. Fig. 9.4, where the argument of the square root crosses zero thus becoming a complex conjugated pair. However there do not exist values of β and ρ_0 , for which σ_1 could become positive for intermediate values of k , while for $k > k^*$ the complex mode is damped since $\lambda = \text{Re}(\sigma) = \frac{1}{2} (\bar{\mathcal{L}}_{11}^{(0)} + \bar{\mathcal{L}}_{22}^{(0)})$ with $\bar{\mathcal{L}}_{11}^{(0)}$ and $\bar{\mathcal{L}}_{22}^{(0)}$ both damped.

Thus we have identified the essential motor parameter to be the α -contribution, which indeed leads for large enough values of α to instabilities, even in the case $\beta = 0$. However, the presence of a nonvanishing β -contribution leads to a qualitative change in the instabilities: from a stationary instability with $\omega = 0$ for the eigenvalue with the largest real part (which holds for $\beta = 0$) to the possibility of an oscillatory instability with $\omega \neq 0$, cf. Eq. (9.7).

Polarity sorting

As has been already discussed at the end of section 7.2, in the one-dimensional limit of our model, the α -contribution reflects interaction of parallel filaments whereas the β -contribution accounts for the interaction of anti-parallel filaments. The latter contribution is responsible for a process called *polarity sorting* [104, 114, 129]: the β -contribution induces a maximum filament separation and thus favors an arrangement with regions of alternating local polarities, i.e. directions of the filaments. Thus I will refer to the case $\beta = 0$ as the case without polarity sorting, which will be discussed in the next section, and to the case $\beta \neq 0$ as the one with polarity sorting, which is postponed to section 9.4.

9.2 Without polarity sorting

In the case $\beta = 0$, the linear problem simplifies to

$$\partial_t \mathbf{w}(\mathbf{r}, t) = \mathcal{L}_0 \mathbf{w}(\mathbf{r}, t) = \begin{pmatrix} \mathcal{L}_{11}^{(0)} & 0 & 0 \\ 0 & \mathcal{L}_{22}^{(0)} & \mathcal{L}_{23}^{(0)} \\ 0 & \mathcal{L}_{32}^{(0)} & \mathcal{L}_{33}^{(0)} \end{pmatrix} \mathbf{w}(\mathbf{r}, t), \quad (9.8)$$

with the components of the linear operator \mathcal{L}_0 reading

$$\begin{aligned} \mathcal{L}_{11}^{(0)} &= \left[\frac{1+D}{2} \left(1 + \frac{2}{\pi} \rho_0 \right) - \frac{\alpha \rho_0}{24} \right] \Delta - \frac{19 \alpha \rho_0}{11520} \Delta^2, \\ \mathcal{L}_{22}^{(0)} &= -D_r + \frac{3D+1}{4} \Delta + \frac{1-D}{2} \partial_x^2 - \frac{\alpha \rho_0}{96} (\Delta + 2\partial_x^2) \\ &\quad - \frac{\alpha \rho_0}{46080} (11\Delta^2 + 64\Delta \partial_x^2), \\ \mathcal{L}_{23}^{(0)} &= \left(\frac{1-D}{2} - \frac{\alpha \rho_0}{48} \right) \partial_x \partial_y - \frac{\alpha \rho_0}{720} \Delta \partial_x \partial_y \end{aligned} \quad (9.9)$$

and the two further components $\mathcal{L}_{32}^{(0)}$ and $\mathcal{L}_{33}^{(0)}$ again obtained by permuting ∂_x and ∂_y in $\mathcal{L}_{23}^{(0)}$ and $\mathcal{L}_{22}^{(0)}$, respectively.

Naturally the mode ansatz

$$\mathbf{w}(\mathbf{r}, t) = \mathbf{E} \exp(\sigma t + i\mathbf{k} \cdot \mathbf{r}) \quad (9.10)$$

with $\mathbf{r} = (x, y)$, the wave vector $\mathbf{k} = (q, p)$ and the eigenvector \mathbf{E} solves the linear homogeneous set of equations (9.8). The solvability condition provides a third order polynomial for the eigenvalues σ , which factorizes here into a linear and a quadratic polynomial describing different types of instabilities: considering moderate filament densities, for intermediate values of α an orientational instability with a finite wavelength occurs first, whereas the density mode, which does not couple to the orientation on the level of the linear equations, is damped. For large values of α however, the density mode becomes unstable first, their growth rate resembling the one typical for spinodal decomposition or demixing of the filament density which is however actively driven by the motors via the α -contribution.

The instability with respect to density fluctuations is governed solely by $\mathcal{L}_{11}^{(0)}$ and the respective eigenvalue is

$$\sigma_d = - \left[\frac{1+D}{2} \left(1 + \frac{2}{\pi} \rho_0 \right) - \frac{\alpha \rho_0}{24} \right] k^2 - \frac{19 \alpha \rho_0}{11520} k^4 \quad (9.11)$$

with $k^2 = q^2 + p^2$. The term $\propto k^4$ is always stabilizing, but the homogeneous basic state becomes unstable with respect to density modulations for a positive coefficient of k^2 , leading to the corresponding critical filament density

$$\rho_d = \frac{1}{\frac{\alpha}{12(1+D)} - \frac{2}{\pi}}, \quad (9.12)$$

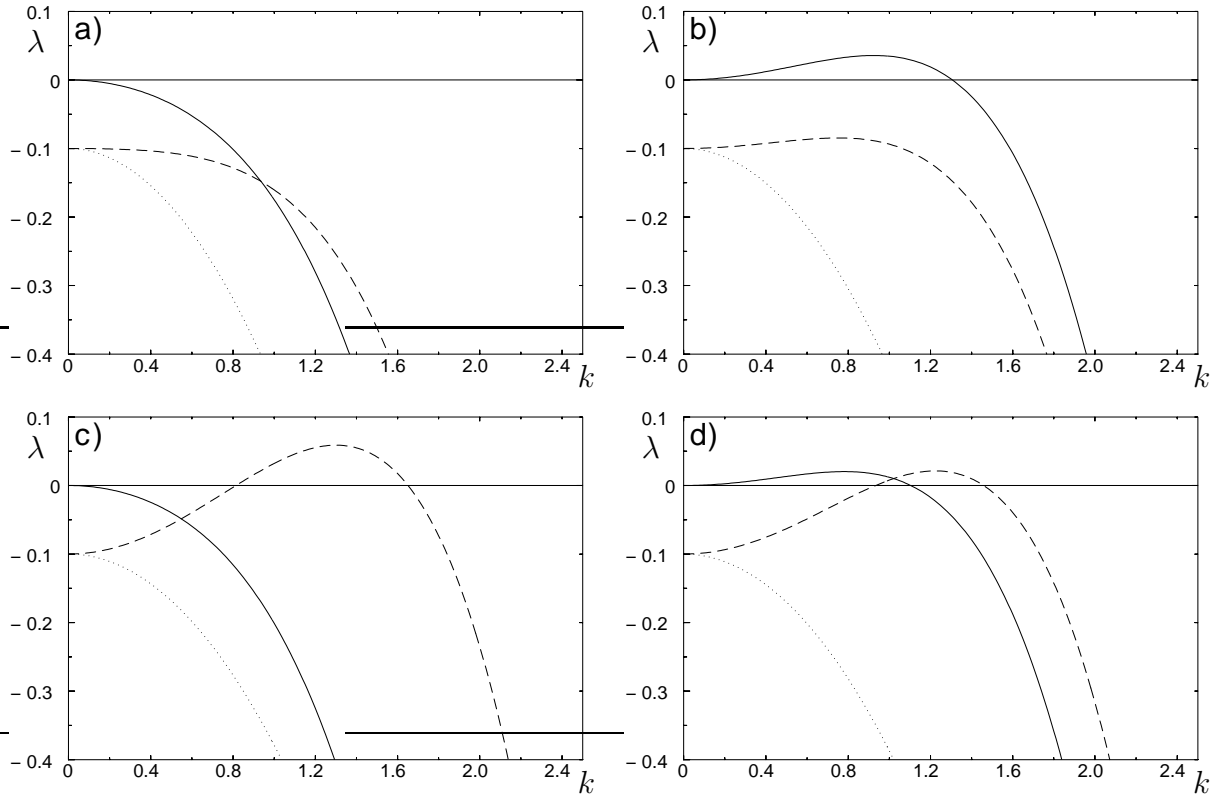


Figure 9.1: The real parts $\lambda(k) = \text{Re}[\sigma(k)]$ of the eigenvalue σ_d corresponding to the instability with respect to density fluctuations (solid line) as well as the one possibly unstable with respect to orientational fluctuations, σ_L (dashed line), are shown as a function of the wavenumber k for $D_r = 0.1$. The third eigenvalue σ_T is damped as depicted by the dotted line. Parameters are a) $\alpha = 25$, $\rho_0 = 1.1$ leading to a linearly stable state; b) $\alpha = 35$, $\rho_0 = 0.85$ leading to a density instability; c) $\alpha = 20$, $\rho_0 = 1.7$ leading to an orientational instability; d) $\alpha = 28$, $\rho_0 = 1.185$ both density and orientational fluctuations are unstable (see also Fig. 9.2).

provided that this value is positive, i.e. if $\alpha > \frac{24}{\pi}(1 + D)$ holds. The corresponding eigenvector is $\mathbf{E}_d = (1, 0, 0)^T$, meaning that this mode is a pure density mode that does not couple to the orientation field in the linear regime. The dispersion, i.e. the wavenumber dependence of the eigenvalue's real part λ , is shown as the solid lines in Fig. 9.1. The fact that the growth rate starts from $\lambda = 0$ at $k = 0$ reflects the conservation of the filament density, since from the latter it follows that

$$\rho(\mathbf{k} = 0) = \int d\mathbf{r} \rho(\mathbf{r}) = \rho_0 \quad (9.13)$$

has to be a constant in time. One should also recognize that since σ_d is a pure density mode, there is no dependence on D_r in this instability.

The two remaining eigenvalues read

$$\sigma_L = -D_r - \frac{1}{4}k^2 \left(3 + D - \frac{\alpha\rho_0}{8} + \frac{5}{768}\alpha\rho_0k^2 \right), \quad (9.14)$$

$$\sigma_T = -D_r - \frac{1}{4}k^2 \left(1 + 3D - \frac{\alpha\rho_0}{24} + \frac{11}{11520}\alpha\rho_0k^2 \right), \quad (9.15)$$

with the corresponding eigenvectors

$$\mathbf{E}_L = \begin{pmatrix} 0 \\ q \\ p \end{pmatrix}, \quad \mathbf{E}_T = \begin{pmatrix} 0 \\ q \\ -p \end{pmatrix}. \quad (9.16)$$

As can be judged from Eqs. (9.14) and (9.15), both growth rates may become positive for high enough motor activity, i.e. for large enough values of α . However, σ_L is always the first one due to the larger coefficient in front of the term $\propto \alpha k^2$. The terms $\propto k^4$ always stabilize the high wavenumber modes, thus σ_L can become positive only in a finite range of k as indicated by the dashed lines in Fig. 9.1. It describes an instability with respect to longitudinal orientational fluctuations, while σ_T , shown as the dotted lines in Fig. 9.1, is usually damped and dominated by diffusion of transverse orientational modes. Only for very high values of α and/or ρ_0 , also σ_T becomes positive, the different prefactors in front of the destabilizing terms proportional to αk^2 thus favoring longitudinal fluctuations. The identification of σ_L and σ_T as longitudinal and transverse modes is made explicit in the next section. Fig. 9.1 displays the dispersions, i.e. the wavenumber dependent growth rates, $\sigma_d(k)$, $\sigma_L(k)$ and $\sigma_T(k)$ as solid, dashed and dotted lines respectively.

It should be mentioned that in the case we are presently discussing, i.e. $\beta = 0$, the eigenvalues $\sigma_d(k)$, $\sigma_L(k)$ and $\sigma_T(k)$ depend only on even powers of the wavenumber modulus reflecting the rotational symmetry, i.e. isotropy.

The restabilizing k^4 -terms, especially the one in Eq. (9.14), were missing in the original reference, Ref. [40], where the model has been proposed. Although the unstable mode starts from $-D_r < 0$ (or in the case with β present from a value $\sigma(k^*) < 0$) and a positive curvature at such a point is not a sufficient criterion since it does not lead automatically to a positive real part of the growth rate, an instability has been claimed by the authors. However, only the interplay between the k^2 and the k^4 contribution as in Eq. (9.14) allows the identification of a finite wavenumber instability as pointed out by us in [46].

Also the critical value of the control parameter and the critical wavenumber of the occurring pattern cannot be calculated without the fourth order contributions in k . Choosing the filament density as the control parameter, the critical filament density ρ_c , above which the orientational instability takes place, and the critical wavenumber k_c of the pattern at threshold have to be obtained by solving simultaneously the extremum condition

$$\left. \frac{d\sigma_L}{dk} \right|_{k_c} = 0 \quad (9.17)$$

and the neutral stability condition

$$\sigma_L(k = k_c) = 0 . \quad (9.18)$$

The first condition can be used to get an expression for k_c in terms of ρ_c , namely

$$k_c^2 = \frac{768}{10} \frac{\left[\frac{\alpha\rho_c}{8} - (3 + D)\right]}{\alpha\rho_c} , \quad (9.19)$$

which can then be inserted into the second one to yield a quadratic equation for ρ_c ,

$$0 = -D_r + \frac{48}{5\alpha\rho_c} \left[\frac{\alpha\rho_c}{8} - (3 + D)\right]^2 . \quad (9.20)$$

Finally one gets

$$\rho_c = \frac{8}{\alpha} \left((3 + D) + \frac{5}{12} D_r \left(1 + \sqrt{1 + \frac{24(3 + D)}{5D_r}} \right) \right) \quad (9.21)$$

and

$$k_c = 4 \left(\frac{12D_r}{5\alpha\rho_c} \right)^{1/4} . \quad (9.22)$$

One should note that the critical density ρ_c is proportional to α^{-1} . This implies that only the product of ρ and α determines the instability and that we could have also used α as the control parameter. In the case $\beta = 0$ it makes no difference whether one considers a system with a high filament density and slow or ineffective or few motors or a system with low filament density but fast, effective or many motors. This is a quite general result that can also be found in different models [119], however it does not hold exactly anymore in the case $\beta \neq 0$, cf. section 9.4.

Since again only the product of ρ and α enters into Eq. (9.22), $k_c = k_c(\rho_c\alpha, D_r)$ holds while in the case $\beta \neq 0$ the dependence is more complex, namely $k_c = k_c(\rho_c, \alpha, D_r)$. As $\rho_c\alpha$ is determined entirely by D_r for $\beta = 0$ and for a fixed diffusion ratio D , one even gets $k_c = k_c(D_r)$ in this case, cf. Fig. 9.6.

Finally, in Fig. 9.2, the critical density ρ_d (dashed line) for the instability with respect to inhomogeneous density fluctuations $\rho(\mathbf{r}, t)$ and the critical density ρ_c (solid line) with respect to inhomogeneous orientational fluctuations $\mathbf{t}(\mathbf{r}, t)$ are shown as a function of the motor activity α . The dash-dotted line describes the critical density ρ_{IN} (3.65) above which the homogeneous isotropic-nematic transition takes place, cf. section 3.2.5, and above which our assumption of negligibility of the nematic order parameter breaks down. We can now specify the different α -regimes mentioned already at the beginning of this section: on the left side of the vertical dotted line, orientational fluctuations have the lowest threshold, while on the right side density fluctuations become unstable at first. For increasing values of the rotational diffusion coefficient D_r , which determines the damping of the dispersions $\sigma_L(k)$ and $\sigma_T(k)$ at $k = 0$, the solid line in Fig. 9.2 is shifted upwards, decreasing the α -range wherein the orientational instability has lowest threshold with $\rho_c < \rho_{IN}$, cf. also Fig. 9.5. As already mentioned above, the dashed line reflecting the density demixing instability is independent of D_r .

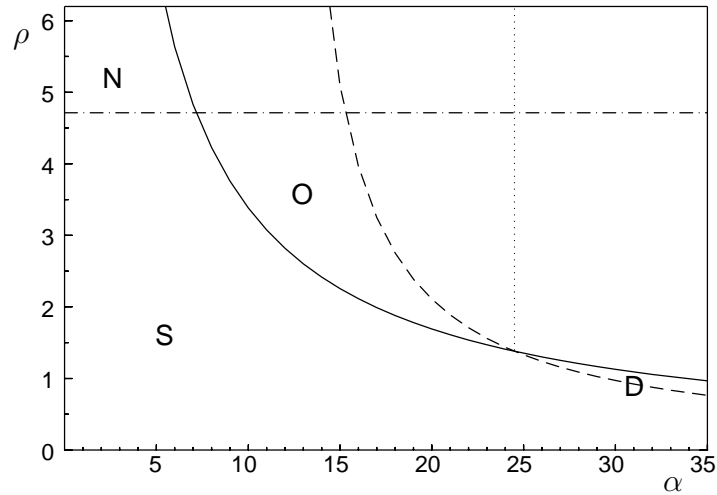


Figure 9.2: The critical densities ρ_c (solid line) and ρ_d (dashed line) for the orientational and density demixing instability respectively are shown as a function of α for $D_r = 0.15$. The dash-dotted horizontal line represents the critical density $\rho_{IN} = \frac{3}{2}\pi$, above which the isotropic-nematic transition due to excluded volume interactions takes place and the neglect of the nematic order parameter breaks down. The region S denotes the parameter range where the homogeneous solution is stable. In the range referred to as N one has a pure homogeneous transition to nematic order. For high enough motor activity, i.e. for high enough values of α , one gets motor driven instabilities, in range O a spatially periodic orientational order and in range D a demixing of the filament density. The vertical dotted line separates the α -region where the orientational instability has lowest threshold from the one where the density demixing instability happens first.

9.3 Separation of longitudinal and transverse modes

In this section we identify σ_L and σ_T as the longitudinal and transverse modes of the orientation field. The respective form of the linear operator is also useful for the next section where the case with polarity sorting is discussed.

By performing the scalar and vector product of the normalized wavenumber $\hat{\mathbf{k}}$ with the orientational field in Fourier space $\mathbf{t}(\mathbf{k})$, one can define the longitudinal

$$t_L = \hat{\mathbf{k}} \cdot \mathbf{t} \quad (9.23)$$

and the transverse orientation field

$$\mathbf{t}_T = \hat{\mathbf{k}} \times \mathbf{t} , \quad (9.24)$$

where in two spatial dimensions one can suppress the vector character of the transverse mode. Applying the two products to the Fourier transformed linear equations, Eqs. (9.4),

one can reformulate the linear problem using

$$\bar{\mathbf{w}}(\mathbf{k}, t) = \begin{pmatrix} \tilde{\rho}(\mathbf{k}, t) \\ t_L(\mathbf{k}, t) \\ t_T(\mathbf{k}, t) \end{pmatrix}, \quad (9.25)$$

leading to the system of equations

$$\partial_t \bar{\mathbf{w}}(\mathbf{k}, t) = \bar{\mathcal{L}}_0 \bar{\mathbf{w}}(\mathbf{k}, t) = \begin{pmatrix} \bar{\mathcal{L}}_{11}^{(0)} & \bar{\mathcal{L}}_{12}^{(0)} & 0 \\ \bar{\mathcal{L}}_{21}^{(0)} & \bar{\mathcal{L}}_{22}^{(0)} & 0 \\ 0 & 0 & \bar{\mathcal{L}}_{33}^{(0)} \end{pmatrix} \bar{\mathbf{w}}(\mathbf{k}, t). \quad (9.26)$$

The components of the newly defined linear operator $\bar{\mathcal{L}}_0$ now read

$$\begin{aligned} \bar{\mathcal{L}}_{11}^{(0)} &= -\left[\frac{1+D}{2} \left(1 + \frac{2}{\pi} \rho_0 \right) - \frac{\alpha \rho_0}{24} \right] k^2 - \frac{19 \alpha \rho_0}{11520} k^4, \\ \bar{\mathcal{L}}_{12}^{(0)} &= \frac{\beta}{96} \frac{5}{2} \rho_0 i k^3, \\ \bar{\mathcal{L}}_{21}^{(0)} &= \frac{\beta}{2} \rho_0 i k - \frac{\beta}{96} \frac{5}{4} \rho_0 i k^3, \\ \bar{\mathcal{L}}_{22}^{(0)} &= -D_r - \frac{3+D}{4} k^2 + \frac{3}{96} \alpha \rho_0 k^2 - \frac{75}{46080} \alpha \rho_0 k^4, \\ \bar{\mathcal{L}}_{33}^{(0)} &= -D_r - \frac{1+3D}{4} k^2 + \frac{1}{96} \alpha \rho_0 k^2 - \frac{11}{46080} \alpha \rho_0 k^4. \end{aligned} \quad (9.27)$$

One should note that the transverse mode is now completely decoupled in the linear regime, while the longitudinal orientation mode is coupled to the density. However, if we consider the case $\beta = 0$ again, the matrix $\bar{\mathcal{L}}_0$ becomes diagonal and one can identify by comparison with Eqs. (9.11), (9.14) and (9.15)

$$\bar{\mathcal{L}}_{11}^{(0)} = \sigma_d, \quad \bar{\mathcal{L}}_{22}^{(0)} = \sigma_L, \quad \bar{\mathcal{L}}_{33}^{(0)} = \sigma_T. \quad (9.28)$$

The separation of longitudinal and transverse modes is always useful for the linear analysis. For the nonlinear analysis however it is not easily applicable since nonlinear equations in real space become convolutions in fourier space. This is the reason why I first discussed the problem with t_x, t_y instead of t_L, t_T .

9.4 With polarity sorting

In the last sections we have established, that the filament-motor model under consideration already displays a rich variety of instabilities in the simple case $\beta = 0 = \gamma$, namely a homogeneous nematic, a spatially periodic orientational and a density demixing instability. Here we investigate the effect of the β -contributions, which describe the interaction of oppositely oriented filaments and lead to the phenomenon of polarity sorting.

These contributions should have a strong effect for the two following reasons: first, the terms $\propto \beta$ couple the density to the longitudinal orientation mode, so density and orientation are no longer decoupled in the linear regime. Second, the β -terms break the $\pm \mathbf{t}$ symmetry which held for all other contributions, namely diffusion, excluded volume, and the two other motor contributions proportional to α and γ .

Accordingly, we have to analyze the full linear problem, i.e. the linear operator defined in Eqs. (9.4) and (9.5) or the equivalent problem of Eqs. (9.26) and (9.27). Looking at the first formulation, one should notice that the components already present in the case $\beta = 0$, namely $\mathcal{L}_{11}^{(0)}, \mathcal{L}_{22}^{(0)}, \mathcal{L}_{33}^{(0)}, \mathcal{L}_{23}^{(0)}$ and $\mathcal{L}_{32}^{(0)}$ are *not* changed. However, the equations of ρ and \mathbf{t} are now coupled and one has to analyze a fully occupied matrix. In the second formulation, the transverse mode is *not* changed at all and is still completely decoupled, cf. Eqs. (9.26), and we have again, as in the case $\beta = 0$,

$$\sigma_T = -D_r - \frac{1}{4}k^2 \left(1 + 3D - \frac{\alpha\rho_0}{24} + \frac{11}{11520}\alpha\rho_0k^2 \right). \quad (9.29)$$

Thus the latter version of the equations is much easier to analyze here and we are left with the reduced problem of

$$\bar{\mathcal{L}}_0 = \begin{pmatrix} \bar{\mathcal{L}}_{11}^{(0)} & \bar{\mathcal{L}}_{12}^{(0)} \\ \bar{\mathcal{L}}_{21}^{(0)} & \bar{\mathcal{L}}_{22}^{(0)} \end{pmatrix}, \quad (9.30)$$

with the entries from Eqs. (9.27).

The eigenvalues are easily obtained to be

$$\sigma_{1,2} = \frac{1}{2} \left(\bar{\mathcal{L}}_{11}^{(0)} + \bar{\mathcal{L}}_{22}^{(0)} \pm \sqrt{(\bar{\mathcal{L}}_{11}^{(0)} - \bar{\mathcal{L}}_{22}^{(0)})^2 + 4\bar{\mathcal{L}}_{12}^{(0)}\bar{\mathcal{L}}_{21}^{(0)}} \right). \quad (9.31)$$

However, it is useful to have at first a look at the growth rates depicted in Figs. 9.3 and 9.4. Generically, the density mode starts from zero at $k = 0$ due to the conservation law, while the two orientational modes start at $-D_r$. Both the density and the longitudinal orientation mode have real growth rates for small wavenumbers k - as in the case with $\beta = 0$. For intermediate wavenumbers however, the two branches meet at a wavenumber k^* , cf. Fig. 9.4, and the growth rate acquires an imaginary part.

If we look now closer at the limit of small k , from Eqs. (9.27) and (9.31) one can see that the β -contribution to the growth rates is at least $\mathcal{O}(k^4)$: first, Eq. (9.31) contains only the product $\bar{\mathcal{L}}_{12}^{(0)}\bar{\mathcal{L}}_{21}^{(0)}$ with $\bar{\mathcal{L}}_{12}^{(0)}$ being $\mathcal{O}(k^3)$ and $\bar{\mathcal{L}}_{21}^{(0)}$ being $\mathcal{O}(k)$. Second in the argument of the square root, terms of order $\mathcal{O}(1)$ and $\mathcal{O}(k^2)$ are present, thus one may expand the square root leading to a contribution $\propto -\beta^2k^4$ in $\sigma_1 = \sigma_d$ and to a contribution $\propto +\beta^2k^4$ in $\sigma_2 = \sigma_L$. The density mode is therefore *not* changed up to order k^2 , the threshold for the growth of density fluctuations thus being the same as in the case $\beta = 0$, cf. Eq. (9.12), namely

$$\rho_d^\beta = \rho_d = \frac{1}{\frac{\alpha}{12(1+D)} - \frac{2}{\pi}}, \quad (9.32)$$

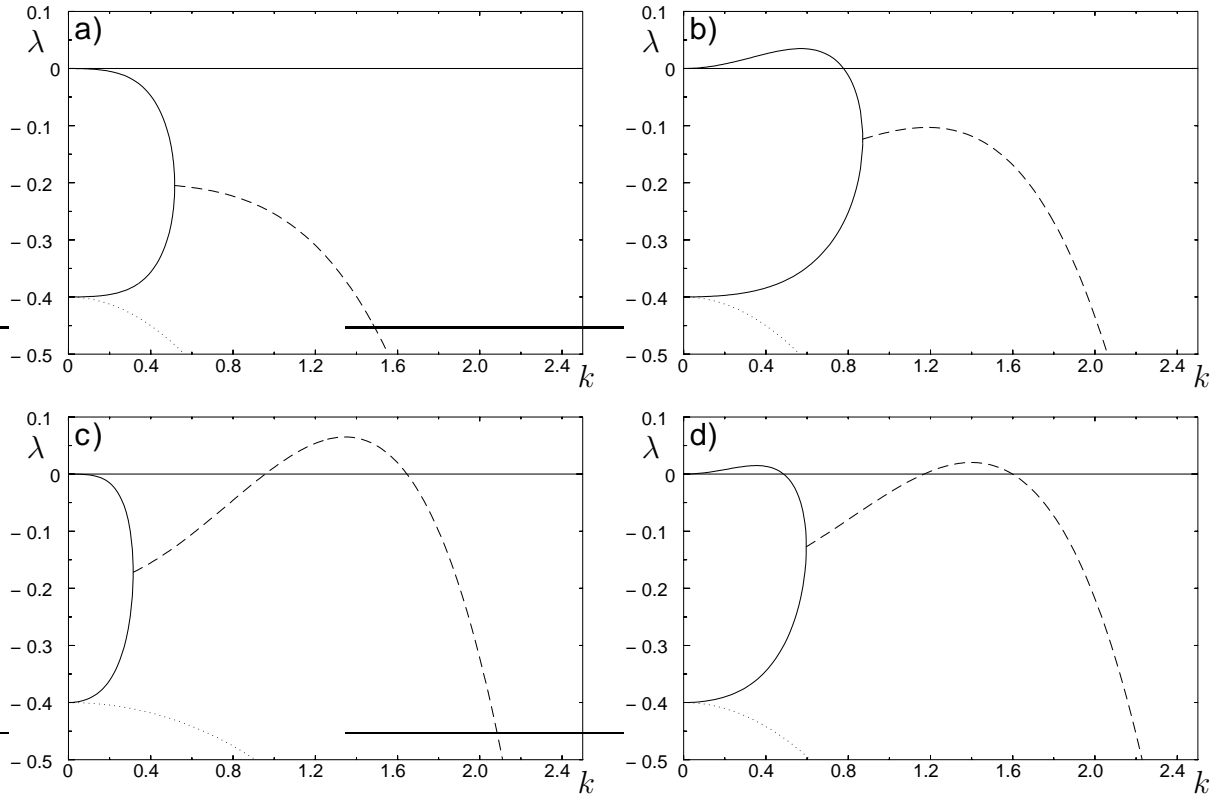


Figure 9.3: The growth rates $\lambda(k) = \text{Re}[\sigma(k)]$ of the eigenvalues of the linear operator are shown as a function of the wavenumber k for $D_r = 0.4$ and $\beta = 5$. The density and longitudinal orientation fluctuations are now coupled via the β -contribution. When those two eigenvalues meet at a finite $k = k^*$, the eigenvalues become a complex conjugated pair, leading to an oscillatory instability if the real part becomes positive. The transverse eigenvalue σ_T is again damped as depicted by the dotted line. Parameters are a) $\alpha = 25$, $\rho_0 = 1.2$ linearly stable state; b) $\alpha = 50$, $\rho_0 = 0.6$ stationary density instability; c) $\alpha = 17$, $\rho_0 = 2.9$ oscillatory orientational instability; d) $\alpha = 35$, $\rho_0 = 1$. both density and orientational fluctuations are unstable.

provided that this value is positive. Nevertheless the growth rates differ compared to the case $\beta = 0$, since the contributions $\propto \beta k^4$, and also higher order terms, strengthen the damping of the conserved mode (the two modes have to meet at k^*) and restrict the window of growing density modes to smaller k , i.e. larger wavelengths, cf. Figs. 9.3b) and d). I should mention that I refer to this mode still as a density demixing mode although this is true only at vanishing wavenumber, $k = 0$. Strictly speaking, for finite wavenumbers it is a coupled density-orientation demixing mode.

Beyond the coincidence of the density and the longitudinal mode at a wavenumber k^* , an oscillatory mode emerges, i.e. a complex conjugated pair of eigenvalues. The growth rate of this mode is given by the dashed lines in Fig. 9.3. As can be seen in parts c) and

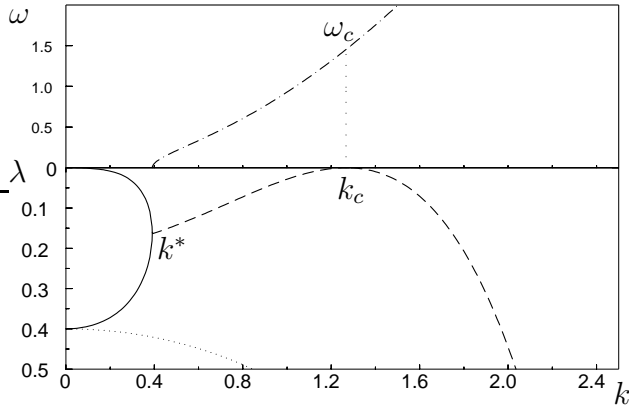


Figure 9.4: The real part λ and the imaginary part ω of the eigenvalues $\sigma_{1,2}$ are shown in dependence of wavenumber k as the dashed and dash-dotted line respectively. At the point $k = k^*$ where the density and the longitudinal orientation branch meet, the growth rate acquires a nonvanishing imaginary part, implying $\sigma_{1,2} = \lambda \pm i\omega$. Parameters are $\alpha = 17$, $\beta = 3$, $D_r = 0.4$ and $\rho = \rho_c$.

d) of this figure, as well as in Fig. 9.4, also this mode can become unstable at a finite wavenumber k_c , as had been the case for $\beta = 0$. However, since the eigenvalue is complex, $\sigma_{1,2} = \lambda \pm i\omega$, in the case $\beta \neq 0$, the unstable mode has a finite frequency $\omega_c = \omega(k_c)$, as shown in Fig. 9.4.

We now determine the threshold, the critical wavenumber and the critical frequency for this oscillatory, coupled density-orientation mode. For the eigenvalues $\sigma = \lambda \pm i\omega$, the root in Eq. (9.31) can be considered imaginary, since we are in the case $k > k^*$. Thus only the term in front of the root determines the instability threshold, namely

$$\begin{aligned} \lambda &= \frac{1}{2} \left(\bar{\mathcal{L}}_{11}^{(0)} + \bar{\mathcal{L}}_{22}^{(0)} \right) \\ &= \frac{1}{2} \left[-D_r - \left(\frac{3D+5}{4} + \frac{1+D}{\pi} \rho_0 - \frac{7}{96} \alpha \rho_0 \right) k^2 - \frac{151}{46080} \alpha \rho_0 k^4 \right]. \end{aligned} \quad (9.33)$$

One should notice that again the terms proportional to β , namely $\bar{\mathcal{L}}_{12}^{(0)}$ and $\bar{\mathcal{L}}_{21}^{(0)}$, do not enter here. The conditions for ρ_c , k_c are, analogously to the treatment of the case $\beta = 0$,

$$\left. \frac{d\lambda}{dk} \right|_{k_c} = 0 \quad \text{and} \quad \lambda(k_c) = 0. \quad (9.34)$$

One gets

$$\rho_c^\beta = \frac{(D_r d + ac)\alpha - ab + \sqrt{D_r d \alpha [(D_r d + 2ac)\alpha - 2ab]}}{b^2 - 2bc\alpha + c^2 \alpha^2} \quad (9.35)$$

and

$$k_c^\beta = \left(\frac{2D_r}{d\alpha\rho_c} \right)^{1/4}, \quad (9.36)$$

where the abbreviations $a = \frac{3D+5}{4}$, $b = \frac{1+D}{\pi}$, $c = \frac{7}{96}$ and $d = \frac{151}{23040}$ have been introduced.

Eqs. (9.35) and (9.36) should be compared to the results for $\beta = 0$, cf. Eqs. (9.21) and (9.22). Although the terms proportional to β do not enter the instability condition

explicitly and ρ_c^β and k_c^β are not functions of β , the threshold and the wavenumber are *different* due to the coupling of ρ and t_L . Additionally, the term $\frac{1+D}{\pi}\rho_0$ in Eq. (9.33) arising from the excluded volume contribution in the linear equation of the density is responsible for the fact that not the product $\rho_0\alpha$ renders the system unstable as in the case $\beta = 0$ but that the dependence is more complicated, cf. Eq. (9.35). This is further discussed in the next section.

The frequency of the unstable mode is given by the square root part of Eq. (9.31),

$$i\omega_c = \frac{1}{2}\sqrt{(\bar{\mathcal{L}}_{11}^{(0)} - \bar{\mathcal{L}}_{22}^{(0)})^2 + 4\bar{\mathcal{L}}_{12}^{(0)}\bar{\mathcal{L}}_{21}^{(0)}} \Big|_{\rho_c, k_c}. \quad (9.37)$$

Since at threshold

$$\lambda(\rho_c, k_c) = 0 = \frac{1}{2}(\bar{\mathcal{L}}_{11}^{(0)} + \bar{\mathcal{L}}_{22}^{(0)}) \Big|_{\rho_c, k_c} \quad (9.38)$$

holds, one can simplify the above expression to

$$\omega_c = \sqrt{-(\bar{\mathcal{L}}_{22}^{(0)})^2 - \bar{\mathcal{L}}_{12}^{(0)}\bar{\mathcal{L}}_{21}^{(0)}} \Big|_{\rho_c, k_c}. \quad (9.39)$$

9.5 Discussion

We have performed a linear analysis of the continuum model, Eqs. (9.1), and obtained a rich variety of instabilities of the homogeneous and isotropic filament-motor solution. The contribution that renders the systems unstable has been identified as the active translational current proportional to α , which leads in the case $\beta = 0$ either to a long wavelength density demixing instability or to a stationary finite wavelength orientational instability, cf. Fig. 9.1. These instabilities remain present in principle also in the case with polarity sorting, i.e. with $\beta \neq 0$, but they change their quality, cf. Fig. 9.3: The density demixing mode becomes a coupled density-orientation demixing mode with the same threshold but with different growth rates and restricted to larger wavelengths. The stationary orientational instability becomes oscillatory and corresponds now to a coupled density-orientation mode.

9.5.1 Influence of polarity sorting

Fig. 9.5 compares the instability diagrams for the cases in absence and presence of polarity sorting, i.e. with $\beta = 0$ (cf. Fig. 9.2) and $\beta \neq 0$ respectively, for different values of the rotational diffusion coefficient D_r . In parts a) and c) of this figure, the case without polarity sorting is shown for a low rotational diffusion coefficient $D_r = 0.1$ and for a high value $D_r = 2$. One can clearly see from the dashed line representing ρ_c that the region, where the orientational instability becomes unstable first, is shrinking with increasing rotational

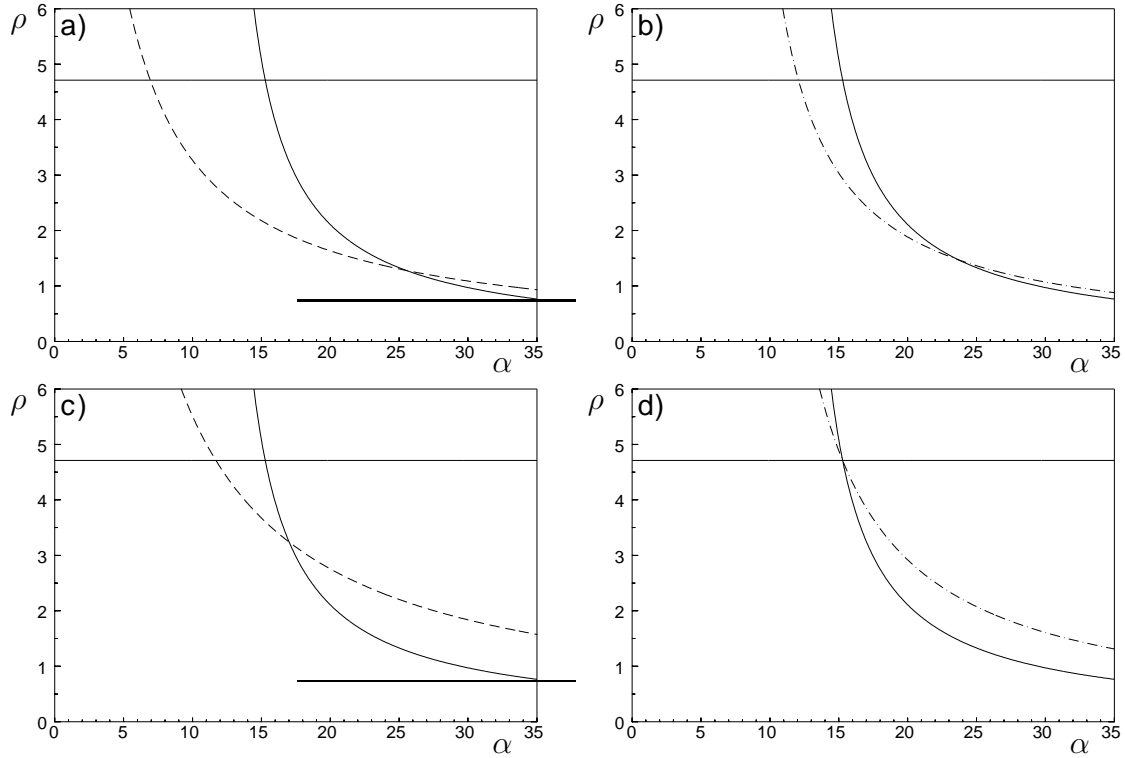


Figure 9.5: Instability diagrams: the critical density ρ_c and ρ_c^β are shown in dependence of α for the case $\beta = 0$ as the dashed and for the case $\beta \neq 0$ as the dash-dotted lines for different values of D_r . The horizontal solid line at $\rho = \rho_{IN}$ refers to the homogeneous isotropic-nematic transition while the second solid curve describes the critical density $\rho_d = \rho_d^\beta$ for the demixing instability, which is independent of D_r . Parameters are $D_r = 0.1$ in a), b) and $D_r = 2$ in c) and d). One can see from part d) that for values larger than $D_r \simeq 2$, the oscillatory orientational instability is suppressed and either the nematic or the density demixing instability always happen first.

diffusion coefficient and that the density demixing, represented by the solid curve, though itself unchanged then occurs first for lower values of α . In parts b) and d) the threshold for the oscillatory orientational instability is shown as the dash-dotted line for the same two values of D_r . The oscillatory instability occurs for higher values of α compared to the stationary instability for $\beta = 0$, which can be traced back to the linear coupling of the density and the orientation by the β -contribution, which are responsible for the merging of the modes. The region of this instability also shrinks with increasing D_r and for the large value $D_r = 2$ the oscillatory instability never occurs first, either the homogeneous nematic or the coupled density-orientation demixing mode always have a lower threshold.

It should be mentioned that the density demixing instabilities with $\rho_d = \rho_d^\beta$, are possible only for values of $\alpha > \alpha_d^{min} = \frac{24}{\pi}(1+D)$. In contrast, the stationary orientational instability is possible for every value of α if only the density is high enough, since the product $\alpha\rho$

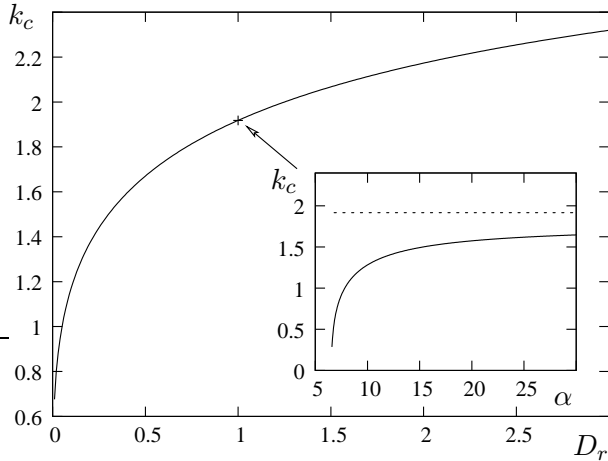


Figure 9.6: The critical wavenumber k_c for $\beta = 0$ is plotted in dependence of the rotational diffusion coefficient D_r . In the inset, k_c is plotted for $D_r = 1$ as a function of α for $\beta = 0$ and $\beta \neq 0$. While in the first case, k_c is independent of α as indicated by the dashed line in the inset, in the second case there is a quite strong dependence and the wavenumber is always smaller as compared to the former case.

renders the system unstable here. This is not the case anymore for $\beta \neq 0$ where $\alpha_{c,\beta}^{min} = \frac{96(1+D)}{7\pi}$. In all the pictures of this chapter we have chosen the diffusion ratio $D = D_{\perp}/D_{\parallel} = 1/2$, implying $\alpha_d^{min} \simeq 11.459$ and $\alpha_{c,\beta}^{min} \simeq 6.548$. One should recognize that the stability borders are of hyperbola type, which reflects the fact that an increase in the filament density and an increase in motor transport have the same effect on the system. Recently, a model for the MT-motor system based on a totally different interaction concept, namely inelastic collisions [119, 130], also yielded hyperbolas as instability borders. Thus this seems to be a quite generic result.

The behavior of the critical wavenumber k_c^{β} is also a bit more involved than in the case without polarity sorting, as can be seen in Fig. 9.6. While k_c is always depending on the rotational diffusion coefficient D_r , since the latter determines from which negative value the growth rate of the longitudinal mode has to start from at $k = 0$, it is independent of α in the case $\beta = 0$. This is due to the fact that the product $\rho_c \alpha$ is a function solely of D_r , cf. Eq. (9.21), thus implying that

$$k_c = 4 \left(\frac{12D_r}{5\alpha\rho_c} \right)^{1/4}. \quad (9.40)$$

is also solely determined by D_r . In the case $\beta \neq 0$ however, the more complicated functional dependence of ρ_c^{β} on α , cf. Eq. (9.35), leads to a quite strong dependence of k_c^{β} on α , as can be seen in the inset of Fig. 9.6.

Moreover, one should note that ρ_c^{β} and k_c^{β} are *independent* of β , but have different values than ρ_c and k_c in the case without polarity sorting. This implies that $\beta \rightarrow 0$ is a singular limit and that one cannot extrapolate behavior for the $\beta \neq 0$ case from the simpler case $\beta = 0$. This is also reflected in the next two chapters, where a weakly nonlinear analysis for the finite wavelength instabilities, with and without polarity sorting, is performed. The underlying reason for this phenomenon is again the linear coupling of the density and the longitudinal orientation mode in the case $\beta \neq 0$ and additionally the $\pm \mathbf{t}$ -symmetry breaking.

In the case of the finite wavelength instability without polarity sorting, only the lon-

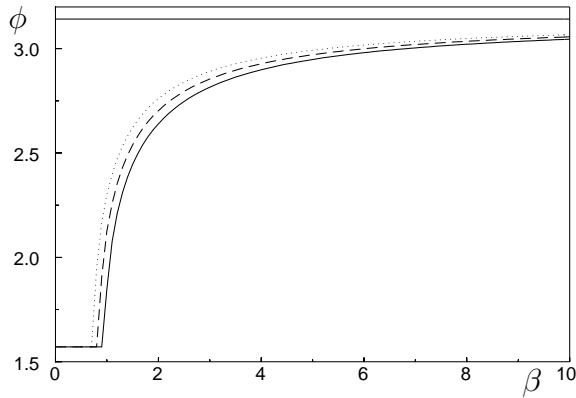


Figure 9.7: The relative phase shift between filament orientation and filament density as a function of the polarity sorting parameter β . For small values of β the phase shift is $\pi/2$ and approaches π for high values. The dependence on the other parameters is minute. The parameters all lie in the region of stable traveling wave (TW) solutions, cf. Fig. 11.2: $\alpha = 14$, $D_r = 0.8$ (solid line), $\alpha = 14.5$, $D_r = 1.2$ (dashed line) and $\alpha = 15$, $D_r = 1.6$ (dotted line).

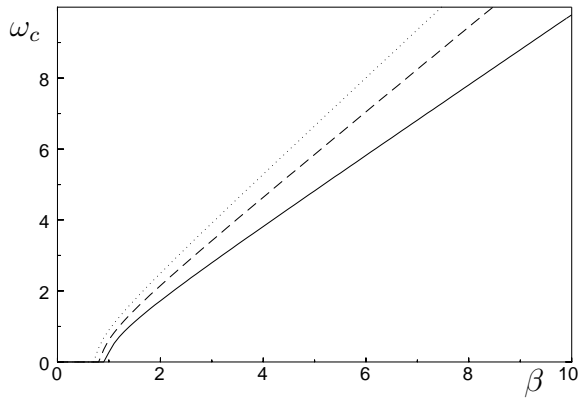


Figure 9.8: The dependence of the critical frequency ω_c on the polarity sorting parameter β . The dependence on the other parameters is minute. The parameters all lie in the region of stable traveling wave (TW) solutions, cf. Fig. 11.2: $\alpha = 14$, $D_r = 0.8$ (solid line), $\alpha = 14.5$, $D_r = 1.2$ (dashed line) and $\alpha = 15$, $D_r = 1.6$ (dotted line).

gitudinal orientation mode gets unstable and the density is involved only in the nonlinear regime. In contrast, in the case with polarity sorting, a coupled density orientation mode becomes unstable and the parameter β is determining the relative phase shift ϕ between filament density and filament orientation, as well as the frequency of the emerging wave solution. However, the qualitative behavior, even in the nonlinear regime, cf. section 11.3, is not much affected provided that β is not too small.

Fig. 9.7 shows the phase shift ϕ between the spatial periodicities of the filament density and the filament orientation in dependence of the polarity sorting parameter β for three different parameter sets. The phase starts at $\pi/2$ for small β and tends to π with increasing β . One can see that β determines the angle while the other parameters have only small effects. However, for large values of β the influence of this very parameter is also only minute.

The critical frequency ω_c is shown as a function of β in Fig. 9.8. One can see that again mostly β determines the behavior: for not too small values of β the frequency increases nearly linearly and the other parameters have only small effects. As can be seen from both Figs. 9.7 and 9.8, the instability is oscillatory only if β exceeds some small critical value.

9.5.2 Influence of the diffusion ratio

As reflected by the diffusion matrix defined in Eq. (7.12),

$$D_{ij} = D_{\parallel} u_i u_j + D_{\perp} (\delta_{ij} - u_i u_j) , \quad (9.41)$$

translational diffusion of rods in general is anisotropic. Before going further to the nonlinear analysis, I want to discuss briefly the influence of the ratio of perpendicular to parallel diffusion, i.e. of the parameter $D = \frac{D_{\perp}}{D_{\parallel}}$ with $0 \leq D \leq 1$, on the model behavior.

From the physical point of view, the value of D distinguishes different model regimes: If the rods were diffusing isotropically, i.e. $D_{\perp} = D_{\parallel}$, D equals one. However, in a viscous solution, a rod can diffuse much easier in the direction parallel to its orientation than perpendicular to it. A hydrodynamic calculation accounting for the rod-like shape [39] yields $D = 1/2$, which is the value we have used for the figures throughout this chapter. One could also consider the case $D = 0$ meaning that $D_{\perp} = 0$ which applies for semi-dilute solutions, where the so-called tube approximation holds and D_{\parallel} dominates the diffusion behavior [39, 126].

Very recently [120] a consideration of the molecular motors before coarse-graining implied that in the case $D \neq 1$, i.e. for $D_{\perp} \neq D_{\parallel}$, there is not only relative filament motion as accounted for in the model under consideration, especially in Eqs. (7.14), but also a net motion of the center of mass of the considered filament pair. Nevertheless, this result has been obtained by neglecting any rotations of the filaments and it is not clear that it prevails if rotational degrees of freedom are accounted for. Second, in the weakly nonlinear and numerical calculations of the subsequent chapters, D from the mathematical viewpoint appears just as a parameter, and we checked that the influence on the behavior was only minute.

Hence for all the nonlinear calculations in the following chapters, I restrict myself to the case $D = 1/2$, reflecting the anisotropic diffusion behavior of the rods in the dilute limit. Center of mass motion may however be possible and could be interesting to investigate in the future.

Chapter 10

Stationary patterns: competition between asters and stripes

In the last section we have discussed the occurrence of instabilities in the filament-motor model under investigation. There it has been shown that already in the case without polarity sorting, $\beta = 0$, two inhomogeneous instabilities can take place, namely a long wavelength density-demixing instability and a stationary finite wavelength orientational instability. Since we are interested in patterns like the asters displayed in Fig. 6.1, that involve inhomogeneous orientations of filaments, we are interested at first in the orientational instability. Moreover, it is legitimate first to analyze the latter instability in the stationary case, in spite of the fact that the case $\beta = 0$ is sort of special since the instability is rendered oscillatory for β beyond some small critical value, cf. Fig. 9.8 and section 9.4. The case of the oscillatory instability which is always a bit more involved than the stationary case, is dealt with in the following chapter.

To characterize the behavior of a finite wavelength instability near threshold, we use the amplitude expansion technique [42, 43, 44], where one derives by a multiscale analysis and separation of time scales an equation of the amplitude of the critical mode with wavenumber $k = k_c$ that covers the slow dynamics near threshold.

I will sketch the treatment in the next section while postponing the details to section 10.1.2. Later on in section 10.2, we will use the derived amplitude equations to determine the existence and stability of the spatial patterns in our two-dimensional filament-motor model. We confirm our analytical calculations by simulations of the underlying model equations in section 10.3 and make a comparison to experiments in section 10.4.

10.1 Weakly nonlinear analysis of the stationary orientational instability

10.1.1 Amplitude equations

In section 9.2 we have investigated the linearization of Eqs. (8.4) around the homogeneously stationary basic state $\rho = \rho_0$ and $\mathbf{t} = 0$ in the absence of polarity sorting, i.e. for $\beta = 0$. We found a stationary finite wavelength instability in the orientation field that is governed by the eigenvalue

$$\sigma_L = -D_r - \frac{1}{4}k^2 \left(3 + D - \frac{\alpha\rho_0}{8} + \frac{5}{768}\alpha\rho_0 k^2 \right) \quad (10.1)$$

of the linear operator defined in Eqs. (9.8) and (9.9), which acquires a positive growth rate for modes around the critical wavenumber

$$k_c = 4 \left(\frac{12D_r}{5\alpha\rho_c} \right)^{1/4}, \quad (10.2)$$

provided that the control parameter chosen as the mean density ρ_0 exceeds

$$\rho_c = \frac{8}{\alpha} \left((3 + D) + \frac{5}{12}D_r \left(1 + \sqrt{1 + \frac{24(3 + D)}{5D_r}} \right) \right). \quad (10.3)$$

The amplitude of the linear solution $\propto \exp(\sigma_L t + i\mathbf{k}_c \cdot \mathbf{r})$ with associated eigenvector

$$\mathbf{E}_L = \begin{pmatrix} 0 \\ q \\ p \end{pmatrix}, \quad (10.4)$$

with $\mathbf{k} = (q, p)$ is limited by the terms in the full Eqs. (8.4) that are nonlinear with respect to density deviations $\tilde{\rho}$ and orientation deviations \mathbf{t} from the basic state.

In this chapter I will investigate the weakly nonlinear behavior beyond this orientational instability, i.e. in the region referred to as O in Fig. 9.2 where $\rho_c < \rho_0 < \min(\rho_d, \rho_{IN})$ holds, with ρ_d and ρ_{IN} the threshold densities for the density demixing and the homogeneous nematic transition respectively. Among the questions of interest for the pattern forming instability which will be answered by our analysis are: which kinds of pattern are preferred in which parameter range, what is the parameter dependence of the amplitudes of the pattern forming modes and what is their stability behavior.

The analysis can be done by numerical simulation of the full nonlinear equations (8.4) as exemplified in section 10.3, and analytically if first ρ_0 is only slightly beyond ρ_c and second the bifurcation is *supercritical*. Pattern forming instabilities can be either continuous, i.e. the amplitude of the pattern increases continuously from zero upon crossing the critical control parameter value, or discontinuous, i.e. there is a jump to a finite pattern

amplitude upon crossing the threshold. The former class of instabilities is said to lead to a *forward* or *supercritical* bifurcation, while the latter are called *backward* or *subcritical* [42]. For a supercritical bifurcation, the amplitude of the mode initially growing with $\sigma_L(k)$ is small immediately above threshold and may be determined in this range by a perturbative analysis, the so-called amplitude expansion. The latter yields generic equations for the spatiotemporal behavior of the amplitudes of the unstable Fourier modes with $|\mathbf{k}| = k_c$ whose dynamics is slow near the threshold of a supercritical bifurcation.

The generic form of the so-called *amplitude equations* depends on the preferred pattern beyond the stationary supercritical bifurcation. Since the underlying model equation displaying the instability is nonlinear, the superposition principle does not hold and the nonlinearities determine which (nonlinear) superpositions are possible. In a laterally infinite system of two spatial dimensions, $\mathbf{r} = (x, y)$, a regular pattern usually can be spatially periodic either in one, two or three directions [42]. The first case corresponds to a stripe pattern,

$$\mathbf{w} = X \mathbf{E} \exp(ik_c x) \quad (10.5)$$

where the coordinate frame has been chosen in such a way that the wavenumber of the pattern coincides with the x -direction, \mathbf{E} is the respective eigenvector of the linear operator and X denotes the amplitude. The corresponding amplitude equation then reads

$$\tau_0 \partial_t X = \varepsilon X - g_1 |X|^2 X. \quad (10.6)$$

Here τ_0 is a relaxation time, ε denotes the relative deviation from the threshold of pattern formation,

$$\varepsilon = \frac{\rho_0 - \rho_c}{\rho_c}, \quad (10.7)$$

and g_1 is a nonlinear coefficient that limits the amplitude of the stripe pattern for $g_1 > 0$ ¹.

A pattern that is spatially periodic in two perpendicular directions corresponds to a square pattern,

$$\mathbf{w} = X \mathbf{E}_x \exp(ik_c x) + Y \mathbf{E}_y \exp(ik_c y), \quad (10.8)$$

with the generic equations

$$\tau_0 \partial_t X = \varepsilon X - g_1 |X|^2 X - g_2 |Y|^2 X, \quad (10.9a)$$

$$\tau_0 \partial_t Y = \varepsilon Y - g_1 |Y|^2 Y - g_2 |X|^2 Y. \quad (10.9b)$$

In this case a second nonlinear coefficient g_2 arises that couples the two orthogonal modes.

¹If $g_1 > 0$ holds, the pattern amplitude is limited by the nonlinear term to a value $|X| = \sqrt{\varepsilon/g_1}$, thus evolving continuously upon crossing the threshold. Correspondingly this refers to the case of a supercritical or forward bifurcation mentioned above. In the case $g_1 < 0$, higher order terms like $\propto |X|^4 X$ have to be incorporated to guarantee saturation and the amplitude can be nonzero for $\varepsilon < 0$, corresponding to a subcritical or backward bifurcation.

Periodicity in three directions leads to a hexagonal pattern

$$\mathbf{w} = A_1 \mathbf{E}_1 \exp(i\mathbf{k}_1 \cdot \mathbf{r}) + A_2 \mathbf{E}_2 \exp(i\mathbf{k}_2 \cdot \mathbf{r}) + A_3 \mathbf{E}_3 \exp(i\mathbf{k}_3 \cdot \mathbf{r}) \quad (10.10)$$

with three wavenumbers enclosing an angle of 120° ,

$$\mathbf{k}_1 = k_c \begin{pmatrix} 1 \\ 0 \end{pmatrix}, \quad \mathbf{k}_2 = \frac{1}{2}k_c \begin{pmatrix} -1 \\ \sqrt{3} \end{pmatrix}, \quad \mathbf{k}_3 = -\frac{1}{2}k_c \begin{pmatrix} 1 \\ \sqrt{3} \end{pmatrix}. \quad (10.11)$$

The respective generic amplitude equations now read

$$\tau_0 \partial_t A_1 = \varepsilon A_1 + g_0^H A_2^* A_3^* - g_1 |A_1|^2 A_1 - g_2^H (|A_2|^2 + |A_3|^2) A_1, \quad (10.12a)$$

$$\tau_0 \partial_t A_2 = \varepsilon A_2 + g_0^H A_1^* A_3^* - g_1 |A_2|^2 A_2 - g_2^H (|A_1|^2 + |A_3|^2) A_2, \quad (10.12b)$$

$$\tau_0 \partial_t A_3 = \varepsilon A_3 + g_0^H A_1^* A_2^* - g_1 |A_3|^2 A_3 - g_2^H (|A_1|^2 + |A_2|^2) A_3. \quad (10.12c)$$

Here g_1 is again² a nonlinear coefficient describing the self-coupling, while g_0^H and g_2^H describe the coupling to the other modes, the asterisk denoting complex conjugation. The quadratic term $\propto g_0^H$ dominates the behavior near threshold and is mainly responsible for the formation of hexagonal structures.

It should be noted that the description of the patterns by amplitude equations is generic, since the specific system under consideration enters into the reduced description only through the coefficients τ_0 , g_1 , and g_2 or g_0^H , g_2^H respectively. The latter are functions of the model parameters, in the case of the stationary finite wavelength instability these are the rotational diffusion coefficient D_r , and the two motor contributions α and γ .

I have to mention also that I restrict myself in the present analysis to patterns with exactly the critical wavenumber k_c . Allowing for deviations of the pattern wavenumber from the critical one leads to additional terms $\partial_t A_i \propto \xi_0^2 \partial_x^2 A_i$ in the amplitude equations, cf. [42]. ξ_0^2 can be easily obtained from the linear spectrum of the unstable mode as the curvature of the neutral curve and the stability with respect to inhomogeneous perturbations can be calculated if the respective term is taken into account in the amplitude equations. However, at the moment this seems not to be an urgent question for the model under consideration since the experimental and theoretical understanding of filament-motor models is far away from such accuracy.

10.1.2 Derivation of the amplitude equations

Numerical simulations of the basic equations (8.4), as described in section 10.3, indicate that stripe and square patterns are favored immediately above threshold of the orientational instability. Moreover, hexagonal structures are not driven in this system, which can be seen below where details of the amplitude expansion are shown. Since the equation for the square pattern already comprises the equation for stripes, it is thus sufficient for us to derive Eqs. (10.9) from the filament-motor model Eq. (8.4), namely

$$\tau_0 \partial_t X = \varepsilon X - g_1 |X|^2 X - g_2 |Y|^2 X, \quad (10.13a)$$

$$\tau_0 \partial_t Y = \varepsilon Y - g_1 |Y|^2 Y - g_2 |X|^2 Y. \quad (10.13b)$$

²One should note that τ_0 and g_1 are the same for all three patterns.

In the following I describe the scheme for the derivation of the two coupled amplitude equations (10.13) from the three underlying nonlinear equations (8.4). First of all one assumes small values for the amplitudes X and Y of the spatially periodic deviations from the homogeneous basic state $\rho = \rho_0$ and $\mathbf{t} = 0$. At threshold, i.e. at $\rho_0 = \rho_c$ and for $|\mathbf{k}| = k_c$, these deviations are assumed either periodic in x - or in y -direction. Using the eigenvectors defined in Eq. (9.16), the ansatz (10.8) explicitly reads

$$\mathbf{w}_1 = \begin{pmatrix} \rho_1 \\ t_{1x} \\ t_{1y} \end{pmatrix} = \begin{pmatrix} 0 \\ X \\ 0 \end{pmatrix} e^{ik_c x} + \begin{pmatrix} 0 \\ 0 \\ Y \end{pmatrix} e^{ik_c y} + c.c.. \quad (10.14)$$

with $c.c.$ denoting the complex conjugate and the index 1 indicating that this is the starting point of our perturbation analysis. Here we have again chosen, without restriction, that the two orthogonal wave numbers lie parallel to the axes. One should note that the two modes are decoupled and moreover do not couple to the density equation either.

Similarly as elaborated in section 9.2, the nonlinear equations (8.4) may be rewritten in terms of the deviations $\mathbf{w} = (\tilde{\rho}, t_x, t_y)$ from the basic state $\mathbf{w}_0 = (\rho_0, 0, 0)$ as follows

$$\partial_t \mathbf{w} = \mathcal{L}_0 \mathbf{w} + \mathbf{N}(\rho, \mathbf{t}), \quad (10.15)$$

with the linear operator as defined in Eqs. (9.8) and (9.9) and the nonlinear operator

$$\mathbf{N}(\rho, \mathbf{t}) = \begin{pmatrix} \mathcal{N}_\rho(\rho, \mathbf{t}) \\ \mathcal{N}_x(\rho, \mathbf{t}) \\ \mathcal{N}_y(\rho, \mathbf{t}) \end{pmatrix}. \quad (10.16)$$

The latter includes all the nonlinear terms with respect to $\tilde{\rho}$ and \mathbf{t} on the right hand sides of Eqs. (8.4).

Naturally, as the small expansion parameter the relative distance from threshold,

$$\varepsilon = \frac{\rho_0 - \rho_c}{\rho_c}, \quad (10.17)$$

is chosen. Close to threshold, i.e. for $0 < \varepsilon \ll 1$, the dynamics of the modes with amplitudes X and Y as defined in Eq. (10.14) is slow due to their small linear growth rates and accordingly a slow time scale

$$T = \varepsilon t \quad (10.18)$$

is introduced. This allows the time derivatives in Eqs. (10.15) to be replaced by

$$\partial_t \rightarrow \varepsilon \partial_T. \quad (10.19)$$

Now we expand the solution \mathbf{w} of the nonlinear equations (10.15) with respect to powers of $\varepsilon^{1/2}$

$$\mathbf{w} = \varepsilon^{1/2} \mathbf{w}_1 + \varepsilon \mathbf{w}_2 + \varepsilon^{3/2} \mathbf{w}_3 + \dots, \quad (10.20)$$

with \mathbf{w}_1 as already defined in Eq. (10.14). The same is done for the nonlinearities

$$\mathbf{N} = \varepsilon \mathbf{N}_1 + \varepsilon^{3/2} \mathbf{N}_2 + \dots, \quad (10.21)$$

where there is no lowest order term since the nonlinearities have to be at least of the order $\mathbf{w}_1^2 \propto \varepsilon$. Sorting now the contributions to Eq. (10.15) with respect to powers of ε , one ends up with the following hierarchy of equations

$$\varepsilon^{1/2} : \mathcal{L}_0 \mathbf{w}_1 = 0, \quad (10.22a)$$

$$\varepsilon : \mathcal{L}_0 \mathbf{w}_2 = -\mathcal{N}_\rho(\mathbf{t}_1) e_\rho, \quad (10.22b)$$

$$\varepsilon^{3/2} : \mathcal{L}_0 \mathbf{w}_3 = \partial_T \mathbf{w}_1 - \mathcal{L}_2 \mathbf{w}_1 - \sum_{i=x,y} \mathcal{N}_i(\rho_2, \mathbf{t}_1) e_i, \quad (10.22c)$$

that has to be solved successively. Here we have introduced $e_\rho = (1, 0, 0)$, $e_x = (0, 1, 0)$, $e_y = (0, 0, 1)$ to address single components of \mathbf{w} . The linear operator \mathcal{L}_2 introduced in Eq. (10.22c) has the form

$$\mathcal{L}_2 = \begin{pmatrix} \mathcal{L}_{11}^{(2)} & 0 & 0 \\ 0 & \mathcal{L}_{22}^{(2)} & \mathcal{L}_{23}^{(2)} \\ 0 & \mathcal{L}_{32}^{(2)} & \mathcal{L}_{33}^{(2)} \end{pmatrix} \quad (10.23)$$

and comprises the terms of \mathcal{L}_0 that are of the order ε . It thus has the entries

$$\begin{aligned} \frac{1}{\rho_0} \mathcal{L}_{11}^{(2)} &= \left(\frac{1+D}{\pi} - \frac{\alpha}{24} \right) \Delta - \frac{19\alpha}{11520} \Delta^2, \\ \frac{1}{\rho_0} \mathcal{L}_{22}^{(2)} &= -\frac{\alpha}{96} (\Delta + 2\partial_x^2) - \frac{\alpha}{46080} (11\Delta^2 + 64\Delta\partial_x^2), \\ \frac{1}{\rho_0} \mathcal{L}_{23}^{(2)} &= -\frac{\alpha}{48} \partial_x \partial_y - \frac{\alpha}{720} \Delta \partial_x \partial_y. \end{aligned} \quad (10.24)$$

The remaining two matrix elements $\mathcal{L}_{32}^{(2)}$ and $\mathcal{L}_{33}^{(2)}$ follow again from $\mathcal{L}_{23}^{(2)}$ and $\mathcal{L}_{22}^{(2)}$ by permuting ∂_x and ∂_y . The nonlinear operators read in detail

$$\begin{aligned} \mathcal{N}_\rho(\mathbf{t}_1) &= -\frac{\alpha}{48} \partial_i \left[t_{1i} \partial_j t_{1j} + t_{1j} \partial_i t_{1j} + t_{1j} \partial_j t_{1i} \right] \\ &- \frac{\alpha}{C_1} \left[11 \partial_i (t_{1j} \partial_i \Delta t_{1j}) + 16 \partial_i \left(t_{1i} \Delta \partial_j t_{1j} + 2 t_{1j} \partial_j \partial_i \partial_l t_{1l} + t_{j1} \partial_j \Delta t_{1i} \right) \right] \end{aligned} \quad (10.25)$$

and ($i = x, y$)

$$\begin{aligned}
\mathcal{N}_i(\rho_2, \mathbf{t}_1) &= \frac{3D+1}{2\pi} \partial_j (t_{1i} \partial_j \rho_2) + \frac{1-D}{2\pi} \left[\partial_j (t_{1j} \partial_i \rho_2) + \partial_i (t_{1j} \partial_j \rho_2) \right] \\
&- \frac{\alpha}{96} \partial_j \left[3t_{1i} \partial_j \rho_2 + t_{1j} \partial_i \rho_2 + \delta_{ij} t_{1l} \partial_l \rho_2 + \rho_2 \left(\partial_i t_{1j} + \partial_j t_{1i} + \delta_{ij} \partial_l t_{1l} \right) \right] \\
&- \frac{\alpha}{2C_1} \partial_j \left[\rho_2 \left(11 \partial_j \Delta t_{1i} + 16 \partial_i \Delta t_{1j} + 32 \partial_j \partial_i \partial_l t_{1l} + 16 \delta_{ij} \Delta \partial_l t_{1l} \right) \right. \\
&\quad \left. + 16 t_{1j} \partial_i \Delta \rho_2 + 32 t_{1l} \partial_l \partial_i \partial_j \rho_2 + 44 t_{1i} \partial_j \Delta \rho_2 + 16 \delta_{ij} t_{1l} \partial_l \Delta \rho_2 \right] \\
&+ \frac{1}{48} \left(\frac{\gamma}{4} - \frac{4}{\pi} D_r \right) \left[t_{1j} \partial_j \partial_i \rho_2 - \frac{1}{2} t_{1i} \Delta \rho_2 \right]. \tag{10.26}
\end{aligned}$$

Solving the hierarchy

Now we have to solve the hierarchy of equations (10.22) successively. The equation in $\mathcal{O}(\varepsilon^{1/2})$ is just the linear eigenvalue problem already discussed in section 9.2, i.e. it is solved already by our ansatz, $\rho_1 = 0$ and

$$t_{1x} = X(T) e^{ik_c x} + c.c., \quad t_{1y} = Y(T) e^{ik_c y} + c.c. \tag{10.27}$$

where we have made explicit that the two amplitudes X and Y are only functions of the slow time scale T .

In the next order, $\mathcal{O}(\varepsilon)$, a nonlinearity is only present in the density equation. Since density and orientation are completely decoupled in the linear operator, cf. Eqs. (9.8) and (9.9), and \mathcal{L}_0 acting on the \mathbf{t} -subspace is nonsingular, it follows that $\mathbf{t}_2 = 0$. The nonlinearity in the density component of Eq. (10.22b), leads upon inserting \mathbf{t}_1 in $\mathcal{N}_\rho(\mathbf{t}_1)$ to an equation for ρ_2 , whose solution is of the following form

$$\begin{aligned}
\rho_2(X, Y) &= r_1 X^2 e^{2ik_c x} + r_2 Y^2 e^{2ik_c y} \\
&+ r_3 XY e^{i(k_c x + k_c y)} + r_4 XY^* e^{i(k_c x - k_c y)} + c.c. \tag{10.28}
\end{aligned}$$

with $r_i = r_i(D_r, \alpha, \gamma)$ for $i = 1, \dots, 4$.

Instead of solving the Eq. (10.22c) at the order $\mathcal{O}(\varepsilon^{3/2})$, one can instead make use of *Fredholm's alternative*, which states that for Eq. (10.22c) having solutions, there must not exist terms on its right hand side that lie in the kernel of \mathcal{L}_0 . Physically this means that there should be no contributions proportional to the critical modes $\exp(ik_c x)$, $\exp(ik_c y)$ that would lead to resonant forcing. From the nonlinear contributions of $\mathcal{N}_i(\rho_2, \mathbf{t}_1)$ one gets such terms $\propto \exp(ik_c x)$ from the following combinations

$$r_1 X^2 e^{2ik_c x} X^* e^{-ik_c x}, \quad r_3 XY e^{i(k_c x + k_c y)} Y^* e^{-ik_c y}, \quad r_4 XY^* e^{i(k_c x - k_c y)} Y e^{ik_c y} \tag{10.29}$$

leading to the desired nonlinear couplings $|X|^2 X$ and $|Y|^2 X$ in the equations for X and analogously for the equation for Y . Collecting the prefactors of these respective modes in

Eq. (10.22c), one gets the two equations (10.13), with analytical but lengthy expressions for τ_0 , g_1 and g_2 as functions of D_r , α and γ .

From the analysis one can see that the nonlinear coupling of the orientational field to the density in $\mathcal{O}(\varepsilon)$ is crucial for the physical stability of the system, since the density contribution ρ_2 is responsible for the saturation of the amplitudes in the equation of next order $\mathcal{O}(\varepsilon^{3/2})$, cf. Eq. (10.22c), while $\mathbf{t}_2 = 0$ and thus \mathbf{t} can not limit the amplitudes by itself. One should also notice that ρ_2 has twice the wavenumber of the orientation field.

Absence of hexagonal pattern

To obtain the amplitude equations for hexagons, Eqs. (10.12), the situation is a bit more subtle [131]. Since the quadratic contributions like $\partial_t A_1 \propto A_2^* A_3^*$ have to be of the same order of magnitude as the cubic contributions, one has to introduce a second slow time scale into the problem, namely

$$\partial_t \rightarrow \sqrt{\varepsilon} \partial_{T_1} + \varepsilon \partial_T, \quad (10.30)$$

which leads to the hierarchy of equations

$$\varepsilon^{1/2} : \mathcal{L}_0 \mathbf{w}_1 = 0, \quad (10.31a)$$

$$\varepsilon : \mathcal{L}_0 \mathbf{w}_2 = \partial_{T_1} \mathbf{w}_1 - \mathcal{N}_\rho(\mathbf{t}_1) e_\rho, \quad (10.31b)$$

$$\varepsilon^{3/2} : \mathcal{L}_0 \mathbf{w}_3 = \partial_T \mathbf{w}_1 + \partial_{T_1} \mathbf{w}_2 - \mathcal{L}_2 \mathbf{w}_1 - \sum_{i=x,y} \mathcal{N}_i(\rho_2, \mathbf{t}_1) e_i, \quad (10.31c)$$

with the ansatz

$$\mathbf{w} = A_1 \mathbf{E}_1 \exp(i\mathbf{k}_1 \cdot \mathbf{r}) + A_2 \mathbf{E}_2 \exp(i\mathbf{k}_2 \cdot \mathbf{r}) + A_3 \mathbf{E}_3 \exp(i\mathbf{k}_3 \cdot \mathbf{r}) \quad (10.32)$$

and the wavenumbers \mathbf{k}_i as defined in Eqs. (10.11). If there would now be a quadratic contribution in the equation for the unstable field, corresponding in our case to a term quadratic in \mathbf{t}_1 in the t_i components of Eq. (10.31b), one gets already a condition of solvability in the order $\mathcal{O}(\varepsilon)$, namely

$$\tau_0 \partial_t A_1 = g_0^H A_2^* A_3^* \quad (10.33)$$

and analogously for the other equations. Both terms arise from contributions $\propto \exp(i\mathbf{k}_1 \cdot \mathbf{r})$, the latter due to

$$-i\mathbf{k}_2 \cdot \mathbf{r} - i\mathbf{k}_3 \cdot \mathbf{r} = i\mathbf{k}_1 \cdot \mathbf{r}. \quad (10.34)$$

The complete amplitude equations for the hexagons are then obtained by combining the two solvability conditions in the orders $\mathcal{O}(\varepsilon)$ and $\mathcal{O}(\varepsilon^{3/2})$, i.e. by regarding the sum

$$\partial_t A_1 = \sqrt{\varepsilon} \partial_{T_1} A_1 + \varepsilon \partial_T A_1 = \dots \quad (10.35)$$

In our case however, in Eq. (10.31b) there is only a quadratic contribution in the density equation, and not one in the unstable orientational modes t_i . Thus hexagonal structures are not driven in our system immediately above threshold.

10.2 Existence and stability of the nonlinear stripe and square state

I will now analyze the amplitude equations

$$\tau_0 \partial_t X = \varepsilon X - g_1 |X|^2 X - g_2 |Y|^2 X , \quad (10.36a)$$

$$\tau_0 \partial_t Y = \varepsilon Y - g_1 |Y|^2 Y - g_2 |X|^2 Y , \quad (10.36b)$$

derived from the filament-motor model Eq. (8.4) in the last two sections. First of all one is interested in the stationary solutions and second in their regions of existence and their regions of stability in the parameter space D_r , α and γ of the underlying model. The diffusion ratio has been chosen to be $D = \frac{D_\perp}{D_\parallel} = 1/2$, as discussed in section 9.5.2.

Apart from the trivial solution $X_0 = Y_0 = 0$, corresponding to the homogeneous and isotropic basic state $\rho = \rho_0$ and $\mathbf{t} = 0$, the coupled amplitude equations (10.36) allow also for stationary finite amplitude solutions. These are at first

$$X_0 = \pm \sqrt{\frac{\varepsilon}{g_1}} , Y_0 = 0 , \quad (10.37a)$$

$$X_0 = 0 , Y_0 = \pm \sqrt{\frac{\varepsilon}{g_1}} , \quad (10.37b)$$

which correspond according to Eq. (10.14) to stripes periodic either in x - or in y -direction. Second, there is the stationary solution of equal amplitudes

$$X_0 = Y_0 = \pm \sqrt{\frac{\varepsilon}{g_1 + g_2}} , \quad (10.38)$$

which constitutes a square pattern. In real space, this square pattern in terms of the components of the vector field $\mathbf{t}(\mathbf{r}, t)$ resembles the aster-structures found in the experiments [31] as will become clear from the simulation pictures in Sec. 10.3.

The range of existence as well as the range of linear stability for the roll solutions and for the squares can be easily investigated in terms of the amplitude equations. Stationary single amplitude solutions as given in Eqs. (10.37), exist beyond threshold, i.e. for $\varepsilon > 0$, only if $g_1 > 0$ holds. Equally obviously, squares exist beyond threshold only in the parameter range $g_1 + g_2 > 0$, cf. Eq. (10.38).

To investigate the stability of the two possible patterns, i.e. of the stripe and square solutions with X_0 and Y_0 from Eq. (10.37) or (10.38) respectively, one uses the ansatz $X = X_0 + \delta X$ and $Y = Y_0 + \delta Y$ and linearizes Eqs. (10.36) with respect to the small perturbations δX and δY to yield two coupled linear equations in both perturbations. Those may be solved by the mode ansatz $(\delta X, \delta Y) \sim (\delta \tilde{X}, \delta \tilde{Y}) e^{\sigma t}$ leading to a second order polynomial in σ providing two eigenvalues. One of them is always negative, i.e. damped, while the second is either

$$\sigma_r = \varepsilon \frac{g_1 - g_2}{g_1} \quad (10.39)$$

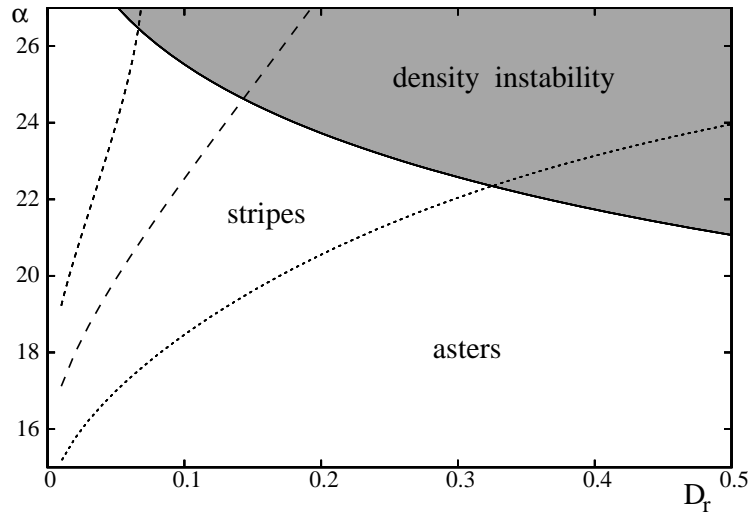


Figure 10.1: The stability regions of stripes and asters are shown as calculated by the amplitude expansion method near threshold, i.e. for $\rho_0 \gtrsim \rho_c(\alpha, D_r)$. The two critical densities ρ_c and ρ_d coincide along the solid line and beyond the instability with respect to density modulations is present which is not included in our nonlinear analysis. The dotted line is given by $g_1 = g_2$ and separates the range of stable square patterns (asters) from the range of stable stripe patterns. Along the long-dashed line one has $g_1 = 0$ and the bifurcation to stripes changes from supercritical (below) to a subcritical one (beyond). Between the short-dashed line, which is determined by $g_1 = -g_2$, and the long-dashed line asters can still exist but are unstable while the amplitudes of stripes cannot be determined by our lowest order expansion. Beyond the short-dashed line, also asters bifurcate subcritically.

for rolls or

$$\sigma_s = 2\varepsilon \frac{g_2 - g_1}{g_1 + g_2} \quad (10.40)$$

for squares.

Thus stripes or squares are stable if σ_r or σ_s is negative, respectively. Accordingly stripes are the preferred solution in the range of the nonlinear coefficients $g_2 > g_1 > 0$, while in the parameter range $|g_2| < g_1$ the square patterns are preferred, cf. also Refs. [132, 42]. These criteria for g_1 and g_2 may be translated according to their parameter dependence into the D_r - α plane, as shown for $\gamma = 0$ in Fig. 10.1, which is the central result of this chapter. The analytic calculations presented here are valid only below the solid line in Fig. 10.1, since above the density instability takes place which has not been accounted for in the amplitude expansion. The dotted line corresponds to the condition $g_1 = g_2 > 0$ which separates the range of stable squares, i.e. asters, from stable stripe solutions. Along the long-dashed line in Fig. 10.1, the bifurcation from the homogeneous basic state to the stripe pattern changes its behavior from a supercritical (below) to a subcritical one (above), where the expansion method is not effective anymore.

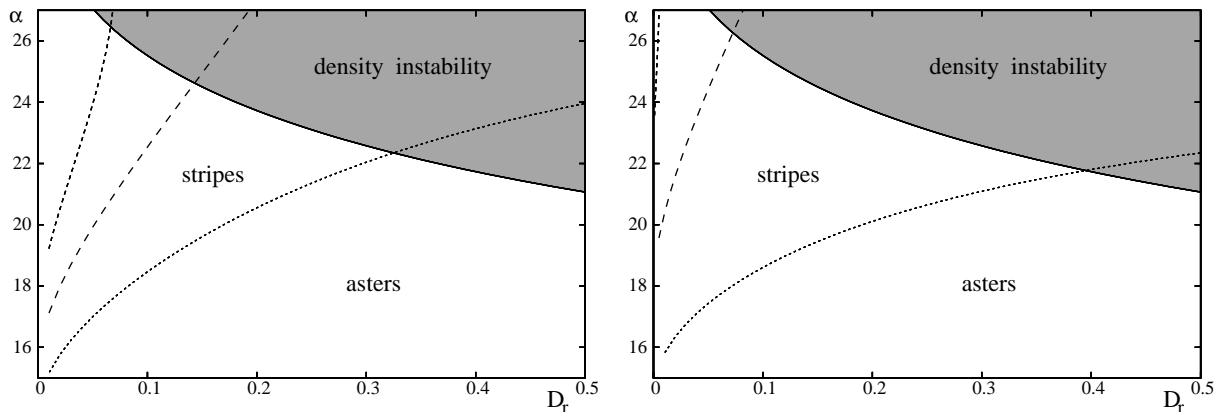


Figure 10.2: The left picture is identical to Fig. 10.1, while at the right the nonlinear contribution of the active rotational current, Eq. (7.18), is taken into account with $\gamma = \alpha$. The region of stable stripes considerably broadens while the regions of subcritical bifurcations are moved to higher α and lower D_r values.

Taking the (nonlinear) effect of the active rotational current into account, the bifurcation behavior from the homogeneous basic state is changed as shown in Fig. 10.2 for $\gamma = \alpha$. It can be seen that the range of stable stripe patterns in the D_r - α plane is enlarged, but nothing changes qualitatively.

10.2.1 Scaling of the diffusion coefficients

One may complement this outline of the bifurcation behavior by a discussion of the two decisive model parameters, namely α and D_r , and analytical estimates for them. Simple models for motor proteins [5, 114, 41, 40] imply that the rate α of the translational active transport grows linearly with the active motor density m and with the length of the filaments, i.e. $\alpha \propto mL$. Hence this rate can be controlled by the cell in the most effective way by the degree of motor activity (i.e. by regulating the ATP concentration) as well as on a much larger timescale by the density of the motors and the filament length.

For the rotational and translational diffusion coefficients in a *dilute solution*, calculations taking the hydrodynamic interaction into account [39] propose the analytical expressions

$$D_r = \frac{3 \ln(L/b)}{\pi \eta L^3} , \quad D_{\parallel} = \frac{\ln(L/b)}{2\pi \eta L} \quad (10.41)$$

with b the rod diameter and η the solvent viscosity. In the rescaled units introduced in Eqs. (8.5), this implies $D'_r = \frac{L^2}{D_{\parallel}} D_r = 6$, lying far in the range of squares (asters).

For *semi-dilute solutions* one can estimate [39, 125, 126, 133] $D_r = 6D_{\parallel}/(L^2(1 + c_r \rho')^2)$

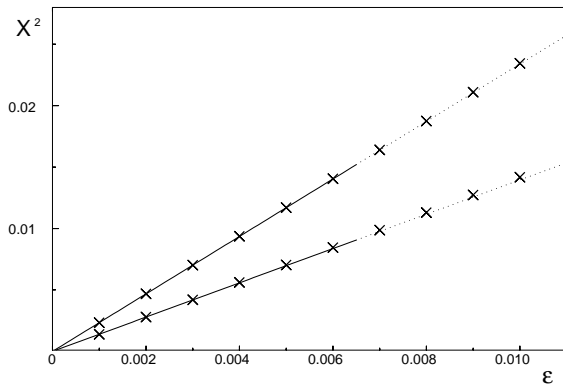


Figure 10.3: A comparison of the amplitudes of a stripe and a square solution as obtained in numerical simulations (crosses) with the analytical predictions, Eq. (10.37) and (10.38), is shown. The solution with the larger amplitude corresponds to the stripes. The agreement remains well for higher values of ε , but in the range between $\varepsilon \simeq 0.006-0.007$ a secondary bifurcation takes place. Parameters are $D_r = 0.5$, $\alpha = 21$ and $\gamma = 0$.

or

$$D'_r = \frac{L^2}{D_{\parallel}} D_r = \frac{6}{(1 + c_r \rho')^2} \quad (10.42)$$

in rescaled units, where $c_r \simeq 1$ is a geometry factor from a tube model calculation. Since stripes or bundle-like structures are stable for $D'_r < 0.3-0.4$, cf. Figs. 10.1 and 10.2, one needs a rather high (but possible) filament density for such a one-dimensional ordering.

According to these estimates the model suggests that asters are the most likely pattern occurring above the stationary bifurcation in dilute or semi-dilute two-dimensional filament-motor systems. For bundle-like structures to emerge rather high filament densities are needed, which is physically intuitive from the overlap nature of all the interactions, namely the excluded volume and the motor-induced filament-filament interaction.

10.3 Results of numerical simulations

Besides the weakly nonlinear analysis described in the previous sections, the continuum equations (8.4) have been solved numerically in order to check the validity range of the perturbation analysis and to further explore the solution space. For this purpose the time evolution has been integrated by a fourth order Runge-Kutta scheme and a Fourier Galerkin pseudo-spectral method has been used in space, imposing periodic boundary conditions on the system.

Since the validity range of the amplitude expansion with respect to the control parameter ε is not known a priori, in Fig. 10.3 we compare the amplitude of a stripe and a square pattern as obtained by a numerical solution of the basic equations (8.4) with the analytical results given by Eq. (10.37) and (10.38) respectively. Close to threshold there is nearly perfect agreement between both approaches. However the validity range of the amplitude equations is actually restricted to a range below $\varepsilon \sim 0.006$ for the parameters used in Fig. 10.3. Around this value a secondary instability takes place, which is not taken into account in the perturbation expansion.

Numerical simulations show that beyond this secondary instability a pronounced accumulation of the filaments to densities even higher than the density ρ_{IN} of the isotropic-nematic transition appear accompanied with high, alternating orientations. These solutions sometimes are numerically stable, depending on parameters. Nevertheless since the maximum density values are larger than ρ_{IN} , these structures are in an invalid range of our model since the nematic order parameter, cf. Eqs. (8.1), has been neglected in the moment expansion. The secondary instability needs the spatial degrees of freedom, which can be seen by the following investigation: if one restricts the numerics to just two modes, namely to the critical wavenumber k_c and to $2k_c$ for reasons of amplitude saturation, the instability is suppressed. A second observation is that the tendency of getting secondary unstable is diminished, i.e. the amplitude expansion is valid for higher values of ε , if the distance from the density demixing instability threshold ρ_d , cf. the solid line in Fig. 10.1, is increased. Thus the instability may be caused by the conserved density mode which is always present in the system and becomes only weakly damped near the demixing instability border ρ_d . The fact that conservation laws modify the stability of both stationary and oscillatory patterns has been addressed quite recently [134, 135, 136, 137].

In addition to the validity range with respect to ε , one may also confirm numerically the stability of the nonlinear solutions as predicted in Fig. 10.1 by the weakly nonlinear analysis. As an example, we started with a square solution as shown in Fig. 10.4a) at the point $\alpha = 21$ and $D_r = 0.15$ in parameter space (and $\varepsilon = 5 \cdot 10^{-4}$) belonging according to Fig. 10.1 to the region of stable stripe patterns. After a slight perturbation, the simulated temporal evolution in Fig. 10.4c) shows that only one of the initially equal amplitudes remains finite in the long time limit leading to the predicted stationary stripe pattern displayed in Fig. 10.4b). By several numerical runs we confirmed the analytically predicted stability diagrams in Figs. 10.1 and 10.2.

In the parameter range of stable asters, a vector plot of the orientation field superposed on the color coded filament density is presented in Fig. 10.5. The filament orientation is indicated by the arrows, the length being a measure of the degree of orientation. The density is high in the bright regions and low in the dark ones. At the right hand side of the simulation picture in Fig. 10.5, one can spot an aster with arrows pointing radially from a center with lowered filament density opposing to an inverse aster top left with arrows pointing radially into the center (we remind the reader that periodic boundary conditions are imposed).

The fact that the centers of the asters have lowered filament densities can be explained by the nonlinear analysis: in the derivation of the amplitude equations in section 10.1.2 one can clearly see that the growing amplitudes of the orientation modulations excite higher density modes - which then limit the orientation amplitudes to render the system stable - and therefore in the center of an aster, where the orientation vanishes, there is no need for a high density. Both the density and the degree of orientation reach their maximum in between the asters and two saddle-like structures building up a square with the two opposing aster centers complete the repetitive structure of this pattern near threshold found in the filament-motor system.

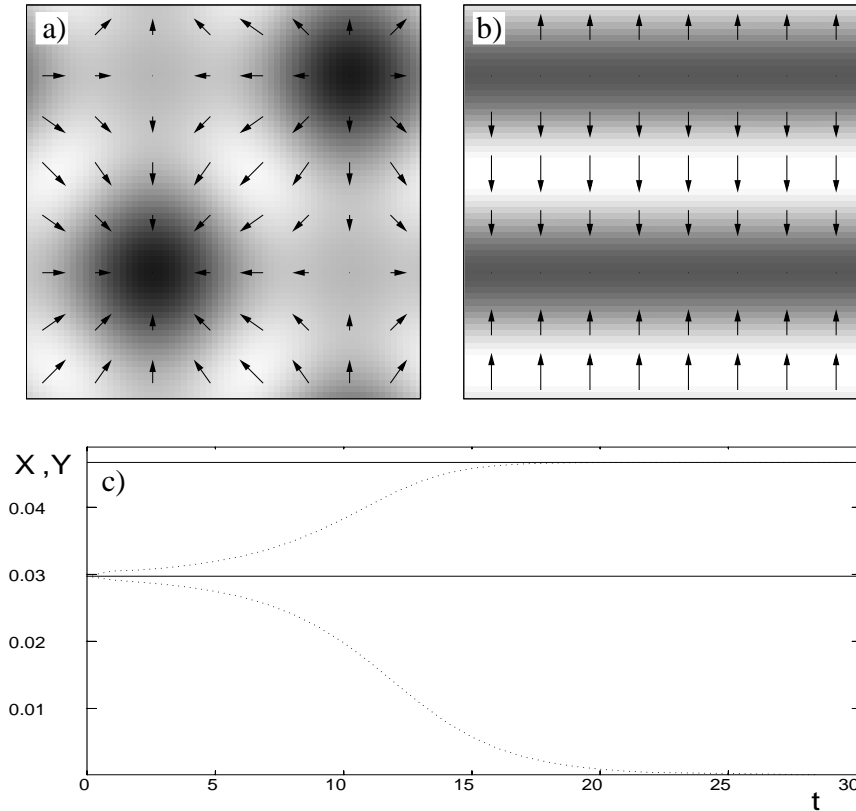


Figure 10.4: A simulation scenario is shown which numerically confirms the predictions of our weakly nonlinear analysis. We started with the aster (square pattern) displayed in a) with the analytically calculated amplitude described by Eq. (10.38) at a point in parameter space where stripes should be preferred according to Fig. 10.1, namely at $\alpha = 21$ and $D_r = 0.15$ (and $\varepsilon = 5 \cdot 10^{-4}$). Part c) shows the temporal evolution of the amplitudes X and Y of the orientation components t_x and t_y as the dotted lines. One can clearly see that one of the two modes building up the square pattern is damped and that the other mode grows to the analytically predicted value described by Eq. (10.37) and displayed as the upper solid line. Part b) shows the final stripe pattern.

10.4 Comparison to experiments

In this section we compare the results of our model analysis to the in vitro experiments. Taking intermediate parameter values, namely $\alpha \simeq 20$ and $D_r \simeq 0.3$, the critical wavenumber of the periodic modulation in scaled units is $k_c \simeq 1.5$ leading for filaments with a mean length of $5\mu\text{m}$ to a wavelength of $20\mu\text{m}$, which lies within the experimental range. The motor contribution for a microtubule-kinesin mixture can be estimated [120] and lies about $\alpha L \simeq 1.2 \cdot 10^{-12} \text{m}^2 \text{s}^{-1}$, while filament diffusion is of the order $10^{-13} - 10^{-15} \text{m}^2 \text{s}^{-1}$, depending on the filament length. Hence values of the scaled parameter $\alpha' = \frac{\alpha L}{D_{\parallel}} \approx 20$ as used

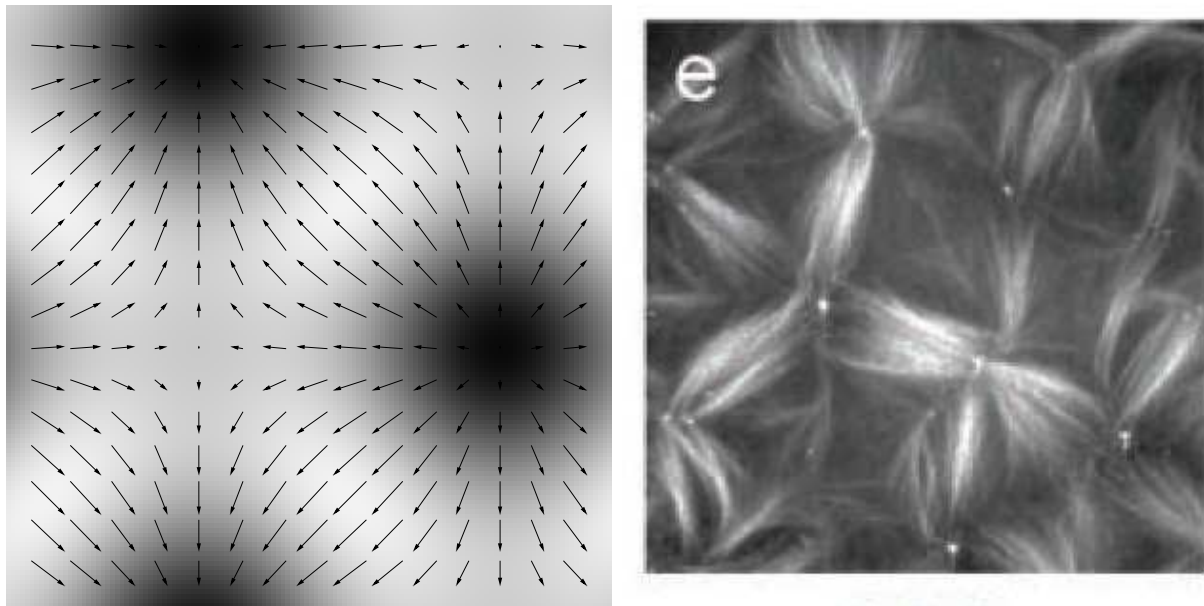


Figure 10.5: Left: A simulation of Eqs. (8.4) in the range of stable stationary asters is shown as a superposed plot of the orientation field (arrows) and the filament density (dark color coding low density, light color high density). Parameters are $\alpha = 21$, $D_r = 0.5$, $\varepsilon = 5 \cdot 10^{-5}$. Right: experimental pattern obtained in the presence of two motor species. This lattice of interconnected poles resembles more the structures obtained by us than the aster patterns shown in Fig. 6.1. Taken from Ref. [33].

by us are sensible. Since even higher values of α are possible, also the density instability, which occurs for all D_r if α is large enough, may be relevant in experiments. It will be discussed in chapter 12.

For any comparison between the weakly nonlinear behavior of the filament density and orientational patterns as described in this work and the experimentally observed inhomogeneous filament distributions, one has to bear in mind the following fundamental difference. In our work the modulation amplitudes around the homogeneous filament density as well as the emerging modulation of orientation are small and periodic and the generic patterns in this situation can only be stripes, squares or hexagons [42], leading to a discrete rotational symmetry of the aster pattern. In the experiments however, the modulation amplitudes are rather strong, the pattern is irregular and most structures have a local continuous rotational symmetry. The reason for this is simply that our analysis corresponds to the weakly nonlinear regime immediately above the threshold of the pattern forming instability, while the experiments correspond to the strongly nonlinear regime far beyond threshold. For the strong modulations as in the experiments, where both motors and filaments accumulate in the aster centers and the regions in between the asters are nearly depleted, it is not surprising that the pattern is not regular anymore and that the restriction to the simple

patterns possible at threshold is not valid anymore. In spite of this however, from models and experiments on pattern formation in driven fluid systems [42], there are well known examples that the small amplitude expansion captures the qualitative behavior of patterns in a considerable range beyond threshold.

With regard to this experience with other systems it is reasonable to compare the stability trends suggested by the phase diagrams presented in Fig. 10.1 and Fig. 10.2 to experimental results as described in Refs. [37, 31, 32]. The patterns occurring there in unconfined geometries for increasing motor concentration, are vortices, mixtures of asters and vortices, asters and finally bundles of microtubules for very high motor densities. The last step, the transition from asters to bundles, is in agreement with our calculations visualized in Fig. 10.1, where for increasing values of α , which is proportional to the (homogeneous) density of motors, a transition from asters to stripes takes place.

The lattice of asters, as shown in the left part of Fig. 10.5, is however different from the aster patterns found in the single-motor experiments [31] with microtubules and kinesin oligomers. While in the experiments only asters with a defined direction occurred, namely for a plus end-directed motor asters with the plus ends pointing inwards, the model predicts a periodic lattice of asters which alternately have filament orientations pointing inwards and outwards, cf. the discussion of Fig. 10.5 in the last section. The reason for this is that we have omitted in the present analysis the polarity sorting contributions proportional to β in Eqs. (8.4). Thus the model equations have $\pm\mathbf{t}$ -symmetry and do not discern the differently oriented asters. Though we have allowed for a nonvanishing orientation field \mathbf{t} in the coarse-graining process that resulted in Eqs. (8.4), the motor interaction proportional to α is not polar. Thus one could imagine that one is in the case where both plus and minus end directed motors are involved. Indeed such experiments in Ref. [33] yielded patterns of interconnected poles that are highly reminiscent to the patterns obtained by the model, cf. Fig. 10.5.

To describe asters of a single orientation in the presence of a single kind of motors, we should analyze the model in the presence of the polarity sorting contributions. If these are accounted for, the finite wavelength instability is rendered oscillatory, cf. the next chapter, and is not a candidate for asters. However, the density demixing instability in the presence of polarity sorting is still a stationary instability and also allows for aster-like patterns as is analyzed in chapter 12.

We did not find vortices. This may be due to the fact that at lower motor concentration the spatial variations of the motor density may become a relevant dynamical degree of freedom that has to be taken into account in the modeling, cf. Ref. [138]. A second possibility could be the inclusion of the first order term in the active angular velocity, namely the one proportional to ω_1 in Eq. (7.31). This term allows for a state of homogeneous polar orientation [123, 124] wherein vortices and asters may be found as defect structures, similar as in the model proposed in Ref. [128].

Chapter 11

Oscillatory patterns: coupled density-orientation waves

The oscillatory orientational instability in the case with polarity sorting, i.e. with $\beta \neq 0$, has already been discussed in section 9.4. The unstable modes correspond to a pair of complex eigenvalues, $\sigma = \lambda \pm i\omega$, with growth rate, cf. Eqs. (9.33) and (9.39),

$$\lambda = \frac{1}{2} \left[-D_r - \left(\frac{3D+5}{4} + \frac{1+D}{\pi} \rho_0 - \frac{7}{96} \alpha \rho_0 \right) k^2 - \frac{151}{46080} \alpha \rho_0 k^4 \right] \quad (11.1)$$

and frequency

$$\omega_c = \sqrt{-(\bar{\mathcal{L}}_{22}^{(0)})^2 - \bar{\mathcal{L}}_{12}^{(0)} \bar{\mathcal{L}}_{21}^{(0)}} \Big|_{\rho_c, k_c} . \quad (11.2)$$

The frequency ω_c is finite if β exceeds some small critical value, cf. Fig. 9.8. In that case the unstable modes give rise to a Hopf bifurcation.

Beyond an oscillatory instability it is well known from a number of physical, chemical and biological systems that the nonlinear behavior is quite different from stationary patterns [42, 139]. Thus in this chapter I will derive from the continuum equations (8.4) the amplitude equations for the oscillatory case. In one spatial dimension this is known to be the *complex Ginzburg-Landau equation* [139], describing a traveling wave (TW) solution. The general case comprises two coupled equations for waves traveling to the right and to the left respectively, which will also allow for a standing wave (SW) solution by nonlinear superposition. I derive the respective equations in some detail in section 11.1.2 and discuss the existence and stability of both types of solutions in section 11.1.3.

Since the oscillatory solution is more prone to subcritical bifurcations than had been the case for the stationary instability, we briefly discuss the effects of higher order (namely third order) excluded volume interaction in section 11.2. These contributions indeed increase the region of supercritical bifurcations, where the Ginzburg-Landau description directly applies. In section 11.3, the influence of the polarity sorting parameter β is discussed, leading to the conclusion that for not too low values of this parameter, its influence on the

nonlinear behavior is only minute. Again some numerical tests have been made to check the validity of the amplitude expansion, as described in section 11.4.

In two spatial dimensions we derive in section 11.5.1 four coupled amplitude equations, for left and right TW solutions in two arbitrary perpendicular directions. The detailed structure of the equations is motivated, but the derivation, made with the help of a computer algebra system, is not shown in detail since the procedure is fully analogous to the one-dimensional case and the technical details give no additional insights. The stability diagrams obtained from the semianalytical treatment are shown and analyzed in section 11.5.2. In the two-dimensional system, possible nonlinear superpositions like standing waves (SW), standing squares (SSq) and traveling squares (TSq) are unstable. There is however competition between traveling waves, i.e. one-dimensional waves propagating through the two-dimensional system, and alternating waves (AW), which are truly two-dimensional solutions, namely standing waves with a phase shift of π in the two perpendicular directions. The spatiotemporal behavior of the AW solution can be understood best by the pictures shown in section 11.5.3, obtained by numerical simulation of the basic equations (8.4).

11.1 Weakly nonlinear analysis in one dimension

If we project the orientation vector \mathbf{t} on the x -axis this implies a vanishing t_y and thus $\mathbf{t} = |\mathbf{t}| = t_x$. The orientation field can then point either in $+$ or in $-x$ -direction, whereby the modulus may be spatially varying. The rotational diffusion contribution, $-D_r t_x$, may be interpreted as spontaneous changes or "flips" of the filament orientation from $+$ to $-x$ -direction or vice versa at a rate D_r .

11.1.1 Amplitude equations

Instead of the stationary ansatz of Eq. (10.14), which in one dimension simply reads

$$\mathbf{w}_1 = \begin{pmatrix} \rho_1 \\ t_1 \end{pmatrix} = \begin{pmatrix} 0 \\ X \end{pmatrix} e^{ik_c x} + c.c., \quad (11.3)$$

one has now to allow for waves traveling to the positive and negative x -direction

$$\mathbf{w}_1 = \begin{pmatrix} \rho_1 \\ t_1 \end{pmatrix} = \begin{pmatrix} E_- \\ 1 \end{pmatrix} X_r e^{i(k_c^\beta x - \omega_c t)} + \begin{pmatrix} E_+ \\ 1 \end{pmatrix} X_l e^{i(k_c^\beta x + \omega_c t)} + c.c., \quad (11.4)$$

with $c.c.$ again denoting the complex conjugate and X_r and X_l the amplitudes of waves traveling to the right and to the left respectively. In addition, the linear mode is not purely orientational anymore, as has been the case in the stationary instability, but it is now a coupled density-orientation mode. This is due to the β -contributions in the linear operator and is reflected in Eq. (11.4) by the eigenvectors $(E_-, 1)^T$ and $(E_+, 1)^T$ of the unstable

eigenvalue pair $\sigma_{1,2} = \lambda \pm i\omega$. The critical wavenumber and frequency have been given in Eq. (9.36),

$$k_c^\beta = \left(\frac{2D_r}{d\alpha\rho_c} \right)^{1/4}, \quad (11.5)$$

and in Eq. (11.2) and the threshold value of the filament density, ρ_c^β , according to Eq. (9.35) reads

$$\rho_c^\beta = \frac{(D_r d + ac)\alpha - ab + \sqrt{D_r d \alpha [(D_r d + 2ac)\alpha - 2ab]}}{b^2 - 2bc\alpha + c^2\alpha^2}, \quad (11.6)$$

with the abbreviations $a = \frac{3D+5}{4}$, $b = \frac{1+D}{\pi}$, $c = \frac{7}{96}$ and $d = \frac{151}{23040}$. In the following I will omit the superscript β on k_c^β and ρ_c^β to simplify notation.

If again a multiscale expansion is performed in the neighborhood of the threshold by using the small parameter

$$\varepsilon = \frac{\rho_0 - \rho_c}{\rho_c}, \quad (11.7)$$

two generic amplitude equations for the two amplitudes X_r and X_l of the right- and left-traveling waves respectively are obtained [43, 42], namely

$$\tau_0 \partial_T X_r = \varepsilon(1 + ib)X_r - (g_1 + ic_1)|X_r|^2 X_r - (g_2 + ic_2)|X_l|^2 X_r, \quad (11.8a)$$

$$\tau_0 \partial_T X_l = \varepsilon(1 + ib)X_l - (g_1 + ic_1)|X_l|^2 X_l - (g_2 + ic_2)|X_r|^2 X_l. \quad (11.8b)$$

In contrast to Eqs. (10.13), the coefficients are now complex. Thus Eqs. (11.8) are referred to as a system of coupled *Complex Ginzburg-Landau Equations*.

Here I consider again only the simplest case, i.e. only traveling waves that are restricted to the critical wavenumber k_c . This neglects two terms usually encountered in Eqs. (11.8), a linear group velocity term $\pm v_g \partial_x X_{r/l}$ and a term associated with a coherence length $(1 + ic_0)\xi_0^2 \partial_x^2 X_{r/l}$. These terms allow in some parameter range waves with wavenumbers slightly different from k_c to be stable, which is however a higher order problem if considering the analysis of a complicated model like Eqs. (8.4). Both terms being linear, they can be extracted from the linear instability spectrum [42].

11.1.2 Derivation of the amplitude equations

The procedure to obtain the coupled amplitude equations (11.8) is similar as in the stationary case, but slightly more involved due to the linear coupling of the density and the orientation, as can be seen by the need for the eigenvectors in the ansatz, Eq. (11.4). To obtain an equation for the amplitude of e.g. the right-traveling coupled density-orientation mode, in the last step of the derivation the vectorial equation has to be projected on a single equation by use of the left eigenvector corresponding to $(E_-, 1)^T$.

The equation we have to solve is of the form

$$\partial_t \mathbf{w} = \bar{\mathcal{L}}_0 \mathbf{w} + \mathbf{N}(\rho, t_x) , \quad (11.9)$$

with the nonlinear operator

$$\mathbf{N}(\rho, t_x) = \begin{pmatrix} \mathcal{N}_\rho(\rho, t_x) \\ \mathcal{N}_t(\rho, t_x) \end{pmatrix} . \quad (11.10)$$

The linear operator is defined by the reduced Eqs. (9.30) and the nonlinear operator \mathbf{N} includes all the nonlinear terms with respect to $\tilde{\rho}$ and t_x on the right hand sides of Eqs. (8.4) where the contributions from both t_y and ∂_y have been omitted, cf. below.

While there are fast oscillations of the overall pattern with the critical frequency ω_c , the dynamics of the *envelope* of the linear solution in Eq. (9.33) is slow close to threshold and accordingly a slow time scale

$$T = \varepsilon t \quad (11.11)$$

can again be introduced. However, the time derivatives can not be replaced like $\partial_t \rightarrow \varepsilon \partial_T$ as has been done in Eq. (10.19) for the stationary case, but the fast oscillations must be accounted for by

$$\partial_t \rightarrow \partial_t + \varepsilon \partial_T , \quad (11.12)$$

since they lead to terms $\propto i\omega_c$ upon action on the ansatz, Eq. (11.4).

The solution \mathbf{w} is again expanded with respect to powers of $\varepsilon^{1/2}$

$$\mathbf{w} = \varepsilon^{1/2} \mathbf{w}_1 + \varepsilon \mathbf{w}_2 + \varepsilon^{3/2} \mathbf{w}_3 + \dots , \quad (11.13)$$

with \mathbf{w}_1 as in Eq. (11.4), as are the nonlinearities

$$\mathbf{N} = \varepsilon \mathbf{N}_1 + \varepsilon^{3/2} \mathbf{N}_2 + \dots . \quad (11.14)$$

Sorting the contributions to Eq. (11.9) with respect to powers of ε , one gets the following hierarchy of equations

$$\varepsilon^{1/2} : \bar{\mathcal{L}}_t \mathbf{w}_1 = 0 , \quad (11.15a)$$

$$\varepsilon : \bar{\mathcal{L}}_t \mathbf{w}_2 = \begin{pmatrix} \mathcal{N}_\rho^1 \\ \mathcal{N}_t^1 \end{pmatrix} , \quad (11.15b)$$

$$\varepsilon^{3/2} : \bar{\mathcal{L}}_t \mathbf{w}_3 = -\partial_T \mathbf{w}_1 + \bar{\mathcal{L}}_2 \mathbf{w}_1 + \begin{pmatrix} \mathcal{N}_\rho^2 \\ \mathcal{N}_t^2 \end{pmatrix} , \quad (11.15c)$$

where I have introduced the linear operator $\bar{\mathcal{L}}_t$ defined as

$$\bar{\mathcal{L}}_t = \mathcal{I} \partial_t - \bar{\mathcal{L}}_0 . \quad (11.16)$$

I should mention that since $\bar{\mathcal{L}}_0$ is contained in $\bar{\mathcal{L}}_t$ with a minus sign, the signs on the right hand sides of Eqs. (11.15) are the opposite of those appearing in the stationary hierarchy, Eqs. (10.22).

One should recognize two main differences between this hierarchy and Eqs. (10.22) for the stationary case: first, instead of a stationary linear operator, $\bar{\mathcal{L}}_0$, now one has to deal with $\bar{\mathcal{L}}_t$, which via the fast time derivative ∂_t introduces the critical frequency $i\omega_c$ in all orders of ε . This is the reason for the coefficients in the amplitude equations (11.8) becoming complex valued. Second, since the unstable mode now is a coupled density-orientation mode, nonlinearities come into play in both components of the vector equation already in Eq.(11.15b), i.e. at the order ε .

As in the stationary case, the equation of order $\varepsilon^{1/2}$, Eq. (11.15a), is solved already by our ansatz Eq. (11.4). Thus one can proceed by solving the next order, the inhomogeneous Eq. (11.15b), for \mathbf{w}_2 . If this solution is obtained, upon insertion of \mathbf{w}_1 and \mathbf{w}_2 into the right hand side of Eq. (11.15c), one has again an inhomogeneous equation to solve. As before, to obtain an equation e.g. for X_r , one is not obliged to solve this equation, but only has to collect all terms that are resonantly forcing the wave traveling to the right, i.e. those $\propto e^{i(k_c x - \omega_c t)}$, which have to vanish due to Fredholm's alternative. The respective vectorial equation has to be projected and one finally obtains a single equation for X_r . In the next section I show how the left eigensystem of $\bar{\mathcal{L}}_t$ can be used for this purpose.

Right and left eigenvectors

We have now to consider the full, time-dependent linear operator

$$\bar{\mathcal{L}}_t = \mathcal{I}\partial_t - \bar{\mathcal{L}}_0 , \quad (11.17)$$

with \mathcal{I} the identity, and to look for the zero-eigenvalues. At threshold, where the real part λ of the growth rate vanishes, the stationary operator $\bar{\mathcal{L}}_0$ has the eigenvalues $\pm i\omega_c$. Thus we can construct two zero eigenvalues of $\bar{\mathcal{L}}_t$ with two different (right) eigenvectors, namely

$$\begin{pmatrix} E_- \\ 1 \end{pmatrix} e^{i(k_c x - \omega_c t)} \quad \text{and} \quad \begin{pmatrix} E_+ \\ 1 \end{pmatrix} e^{i(k_c x + \omega_c t)} , \quad (11.18)$$

$$(11.19)$$

with the definitions

$$E_- = - (\bar{\mathcal{L}}_{21}^{(0)})^{-1} \left(\bar{\mathcal{L}}_{22}^{(0)} + i\omega_c \right) \Big|_{\rho_c, k_c} , \quad (11.20)$$

$$E_+ = - (\bar{\mathcal{L}}_{21}^{(0)})^{-1} \left(\bar{\mathcal{L}}_{22}^{(0)} - i\omega_c \right) \Big|_{\rho_c, k_c} . \quad (11.21)$$

To motivate this let's consider the action of $\bar{\mathcal{L}}_t$ on a wave solution traveling to the right, i.e. $\propto e^{i(k_c x - \omega_c t)}$, which transforms the former operator into the matrix

$$\begin{pmatrix} -i\omega_c - \bar{\mathcal{L}}_{11}^{(0)} & -\bar{\mathcal{L}}_{12}^{(0)} \\ -\bar{\mathcal{L}}_{21}^{(0)} & -i\omega_c - \bar{\mathcal{L}}_{22}^{(0)} \end{pmatrix} , \quad (11.22)$$

with the elements of the linear operator again evaluated at threshold, i.e. at (ρ_c, k_c) . Multiplying this matrix from the right by a vector $(E_-, 1)^T$ leads to the equations

$$\begin{aligned} (-i\omega_c - \bar{\mathcal{L}}_{11}^{(0)})E_- - \bar{\mathcal{L}}_{12}^{(0)} &= 0, \\ -\bar{\mathcal{L}}_{21}^{(0)}E_- - i\omega_c - \bar{\mathcal{L}}_{22}^{(0)} &= 0, \end{aligned} \quad (11.23)$$

where the latter has been used to define E_- in Eq. (11.20). It can however easily be shown that a definition arising from the first equation yields the same. Similarly, a left eigenvector can be obtained by multiplying the matrix from the left by a vector $(1, F_-)$, leading e.g. to $(-i\omega_c - \bar{\mathcal{L}}_{11}^{(0)}) - \bar{\mathcal{L}}_{21}^{(0)}F_- = 0$ and implying

$$F_- = -(\bar{\mathcal{L}}_{21}^{(0)})^{-1} \left(\bar{\mathcal{L}}_{11}^{(0)} + i\omega_c \right) \Big|_{\rho_c, k_c}. \quad (11.24)$$

Fully analogously, by looking on the action of $\bar{\mathcal{L}}_t$ on a solution $\propto e^{i(k_c x + \omega_c t)}$ one gets the right-eigenvector $(E_+, 1)^T$ with E_+ as defined above and the left-eigenvector $(1, F_+)$ with

$$F_+ = -(\bar{\mathcal{L}}_{21}^{(0)})^{-1} \left(\bar{\mathcal{L}}_{11}^{(0)} - i\omega_c \right) \Big|_{\rho_c, k_c}. \quad (11.25)$$

I should also mention two useful relations. First, the diagonal elements of $\bar{\mathcal{L}}^{(0)}$, namely $\bar{\mathcal{L}}_{11}^{(0)}$ and $\bar{\mathcal{L}}_{22}^{(0)}$, are real since they arise from even spatial derivatives, while the outer diagonal elements, $\bar{\mathcal{L}}_{21}^{(0)}$ and $\bar{\mathcal{L}}_{12}^{(0)}$, are purely imaginary since they come from odd spatial derivatives, cf. Eqs. (9.30) and (9.27). Thus for the special structure of our model follows that

$$(E_-)^* = \left(-(\bar{\mathcal{L}}_{21}^{(0)})^{-1} \left(\bar{\mathcal{L}}_{22}^{(0)} + i\omega_c \right) \Big|_{\rho_c, k_c} \right)^* = (\bar{\mathcal{L}}_{21}^{(0)})^{-1} \left(\bar{\mathcal{L}}_{22}^{(0)} - i\omega_c \right) \Big|_{\rho_c, k_c} = -E_+ \quad (11.26)$$

holds. Second, it is a generic situation that the right and the left eigenvectors of the two different eigenvalues are orthogonal. This can be easily seen, exemplarily

$$(1, F_+) \begin{pmatrix} E_- \\ 1 \end{pmatrix} = E_- + F_+ \quad (11.27)$$

$$= -(\bar{\mathcal{L}}_{21}^{(0)})^{-1} \left(\bar{\mathcal{L}}_{22}^{(0)} + i\omega_c \right) - (\bar{\mathcal{L}}_{21}^{(0)})^{-1} \left(\bar{\mathcal{L}}_{11}^{(0)} - i\omega_c \right) \Big|_{\rho_c, k_c} = 0, \quad (11.28)$$

with use of the fact that at threshold $\lambda = \frac{1}{2}(\bar{\mathcal{L}}_{11}^{(0)} + \bar{\mathcal{L}}_{22}^{(0)}) = 0$ holds, implying $\bar{\mathcal{L}}_{11}^{(0)} = -\bar{\mathcal{L}}_{22}^{(0)}$.

Solving the hierarchy

Now we are prepared to extract the amplitude equations (11.8) from the hierarchy given by Eqs. (11.15). First we have to solve Eq. (11.15b),

$$\bar{\mathcal{L}}_t \mathbf{w}_2 = \begin{pmatrix} \mathcal{N}_\rho^1(\rho_1, t_{1x}) \\ \mathcal{N}_t^1(\rho_1, t_{1x}) \end{pmatrix}, \quad (11.29)$$

where

$$\begin{aligned} \mathcal{N}_\rho^1(\rho, t_x) = & \left(\frac{1+D}{\pi} - \frac{\alpha}{24} \right) \partial_x (\rho \partial_x \rho) - \frac{3\alpha}{48} \partial_x (t_x \partial_x t_x) \\ & - \frac{\alpha}{C_1} \left[38 \partial_x (\rho \partial_x^3 \rho) + 75 \partial_x (t_x \partial_x^3 t_x) \right] - \frac{\beta}{96} \frac{5}{2} \partial_x [\rho \partial_x^2 t_x - t_x \partial_x^2 \rho] \end{aligned} \quad (11.30)$$

and

$$\begin{aligned} \mathcal{N}_t^1(\rho, t_x) = & \frac{3-D}{2\pi} \partial_x (t_x \partial_x \rho) - \frac{\alpha}{96} \partial_x \left[5 t_x \partial_x \rho + 3 \rho \partial_x t_x \right] \\ & - \frac{\alpha}{2C_1} \partial_x \left[75 \rho \partial_x^3 t_x + 108 t_x \partial_x^3 \rho \right] \\ & + \frac{\beta}{2} \partial_x \left[\frac{1}{2} \rho^2 - t_x^2 \right] + \frac{\beta}{96} \partial_x \left[\frac{5}{4} \rho \partial_x^2 \rho - 3 t_x \partial_x^2 t_x \right]. \end{aligned} \quad (11.31)$$

These nonlinearities yield in the order $\mathcal{O}(\varepsilon)$ contributions of the form (with $*$ = ρ, t_x)

$$\begin{aligned} \mathcal{N}_*^1 = & N_{*1}^1 X_r^2 e^{2i(k_c x - \omega_c t)} + N_{*2}^1 X_l^2 e^{2i(k_c x + \omega_c t)} \\ & + N_{*3}^1 X_r X_l e^{2ik_c x} + c.c. , \end{aligned} \quad (11.32)$$

which naturally leads us to the ansatz

$$\begin{aligned} \mathbf{w}_2 = & \begin{pmatrix} A_{\rho 1} \\ A_{t 1} \end{pmatrix} X_r^2 e^{2i(k_c x - \omega_c t)} + \begin{pmatrix} A_{\rho 2} \\ A_{t 2} \end{pmatrix} X_l^2 e^{2i(k_c x + \omega_c t)} \\ & + \begin{pmatrix} A_{\rho 3} \\ A_{t 3} \end{pmatrix} X_r X_l e^{2ik_c x} + c.c. . \end{aligned} \quad (11.33)$$

The various coefficients of \mathbf{w}_2 can be determined by inverting the linear operator in Eq. (11.29) yielding

$$\begin{aligned} \begin{pmatrix} A_{\rho 1} \\ A_{t 1} \end{pmatrix} &= \left(\bar{\mathcal{L}}_t \Big|_{2k_c, -2\omega_c} \right)^{-1} \begin{pmatrix} N_{\rho 21} \\ N_{t 21} \end{pmatrix}, \\ \begin{pmatrix} A_{\rho 2} \\ A_{t 2} \end{pmatrix} &= \left(\bar{\mathcal{L}}_t \Big|_{2k_c, +2\omega_c} \right)^{-1} \begin{pmatrix} N_{\rho 22} \\ N_{t 22} \end{pmatrix}, \\ \begin{pmatrix} A_{\rho 3} \\ A_{t 3} \end{pmatrix} &= \left(\bar{\mathcal{L}}_t \Big|_{2k_c, \omega=0} \right)^{-1} \begin{pmatrix} N_{\rho 23} \\ N_{t 23} \end{pmatrix}, \end{aligned} \quad (11.34)$$

where e.g. $\bar{\mathcal{L}}_t \Big|_{2k_c, -2\omega_c}$ has to be read as the Fourier transformed linear operator evaluated at $k = 2k_c$ and $\omega = -2\omega_c$.

Now we put \mathbf{w}_1 and \mathbf{w}_2 into Eq. (11.15c),

$$\bar{\mathcal{L}}_t \mathbf{w}_3 = -\partial_T \mathbf{w}_1 + \bar{\mathcal{L}}_2 \mathbf{w}_1 + \begin{pmatrix} \mathcal{N}_\rho^2(\rho_1, \rho_2, t_{1x}, t_{2x}) \\ \mathcal{N}_t^2(\rho_1, \rho_2, t_{1x}, t_{2x}) \end{pmatrix}, \quad (11.35)$$

where the components of the nonlinear operator read

$$\begin{aligned}\mathcal{N}_\rho^2(\rho_1, \rho_2, t_{1x}, t_{2x}) &= \mathcal{N}_\rho^1(\rho_2, t_{1x}) + \mathcal{N}_\rho^1(\rho_1, t_{2x}), \\ \mathcal{N}_t^2(\rho_1, \rho_2, t_{1x}, t_{2x}) &= \mathcal{N}_t^1(\rho_2, t_{1x}) + \mathcal{N}_t^1(\rho_1, t_{2x}).\end{aligned}\quad (11.36)$$

As already discussed, it is sufficient to collect the resonantly forcing terms, namely those $\propto e^{i(k_c x - \omega_c t)}$ for the equation of X_r . Then we project on X_r by multiplying with $(1, F_-)$ leading us to the solvability condition

$$\begin{aligned}0 &= -(E_- + F_-)\partial_T X_r + (1, F_-)\bar{\mathcal{L}}_2|_{k_c, -\omega_c} \begin{pmatrix} E_- \\ 1 \end{pmatrix} X_r \\ &\quad + \int dx (1, F_-) \begin{pmatrix} \mathcal{N}_\rho^2 \\ \mathcal{N}_t^2 \end{pmatrix} e^{-i(k_c x - \omega_c t)},\end{aligned}\quad (11.37)$$

where the integral in the third term picks out the resonant contributions in the nonlinear operators.

From the structure of \mathbf{w}_2 , Eq. (11.33), which comprises terms proportional to

$$X_r^2 e^{2i(k_c x - \omega_c t)} + c.c., \quad X_l^2 e^{2i(k_c x + \omega_c t)} + c.c. \quad \text{and} \quad X_r X_l e^{2ik_c x} + c.c.,$$

the nonlinearities in $\mathcal{O}(\varepsilon^{3/2})$, \mathcal{N}_ρ^2 and \mathcal{N}_t^2 , yield the two resonant contributions

$$X_r^2 e^{2i(k_c x - \omega_c t)} X_r^* e^{-i(k_c x - \omega_c t)} \quad \text{and} \quad X_r X_l e^{2ik_c x} X_l^* e^{-i(k_c x + \omega_c t)}.$$

Thus the solvability condition has the form

$$\tau' \partial_T X_r = (a' + ib')X_r + (g'_1 + ic'_1)|X_r|^2 X_r + (g'_2 + ic'_2)|X_l|^2 X_r \quad (11.38)$$

and we obtain the first amplitude equation of Eqs. (11.8),

$$\tau_0 \partial_T X_r = \varepsilon(1 + ib)X_r - (g_1 + ic_1)|X_r|^2 X_r - (g_2 + ic_2)|X_l|^2 X_r, \quad (11.39)$$

by replacing $\tau_0 = \tau'/a'$, $b = b'/a'$, $g_i = -g'_i/a'$, $c_i = -c'_i/a'$ for $i = 1, 2$ and using $X_r \sim \varepsilon^{1/2}$. The signs of the real parts of the nonlinear coefficients have been chosen in such a way that $g_1 > 0$ corresponds to a forward bifurcation of a traveling wave.

11.1.3 Existence and stability of the nonlinear waves

Similar as in the stationary case, one can read from the amplitude equations (11.8) the existence and stability ranges for the patterns which are generic at threshold. Looking for stationary solutions, we put a single wave traveling to the right, i.e. $X_r = F e^{i\Omega T}$ and $X_l = 0$, into Eq. (11.8a) while Eq. (11.8b) is then trivially fulfilled. Separating

$$\tau_0 i \Omega F = \varepsilon(1 + ib)F - (g_1 + ic_1)F^2 F \quad (11.40)$$

into the real part and the imaginary part,

$$0 = \varepsilon - g_1 F^2, \quad (11.41)$$

$$\tau_0 \Omega = \varepsilon b - c_1 F^2 = \varepsilon \left(b - \frac{c_1}{g_1} \right), \quad (11.42)$$

these two equations define the amplitude $F = \sqrt{\varepsilon/g_1}$ and the frequency Ω of the nonlinear solution. Again $g_1 > 0$ is needed for the bifurcation to be supercritically or forward. Due to symmetry, a wave traveling to the left with $X_r = 0$ and $X_l = F e^{i\Omega T}$ is a second stationary oscillating solution.

Additionally a solution with equal amplitudes exists, corresponding to a standing wave (SW). This case is treated fully analogously by inserting $X_l = F e^{i\Omega T + \phi_r}$ and $X_l = F e^{i\Omega T + \phi_l}$ into Eqs. (11.8), leading to the amplitude and the frequency

$$F = \sqrt{\frac{\varepsilon}{g_1 + g_2}}, \quad \Omega = \tau_0^{-1} \varepsilon \left(b - \frac{c_1 + c_2}{g_1 + g_2} \right). \quad (11.43)$$

Obviously this solution exists for $g_1 + g_2 > 0$.

The stability of each solution in their respective regions of existence can again be easily established by looking at the temporal evolution of small deviations of the stationary oscillating solutions, e.g. for the case of the wave traveling to the right by $X_r = F e^{i\Omega T} + \delta x_r$ and $X_l = \delta x_l$. From the real parts $\text{Re}(\sigma)$ of the growth rates of $\delta x_r, \delta y_r \propto e^{\sigma t}$ one can then decide the stability. One gets that TW are stable if $g_2 > g_1 > 0$ holds for the coefficients of Eqs. (11.8) and that SW are stable in case of $|g_2| < g_1$.

As has been done in the stationary case, one can again relate the coefficients g_1 and g_2 of the amplitude equations to the parameters of the underlying continuum model, Eqs. (8.4), namely to D_r , α and β ¹. The resulting stability diagram is shown in Fig. 11.1. Our weakly nonlinear analysis is valid in the region between the two areas shaded in grey and describing the occurrence of the density instability (dark grey) and the homogeneous nematic transition (light grey). Traveling wave (TW) solutions exist to the right of the solid line, defined by $g_1 = 0$, while standing waves (SW) exist to the right of the dotted line, where $g_1 + g_2 = 0$ holds. If SW exist they are also stable, the line of exchange of stability, defined by $g_1 = g_2 > 0$, lying in the region where the nematic instability occurs. To the left of the solid line, TW bifurcate subcritically.

As discussed in detail in section 9.5.1, the influence of the polarity sorting parameter β on the nonlinear pattern selection is minute. Thus the stability borders in Fig. 11.1 change only by very small amounts if this parameter is varied.

As can be seen from the solid line in Fig. 11.1, the existence range of supercritical traveling waves is restricted to values of the rotational diffusion coefficient larger than $D_r \simeq 1$. Thus comparing it to the stationary case, cf. Fig. 10.1, where stationary stripes existed for values larger than $D_r \sim 0.15$, in the presence of polarity sorting there is a stronger tendency towards subcritical bifurcation behavior.

¹We use again $D = 1/2$, as discussed in section 9.5.2.

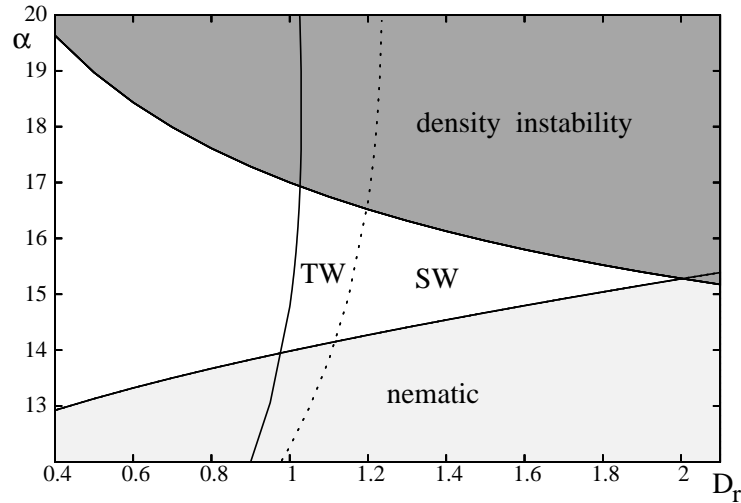


Figure 11.1: Stability diagram for the weakly nonlinear solutions of the oscillatory finite wavelength instability. The regions in dark and light grey correspond to the density instability and to the homogeneous nematic instability respectively, which are beyond the validity range of our expansion. Traveling waves (TW) exist at the right side of the solid line and standing waves (SW) to the right of the dotted one. If SW exist they are also stable. To the left of the solid line, TW bifurcate subcritically. The polarity sorting parameter has been chosen to be $\beta = 5$, larger values leading only to very small changes in the diagram, cf. Fig. 11.3.

11.2 Higher order excluded volume effects

In the mesoscopic filament-motor model, Eqs. (7.10-7.18), that has been the starting point to derive the continuum equations (8.4) now under investigation, all interactions have been restricted to filament pairs. In three spatial dimensions this is a sensible approximation for long rods, since contributions from higher order virials $\propto \Psi^3$, with Ψ the probability distribution function of the filaments, decrease at least like b/L , the ratio between the rod diameter and the rod length [81]. The main reason for this is that in three dimensions it is quite unlikely for three or more rods to overlap simultaneously, since to do so they have to be approximately in the same plane. Thus such higher order contributions are small, since only a tiny part of the configuration space contributes to them.

In two dimensions however, as considered here, this is not the case anymore: the rods are automatically in a planar configuration and thus three-particle contributions and even higher orders are not negligible [27].

Moreover, a consequence of the restriction to two-particle interaction is the fact that the continuum model has only quadratic nonlinear contributions, which is a case known to lead not necessarily to a saturation of the amplitudes. In contrast, the presence of a third order contribution with the right sign always restricts the amplitudes of patterns. Such

a term, as we have already met in the Cahn-Hilliard model introduced in section 3.3, is usually motivated by excluded volume interaction, i.e. high density deviations are punished since the particles need space.

We restrict ourselves here to higher order contributions to the passive excluded volume interaction, although accounting for higher order motor-mediated interactions could be a very delicate problem. However, for a situation to be relevant where three filaments intersect to form a triangle and motors are present in all intersection points one would need a really high motor density. Already for the excluded volume contribution, i.e. the third virial coefficient of a rod solution, the problem is very intricate, cf. Ref. [27]. However, to account for the rod-like shape of the filaments, one can use an approximation proposed in Ref. [81] which yields for the translational excluded volume part, cf. Eqs. (7.11a) and (8.26b), the following third order contribution

$$\partial_t \Psi \sim c_r D_{ij} \partial_i \left[\Psi(\mathbf{u}) \partial_j \int d\mathbf{u}' \int d\mathbf{u}'' \left(|\mathbf{u} \times \mathbf{u}'| + |\mathbf{u}' \times \mathbf{u}''| + |\mathbf{u}'' \times \mathbf{u}| \right) \Psi(\mathbf{u}') \Psi(\mathbf{u}'') \right], \quad (11.44)$$

with c_r as a phenomenological coefficient and D_{ij} the anisotropic diffusion matrix defined in Eq. (7.12). Performing the moment expansion as explained in sections 8.2.2 and 8.2.3, one gets the following additional contributions to the density and the orientation equation

$$\begin{aligned} \partial_t \rho &\sim c_r \frac{3(1+D)}{\pi} \partial_i (\delta \rho \partial_i \delta \rho^2) \quad , \\ \partial_t t_i &\sim c_r \frac{6(1-D)}{4\pi} \left[\partial_i (t_j \partial_j \delta \rho^2) + \partial_j (t_j \partial_i \delta \rho^2 + t_i \partial_j \delta \rho^2) \right] + c_r \frac{6D}{\pi} \partial_j (t_i \partial_j \delta \rho^2) . \end{aligned} \quad (11.45)$$

In the above expressions we have used density deviations from the mean value, $\delta \rho = \rho - \rho_0$, instead of ρ . If not, these terms would lead to a linear contribution $\propto \rho_0^2 \partial_x^2 \rho$ in the density equation and to an increase of the threshold for the density demixing instability, which makes no sense since Eq. (11.44) is assumed to be a higher order correction.

Looking at the weakly nonlinear analysis of the stationary orientational instability, the contributions from Eqs. (11.45) have no effect at threshold. This is due to the fact that the first order contribution in the density $\propto \varepsilon^{1/2}$ is zero, $\rho_1 = 0$, while the nonvanishing $\rho_2 \neq 0$ comes into play only in orders higher than those needed for the derivation of the amplitude equations. In contrast, in case of the oscillatory orientational instability, $\rho_1 \neq 0$ holds due to the linear coupling of the density and the orientation, and thus one gets a stabilizing effect.

However, the effect of the rod shape on the qualitative features of the higher order excluded volume is small. If the excluded volume is incorporated by totally ignoring the rod-like structure of the particles and adding the following contributions

$$\partial_t \rho \sim c(\partial_x^2 + \partial_y^2)(\delta \rho^3) \quad \text{and} \quad \partial_t t_i \sim 0 \quad , \quad (11.46)$$

with c another phenomenological parameter, one gets a stability diagram as shown in Fig. 11.2. There are no qualitative changes if one uses Eqs. (11.45) instead, if one adapts

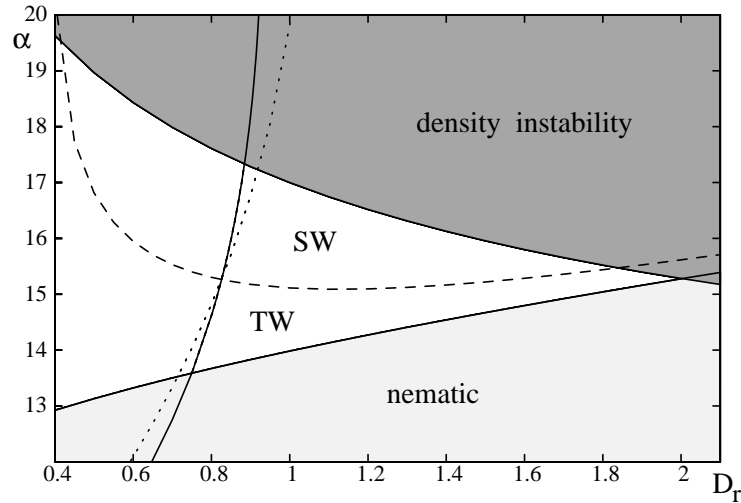


Figure 11.2: Stability diagram with third order excluded volume contributions taken into account. Again the regions in dark and light grey denote the density and homogeneous nematic instabilities. In between, traveling waves (TW, solid line) and standing waves (SW, dotted line) exist now in a larger range of D_r compared to the case without higher order excluded volume, cf. Fig. 11.1. The exchange of stability between TW and SW is shifted to the accessible α - D_r -range as shown by the dashed line, which is defined by $g_1 = g_2 > 0$. Parameters are $\beta = 5$, $c = 0.5$.

the values of c or c_r properly. Thus to catch the effects of the third order excluded volume interactions, we opt for the use of Eq. (11.46) to keep the description as simple as possible.

Fig. 11.2 can now be compared to the case without third order excluded volume as shown in Fig. 11.1. In the latter case the line of exchange of stability between traveling and standing waves, i.e. the line where $g_1 = g_2 > 0$ holds, lies deep in the region of the homogeneous nematic instability, where our weakly nonlinear expansion does not apply, and thus if SW exist, they are always stable. Taking the simple third order excluded volume contribution from Eqs. (11.46) into account with a rather small value of $c = 0.5$ (or the contribution approximately accounting for the rod-like shape from Eqs. (11.45) with an even smaller c_r) shifts the transition line, depicted as the dashed line in Fig. 11.2, into the region where the analysis applies. An even higher value shifts the dashed line into the region of the demixing instability, totally destabilizing the SW solutions, so that only TW are stable in that case. As a second effect, the range of supercritical wave patterns is slightly increased by the excluded volume term, as expected from the stabilizing effects of such a third order contribution.

The discussion of the third order excluded volume term may seem kind of artificial, however such a contribution is always present and most probably important in two dimensions already for quite low densities, due to the poor convergence of the virial expansion for rods [78, 81] in two dimensions. The following tendencies may therefore be important:

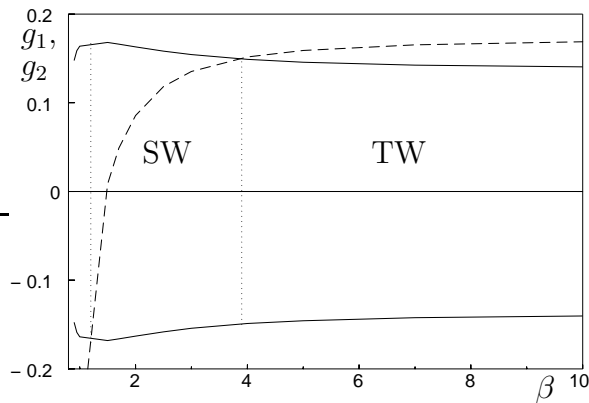


Figure 11.3: The dependence of the real parts of the nonlinear coefficients of Eqs. (11.8), g_1 (upper solid line) and g_2 (dashed line), on the polarity sorting parameter β . For large β there is only minute dependence. For small β however TW are becoming unstable versus SW and for very small β there are no stable solutions as g_2 becomes smaller than $-g_1$ (lower solid line). The parameters are $\alpha = 14.5$, $D_r = 1.2$ and $c = 0.5$.

For the oscillatory instability investigated here the third order excluded volume leads to a destabilization of SW in favor of TW. In the case of strong excluded volume effects, only TW are stable.

A side effect of the third order term is the improvement of numerical stability of the wave patterns, cf. section 11.4. Moreover, for the investigation of the demixing instability, cf. section 12, a third order term is definitely needed to guarantee a saturation of the pattern amplitudes, as usual for a Cahn-Hilliard-like instability, cf. section 3.3.

11.3 Nonlinear influence of the polarity sorting

Fig. 11.3 shows the influence of the polarity sorting parameter β on the nonlinear behavior, namely on the two nonlinear coefficients g_1 and g_2 occurring in the amplitude equations (11.8). One can see that for intermediate and high values of the polarity sorting parameter (for the parameters used to obtain the figure, approximately for $\beta > 4$), the influence is quite minute and that TW are preferred at the chosen point in parameter space. In contrast, for smaller β there is a dependence on β , namely with decreasing β an exchange of stability from TW to SW and ultimately a total destabilization of wave solutions, due to $g_2 < -g_1$.

One can estimate that β should be of the same order of magnitude as the instability-causing motor parameter α [40], which roughly lies in between 10-20 in dimensionless units and thus in the region where the detailed value of β is typically not important, cf. Fig. 11.3. However, one has to make a compromise: a high value of β leads to ineffective numerics, since one has to resolve the slow dynamics of the pattern, while ω_c becomes very large for large values of β , cf. Fig. 9.8, implying that one has to choose a high resolution in the time discretization to account for these fast oscillations. With regard to the phase dependence from section 9.5.1 and the nonlinear influence, i.e. from Figs. 9.7 and 11.3, we have chosen $\beta = 5$ as a sensible value working also well with the numerics. The analytical stability analysis pictures, cf. Figs. 11.1 and 11.2, have also been generated for this parameter value.

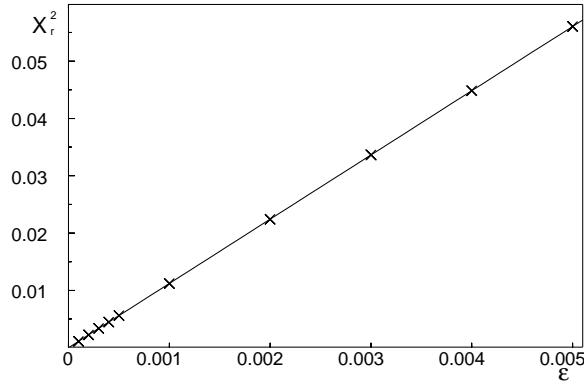


Figure 11.4: The oscillatory finite wavelength instability allows for stable traveling wave (TW) solutions. The squared amplitudes X_r^2 of a right-traveling wave observed numerically are shown as crosses and are compared to the analytical values from the amplitude expansion, Eq. (11.41), depicted as the solid line. The parameters are $\alpha = 14.5$, $\beta = 5$, $D_r = 1$, $c = 0.5$.

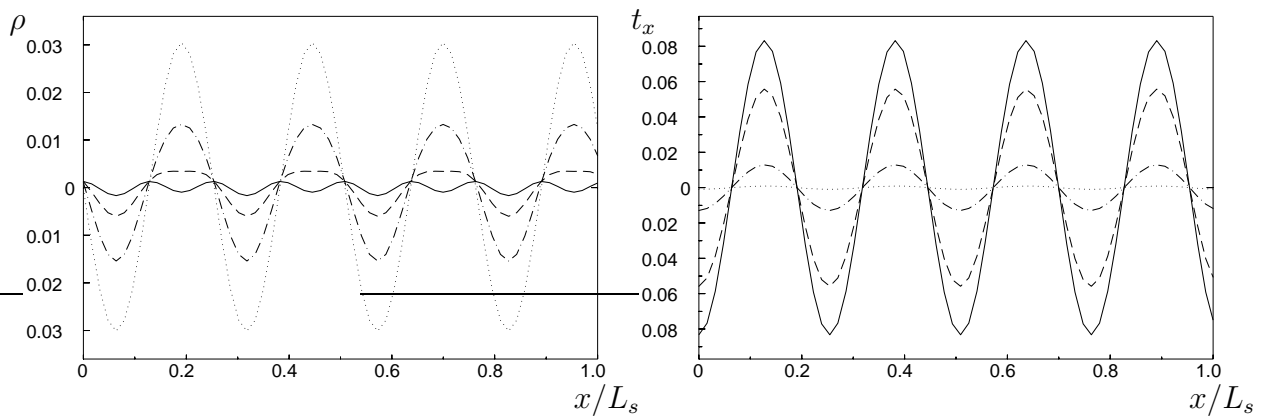


Figure 11.5: A quarter period of a numerically obtained standing wave is shown. One can see from the solid line that for the filament density the second harmonic has to be taken into account. x -axis is scaled with the system length L_s . Parameters are $\alpha = 16$, $\beta = 5$, $D_r = 1.1$, $c = 0.5$ and $\epsilon = 10^{-4}$.

11.4 Results of numerical simulations

We have again tested the validity range of the amplitude expansion by performing numerical simulations. In Fig. 11.4, a comparison between the analytical result $|A| = F = \sqrt{\epsilon/g_1}$ from Eq. (11.41) and a numerical simulation is shown for parameters leading to a stable traveling wave solution.

In addition, we tested the standing wave solutions. Here it happens that a mode $\propto \exp(2ik_c)$ occurs in the density pattern already very near to the threshold as can be seen in Fig 11.5. However, taking the next order correction, i.e. $\mathbf{w} = \epsilon^{1/2}\mathbf{w}_1 + \epsilon\mathbf{w}_2$ into account with \mathbf{w}_2 given as a function of the amplitudes of \mathbf{w}_1 from the derivation of the amplitude equation, cf. Eq. (11.33), one again gets nearly perfect agreement with the numerics.

For both kinds of solutions, TW and SW, we encountered numerical stability problems, i.e. the amplitudes did not reach the predicted values, stayed there for a while and then got unstable against high amplitude oscillations. Accounting for the third order excluded vol-

ume always stabilized the amplitudes and led to perfect agreement. Probably the problems result from numerical artifacts due to the use of an explicit integration scheme (we again used a fourth order Runge-Kutta scheme for the time evolution and a Fourier-Galerkin pseudo spectral code in space).

11.5 Weakly nonlinear analysis in two dimensions

11.5.1 Amplitude equations

For two spatial dimensions, I only sketch the derivation of the amplitude equations since it is completely analogous to the one-dimensional case and just involves more book keeping. The ansatz of waves traveling in opposite directions, Eq. (11.4), has to be generalized for $\mathbf{w}_1 = (\rho_1, t_{1x}, t_{1y})^T$ and reads

$$\begin{aligned} \mathbf{w}_1 = & \begin{pmatrix} E_- \\ 1 \\ 0 \end{pmatrix} X_r e^{i(k_c x - \omega_c t)} + \begin{pmatrix} E_+ \\ 1 \\ 0 \end{pmatrix} X_l e^{i(k_c x + \omega_c t)} \\ & + \begin{pmatrix} E_- \\ 0 \\ 1 \end{pmatrix} Y_r e^{i(k_c y - \omega_c t)} + \begin{pmatrix} E_+ \\ 0 \\ 1 \end{pmatrix} Y_l e^{i(k_c y + \omega_c t)} + c.c., \end{aligned} \quad (11.47)$$

with *c.c.* the complex conjugate. So one has to allow for traveling waves in opposite directions (right and left) in two arbitrary perpendicular directions, chosen here without restriction as the x- and y-directions. This is reflected by X_r and X_l as the amplitudes of waves in x-direction and Y_r and Y_l in y-direction, respectively.

The generic structure of the amplitude equations can be motivated by the following reasoning. First of all, the one-dimensional case, namely Eqs. (11.8), should be contained as a special case. One further expects that the waves in orthogonal directions are coupled. If we look exemplarily at the equation for X_r , one has to find couplings to Y_r , Y_l that are proportional to $\exp(i(k_c x - \omega_c t))$. This is due to the amplitude equation being the solvability condition of the perturbation hierarchy and thus containing only the resonantly forcing contributions in order $\mathcal{O}(\varepsilon^{3/2})$. Thus the y -dependence of the exponentials of the orthogonal waves have to cancel, which is only possible in the combinations

$$|Y_r^2| X_r e^{i(k_c x - \omega_c t)}, \quad |Y_l^2| X_r e^{i(k_c x - \omega_c t)}, \quad Y_r e^{i(k_c y - \omega_c t)} Y_l^* e^{-i(k_c y + \omega_c t)} X_l e^{i(k_c x + \omega_c t)}. \quad (11.48)$$

The last contribution is perhaps slightly unexpected, but also interesting, since it couples X_r with all three other amplitudes.

We can now write down the generalization of the amplitude equations (11.8) to two spatial dimensions

$$\tau_0 \partial_T X_r = \varepsilon(1 + ib)X_r - z_1 |X_r|^2 X_r - z_2 |X_l|^2 X_r - z_3 (|Y_r|^2 + |Y_l|^2) X_r - z_5 Y_r Y_l^* X_l, \quad (11.49a)$$

$$\tau_0 \partial_T X_l = \varepsilon(1 + ib)X_l - z_1 |X_l|^2 X_l - z_2 |X_r|^2 X_l - z_3 (|Y_r|^2 + |Y_l|^2) X_l - z_5 Y_l Y_r^* X_r, \quad (11.49b)$$

$$\tau_0 \partial_T Y_r = \varepsilon(1 + ib)Y_r - z_1 |Y_r|^2 Y_r - z_2 |Y_l|^2 Y_r - z_3 (|X_r|^2 + |X_l|^2) Y_r - z_5 X_r X_l^* Y_l, \quad (11.49c)$$

$$\tau_0 \partial_T Y_l = \varepsilon(1 + ib)Y_l - z_1 |Y_l|^2 Y_l - z_2 |Y_r|^2 Y_l - z_3 (|X_r|^2 + |X_l|^2) Y_l - z_5 X_l X_r^* Y_r, \quad (11.49d)$$

where the asterisk again denotes the complex conjugate and $z_n = g_n + ic_n$ holds with g_n and c_n real for $n = 1, 2, 3, 5$, and also b is real. The linear terms and the first two nonlinear contributions coupling waves with the same or the opposite direction on the same axis have already been present in the one-dimensional Eqs. (11.8). The third nonlinear term represents the coupling to waves in perpendicular direction, and due to symmetry the coefficient for the left and right traveling waves is the same, namely z_3 . The last term couples together all modes and will be important for the four-mode solutions, cf. below. One should also note that the coefficients τ_0 , b , g_1 , c_1 , g_2 and c_2 are identical with the ones already obtained in the one-dimensional problem. Various problems related to Eqs. (11.49) have been addressed to in Refs. [140, 141, 142, 143].

11.5.2 Existence and stability of two-dimensional waves

In Ref. [141], the stationary oscillating solutions of Eqs. (11.49) have been identified. The solution space is now quite diverse allowing for one- and two-dimensional wave solutions, namely traveling waves (TW) and standing waves (SW) as already treated in section 11.1.3, and also traveling squares (TSq), standing square waves (SSq) and alternating waves (AW). The traveling square solution corresponds to two waves traveling in perpendicular direction. The standing square and the alternating wave solutions are nonlinear superpositions of two perpendicular standing waves, either being in phase (SSq) or having a $\pi/2$ phase shift. Thus only these two latter solutions involve all four modes.

The stationary oscillating solutions of Eqs. (11.49) can be obtained by the same procedure as in section 11.1.3. The form and the existence range of the TW and SW solutions are not changed as compared to the one-dimensional case, however their stability is affected by the possibility of orthogonal waves as will be discussed below. They read explicitly

$$X_r = A_1 e^{i\Omega_1 t}, \quad X_l = 0, \quad Y_r = 0, \quad Y_l = 0 \quad (11.50)$$

with

$$A_1 = \sqrt{\frac{\varepsilon}{g_1}} \quad \text{and} \quad \Omega_1 = \tau_0^{-1} \varepsilon \left(b - \frac{c_1}{g_1} \right) \quad (11.51)$$

for the TW solution and

$$X_{r,l} = A_2 e^{i(\Omega_2 t + \phi_{r,l}^x)}, \quad Y_r = 0, \quad Y_l = 0 \quad (11.52)$$

with

$$A_2 = \sqrt{\frac{\varepsilon}{g_1 + g_2}} \quad \text{and} \quad \Omega_2 = \tau_0^{-1} \varepsilon \left(b - \frac{c_1 + c_2}{g_1 + g_2} \right) \quad (11.53)$$

for the SW solution. Solutions with waves in the other possible directions are fully analogous and thus not explicitly mentioned in the following.

Instead of two traveling waves with equal amplitude in opposite directions on the same axis leading upon superposition to a standing wave, in two dimensions there is a new two-mode solution possible where the two waves travel in two perpendicular directions. Such a traveling square (TSq) solution is described by

$$X_r, Y_r = A_3 e^{i(\Omega_3 t + \phi_r^{x,y})}, \quad X_l = 0, \quad Y_l = 0 \quad (11.54)$$

with

$$A_3 = \sqrt{\frac{\varepsilon}{g_1 + g_3}} \quad \text{and} \quad \Omega_3 = \tau_0^{-1} \varepsilon \left(b - \frac{c_1 + c_3}{g_1 + g_3} \right). \quad (11.55)$$

Moreover, two stable four-mode solutions can be obtained: a standing square (SSq) solution and an alternating wave (AW) solution. Both are built up of two standing waves in x - and y -direction which have equal amplitudes and which are superimposed in phase in the case of the SSq and with a phase shift of $\pi/2$ in the case of the AW. The standing square solution thus reads

$$X_{r,l}, Y_{r,l} = A_4 e^{i(\Omega_4 t + \phi_{r,l}^{x,y})} \quad (11.56)$$

with

$$A_4 = \sqrt{\frac{\varepsilon}{g_1 + g_2 + 2g_3 + g_5}} \quad \text{and} \quad \Omega_4 = \tau_0^{-1} \varepsilon \left(b - \frac{c_1 + c_2 + 2c_3 + g_5}{g_1 + g_2 + 2g_3 + g_5} \right) \quad (11.57)$$

and the phase condition

$$\phi_r^x - (\phi_r^y - \phi_l^y + \phi_l^x) = 2n\pi \quad (11.58)$$

for integer valued n . The alternating wave solution is given by

$$X_{r,l}, Y_{r,l} = A_5 e^{i(\Omega_5 t + \phi_{r,l}^{x,y})} \quad (11.59)$$

with

$$A_5 = \sqrt{\frac{\varepsilon}{g_1 + g_2 + 2g_3 - g_5}} \quad \text{and} \quad \Omega_5 = \tau_0^{-1} \varepsilon \left(b - \frac{c_1 + c_2 + 2c_3 - g_5}{g_1 + g_2 + 2g_3 - g_5} \right) \quad (11.60)$$

and the respective phase condition

$$\phi_r^x - (\phi_r^y - \phi_l^y + \phi_l^x) = (2n + 1)\pi, \quad (11.61)$$

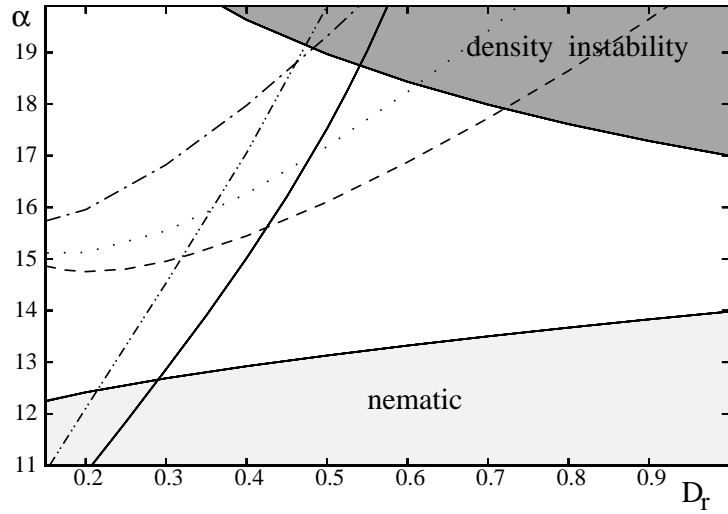


Figure 11.6: The borders of existence for the various solution branches of Eqs. (11.49). Again the dark and light grey regions correspond to the demixing and nematic instabilities, where the amplitude expansion does not apply. In between these regions the various two-dimensional wave solutions exist on the right sides of their respective borders: TW (solid line), AW (dashed line), TSq (dotted line), SW (dashed-two-dots) and SSq (dash-dotted line). Parameters are $\beta = 5$ and $c = 4$.

again for integer valued n .

As before, one can read from the amplitudes A_i with $i = 1, \dots, 5$ the existence ranges. Assuming $\epsilon > 0$, one obtains the following conditions for the various solutions to bifurcate supercritically:

$$\text{TW : } \quad g_1 > 0 \quad , \quad (11.62a)$$

$$\text{SW : } \quad g_1 + g_2 > 0 \quad , \quad (11.62b)$$

$$\text{TSq : } \quad g_1 + g_3 > 0 \quad , \quad (11.62c)$$

$$\text{SSq : } \quad g_1 + g_2 + 2g_3 + g_5 > 0 \quad , \quad (11.62d)$$

$$\text{AW : } \quad g_1 + g_2 + 2g_3 - g_5 > 0 \quad . \quad (11.62e)$$

The respective existence ranges are shown in the α - D_r -plane in Fig. 11.6. Since the coefficients g_1 and g_2 are the same as for the one-dimensional equations, the regions of existence for the one-dimensional patterns TW and SW are not changed when considering a two-dimensional system.

The conditions of stability can be obtained by a similar analysis as exemplified in section 11.1.3. However, due to the nonlinear coupling in Eqs. (11.49) proportional to z_5 , also the complex conjugates of the small deviations δx_r^* , δx_l^* , etc. come into play and

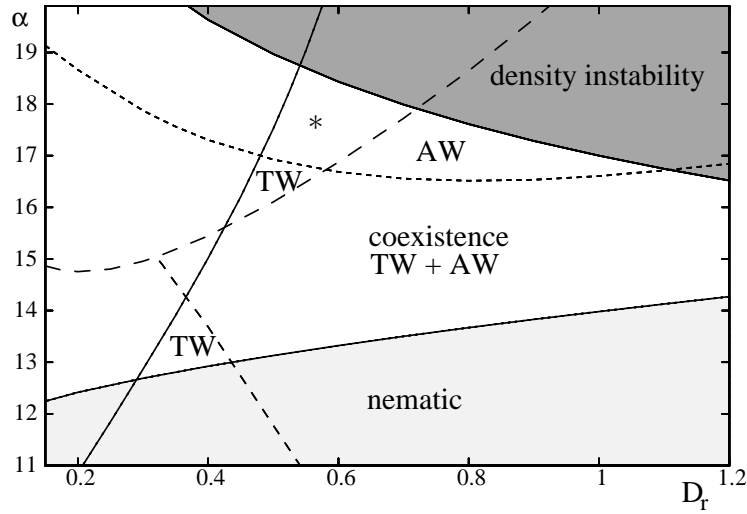


Figure 11.7: Stability diagrams for $\beta = 5$ and $c = 4$. For these parameters there exist two regions of stable TW solutions, a region of stable AW and a region where both patterns are in coexistence. The other existing patterns, namely SW, TSq and SSq are unstable. Again the dark and light grey regions correspond to the demixing and nematic instabilities. In the region denoted with *, between the stable TW and AW solutions and the density demixing instability, TW bifurcate supercritically but are unstable, while AW bifurcate subcritically. In this parameter range one numerically finds subcritical AW solutions, cf. Fig. 11.11.

one thus has to discuss an eight-dimensional square matrix to obtain the growth rates of these perturbations. Due to the high symmetry of the latter matrix, one can extract the eigenvalues by means of a computer algebra system (Maple) and one gets the following stability conditions:

$$\text{TW : } \quad g_2 > g_1 > 0 \quad \text{and} \quad g_3 > g_1 > 0 , \quad (11.63a)$$

$$\text{SW : } \quad |g_2| < g_1 \quad \text{and} \quad g_1 + g_2 - 2g_3 \pm g_5 < 0 , \quad (11.63b)$$

$$\text{TSq : } \quad |g_3| < g_1 \quad \text{and} \quad g_1 - g_2 \pm g_5 < 0 , \quad (11.63c)$$

$$\begin{aligned} \text{SSq : } \quad & g_2 - g_1 + g_5 < 0 , \quad g_1 + g_2 - g_5 - 2g_3 > 0 \\ & \text{and} \quad -g_1 + g_2 + 3g_5 \pm \sqrt{(g_1 - g_2 + g_5)^2 + 8c_5(c_1 - c_2 - c_5)} , \end{aligned} \quad (11.63d)$$

$$\begin{aligned} \text{AW : } \quad & g_2 - g_1 - g_5 < 0 , \quad g_1 + g_2 + g_5 - 2g_3 > 0 \\ & \text{and} \quad -g_1 + g_2 - 3g_5 \pm \sqrt{(g_1 - g_2 - g_5)^2 - 8c_5(c_1 - c_2 + c_5)} . \end{aligned} \quad (11.63e)$$

The coefficients $z_n = g_n + ic_n$ with $n = 1, \dots, 5$ can be obtained from the underlying model equations (8.4) as functions of the model parameters α , β , D_r and the higher order excluded volume parameter c . The value of β has only minor influence on the borders, as

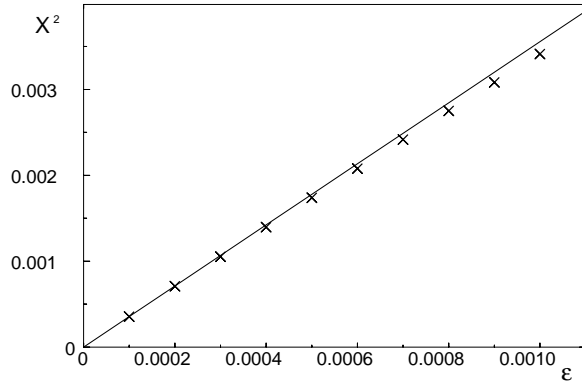


Figure 11.8: The oscillatory finite wavelength instability in two spatial dimensions allows for stable alternating wave (AW) solutions. The squared amplitude of one of the four modes of an AW observed numerically is shown as crosses and is compared to the analytical value from the amplitude expansion, Eq. (11.60), drawn as the solid line. The parameters are $\alpha = 12$, $\beta = 5$, $D_r = 0.8$ and $c = 2$.

already discussed, cf. Fig. 11.3.

For the filament-motor model under consideration, we find that the solution space is quite reduced: SW, TSq and SSq solutions are unstable for all sensible parameter values and only TW and AW have finite regions of stability, as shown exemplarily in Fig. 11.7 for an intermediate value of the third order excluded volume term. Especially, the SW solution which had a finite stability range in one dimension now is destabilized due to the second condition in Eq. (11.63b), $g_1 + g_2 - 2g_3 \pm g_5 < 0$, which describes fluctuations in the direction perpendicular to the wave and can practically never be fulfilled in our system.

As in the one-dimensional case, the higher order excluded volume term favors traveling waves: the dashed lines in Fig. 11.7 are shifted in the upper right direction and for high values of c only TW are stable.

SW, TSq and SSq solutions can however be seen in numerical simulations of Eqs. (8.4) as long-time transient structures if one puts them in as a starting solution. This is due to the extremely slow dynamics of the pattern compared to the propagation of the waves that build the pattern.

11.5.3 Numerical simulations

We again tested the amplitudes of numerically obtained solutions. First we simulated the two-dimensional traveling wave solution. Since the amplitudes obtained by numerical and analytical calculations have already been compared in the one-dimensional case, only the stability in the two-dimensional system has to be checked. We obtained stable TW solutions in the predicted regions, cf. Fig. 11.7, but I do not show simulation pictures, since it is clear how TW look like.

For the alternating wave solution a comparison between the analytically predicted amplitude from Eq. (11.60) and the numerical simulation of the underlying model Eqs. (8.4) is shown in Fig. 11.8. By comparison with Fig. 11.4 one can see that the expansion is not as good in this case, presumably due to the complicated interactions of all four modes that build the AW pattern.

To get a feeling for the dynamics of an AW, Fig. 11.9 shows a combined density and orientation plot of one period of such a pattern. One can see that alternately one wave

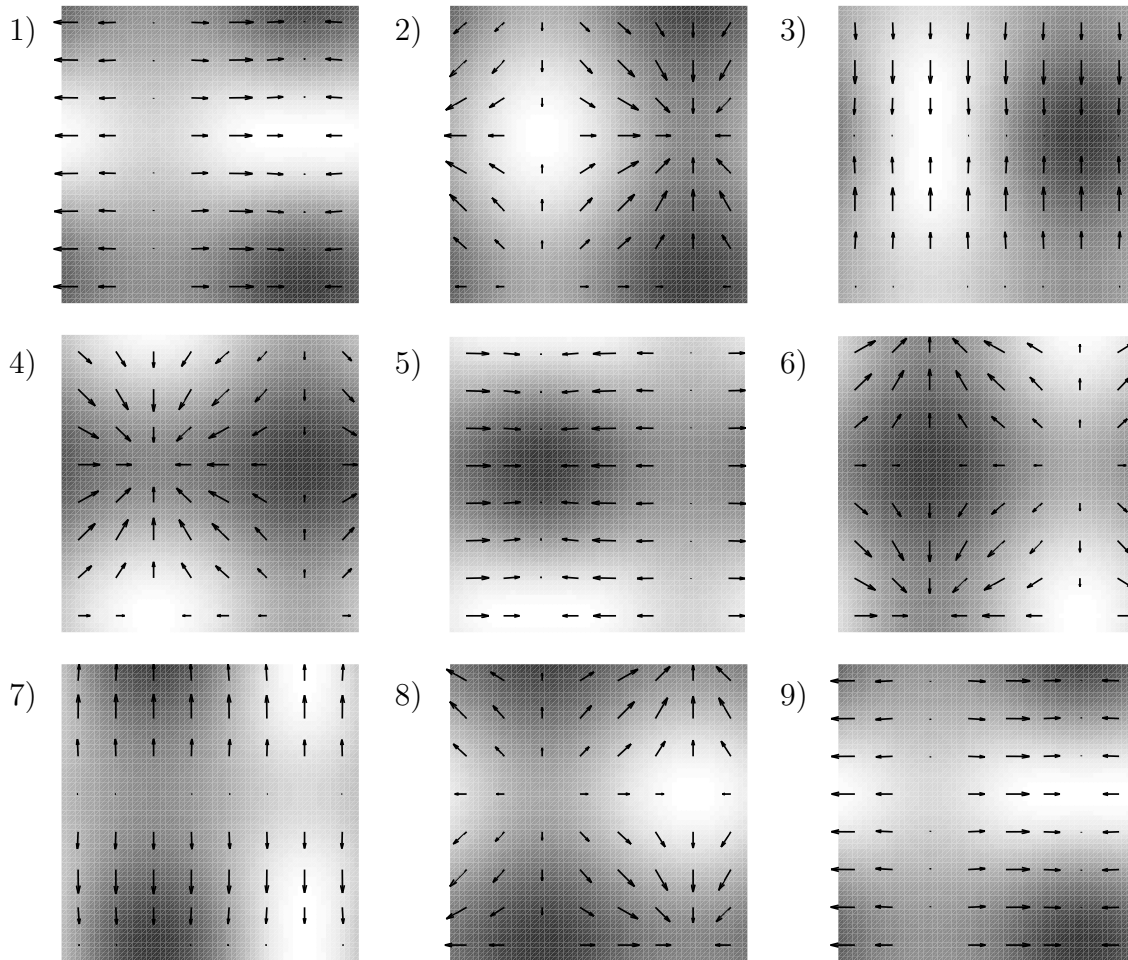


Figure 11.9: A period of a numerically obtained alternating wave (AW) is shown. The filament density is color-coded (bright and dark colors corresponding to high and low density respectively) and the orientation field is shown as the arrows. One can clearly see that alternately waves in one of the two perpendicular directions dominate the pattern. So the AW pattern comprises two orthogonal standing waves having a $\pi/2$ phase shift. Parameters are as in Fig. 11.8.

structure of the two perpendicular directions is dominating, namely the one in x -direction in pictures 1 and 5 and the one in y -direction in pictures 3 and 7. In between aster-like patterns emerge, cf. pictures 2, 4 etc.. The filament density is coupled to the oscillating filament orientation and a region of high density, indicated by the bright color in Fig. 11.9, is moving on a square defined by the stationary points in the orientation field, cf. also Fig. 11.10. One could also refer to this pattern as an oscillating or breathing aster.

In Fig. 11.10 I concentrated on the behavior of the orientation field. The arrows describing the latter are shown for one period of the pattern and one can clearly distinguish positions in space behaving differently: there are stationary points (e.g. the one referred

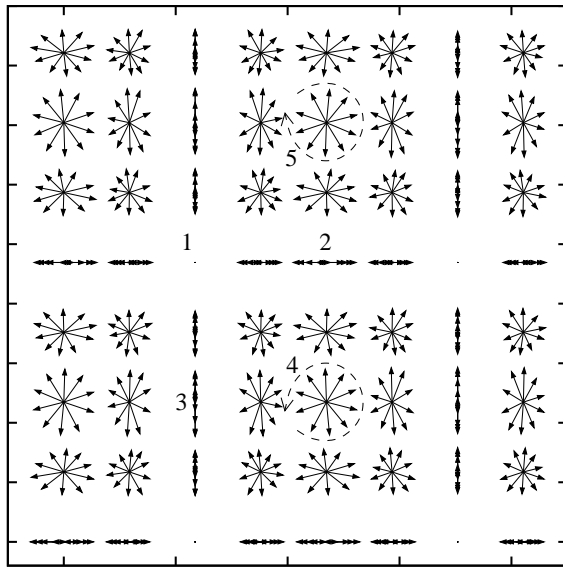


Figure 11.10: Behavior of the orientation field (solid arrows) of a numerically obtained AW solution. There are stationary points (1), points with orientation oscillating parallel to one of the perpendicular axes (2 and 3) and points with rotating orientation (4 and 5, direction of rotation indicated by the dashed arrow). Parameters are as in Fig. 11.8.

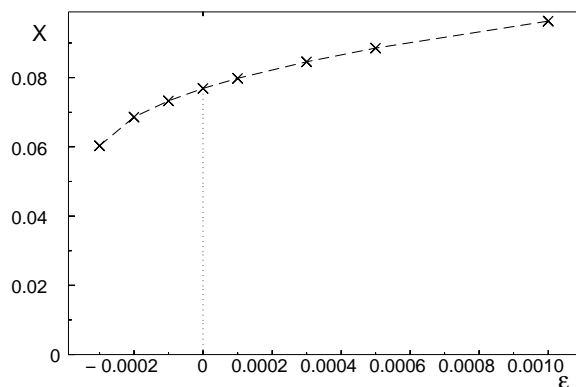


Figure 11.11: In the region denoted with * in Fig. 11.7, the oscillatory finite wavelength instability also favors alternating wave (AW) solutions, which bifurcate subcritically. The amplitude X of such a subcritical AW observed numerically is shown as the dashed line. The parameters are $\alpha = 18$, $\beta = 5$, $D_r = 0.6$ and $c = 4$.

to as 1 in Fig. 11.10), points where the orientation oscillates parallel to one of the two perpendicular axes (points 2 and 3) and points with rotating orientation (points 4 and 5). Due to symmetry, the orientation has to rotate in opposite senses in points 4 and 5.

In the region in Fig. 11.7 denoted with *, where TW are bifurcating supercritically but are unstable and AW bifurcate subcritically, one numerically finds subcritical AW, as shown in Fig. 11.11.

Additionally, when starting the numerical simulations from a random initial solution, at least transiently always AW are formed. Thus one can conclude that in general the alternating wave seems to be the dominating pattern (at least for small or moderate values of the third order excluded volume parameter). This is analogous to the stationary case without polarity sorting, where the aster pattern dominates, c.f. the last chapter.

11.6 Discussion and conclusions

In this chapter, we have analyzed the oscillatory orientational instability predicted in section 9.4 in the weakly nonlinear regime in both one and two spatial dimensions. The orientational instability discussed in the last chapter is rendered oscillatory by the polarity sorting contributions, i.e. those terms in Eqs. (8.4) that are proportional to β . In addition, the $\pm\mathbf{t}$ symmetry is broken by these terms. However, apart from the critical frequency ω_c , which increases almost linearly with increasing β , cf. Fig. 9.8, there is not much dependence, neither in the linear nor in the nonlinear regime, on the distinct value of β in the range $\beta \simeq \alpha$, which is expected to be relevant [40]. Thus one can conclude that the presence of the polarity sorting contributions changes the quality of the orientational instability from stationary to oscillatory, but that the patterns and their stability are governed by the other parameters, namely by the instability-inducing α -contribution of the motor-mediated translations and by the rotational diffusion coefficient D_r , as well as by the third order excluded volume contribution introduced and discussed in section 11.2, proportional to an additional phenomenological parameter c .

The existence and the stability ranges of the wave patterns in one and two dimensions have been calculated analytically by means of amplitude expansions and have been confirmed by numerical simulations. In one spatial dimension, as could be expected, there is competition between traveling waves (TW) and standing waves (SW). The system more likely shows subcritical bifurcations than for the stationary instability discussed in the last chapter. The third order excluded volume contribution, which may be relevant in a two-dimensional rod system, increases the regions of supercritical bifurcation and favors TW against SW solutions.

In two spatial dimensions, although there is quite a huge solution space comprising one-mode solutions (TW), two-mode solutions (SW and traveling squares (TSq)), as well as four-mode solutions (standing squares (SSq) and alternating waves (AW)), the dominating patterns are TW and AW. Only for small values of β , also stable SW have been found in a small region of the parameter space. The third order excluded volume again favors TW, but the stability range of the alternating waves is quite large, comprising the high values of D_r , cf. Fig. 11.7. Thus as in the stationary case, where the stationary two-dimensional pattern, i.e. the asters, dominated the dilute limit of high D_r , also in the oscillatory case the two-dimensional alternating waves dominate in this region.

The experimental observation of waves in active filament-motor systems is not yet in the focus compared to the stationary patterns. Spontaneous oscillations in muscle bundles, i.e. quasi one-dimensional filament structures, have been observed [104, 144, 145]. The fact that they prevail in the absence of regulatory proteins implies that they are inherent to the filament-motor interaction. In reconstructed, quasi-two-dimensional filament-motor solutions, experiments are not available yet. However in two-dimensional microtubule networks connected with the cell membrane, a special kind of kinesin causes surface contraction waves *in vivo*, known to be relevant in cell development of amphibian eggs [146]. In addition, actin-myosin waves are known to be involved in cell spreading [147, 148]. In these two systems, however, one expects that the attachment to the membrane or to the

surface the cell spreads on, respectively, are extremely important, i.e. complicated boundary effects are involved. Moreover, the active polymerization of actin is also involved in cell spreading, this process being a delicate balance between actomyosin-related forces that contract the cell into a compact shape and forces associated with directed polymerization that extends the boundaries of the cell [102]. However, from theoretical investigations, which prior to this work have been carried out only in one-dimensional models concerning filament bundling [114, 41, 105], patterns involving the density of the filaments have been identified as connected to contraction of the filament-motor system. This implies that density waves are related to contraction waves, which surely are of relevance concerning cell spreading and cell motility.

To conclude, albeit definite experiments on oscillations in filament-motor solutions are lacking, it is important to study the vocabulary of such systems. The general tendencies as implied by the calculations in this chapter, i.e. the emergence of alternating waves in the dilute limit and the favoring of traveling waves in the less dilute regime where higher order excluded volume effects become relevant, should be testable and may guide new experiments.

Chapter 12

Density instability

In this chapter I briefly address the density demixing instability encountered already in chapter 9. I call it a demixing instability, since it is not a pattern forming instability with a finite critical wave number k_c , as has been the case for the orientational patterns investigated in the last chapters, but rather shares similarities with dynamics involved in early stage spinodal decomposition. The unstable mode has the structure of a linearized Cahn-Hilliard (CH) equation, cf. section 3.3, with a fastest growing mode k_{fg} dominating the initial stages of the instability, while for late stages simulations of Eqs. (8.4) in the density demixing region display *coarsening* processes that are a common feature of phase separation kinetics. However, though sharing these similarities, while phase separating systems usually are governed by a free energy and the systems gets unstable against density modulations in the spinodal region, cf. Fig. 3.2, the filament-motor system is rendered inhomogeneous due to the nonequilibrium motor activity.

12.1 Linear properties

Looking at the linear operator $\tilde{\mathcal{L}}_0$ of the continuum model equations (8.4) as defined by Eqs. (9.27), the density demixing instability is governed by the eigenvalue

$$\sigma_d = - \left[\frac{1+D}{2} \left(1 + \frac{2}{\pi} \rho_0 \right) - \frac{\alpha \rho_0}{24} \right] k^2 - \left[\frac{19 \alpha \rho_0}{11520} + \frac{5}{384} \frac{\rho_0^2 \beta^2}{D_r} \right] k^4 \quad (12.1)$$

up to fourth order in the wavenumber k . One can see from Eq. (12.1) that σ_d describes a conserved mode, since $\sigma_d(k=0) = 0$. Second, while the fourth order contributions in k are always stabilizing, the contribution proportional to k^2 (the effective diffusion coefficient in the framework of Cahn-Hilliard theory) changes sign for a critical filament density

$$\rho_d = \frac{1}{\frac{\alpha}{12(1+D)} - \frac{2}{\pi}}, \quad (12.2)$$

provided that this value is positive, i.e. if $\alpha > \frac{24}{\pi}(1+D)$ holds (independent of β). Thus the unstable mode σ_d has exactly the linear behavior of the CH equation, cf. Eq. (3.74),

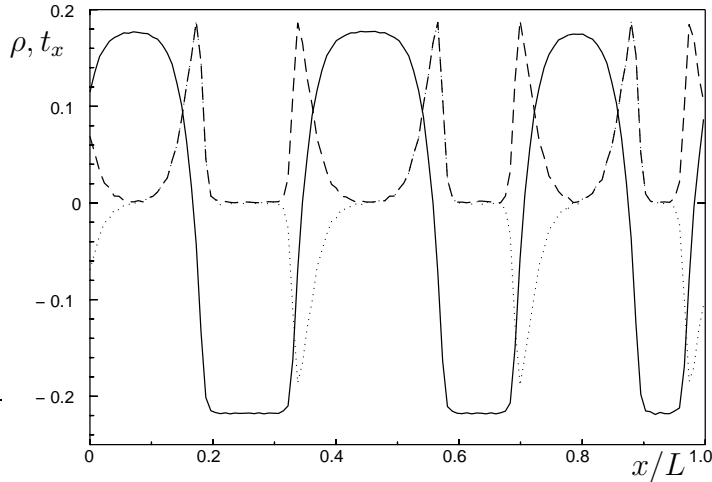


Figure 12.1: A late stage solution of the density instability. The density is shown as the solid line and the orientation field as the dotted line. To make the symmetry visible, also the absolute value of the orientation field is shown as the dashed line. Parameters are $\alpha = 30$, $\beta = 5$, $D_r = 0.8$, $\rho_0 = 1.2$, $c = 4$.

whereby the motor contributions proportional to α render the effective diffusion coefficient negative. For $\rho_0 > \rho_d$, there exists an unstable wavenumber range $[0, k_{max}]$ with a fastest growing mode k_{fg} having maximum growth rate and dominating the initial dynamics of the instability.

From Eq. (12.1) one can read the following tendencies¹: the leading order term proportional to β implies that k_{fg} and k_{max} are decreasing with β but growing with D_r . Second, increasing either the relative distance from threshold, $\varepsilon = \frac{\rho_0 - \rho_d}{\rho_d}$, or the parameter α , increases k_{fg} and k_{max} , since the k^2 -term proportional to $\alpha\rho_0$ dominates over the k^4 -term.

The eigenvector of σ_d reads in leading order in the wavenumber k

$$\mathbf{E}_d = \begin{pmatrix} 1 + f(\rho_0, \alpha, D_r)k^2 + \mathcal{O}(k^4) \\ \beta \frac{\rho_0}{2D_r} ik \end{pmatrix}, \quad (12.3)$$

showing that the respective mode is purely related to the filament density at $k = 0$, but coupled to the orientation field via the polarity sorting contributions² proportional to β for any finite wavenumber k . Moreover, the relative phase between filament density and filament orientation is $\pm\pi/2$ depending on the sign of β . This allows to distinguish asters with different orientations, cf. the discussion below.

12.2 Numerical simulations

First I investigated the density demixing instability in a one-dimensional system to achieve a high enough accuracy for the long wavelength modes. To obtain pictures like the one displayed in Fig. 12.1 we used a spectral code with 64 modes. The system indeed showed the

¹These tendencies remain valid using the full dispersion instead of the approximation up to fourth order in the wavenumber k . However, the general case can not be as easily discussed.

²In case of $\beta = 0$, this instability is not really interesting since density and orientation are completely decoupled.

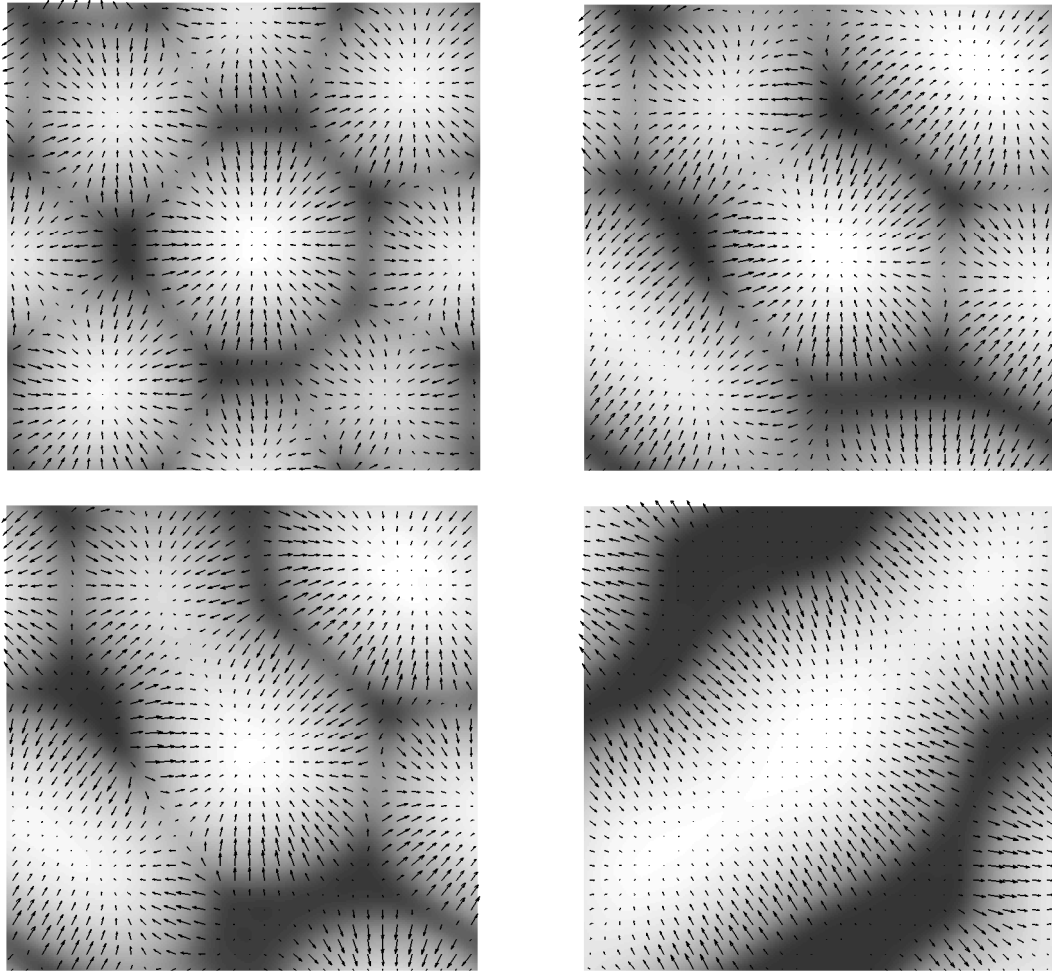


Figure 12.2: Simulation of the temporal evolution of the density instabilities. A aster-like pattern arises but coarsens to lower wavelengths and ultimately leads (for periodic boundary conditions) to a two-domain solution with high orientation in between the high and low density regions. Elapsed times from a) to d): $t = 1000, 1500, 2000$ and 3000 in dimensionless units. Parameters are $\alpha = 30$, $\beta = 5$, $D_r = 0.8$, $\rho_0 = 1.2$, $c = 4$.

typical behavior known from phase ordering dynamics: after a short time where the fastest growing mode (the one with wavenumber k_{fg}) dominated, the amplitudes saturated and the dynamics became extremely slow. Then the system successively destroyed periodicities and in this way increased the wavelength of the pattern, corresponding to a coarsening of the structure.

A late stage solution of the one-dimensional equations is shown in Fig. 12.1. One can clearly see that both the $\pm \mathbf{t}$ - and the $\pm \rho$ -symmetry are broken through the presence of the β -contributions. The density has the typical form known from Cahn-Hilliard theory

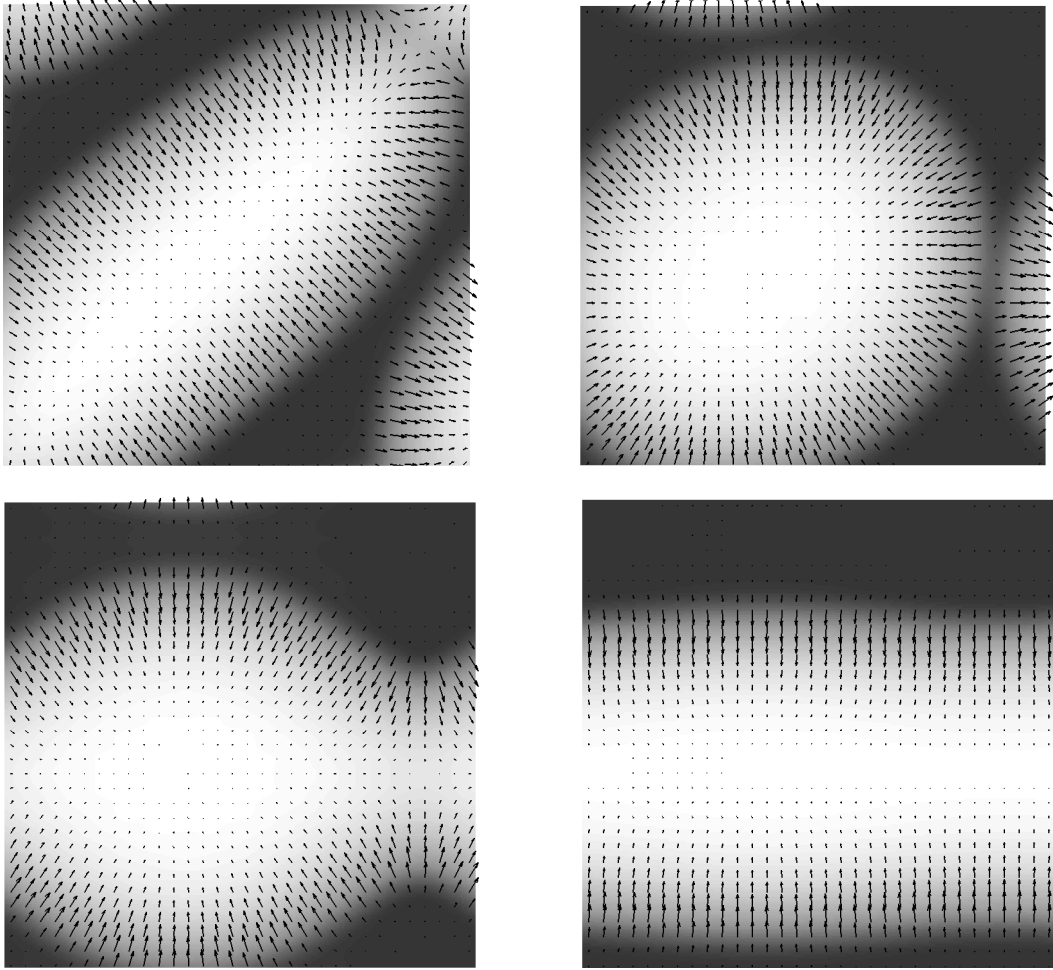


Figure 12.3: Simulation of the temporal evolution of the density instabilities. A aster-like pattern arises but coarsens to lower wavelengths and ultimately leads (for periodic boundary conditions) to a two-domain solution with high orientation in between the high and low density regions. Elapsed times from a) to d): $t = 7000, 7500, 8500$ and 9000 in dimensionless units. Parameters as in Fig. 12.2.

with broken up-down symmetry, i.e. with a quadratic contribution added to Eq. (3.73), interpolating quite anharmonically between states of high and low densities.

The orientation field vanishes in the regions where the density is nearly homogeneous and shows sharp extrema at the interfaces between the high and low density states. The direction of the orientation with respect to the density is governed by the sign of β . In Fig. 12.1, where β is positive, the orientation is pointing away from the high density regions, as shown by the dotted line (negative values of t_x imply that the orientation vector points in negative x -direction). If β is negative, the opposite is true, i.e. the orientation is pointing inwards to the high density region. This is clear from the symmetry $(\mathbf{t}, \beta) \rightarrow (-\mathbf{t}, -\beta)$ of

Eqs. (8.4). Also the eigenvector, cf. Eq. (12.3), reflects this governing the relative phase between filament density and filament orientation of the spatially periodic modes growing in the initial stage.

The experimental experience suggests that the density in the center of an aster is high. Assuming that the high density region defines the center of an aster, which is better justified in the two-dimensional pictures, Figs. 12.2 and 12.3, the above behavior can be interpreted in the following way: positive values of the polarity sorting parameter imply asters with the filaments pointing outwards, while negative values imply inward-directed asters.

Figs. 12.2 and 12.3 show a two-dimensional simulation, where the number of modes had to be restricted to 16 in order to reduce the required integration time. In the first few steps one can see that the aster-like structures coarsen, involving also some more stripe-like configurations. One can see that the orientation field again is nonvanishing only where a high density gradient occurs. Second, the orientation is always parallel to this gradient, which is due to the linearly unstable mode involving (apart from the density) only the longitudinal orientation mode, while the transverse orientation mode is damped. The simulations show that this remains valid also in the nonlinear regime.

Finally, in the upper right part of Fig. 12.2 there remains a cluster in the middle. The two following pictures are sort of an artifact from the periodic boundary conditions, the cluster forming a stripe upon interacting with its own back. To study such late stage configurations in a proper way, and also the interesting question of the influence of boundary preparation of the orientation field (similar as planar and homeotropic³ anchoring in a usual liquid crystal), one has to simulate the equations in a finite system, which is beyond the scope of this work [124].

I also performed some simulations near the codimension-2 point, i.e. in a situation as shown in Fig. 9.3d), where both the density demixing and the (oscillatory) orientational instability are present. At the beginning of these simulations, traveling waves superposed on the large scale demixing pattern could be obtained, however for large times the density instability did win and the pattern finally became non-oscillatory, i.e. just demixing.

12.3 Discussion

The density demixing instability might be a better candidate for the explanation of aster formation than the finite wavelength instability analyzed in chapter 10 for the following reasons: First it solves the problem concerning the direction of the filament orientation for the lattice of asters formed through the stationary finite wavelength instability, cf. section 10.4. The predicted pattern consisted of asters of both orientations, i.e. the filaments pointed inwards or outwards from the aster center respectively, and the density was low in the aster center. This could be traced back to the $\pm\mathbf{t}$ -symmetry of the model in the absence of the polarity sorting contributions. For the density demixing instability,

³Planar anchoring means that the director of a nematic liquid crystal is preferentially aligned along a direction parallel to the boundary, while for homeotropic anchoring it is perpendicularly aligned.

the discrimination of asters with the filaments pointing inwards and outwards respectively depending on the sign of β solves this problem.

Second, the coarsening dynamics occurring in the late stages of the temporal evolution could be related to the merging of asters observed in experiments: e.g. from Fig. 6.1 one can see that the length scale of the final pattern is larger than those in the former pictures, implying that small asters can coalesce to larger ones.

A problem is however the fact that (at least with the periodic boundary conditions investigated so far) asters are only intermediate states, while for the late stages a single cluster is predicted by the numerics. However, experimental systems are large compared to the small simulation box in the present numerical investigations and thus the late stages might be beyond the possible observation times in the experiments.

Chapter 13

Patterns in actomyosin

As described in the previous chapters, pattern formation in filament-motor systems can be explained in terms of bifurcations. All the primary instabilities of the homogeneous and isotropic initial state and the pattern competition in the weakly nonlinear regime have been investigated. However, the model applies more likely to systems with processive motors, as is the case e.g. in the mixture of MTs and kinesin/Ncd-oligomers in the experiments of Refs. [31, 33]. In these experiments dissipative patterns have been found, i.e. the formation of stable patterns needed the presence of the fuel ATP that keeps the motors walking on the filaments.

In the recent experiments of Smith et al. [38], however, a solution of actin interacting via myosin oligomers has been investigated and this filament-motor system behaves quite differently in spite of the apparent similarities of the constituents, cf. chapter 2. What these experiments yield is in brief as follows: after introduction of a large amount of ATP into the actomyosin solution, the solution remains homogeneous and isotropic for a time lag of about half an hour, while then quite suddenly aster- and cluster-like patterns arise¹ as shown in Fig. 13.1. However, if the amount of ATP is measured by means of a second reference sample, one finds that after the lag time ATP is already nearly consumed and that only an amount of about 10% remains at the time when the patterns start to form.

Thus it seems that the high ATP state of actomyosin has no propensity for pattern formation, while the low ATP state has, in contrast to the MT-motor system, which showed patterns upon increasing the density of active motors. To confirm this interpretation, in a second experiment a 50 : 50 mixture of ATP and caged-ATP (ATP that has been made inactive by caging the actin binding sites) has been introduced to the actomyosin. As in the first experiment, patterns appeared after a time lag. Then the system was flashed by UV light which destroys the cages and releases an amount of ATP as high as in the beginning of the experiment. Within a few minutes, the patterns were dissolved completely and one

¹Aster formation in actin-myosin systems has been first reported in Ref. [129] for cultured fibroblasts that have been treated with the drug cytochalasin. This drug weakens the actin network without depolymerizing filaments, so that the actin can be effectively transported by myosin clusters. Asters formed both by contraction of existing stress fibers and by recruiting loose actin from the lamella. However, these experiments being *in vivo*, it is difficult to relate them directly to the model under consideration.

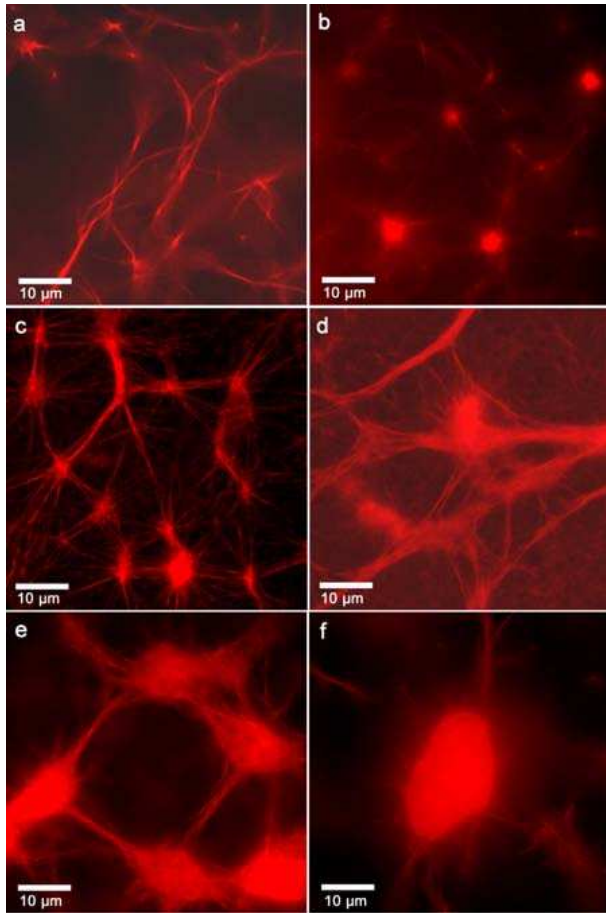


Figure 13.1: Patterns in an actin-myosin system with varying myosin density from a) to f). The variety of patterns ranges from bundle-like structures in a) to aster-like structures in c)-e) to so-called super-precipitates in f). In spite of the similarities to MT-motor patterns, the patterns in actomyosin are frozen-in structures since they form after ATP is nearly completely depleted. We propose that the patterns are also formed through an instability, where the stability border is crossed upon the formation of small filament clusters due to the rigor coupling of ADP-myosin to the filaments. Such a clustering is supported by the micrographs, where one can see that not single filaments are found in the structures, but that also the aster-like patterns are formed by bundles, cf. e.g. part d). The picture will be published in [38].

gets again the initial state of a homogeneous and isotropic solution, which after a time lag again starts to form patterns.

Our interpretation is as follows, cf. also part 1) and 4) of Fig. 13.2: In the presence of ATP, due to the low processivity of the myosin oligomers, the motors act as stochastic kicking forces on the filaments leading to disordered motion similar as in a simple fluid, but not to a coordinated sliding motion as required for pattern formation. This state I will call "dynamical disorder". When the ATP concentration decreases during its consumption by active motors, patterns are formed that have to be frozen-in structures, since they can not be interpreted as dissipative patterns anymore: first the external driving, the fuel ATP, is nearly completely consumed and second, if the driving is enhanced, as by the release of the caged-ATP in the second experiment, the patterns dissolve. This state of frozen patterns may be denoted as "frozen-in order".

In section 13.1 of this chapter we propose a mechanism that could lead from the dynamical disordered state to the frozen-in ordered state upon ATP depletion, namely a clustering process due to the rigid coupling of myosin to the actin filament in the absence of ATP. By a simple scaling argument we show that small clusters of filaments formed by such rigidly coupling myosins can be transported more efficiently than single filaments and that one of the instability borders of the model discussed so far in part II of this work

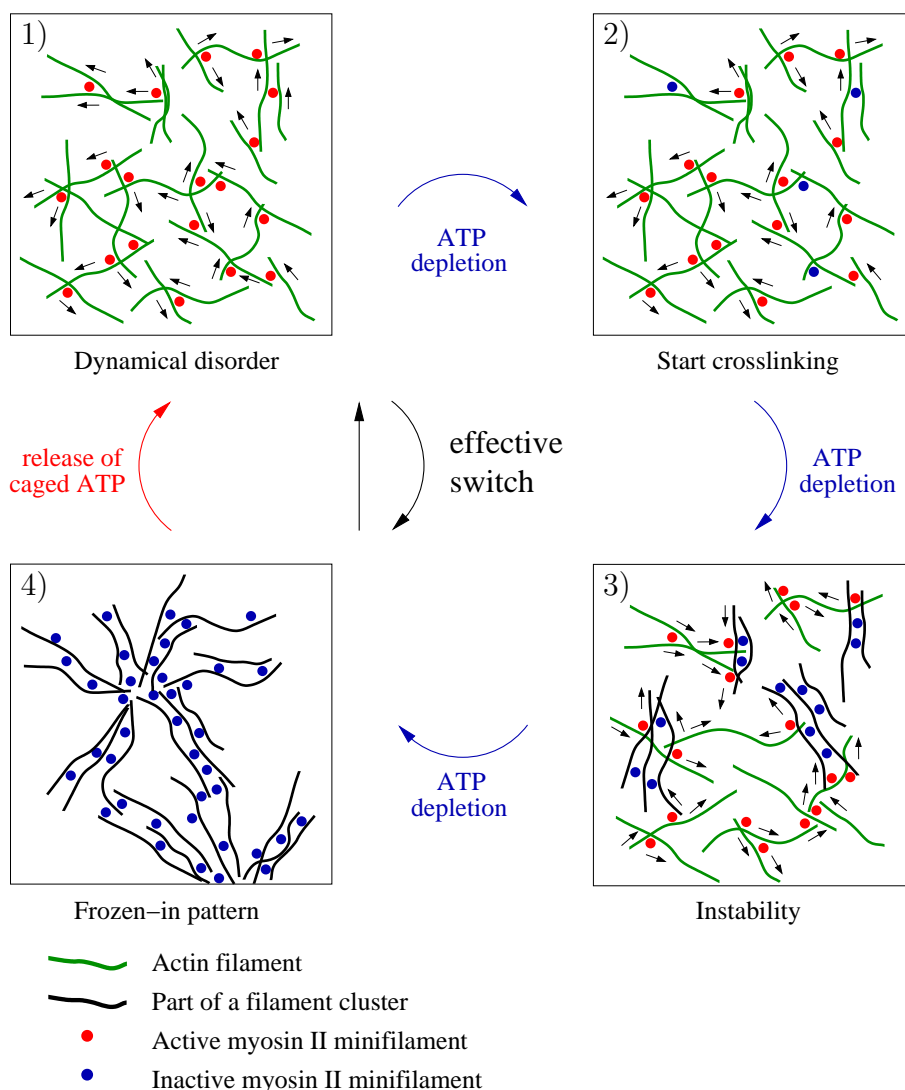


Figure 13.2: A cartoon of the mechanism we propose for the frozen-in patterns in actomyosin. We claim that the situation where the experiment starts is a dynamically disordered state as depicted in box 1). Here the transiently attached active motors do not lead to efficient filament sliding. Upon ATP depletion, some motor complexes become inactive and stick to the actin filaments as indicated in box 2). If such ADP-carrying motors are attached to two filaments, they form small filament clusters like those sketched in box 3). If the relative filament transport becomes more effective, cf. the discussion in section 13.1, the system becomes unstable and forms patterns until ultimately all the ATP is consumed and the system freezes, cf. box 4). If caged-ATP is released, one reaches again the starting point. Thus the control of ATP can be considered as a switch between the dynamical disordered state and the frozen-in ordered state.

could be crossed through a change of cluster density and of cluster-related motor activity with time. If the clusters become too large and ATP totally depleted, the system freezes and also the patterns initiated by the instability are frozen in.

In section 13.2, we propose a second mechanism that is important in the context of the experiments of Smith et al. [38]: after applying a more sophisticated purification process than in the first experiments, myosin and actin alone seem not to be sufficient to generate patterns. Only by the addition of crosslinking proteins, patterns do occur again. This is however not in contradiction to our proposed mechanism, but can be traced back to the fact that additional small clusters are caused by the non-moving crosslinkers from the very beginning of the experiments which are inhomogeneously distributed. We argue that these randomly distributed clusters can be interpreted as a disorder in the filament-motor system. In the framework of pattern formation, it is known that disorder lowers the threshold [149, 150] or renders the bifurcation imperfect [151]. Thus it could be the case that the above-mentioned clustering process due to ATP depletion is not sufficient to cross the stability border in a pure actomyosin solution, while in the presence of crosslinkers, where the threshold is reduced, patterns can be formed. This is also exemplified for the simplest case of the one-dimensional stationary instability in section 13.2.

13.1 ATP depletion and filament clustering

In fluorescence microscope pictures of the initial state, cf. Ref. [38], the system is quite homogeneous and isotropic, implying that one is in a situation near the basic state of homogeneous filament density $\rho = \rho_0$ and isotropic filament orientation $\mathbf{t} = 0$, which has been the starting point of our analyses in the last chapters. Second, in the experiments the actin filament density is very low, so one is most probably in a situation where the demixing instability occurs well before the orientational instability. This is the case whether one considers the system with or without polarity sorting ($\beta = 0$ or $\beta \neq 0$) and in both situations also the threshold for the density demixing instability is the same, $\rho_d = \rho_d^\beta$, cf. the discussion in chapter 9.

At the beginning of the experiments, the system is homogeneous and isotropic, corresponding to parameters that belong to the linearly stable range in Fig. 13.3. In this regime, the motors interact with the filaments, since ATP is continuously consumed, but there is not efficient filament transport. Rather the motors act as stochastic kicking forces on the filaments keeping the filament solution homogeneous and isotropic, cf. box 1) in Fig. 13.2. Such a state is the consequence of the lower processivity of the myosin oligomers compared to the microtubule-associated motors in the experiments of Refs. [31, 33]. Due to the small processivity, the motors are attached only transiently and are not able to effectively reorient filament pairs. We should mention that while a single myosin II has a very low processivity of about $r = 0.01-0.02$, cf. section 2.2.2, the myosin oligomers or minifilaments used in the experiments of Smith et al. [38, 36] are built of about 13 myosin II heads and thus may reach a processivity of about $r = 0.1$, which is still much smaller than $r \simeq 2 \times 0.5$ for the two-headed kinesin.

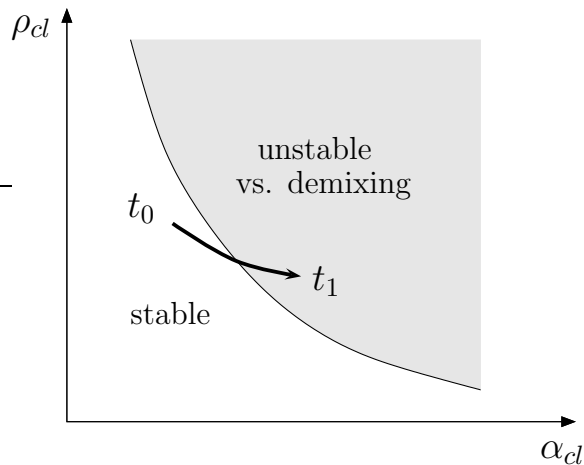


Figure 13.3: Schematic instability diagram, cf. Fig. 9.5. Since the filament density is extremely low in the experiments, one is most probably in the region where the density demixing instability appears first. Both the density ρ_{cl} and the motor coefficient α_{cl} have to be regarded as related to clusters of a few filaments rather than to single filaments. Then with ATP depletion (i.e. with elapsing time from t_0 to t_1) the density decreases while the motor transport coefficient increases and thus the system may cross the instability border given by the solid line.

In the model investigated so far, which seems especially to be applicable to MT-motor systems, the ATP supply has been assumed either to be held constant or to be abundantly supplied externally, since the motor coefficients and therefore the density of active motors have been considered as constants. In the actomyosin experiments of Smith et al. however, in the course of time the motors consume ATP which leads to transitions from active to nearly permanently inactive motors upon depletion of ATP. As has been mentioned in the discussion of the motor cycles in section 2.2.3, a myosin head carrying ADP sticks to the filament until it gets a new ATP. Thus upon ATP depletion, the actin filaments become coated with inactive motor heads while however some other heads of the same oligomer still may carry ATP. If the latter attach to other filaments they also hydrolyze their ATP and stick. In this way the inactive motors tend to crosslink the actin filaments to form small filament clusters or bundles as sketched in the boxes 2) and 3) of Fig. 13.2 and as confirmed experimentally in Fig. 13.4. At the beginning of the experiment, this crosslinking effect should be only temporary while later on it should be quite permanent since the free ATP is depleted.

I propose here a simple scaling argument, why this clustering may render the system unstable, i.e. crossing the instability border. As discussed above, in the initial stage the local and temporary crosslinking by inactive motors should enhance the actin filament concentration locally and induce bundling, similar to the so-called zipping effect proposed in Ref. [153] near the point of gelation of actomyosin. Thus instead of the density of single filaments, ρ , as before we introduce the density ρ_{cl} of clusters containing N filaments, where N is assumed to be increasing with time due to the ATP depletion induced clustering. The overall number of filaments, i.e. the total amount of single filaments and filaments contained in clusters, is however a conserved quantity and thus the cluster density will decrease with time upon the clustering.

Let's have a look which consequences the clustering process has for the dynamics. First of all, diffusion scales with mass, and therefore decreases like $D_{cl} \propto 1/N$. For the active motor transport however there is evidence that it has not to decrease at the beginning:

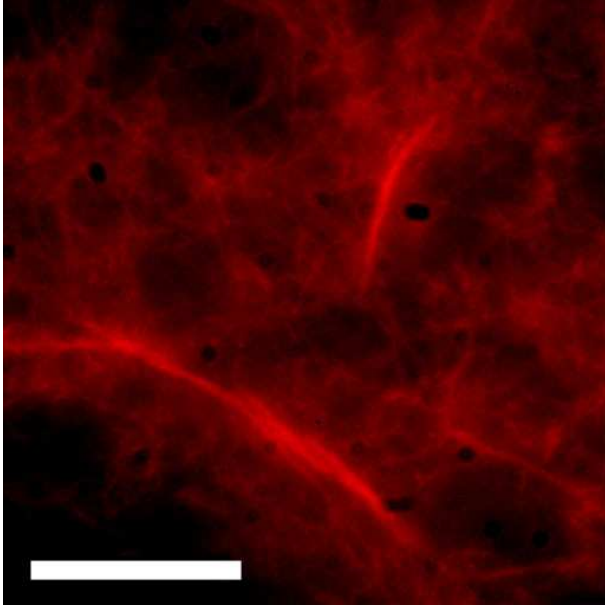


Figure 13.4: Confirmation of the actin bundling by inactive myosins: the myosin has been treated with NEM that forces it to the rigid coupling state [152]. One can clearly see at least two distinct bundles. No permanent crosslinkers are present. The scale bar is $15\mu\text{m}$, actin concentration is $2.4\mu\text{M}$, and there are approximately 50 myosin oligomers per actin filament. The picture will be published in [38].

First, in spite of myosin forming rigor bonds during depletion, a moderate increase of the rigor bonds does not impede filament motion since ADP-HMM-actin bonds are strongly weakened by tangential forces of the order of 10pN [154]. Second, it is known that the motor force of both kinesin and myosin exceeds the force needed for transport. E.g. a kinesin motor can move a small MT fragment as fast and efficiently as a MT of up to $50\mu\text{m}$ length [5]. Therefore as proposed for the zipping effect in Ref. [153], clusters of a few filaments can still be transported.

Moreover, if one looks closer at the motor transport rate α , there is evidence that the transport may even be more efficient in the case of clusters. This is due to the fact that α contains also the probability that a motor attaches to a filament pair, i.e. the cross section. It has been estimated [40, 120] that (in three dimensions and in the nomenclature of section 2)

$$\alpha \simeq \beta \simeq L\gamma = (mrs/\tau_{total}) \times (Lb^2) , \quad (13.1)$$

where m is the (assumed homogeneously distributed) motor density, r the duty ratio, s the step size of the motor and τ_{total} the time it needs for one motor cycle. L and b are the length and the diameter of the filaments respectively. For the first part reflecting the motor properties, it has been already argued above that it should not decrease in the beginning of the crosslinking - of course at a certain degree of depletion the dependence on m will finally lead to the freezing. The latter part however, governed by the filament properties, can be interpreted as the cross section of two intersecting filaments. The probability of a motor to attach to two filaments is larger if the filaments are thicker or longer. Thus the crosslinking leads to an enhancement of the cross section, i.e. it is more probable for a motor to hit a filament cluster than to hit a single filament. Together with the decreased diffusion this leads to an increase of the cluster-related motor activity α_{cl} .

We conclude that the system should show the following tendency: The cluster density ρ_{cl} decreases due to the conservation of mass and the diffusion coefficient D_{cl} also decreases. However, at moderate depletion where there are still enough active motors to overcome the bonds of the inactive ones, the cluster-related active motor transport α_{cl} increases since it is more probable to find and then transport another cluster as compared to single filaments. In a linear instability diagram in the ρ_{cl} - α_{cl} -plane², cf. the ones in the ρ - α -plane discussed in chapter 9, e.g. Fig. 9.5, this behavior translates into the tendency depicted by the arrow in Fig. 13.3. Thus the clustering process due to ATP depletion may drive the system into the unstable, i.e. pattern forming, range of the instability diagram. If the depletion process proceeds, ultimately the factor m in Eq. (13.1), i.e. the density of the active motors, goes down and leads to a freezing of the pattern.

One should notice that the process discussed above could be considered as a switching, as suggested in Fig. 13.2: if the structure is frozen-in and ATP afresh is introduced into the system, e.g. as in the experiments with the ATP/caged-ATP mixture, one gets very quickly the dynamical disordered state again. This switching between dynamical disorder and frozen-in order may be of use for the cell, especially since such a process is not possible in the microtubule-motor system.

13.2 Permanent crosslinkers introduce disorder

Describing a complex fluid like the cytoskeleton by a mean field approach - as all theoretic efforts do so far apart from the MD simulations in Refs. [31, 33] - neglects the inherent presence of disorder in biological cells. Especially, besides the dynamic filament interaction via the motor proteins, actin filaments may also be linked quasi-permanently by various crosslinker proteins, e.g. streptavidin, α -actinin, filamin, fimbrin and others [2]. Such crosslinkers are used by the cell in rather high concentrations to form gels and networks, e.g. the cell cortex underneath the membrane. *In vitro*, these actin-linking proteins lead in high concentrations to gels and networks of semiflexible polymers which are in the focus of a number of mechanical investigations [155, 4].

Prior to the *in vitro* experiments, both the motors and the filaments are extracted from cells and undergo several purification procedures. However, it is very likely that a small amount of such linking proteins still remains in the solution. Such small fractions of crosslinking proteins may cause small clusters of actin filaments. Since the oligomeric motor proteins can still bind to such clusters, filaments may still undergo motor transport relative to these clusters. Therefore the cross-linked clusters represent a realization of a disorder in the cytoskeleton problem.

It is known in the framework of pattern formation, that the influence of disorder may change a bifurcation from a spatially homogeneous state to a spatially periodic state considerably, as has been studied and established for models of pattern formation in hydrody-

²In the case of the demixing instability, since ρ_d^β is independent of both β and D_r , only α and ρ determine the instability. However the dispersion, i.e. the growth rates of the unstable wavenumbers, is changed also through varying β and D_r , which however is a higher order effect.

dynamic [149, 156, 151, 150] and chemical systems [157, 158]. Especially, the onset of pattern formation is reduced by the disorder, a mechanism which could explain the different behavior of the actomyosin in the presence and absence of crosslinking proteins.

Our modeling efforts so far were based on the assumption that filaments are only temporarily and dynamically linked by motor proteins. The coarse-grained description by Eqs. (8.4) led to *ideal* patterns like stripes or asters in the stationary case discussed in chapter 10, traveling waves in the oscillatory case, cf. chapter 11, and to demixing patterns as shortly addressed to in chapter 12. If there additionally is a small but finite amount of crosslinkers in the solution, which is too small for the system to percolate and build up a gel or a network structure like in the cortex, this should be captured in the modeling by some noise contributions. As already mentioned above, the small amount of crosslinkers may cause randomly distributed small clusters of several filaments. The motors still walk on such clusters and transport the single filaments from the solution. Since the clusters contain several filaments and diffusion scales with mass, these clusters diffuse much slower than single filaments, if at all, and thus can be regarded in a first approach as a time independent, frozen random contribution that effects both the mean filament density ρ_0 and the motor transport parameters. The contribution to the density is clear since at the place of a cluster the density is higher. Additionally there is a much higher probability that an oligomeric motor protein hits a cluster than a single filament. Thus single filaments may be transported with a higher efficiency with respect to clusters than with respect to single filaments, similar as during the clustering process due to ADP-myosin in the last section. Therefore the effective motor transport parameter α (and also β and γ) adapts different values close to such a cluster than close to a single filament.

To conclude, a small amount of crosslinkers leads to randomly distributed clusters which cause a frozen random contribution either to the mean density or to the motor parameters (or to both in the general case). To catch the qualitative features, I will discuss here only one of these possible contributions. As discussed in section 9.5.1, the instability borders are of hyperbola type in the ρ - α -plane, thus both contributions should lead at least qualitatively to the same effect. Moreover we can also decide to regard the motor transport parameter α as being the control parameter instead of the filament density ρ_0 . We will choose here the latter interpretation just for technical reasons: it is more convenient to regard a parametric noise term $\alpha(x)$, which enters the equations as a multiplicative parameter, instead of a noise in ρ which would appear in Eqs. (8.4) in the arguments of spatial derivatives.

If we assume a small magnitude of the random contribution, the major effects of the disorder should be taken into account close to the bifurcation point in the framework of the respective amplitude equations. For simplicity, I discuss here only the case of a stationary supercritical bifurcation to a pattern that is spatially periodic in one direction³, i.e. the stripe solution.

³The same arguments hold also for the two-dimensional aster case as well as for the oscillatory case. The demixing instability however can not be treated this way, since there is not a simple amplitude equation due to the inherent coarsening. It should be investigated by a Cahn-Hilliard-like model with similar disorder contributions.

Performing the same analysis as discussed extensively in section 10.1.2, but with a motor parameter that has small spatially randomly distributed contributions

$$\alpha = \alpha_0 + \alpha_1(x)\varepsilon^{1/2} + \alpha_2(x)\varepsilon + \dots, \quad (13.2)$$

where α_0 corresponds to the homogeneous contribution discussed so far in this work, one gets the hierarchy of equations, cf. Eqs.(10.22),

$$\varepsilon^{1/2} : \mathcal{L}_0 \mathbf{w}_1 = 0, \quad (13.3a)$$

$$\varepsilon : \mathcal{L}_0 \mathbf{w}_2 = -\mathcal{L}_1^\alpha \mathbf{w}_1 - \mathcal{N}_\rho(\mathbf{t}_1) e_\rho, \quad (13.3b)$$

$$\varepsilon^{3/2} : \mathcal{L}_0 \mathbf{w}_3 = \partial_T \mathbf{w}_1 - \mathcal{L}_2 \mathbf{w}_1 - \mathcal{L}_2^\alpha \mathbf{w}_1 - \mathcal{N}_x(\rho_2, \mathbf{t}_1). \quad (13.3c)$$

Here the additional linear operators \mathcal{L}_1^α and \mathcal{L}_2^α contain the contributions of \mathcal{L}_0 proportional to α with the latter parameter replaced by α_1, α_2 respectively.

In the order $\mathcal{O}(\varepsilon)$, the term $\mathcal{L}_1^\alpha \mathbf{w}_1$ is the only resonantly forcing one implying that $\alpha_1 = 0$ must hold. In the next order $\mathcal{O}(\varepsilon^{3/2})$ however, the respective term $\mathcal{L}_2^\alpha \mathbf{w}_1$ yields a contribution $\propto \alpha_2(x)X$ with X the pattern amplitude. Thus the respective amplitude equation reads

$$\tau_0 \partial_t X = (\varepsilon + \xi(x) + \lambda^2 \partial_x^2) X - g_1 |X|^2 X, \quad (13.4)$$

with the random contribution $\xi(x) \propto \alpha_2(x)$. As compared to Eqs. (10.13) in their one-dimensional limit, we have additionally allowed for slow spatial variations of the amplitude with the coherence length λ , cf. e.g. [42], which can also be derived straightforwardly from the underlying model.

In principle, the disorder may cause different contributions: it can enter additively or multiplicatively. Additionally, a frozen randomness destroys the translational invariance and therefore allows for quadratic contributions in the amplitude. In the simplified case investigated here, the parametric noise term $\xi(x)$ enters into Eq. (13.4) multiplicatively.

The effect of the multiplicative noise in this amplitude equation has been studied recently [150, 159]. Assuming for the noise a vanishing mean value $\langle \xi(x) \rangle = 0$ and correlation

$$\langle \xi(x) \xi(x') \rangle = B \delta(x - x'), \quad (13.5)$$

one gets two main effects due to the noise. First, while in the absence of noise the solutions $A(x)$ are ideal patterns, i.e. spatially periodic functions, in the presence of noise, and depending on the noise amplitude, $A(x)$ becomes localized. This effect however is most strongly pronounced at the threshold and becomes weaker for larger values of the control parameter. Second, and more important for the actomyosin system under investigation, a reduction of the threshold has been found. While in the case without noise the threshold is simply $\varepsilon_c = 0$, the ensemble average of the threshold in the presence of noise decreases like $\langle \varepsilon_c \rangle \propto -B$, as has been shown in Ref. [150].

We can conclude that the occurrence of disorder in the filament-motor system caused by small amounts of permanent crosslinkers leads to a threshold reduction. Thus we expect pattern formation in cytoskeletal solutions to be more likely in the presence of crosslinkers than in a pure filament-motor solution, as reflected in the experiments in Ref. [38].

13.3 Discussion

In this chapter we gave arguments how the model investigated so far should be interpreted and generalized to account for the recent experiments with actomyosin in Ref. [38]. First, we highlighted the importance of temporary clustering due to the ATP depletion. In the continuum model, this could be caught by interpreting both density and orientation field as related to such clusters, which are still growing in size. Thus the system should behave as indicated by the arrow in Fig. 13.3, i.e. it may cross the instability border after some time of depletion and clustering. Ultimately however, the system and the emerging patterns will freeze. Further on we mentioned that the mechanism of ATP depletion could be used as a switch between a dynamical disordered state and a frozen-in ordered state in the actin-myosin system, which may be used by the cell. This mechanism is not possible in the microtubule-kinesin system, since kinesin binds to the microtubule only in the presence of ATP, i.e. upon depletion there is no more contact between the motors and the filaments and the solution gets isotropic and homogeneous again.

In the second part of this chapter we discussed pattern formation in a cytoskeletal solution consisting of filaments, motor proteins and crosslinkers, e.g. streptavidin as in the experiments of Ref. [38]. Such an addition of crosslinkers introduces in the dilute case, due to the formation of small filament clusters, an inherent parametric disorder into the pattern formation problem. If this disorder is weak, its effects can be taken into account close to the threshold by the amplitude equations, or in case of the demixing instability this should be done by a reduced equation of Cahn-Hilliard form. For the stationary orientational instability, we have exemplified that the disorder enters multiplicatively in the amplitude equation and that it reduces the onset of pattern formation considerably. The multiplicative noise in Eq. (13.4) is however only the simplest to achieve. Also additive noise can be included if both ρ and \mathbf{t} have disorder contributions. We expect that additional random effects amplify the trend further and make pattern formation possible at even smaller values of the control parameter. One could even imagine nonlinear multiplicative contributions like $\xi_2(x)A^2$ and $\xi_3(x)|A|^2$, since the frozen randomness destroys the translational invariance and therefore allows for quadratic contributions in the amplitude.

The recent experiments in actin-myosin systems with small fractions of streptavidin crosslinkers [38] support the importance of the disorder-induced threshold lowering effect. The inherent presence of disorder in biological systems should provide many other examples rendering the general problem of the effects of disorder on pattern forming systems, which has not been in the focus up to now, an interesting field of investigation.

Chapter 14

Summary/Zusammenfassung

14.1 Summary

In this work I have studied pattern formation in nonequilibrium biopolymer systems motivated from cell biology. The biopolymers actin and microtubules are met both *in vivo* and *in vitro* either in a state with rather fixed lengths (regulated by proteins) or in a state where they are continuously polymerized and depolymerized. In the latter case, which is extensively used by the cell e.g. during cell locomotion, the system is in nonequilibrium since the polymerization is actively coupled to ATP or GTP hydrolysis. A second interesting nonequilibrium state of highly biological relevance is caused by so-called motor proteins. These are mobile crosslinkers that walk on the filaments whereby creating forces and reorienting or transporting them if in contact with several biofilaments.

The cell displays manifold highly ordered structures related to filaments like aster patterns in the mitotic spindle [8, 108], bundles in actin stress fibers [160], two-dimensional networks in the actin cortex underneath the cell membrane [161], three-dimensional actin gels [162], and also oscillating structures are known from skeletal muscle bundles [144, 145] and during cell development of amphibian eggs [146]. It is an interesting question to what extent these structures inside the cell are governed by biochemistry, i.e. regulation, and to what extent the physics of active polymers contributes to its formation.

A living cell is a nonequilibrium system since the ATP hydrolysis reaction is kept far on the side of ATP by means of metabolic reactions, and is highly regulated by complex interaction of many proteins. However, recent experiments [30] are indicating that the regulation pathways of the cell are not necessary for the above mentioned processes. Thus the above mechanisms have been recently studied in reconstituted systems, like purified actin and microtubule solutions for the polymerization effects [17, 15, 107] and microtubules mixed with oligomeric kinesins [31, 33] as well as actin with myosin or myosin-minifilaments [104, 38] for the motor-related transport effects. The conditions, i.e. temperature, ionic strength etc., are kept similar as in a cell and the chemical fuel, namely ATP or GTP, can be varied. In contrast to a living cell, such model systems can be controlled externally and thus open the way for qualitative and in the future hopefully quantitative data, making

also theoretical work necessary to which I want to contribute in this work.

In the first part of my work, I addressed the active polymerization state of both actin filaments and microtubules and we proposed a pattern forming mechanism in a filament solution at high density that is subject to such a polymerization. Since actin and microtubules are rather stiff rod-like objects, at high filament concentration a transition to lyotropic nematic order occurs [19, 20, 21]. As known from both Onsager and Landau theory, this transition is first order and thus accompanied by a phase separation process. Thus a solution of high filament density in the absence of polymerization kinetics will ultimately tend to decompose into an isotropic domain with low density and a second domain of high density with nematic order, i.e. the filaments preferentially aligned in one direction. The complex polymerization processes present in the biopolymers actin and microtubules should interplay with this transition. To highlight this we chose the most simple process, namely we assumed that filaments are generated and decaying with some specific rates, implying that the filaments have a finite lifetime. Accordingly the filaments can only diffuse a finite length during their lifetime, which competes with the tendency of the system to phase separate. Both processes in sum give a finite wavelength instability towards a pattern with alternating isotropic and nematic regions, as predicted by us in a phenomenological model.

The phenomenological model that is developed and motivated by us is interesting for several reasons. It is the first model that allows for a feasible linear stability analysis of the homogeneous nematic branch with respect to inhomogeneous perturbations and has been used by us to investigate the pattern forming instability in the presence of polymerization kinetics. Second it corrects the contradiction between microscopic theories predicting that the isotropic state is linearly unstable against phase separation for densities larger than the density of the isotropic-nematic transition, while Onsager theory predicts phase separation only within the coexistence region, i.e. only up to an upper density border. In our model the nonlinearities favor a homogeneous nematic phase for large enough filament density, in agreement with the Onsager model, stressing that a linear analysis on its own can give a misleading picture. Third, though the model is phenomenological and based on the most simple ingredients like a Landau-deGennes-type contribution to model the isotropic-nematic transition and Cahn-Hilliard-like contributions to implement the phase separation, various parameters can be fixed by comparison with the Onsager model or with experimental data.

The phenomenological model has been extended by a simplified polymerization/depolymerization kinetics and we could show that the pattern forming process results in a pattern of alternating isotropic and nematic regions. This process is very robust against parameter variations and the wavelength of the pattern can be estimated by the diffusion coefficient and the lifetime of the filaments to be of the order of $10\mu\text{m}$, implying a few filament lengths. The periodic solutions also prevail in a quite large density range to be observable.

In the second part of my work, the nonequilibrium interaction of motor proteins with the filaments has been addressed. Various structures like asters, vortices and bundles have been reported in microtubule-kinesin mixtures in Refs. [31, 33]. There it has also been

argued that these patterns could be dissipative structures driven by ATP hydrolysis. This chemical fuel is consumed by the motors which transport and reorient the filaments while moving on several filaments simultaneously.

As the starting point of our modeling we chose a mesoscopic approach based on propositions for one-dimensional filament bundles in Refs. [114, 41] and applied to two- and three-dimensional filament-motor solutions in Ref. [40]. I extensively review the statistical basis of the model and how the Smoluchowski equation can be coarse-grained to obtain equations for physical observables like the filament density and the filament orientation field. The main ingredient that distinguishes the filament-motor model from a usual solution of rigid rods, as described e.g. by the Doi model, are active motor-mediated currents which are assumed to be caused by a sufficiently high and homogeneously distributed motor density. These active contributions can be determined by considering two-filament interaction mediated by molecular motors, which involve some phenomenological motor transport rates containing details of the motors like active motor density, step size, duty ratio, etc.

The coarse-grained model can be cast into a rescaled form, with very few and distinctive parameters: first the overall filament density, which upon filament-filament interaction is involved in any ordering process. Second the rescaled rotational diffusion coefficient, which favors an isotropic solution (translational diffusion favoring a homogeneous solution is also present in the model but the parameter can be rescaled) and third two parameters involved in translational and one in rotational motor-induced transport.

In order to make an investigation of the coarse-grained equations with respect to its propensity for pattern formation possible, it turned out that the gradient expansion of the motor-mediated filament-filament interaction had to be continued up to fourth order, which has been not recognized in Ref. [40] leaving that analysis questionable [46]. After a thorough linear analysis we obtained a rich instability diagram with an orientational finite wavelength instability which is either stationary or oscillatory and a demixing instability similar in behavior to spinodal decomposition but also mediated actively by the motors. In addition, a homogeneous nematic transition may take place, which is not of relevance in the pattern forming experiments since the filament densities are by orders of magnitudes lower than the density for the isotropic-nematic transition. The relevant motor parameter rendering the system unstable could be identified as the one in front of the active motor-mediated translational current that describes in the one-dimensional model the interaction of parallel filaments. However, increasing the filament density equally leads to the crossing of instability borders, a result which is robust and also found in different models [119].

With regard to the aster-like patterns seen in experiments in a quasi-two-dimensional geometry, we first analyzed the stationary finite wavelength instability in detail, namely by a weakly nonlinear perturbation analysis and by numerical simulation of the coarse-grained model equations. In a two-dimensional system, at threshold either stripes, squares or hexagonal patterns are preferred. In the model under consideration, hexagons could be ruled out and we could calculate the existence and stability regions of stripes and squares as functions of the relevant system parameters. Translating the critical eigenvector back to the density and the orientation field of the filaments, the obtained stripe and

square patterns can be identified with a bundle-like structure and with a regular lattice of asters respectively. The tendency that upon increase of motor activity a transition from asters to bundles takes place could be found in the model, however we did not obtain any vortex patterns as found in the experiments. The wavelength of the aster patterns and the phenomenological motor transport rates needed to obtain them can be estimated and lie in the range suggested by the experiments.

We also studied the oscillatory finite wavelength instability both in one and two dimensions, although concrete and detailed experiments are lacking. There is however evidence for an oscillatory behavior in filament-motor systems both in one-dimensional structures like in a muscle bundle [144, 145] as well as in two-dimensional networks connected with the membrane as the surface contraction waves known to be relevant in cell development of amphibian eggs [146]. The parameter that renders the finite wavelength instability oscillatory could be identified as the one in front of the so-called polarity sorting contribution, which in the one-dimensional model describes interaction of oppositely oriented filaments. Both the phase between the spatial periodicity of the density and the orientation of the filaments and the critical frequency of the oscillatory pattern increase with the polarity sorting, the relative phase approaching π for large values of it. In the weakly nonlinear regime, there is competition between traveling and standing waves in one dimension and between traveling and alternating waves in two dimensions. Alternating waves are four mode solutions built from two standing waves in perpendicular directions with a phase shift of $\pi/2$. The oscillatory bifurcation is subcritical in a larger fraction of the parameter space as compared to the stationary bifurcation. We also investigated the influence of a third order excluded volume term, which enlarges the supercritical region and in both one and two dimensions favored traveling waves against two or four mode solutions respectively. The nonlinear pattern competition is only slightly affected by variations of the polarity sorting parameter.

The long-wavelength demixing instability has also been investigated. It is not a true pattern forming instability with a definite critical wavenumber but rather has a fastest growing mode governing the initial dynamics followed by a slow coarsening behavior similar to spinodal decomposition and phase ordering dynamics [88]. However, it is also a good candidate for the aster patterns seen in the experiments of Refs. [31, 33]. The presence of the polarity sorting parameter breaks the \pm -symmetry with respect to the orientation and introduces a relative phase shift between density and orientation of $\pm\pi/2$, depending on the sign of the polarity sorting parameter. This allows to discriminate aster-like structures with the filaments pointing outwards from those with the filaments pointing inwards. This has not been the case for the asters formed through the finite wavelength instability discussed above, but is suggested from the experiments where plus end-directed motors favored asters pointing inwards and minus end-directed motors those pointing outwards.

Recently performed experiments on mixtures of actin filaments and myosin minifilaments show a rather surprising pattern formation behavior [38]. Although this is a similar system as the microtubule-kinesin mixture, its behavior is very different: In contrast to the microtubule-motor solution which displays dissipative patterns in the nonequilibrium, high-ATP state, in the case of actomyosin cluster-like patterns appear not until ATP is nearly

fully depleted. We propose here two qualitative mechanisms which we believe are relevant in causing these patterns. First, it is known that myosin in its inactive, ADP-carrying state forms rigor bonds with actin and thus may induce small clusters or bundles of actin. Due to a combination of reduced diffusivity and enhanced interaction cross-section, these clusters can be transported more efficiently than single filaments and the system may cross one of the instabilities as investigated above in the filament-motor model. If ATP becomes more depleted, i.e. as more and more myosins are forming rigid bonds, the dependence of the motor transport on the active motor density ultimately leads to a freezing of the pattern.

A second important ingredient in actomyosin patterns is the presence of crosslinking proteins, namely streptavidin, in the experiments in Ref. [38]. Such proteins permanently (on the time scale of the experiments) link filaments in contrast to the motor proteins which can be considered as mobile, temporary crosslinkers. The experiments show that pattern formation is more likely and that patterns become more pronounced with increasing crosslinker to actin filament ratio. Here we propose that as discussed before for the actomyosin system, an instability could be crossed due to temporary clustering through inactive motors. However, the permanent crosslinkers also lead to a formation of clusters from the very beginning and the presence of the latter can be interpreted as a parametric disorder in the problem. It is known from other pattern forming systems [149, 151] that such a disorder lowers the threshold. Indeed, assuming a random contribution to the active translational current in the filament-motor model, a Ginzburg-Landau equation with multiplicative stationary noise term could be derived, for which the threshold lowering has been established recently [150].

To conclude, inspired by the recent experimental investigations of the cytoskeleton it seems to be fruitful to apply and combine methods from statistical physics such as probability distribution functions and coarse-grained or macroscopic equations, as well as methods inspired from pattern formation in e.g. hydrodynamic systems like stability analysis and amplitude equations, to nonequilibrium problems in cell biology. One has to keep in mind that such highly complicated processes like e.g. the formation of the mitotic spindle are of course bioregulated and presumably cannot be explained within a mathematical model that relies solely on physical arguments. Nevertheless it is crucial to better understand the constituents like actively polymerizing filament and motor proteins in their different nonequilibrium states to which this work is devoted.

14.2 Zusammenfassung

In dieser Arbeit wurde die Musterbildung von Polymersystemen im Nichtgleichgewicht, wie sie in der molekularen Zellbiologie auftreten, untersucht. Die Biopolymere Aktin und Mikrotubuli können sowohl *in vivo* als auch *in vitro* entweder in einem Zustand fester Länge, die durch zusätzliche Proteine reguliert wird, oder in einem Zustand der kontinuierlichen Polymerisation und Depolymerisation vorliegen. Im letzteren Zustand, der essentiell z.B. für die Zellbewegung ist, liegt ein Nichtgleichgewichtszustand vor, da die Polymerisation an die Hydrolyse des Zelltreibstoffs ATP oder GTP gekoppelt ist. Ein zweiter interessanter Nichtgleichgewichtszustand von großer biologischer Bedeutung wird durch sogenannte Motorproteine verursacht. Das sind Proteine, die auf den Biopolymeren entlanglaufen, wobei sie auf diese Kräfte ausüben und diese reorientieren und transportieren können, sofern sie in Kontakt mit mehreren solcher Biofilamente sind.

Die Zelle weist mannigfaltige hochgeordnete Strukturen auf, die mit den Biofilamenten zusammenhängen, wie z.B. sogenannte Astern in der mitotischen Zellspindel [8, 108], Bündelstrukturen in Aktin-Streißfasern [160], zweidimensionale Netzwerke im Aktinkortex unterhalb der Zellmembran [161] und dreidimensionale Aktin-Gele [162]. Auch oszillierende Strukturen wurden gefunden, so z.B. in Muskelbündeln [144, 145] und im Laufe der Zellentwicklung von Amphibieneiern [146]. Es stellt sich die interessante Frage, inwiefern diese Strukturen in der Zelle von der Biochemie, etwa durch Regulierung durch zusätzliche Proteine, und inwiefern von der Physik der aktiven Biopolymere bestimmt werden.

Eine lebende Zelle ist ein Nichtgleichgewichtssystem, da die ATP-Hydrolyse durch den Zellstoffwechsel stark auf der Seite des hochenergetischen ATPs gehalten wird. Zur Aufrechterhaltung dieses Zustands sind im Allgemeinen komplexe Regulierungsprozesse nötig. Kürzlich haben jedoch Experimente aufgezeigt [30], daß diese Regulierung - zumindest für die oben beschriebenen Prozesse - nicht unbedingt notwendig ist. Deshalb wurden diese Prozesse anhand von einfacheren Modellsystemen experimentell untersucht, so z.B. in zellextrahierten und gereinigten Lösungen von Aktinfilamenten und Mikrotubuli im Falle der Polymerisationseffekte [17, 15, 107] und in Mischungen aus Mikrotubuli und oligomeren Kinesin-Motoren [31, 33] sowie in solchen von Aktin und Myosin-Motoren [104, 38] im Falle des von den Motoren verursachten Transports. Die äußeren Bedingungen, d.h. Temperatur, Ionenkonzentrationen etc. werden dabei ähnlich denen der Zelle gehalten und der chemische Treibstoff, ATP oder GTP, kann variiert werden. Im Gegensatz zu einer lebenden Zelle können solche Modellexperimente extern kontrolliert werden und eröffnen daher Wege zu zunächst qualitativen und hoffentlich bald quantitativen Untersuchungen, die wiederum theoretische Modellarbeit erfordern, zu der ich hier mit beitragen möchte.

Der erste Teil meiner Arbeit befasst sich mit dem Zustand der aktiven Polymerisation, wie er sowohl in Aktinfilamenten als auch in Mikrotubuli vorkommt. Für eine hochkonzentrierte Biopolymerlösung, die solch eine Polymerisation durchläuft, schlagen wir einen neuen Mechanismus der Musterbildung vor. Da Aktinfilamente und Mikrotubuli recht steife, stäbchenförmige Objekte sind, kommt es für hohe Konzentrationen zur Ausbildung einer lyotropen nematischen Phase [19, 20, 21]. Wie von der Onsager- und auch der Landau-Theorie bekannt, ist dieser Phasenübergang von erster Ordnung und daher von

einem Prozess der Phasentrennung begleitet. Eine hochkonzentrierte Biopolymerlösung wird daher - in Abwesenheit der Polymerisationskinetik - schließlich separieren in eine isotrope Domäne mit niedriger Filamentdichte und in eine nematisch orientierungsgeordnete Domäne mit hoher Dichte. Der komplexe Polymerisationsprozess der Biopolymere sollte mit dieser Phasenseparation im Wechselspiel stehen. Um dies zu untersuchen, haben wir den einfachstmöglichen Polymerisationsprozess betrachtet und angenommen, daß die Filamente mit jeweils einer festen Rate generiert werden und wieder zerfallen. Dies führt insbesondere dazu, daß die Filamente eine endliche Lebensdauer erhalten. Folglich können die Filamente innerhalb ihrer Lebensdauer auch nur eine endliche Strecke durch Diffusion zurücklegen. Diese Beschränkung steht im Wettbewerb mit dem Bestreben des Systems zur Phasentrennung. Anhand eines phänomenologischen Modells sagen wir voraus, daß dieses Wechselspiel eine Instabilität mit endlicher Wellenlänge ergibt, aus der sich ein alternierendes Muster von isotropen und nematischen Bereichen ausbildet.

Das phänomenologische Modell, das von uns entwickelt wurde, um den neuen Musterbildungsprozess zu beschreiben, ist auch aus anderen Gründen interessant. Es ist das erste Modell, an dem eine lineare Analyse des homogenen nematischen Astes gegenüber inhomogenen Störungen machbar ist, was von uns ausgenutzt wurde, um die Musterbildung analytisch zu untersuchen. Zum Zweiten löst es den Widerspruch zwischen mikroskopischen Theorien, die vorhersagen, daß der isotrope Zustand für alle Dichten, die größer als die Dichte des isotrop-nematischen Überganges sind, linear instabil gegenüber einer Phasenseparation ist, wohingegen die Onsager-Theorie, d.h. die Thermodynamik, eine solche Phasentrennung nur im endlichen Dichteintervall des Koexistenzbereiches zulässt: in unserem phänomenologischen Modell bevorzugen die Nichtlinearitäten für große Dichten den homogenen nematischen Zustand, wie von der Thermodynamik gefordert und es zeigt sich damit, daß eine lineare Analyse für sich genommen ein irreführendes Bild liefern kann. Zum Dritten können, obwohl das Modell phänomenologisch und auf den einfachstmöglichen Argumenten wie einem Landau-deGennes-Anteil, der den isotrop-nematischen Übergang implementiert, und Cahn-Hilliard-Anteilen, die die Phasenseparation modellieren, aufgebaut ist, mehrere Parameter durch Vergleich mit der Onsager-Theorie oder auch experimentellen Daten festgelegt werden, was die Anzahl der freien Parameter einschränkt.

Das phänomenologische Modell wurde von uns um eine vereinfachte Polymerisationskinetik erweitert und wir konnten zeigen, daß der Musterbildungsprozess in einem alternierenden Muster von isotropen und nematischen Bereichen resultiert. Es wurde gezeigt, daß dieser Prozess robust gegenüber Parametervariationen ist, und die Wellenlänge konnte über den Diffusionskoeffizienten und die Lebensdauer der Filamente abgeschätzt werden und liegt in der Größenordnung $10\mu\text{m}$, also im Bereich weniger Filamentlängen. Zudem existiert das Muster in einem recht großen Bereich der Filamentdichte und sollte also beobachtbar sein.

Der zweite Teil meiner Arbeit ist der von den Motorproteinen verursachten Wechselwirkung der Biofilamente gewidmet. In Experimenten an Mischungen von Mikrotubuli und Kinesinmotoren wurden zahlreiche Strukturen wie Asten, Vortizes und Bündelstrukturen beobachtet [31, 33]. Dort wurde auch erstmals argumentiert, daß diese Muster dissipative Strukturen sein könnten, die von der ATP-Hydrolyse aufrechterhalten werden. Dieser

chemische Treibstoff ATP wird von den Motoren verbraucht, um die gerichtete Bewegung längs der Filamente auszuführen bzw. um die Filamente zu transportieren und zu reorientieren, wenn ein Motoroligomer mit mehreren Filamenten in Kontakt ist.

Als Ausgangspunkt unserer Modellierung wurde ein mesoskopischer Zugang gewählt, der für eindimensionale Filamentbündel vorgeschlagen [114, 41] und auf Mischungen von Motoren und Filamenten in mehreren Dimensionen verallgemeinert wurde [40]. Ich bespreche ausführlich die statistische Grundlage des Modells und wie die Smoluchowski-Gleichung vergrößert werden kann, um Kontinuumsgleichungen für physikalische Observablen wie die Filamentdichte und die Filamentorientierung zu erhalten. Der Hauptunterschied des Motor-Filament-Modells im Vergleich zu einer passiven Flüssigkeit von starren Stäbchen, wie sie z.B. von der Doi-Gleichung beschrieben wird, sind aktive Ströme, die von den Motoren verursacht werden, deren Konzentration als ausreichend hoch und nahezu homogen angenommen wird. Diese aktiven Beiträge der Gleichung können bestimmt werden, indem die Wechselwirkung eines Filamentpaares betrachtet wird, und sie enthalten phänomenologische Transportraten, die die Details der Motoren, wie z.B. die Motorkonzentration, die Schrittweite, die Verweildauer auf dem Filament, etc. enthalten.

Die Kontinuumsgleichungen können in eine reskalierte Form gebracht werden, in der nur sehr wenige freie Parameter übrig bleiben: zunächst natürlich die Dichte der Filamente, die über die Filamentwechselwirkung an jedem Ordnungsprozess beteiligt ist. Zum Zweiten der Koeffizient der Rotationsdiffusion, die eine isotrope Lösung bevorzugt (der Parameter der Translationsdiffusion, die ein homogenes System bevorzugt, kann reskaliert werden) und schließlich drei Motortransportraten, zwei für die Translations- und eine für die Rotationsanteile des aktiven Transports.

Um das Kontinuumsmodell im Hinblick auf die Musterbildung analysieren zu können, hat sich herausgestellt, daß die Gradientenentwicklung der von den Motoren verursachten Filament-Filament-Wechselwirkungen bis zur vierten Ordnung durchgeführt werden muß. Dies wurde in der Originalarbeit von Liverpool et al. [40] nicht realisiert und läßt die dortige Analyse fragwürdig erscheinen [46]. Durch eine gründliche lineare Stabilitätsanalyse erhielten wir ein reichhaltiges Instabilitätsdiagramm, das eine Orientierungsinstabilität, die eine endliche Wellenlänge hat und entweder stationär oder oszillatorisch sein kann und eine Entmischungsinstabilität, die in ihrem Verhalten ähnlich der spinodalen Phasenseparation ist, jedoch von den Motoren aktiv verursacht wird, aufweist. Zusätzlich kann auch ein homogener isotrop-nematischer Phasenübergang stattfinden, der jedoch hier nicht von Relevanz ist, da die Dichten der Filamente in den Strukturbildungsexperimenten sehr viel geringer als die Übergangsdichte sind. Der Parameter der Motorraten, der die Instabilitäten verursacht, konnte mit demjenigen Parameter identifiziert werden, der im Translationsbeitrag in der eindimensionalen Version des Modells die Wechselwirkung parallel orientierter Filamente beschreibt. Eine Erhöhung in der Filamentdichte führt ebenfalls zum Überqueren der Stabilitätsgrenzen, ein Resultat das robust ist und auch in anderen Modellen gefunden wurde [119].

In Hinblick auf die Astermuster, die in den Experimenten in quasi-zweidimensionalen Geometrien gesehen wurden [31, 33], haben wir zuerst die stationäre Instabilität mit endlicher Wellenlänge genauer analysiert, und zwar sowohl analytisch mit einer schwach nicht-

linearen Störungsrechnung als auch numerisch durch Simulation des Kontinuumsmodells. In einem zweidimensionalen System werden nahe der Schwelle zur Musterbildung entweder Streifen-, Quadrat- oder Hexagonmuster bevorzugt. In dem hier betrachteten Modell können jedoch hexagonale Strukturen ausgeschlossen werden und wir konnten die Existenz- und Stabilitätsbereiche der Streifen- und Quadratlösungen als Funktion der relevanten Systemparameter berechnen. Übersetzt man den Eigenvektor der kritischen Mode zurück in Dichte und Orientierung der Filamente, so können die erhaltenen Streifenmuster mit Bündelstrukturen und das Quadratmuster mit einer regelmäßigen Anordnung von Atern identifiziert werden. Die Tendenz, daß eine Erhöhung der Motordichte zu einem Übergang der Atern zu Bündeln führt, wird im Modell korrekt wiedergegeben. Es konnten jedoch keine Vortizes, wie in den Experimenten gesehen, gefunden werden. Die Wellenlänge des Astermusters und die Größenordnung der phänomenologischen Motortransportraten können abgeschätzt werden und liegen in der experimentell realisierten Größenordnung.

Die oszillatorische Instabilität mit endlicher Wellenlänge wurde ebenso untersucht, sowohl in einer als auch in zwei Dimensionen. Es gibt zwar noch keine konkreten Experimente, wohl aber Hinweise auf oszillatorisches Verhalten in Motor-Filament-Systemen wie in Muskelbündeln [144, 145] und in zweidimensionalen Netzwerken in Verbindung mit der Zellmembran [146]. Der Modellparameter, der die Instabilität mit endlicher Wellenlänge oszillatorisch werden läßt, konnte identifiziert werden als derjenige im Translationsbeitrag der Motoren, der in der eindimensionalen Version des Modells die Wechselwirkung antiparallel orientierter Filamente beschreibt. Diese Wechselwirkung bewirkt auch das sogenannte "Sortieren nach Polaritäten". Sowohl die relative Phase zwischen der Filamentdichte und der Filamentorientierung als auch die kritische Frequenz des oszillatorischen Musters wachsen mit diesem Parameter an, wobei die Phase für große Werte des Parameters gegen π geht. Im schwach nichtlinearen Regime wurde in einer Dimension der Wettbewerb zwischen laufenden und stehenden und in zwei Dimensionen derjenige von laufenden mit sogenannten alternierenden Wellen beschrieben. Alternierende Wellen sind dabei Vier-Moden-Lösungen, die aus zwei stehenden Wellen in zueinander orthogonalen Richtungen bestehen, die eine zeitliche Phasenverschiebung von $\pi/2$ haben. Die oszillatorische Verzweigung ist in einem größeren Parameterbereich subkritisch, d.h. unstetig, als die stationäre Verzweigung. Der superkritische, d.h. stetige Bereich der Verzweigung konnte vergrößert werden durch einen Volumenausschlußterm in dritter Ordnung in der Filamentdichte - alle übrigen Terme des Modells sind höchstens von zweiter Ordnung, da diese auf der Wechselwirkung von zwei Filamenten gründen. Dieser Zusatzterm favorisiert sowohl in einer als auch in zwei Dimensionen die laufenden Wellen gegenüber den stehenden bzw. alternierenden. Der nichtlineare Wettbewerb der Muster wurde dagegen von dem Parameter, der die Polaritäten sortiert, nur sehr wenig beeinflusst.

Die langwellige Entmischungsinstabilität wurde ebenfalls untersucht. Dabei handelt es sich nicht um eine Musterbildungsinstabilität im engeren Sinne, die eine definierte kritische Wellenzahl aufweist und im Langzeitverhalten ein stationäres oder oszillatorisches Muster ergibt, sondern um eine Instabilität, bei der die Mode mit der schnellsten Wachstumsrate das Anfangsverhalten bestimmt und die für große Zeiten ein Vergrößerungsverhalten hin zu immer langwelligeren Mustern aufweist, wie man es von der spindodalen Entmischung her

kennt [88]. Dennoch kommt auch diese Instabilität für die Ausbildung der experimentell gefundenen Astermuster [31, 33] in Betracht. Die Anwesenheit des Parameters, der die Wechselwirkung der antiparallelen Filamente beschreibt, bricht die \pm -Symmetrie bezüglich der Filamentorientierung und bewirkt eine relative Phase von $\pm\pi/2$ zwischen Filamentdichte und Filamentorientierung, abhängig von dem Vorzeichen dieses Parameters. Dadurch werden verschiedene Asterstrukturen unterscheidbar, in denen die Filamente entweder nach außen oder ins Asterzentrum gerichtet sind. Dies war für die stationäre Instabilität mit endlicher Wellenlänge nicht der Fall, wird aber von den Experimenten nahegelegt, in denen Motoren, die zum Plusende des polaren Filaments wandern, Asten mit nach innen gerichteten Filamenten erzeugen und Motoren, die zum Minusende wandern, Asten mit nach außen gerichteten Filamenten.

Kürzlich wurde in Experimenten, die an Mischungen von Aktinfilamenten und Myosin-Oligomeren durchgeführt wurden, ein überraschendes neues Musterbildungsverhalten gefunden [38]. Obwohl das untersuchte System dem Mikrotubuli-Kinesin-System sehr ähnlich sieht, ist sein Verhalten völlig anders: Im Gegensatz zu der Mischung von Mikrotubuli mit Kinesin, die dissipative Strukturen im Nichtgleichgewichtszustand hoher ATP-Konzentration zeigt, bildet das Aktin-Myosin-System erst Muster aus, wenn der Treibstoff ATP fast gänzlich verbraucht ist. Wir haben hierzu zwei qualitative Mechanismen vorgeschlagen, von denen wir glauben, daß sie diese Muster erklären können. Zum Einen ist bekannt, daß der Myosinmotor in seinem inaktiven Zustand, in dem er an Stelle des Treibstoffs ATP das Hydrolyseprodukt ADP mit sich führt, fest an das Aktinfilament bindet. Daher können solche inaktiven Motoren durch Verarmungseffekte des zunehmend verbrauchten ATPs kleine Aktinbündel ausbilden. Durch eine Kombination von verringerter Diffusivität und einer erhöhten Transportwahrscheinlichkeit, können diese Bündel effizienter transportiert werden und das System im Zuge der ATP-Verarmung eine der oben diskutierten und analysierten Instabilitätsgrenzen überschreiten. Schließlich wird jedoch der Transport durch die stark verminderte Anzahl von aktiven Motoren einbrechen, und das System und die sich durch die Instabilitäten ausbildenden Muster "frieren" ein.

Ein zweiter wichtiger Faktor für die Ausbildung der Muster in den Aktin-Myosin-Systemen ist die Anwesenheit von Vernetzungsproteinen, im Falle der oben erwähnten Experimente Streptavidin [38]. Solche Proteine vernetzen die Aktinfilamente permanent (auf der Zeitskala der Experimente), im Gegensatz zu den Motorproteinen, die zwar, wenn sie in Kontakt mit zwei Filamenten sind, diese auch vernetzen, aber auf ihnen entlangwandern und sich mit einer gewissen Wahrscheinlichkeit wieder von ihnen lösen. Die Experimente zeigen, daß die Anwesenheit der permanenten Vernetzer die Musterbildung wahrscheinlicher macht. Wie oben vorgeschlagen, kann durch das temporäre Bündeln der Filamente durch die inaktiven Motoren eine der diskutierten Instabilitätsgrenzen überquert werden. Zusätzlich führen die permanenten Vernetzer ebenfalls zu einer Bündelung, und die Anwesenheit solcher Bündel von Beginn des Experiments an kann als eine inhärente Unordnung in dem System interpretiert werden. Von anderen Strukturbildungssystemen ist bekannt, daß solche Unordnungsbeiträge die Schwelle der Musterbildung absenken [149, 151]. Tatsächlich konnte durch Annahme einer Zufallskomponente im aktiven Translationsbeitrag der Motoren ähnlich wie bei den obigen Untersuchungen der Instabilitäten,

durch eine schwach nichtlineare Analyse eine Amplitudengleichung mit multiplikativem stationären Rauschen abgeleitet werden, für die kürzlich eine solche Absenkung der Schwelle berechnet wurde [150].

Im Hinblick auf die wachsende Zahl der Experimente an zellbiologischen Systemen, insbesondere dem Zellskelett und seinen Bestandteilen, kann man abschließend sagen, daß es sehr vielversprechend erscheint, Konzepte aus der statistischen Physik, der makroskopischen Beschreibung und der Strukturbildung auf diese Nichtgleichgewichtssysteme anzuwenden und diese zu kombinieren. Ich möchte nicht den Eindruck erwecken, als könne man ein solch komplexes Gebilde wie z.B. die mitotische Spindel, die durch eine komplizierte Biochemie reguliert wird, durch ein mathematisches Modell beschreiben, das nur auf physikalischen Prinzipien beruht. Dennoch ist es für das Verständnis dieser biologisch relevanten Strukturen unerlässlich, die beteiligten zellulären Bestandteile, in diesem Falle die aktiv polymerisierenden Biopolymere und die Motorproteine, in ihren unterschiedlichen Nichtgleichgewichtszuständen und ihre physikalischen Selbstorganisationsprozesse besser zu verstehen, wodurch ich hoffe durch diese Arbeit beigetragen zu haben.

Appendix A

Isotropic averages

The Doi Equation for rigid rods explicitly contains the orientation vector \mathbf{u} of the rods, which is a unit vector, $|\mathbf{u}| = 1$. To derive equations for the mean density or the mean orientation of the rods by the moment expansion technique as carried out in sections 4.1, 8.2.2 and 8.2.3, the following definitions and formulas are useful.

A.1 Isotropic averages in three dimensions

The three-dimensional isotropic distribution function is $\Psi(\mathbf{u}) = \frac{1}{4\pi}$ and the isotropic average can be defined by

$$\langle A(\mathbf{u}) \rangle = \int \frac{d\mathbf{u}}{4\pi} A(\mathbf{u}) = \int_0^{2\pi} \frac{d\varphi}{2\pi} \int_0^\pi \frac{d\theta}{2} \sin(\theta) A(\theta, \varphi) . \quad (\text{A.1})$$

with θ and φ two angles parameterizing the vector \mathbf{u} on the unit sphere. Averages of odd powers of components of \mathbf{u} vanish due to the $\pm\mathbf{u}$ -symmetry, while

$$\langle u_\alpha u_\beta \rangle = \frac{1}{3} \delta_{\alpha\beta} \quad (\text{A.2})$$

and

$$\langle u_\alpha u_\beta u_\mu u_\nu \rangle = \frac{1}{15} (\delta_{\alpha\beta} \delta_{\mu\nu} + \delta_{\alpha\mu} \delta_{\beta\nu} + \delta_{\alpha\nu} \delta_{\beta\mu}) \quad (\text{A.3})$$

hold. For the rotational contributions to the Doi equation, with the rotational operator as defined in Eq. (3.23),

$$\mathcal{R} = \mathbf{u} \times \partial_{\mathbf{u}} , \quad (\text{A.4})$$

one can use the integration by parts rule

$$\langle A(\mathbf{u}) \mathcal{R} [B(\mathbf{u})] \rangle = -\langle \mathcal{R} [A(\mathbf{u})] B(\mathbf{u}) \rangle \quad (\text{A.5})$$

and

$$\mathcal{R}^2 u_\alpha u_\beta = -6 \left(u_\alpha u_\beta - \frac{1}{3} \delta_{\alpha\beta} \right) . \quad (\text{A.6})$$

A.2 Isotropic averages in two dimensions

The two-dimensional isotropic distribution function is $\Psi(\mathbf{u}) = \frac{1}{2\pi}$ and the isotropic average is defined as

$$\langle A(\mathbf{u}) \rangle = \int \frac{d\mathbf{u}}{2\pi} A(\mathbf{u}) = \int_0^{2\pi} \frac{d\theta}{2\pi} A(\theta) , \quad (\text{A.7})$$

with θ the angle parameterizing the vector \mathbf{u} on the unit circle.

As in the three dimensional case all mean values depending on odd powers of \mathbf{u} vanish due to the $\pm\mathbf{u}$ -symmetry. The same is true for the mean values of any product of $|\mathbf{u} \times \mathbf{u}'|$ and odd powers of \mathbf{u} or \mathbf{u}' , since $|\mathbf{u} \times \mathbf{u}'| = \sqrt{1 - (\mathbf{u} \cdot \mathbf{u}')^2}$ contains only even powers of \mathbf{u}, \mathbf{u}' . For the even powers one gets

$$\langle u_\alpha u_\beta \rangle = \frac{1}{2} \delta_{\alpha\beta} , \quad (\text{A.8})$$

$$\langle u_\alpha u_\beta u_\mu u_\nu \rangle = \frac{1}{8} (\delta_{\alpha\beta} \delta_{\mu\nu} + \delta_{\alpha\mu} \delta_{\beta\nu} + \delta_{\alpha\nu} \delta_{\beta\mu}) \quad (\text{A.9})$$

and

$$\langle u_\alpha u_\beta u_\mu u_\nu u_\sigma u_\tau \rangle = \frac{1}{48} \{ \delta_{\alpha\beta} \delta_{\mu\nu} \delta_{\sigma\tau} + \text{perm.} \} , \quad (\text{A.10})$$

perm. meaning that all permutations of $\{\alpha, \beta, \mu, \nu, \sigma, \tau\}$ generating different index combinations of the Kronecker delta products are present. Furthermore one needs

$$\langle |\mathbf{u} \times \mathbf{u}'| \rangle' = \int \frac{d\theta'}{2\pi} |\sin(\theta - \theta')| = \frac{2}{\pi} = \langle |\mathbf{u} \times \mathbf{u}'| \rangle , \quad (\text{A.11})$$

where the brackets with ' denote averaging over \mathbf{u}' , and

$$\langle |\mathbf{u} \times \mathbf{u}'| u'_\alpha u'_\beta \rangle' = -\frac{2}{3\pi} (u_\alpha u_\beta - 2\delta_{\alpha\beta}) . \quad (\text{A.12})$$

The operator of rotational diffusion can be expressed in two dimensions as

$$[\mathcal{R}]_i = [\mathbf{u} \times \partial_{\mathbf{u}}]_i = \delta_{i3} (u_1 \partial_{u_2} - u_2 \partial_{u_1}) \quad (\text{A.13})$$

and one gets

$$\mathcal{R}^2 u_\alpha u_\beta = -4 \left(u_\alpha u_\beta - \frac{1}{2} \delta_{\alpha\beta} \right) . \quad (\text{A.14})$$

Again an integration by parts formula can be established,

$$\langle A(\mathbf{u}) \mathcal{R} [B(\mathbf{u})] \rangle = -\langle \mathcal{R} [A(\mathbf{u})] B(\mathbf{u}) \rangle . \quad (\text{A.15})$$

Danksagung

Mein Dank gilt zuerst Walter Zimmermann für die Betreuung dieser Arbeit und dafür, mir in der Themenwahl und -bearbeitung viel Freiheit gelassen zu haben. Weiterhin danke ich ihm, daß er mir die Möglichkeit zahlreicher Konferenzbeiträge gegeben hat, bei denen ich ihn in Japan und Israel auch auf internationaler Ebene habe vertreten dürfen.

Ich danke meiner Arbeitsgruppe in Saarbrücken und Bayreuth für die interessanten Jahre und die Unterstützung. Insbesondere ist Markus Hilt zu nennen, der mit mir gut fünf Jahre das Büro geteilt hat, was vermutlich nicht immer einfach war, für die Hilfe bezüglich allerlei Untiefen von Betriebssystemen, Programmiersprachen, etc.. Ronny Peter gilt mein Dank für die kritische Durchsicht dieses Manuskriptes.

Für die interessanten und fruchtbaren Kollaborationen danke ich neben den Mitgliedern der Arbeitsgruppe Dave Smith, Josef Käs, Harald Pleiner und Helmut R. Brand.

Schließlich noch zwei private Danksagungen. Meinen Eltern möchte ich danken für die Unterstützung und Geduld in den letzten Jahren. Meiner Freundin Sarah danke ich dafür, daß sie den Mut hatte, im letzten Jahr die Entfernung Saarbrücken-Bayreuth zu überbrücken und für alles andere.

Bibliography

- [1] H. Lodish, A. Berk, S. L. Zipursky, P. Matsudaira, D. Baltimore and J. Darnell: *Molecular Cell Biology*, W. H. Freeman, New York (1999).
- [2] B. Alberts, A. Johnson, J. Lewis, M. Raff, K. Roberts and P. Walter: *Molecular Biology of the Cell*, Garland Publishing, New York (2001).
- [3] D. Boal: *Mechanics of the cell*, Cambridge University Press, Cambridge (2002).
- [4] A. Bausch and K. Kroy: *A bottom-up approach to cell mechanics*, *Nature physics* **2**, 231 (2006).
- [5] J. Howard: *Mechanics of Motor Proteins and the Cytoskeleton*, Sinauer, Sunderland (2001).
- [6] D. Bray: *Cell movements*, Garland Publishing, New York (2001).
- [7] D. Pantaloni, C. LeClainche and M. F. Carrier: *Mechanism of actin-based motility*, *Science* **292**, 1502 (2001).
- [8] E. Karsenti and I. Vernos: *The Mitotic spindle: A Self-Made Machine*, *Science* **294**, 543 (2001).
- [9] D. Sharp, G. Rogers and J. Scholey: *Microtubule motors in mitosis*, *Nature* **407**, 41 (2000).
- [10] M. Dogterom, A. Maggs and S. Leibler: *Diffusion and formation of microtubule asters: Physical processes versus biochemical regulation*, *Proc. Natl. Acad. Sci. USA* **92**, 6683 (1995).
- [11] T. Bretschneider, S. Diez, K. Anderson, J. Heuser, M. Clarke, A. Müller-Taubenberger, J. Köhler and G. Gerisch: *Dynamic Actin Patterns and Arp2/3 Assembly at the Substrate-Attached Surface of Motile Cells*, *Curr. Biol.* **14**, 1 (2004).
- [12] A. Ponti, M. Machacek, S. Gupton, C. Waterman-Storer and G. Danuser: *Two Distinct Actin Networks Drive the Protrusion of Migrating Cells*, *Science* **305**, 1782 (2004).

- [13] T. Holy and S. Leibler: *Dynamic instability of microtubules as an efficient way to search in space*, *Proc. Natl. Acad. Sci. USA* **91**, 5682 (1994).
- [14] A. Hyman and E. Karsenti: *Morphogenetic Properties of Microtubules and Mitotic Spindle Assembly*, *Cell* **84**, 401 (1996).
- [15] M. F. Carlier, R. Melki, D. Pantaloni, T. L. Hill and Y. Chen: *Synchronous oscillations in microtubule polymerization*, *Proc. Natl. Acad. Sci.* **84**, 5257 (1987).
- [16] E. Mandelkow, E.-M. Mandelkow, H. Hotani, B. Hess and S. C. Müller: *Spatial Patterns from Oscillating Microtubules*, *Science* **246**, 1291 (1989).
- [17] A. Wegner: *Head to tail polymerization of actin*, *J. Mol. Biol.* **108**, 139 (1976).
- [18] F. C. Bawden, N. W. Pirie, J. D. Bernal and I. Fankuchen: *Liquid crystalline substances from virus-infected plants.*, *Nature* **138**, 1051 (1936).
- [19] A. L. Hitt, A. R. Cross and J. R. C. Williams: *Microtubule Solutions Display Nematic Liquid Crystalline Structure*, *J. Bio. Chem.* **265**, 1639 (1990).
- [20] A. Kerst, C. Chmielewski, C. Livesay, R. Buxbaum and S. Heidemann: *Liquid crystal domains and thixotropy of filamentous actin suspensions*, *Proc. Natl. Acad. Sci. USA* **87**, 4241 (1990).
- [21] A. Suzuki, T. Maeda and T. Ito: *Formation of liquid crystalline phase of actin filament solutions and its dependence on filament length as studied by optical birefringence*, *Biophys. J.* **59**, 25 (1991).
- [22] C. M. Coppin and P. C. Leavis: *Quantitation of liquid-crystalline ordering in F-actin solutions*, *Biophys. J.* **63**, 796 (1992).
- [23] R. Furukawa, R. Kundra and M. Fechheimer: *Formation of Liquid Crystals from Actin Filaments*, *Biochem.* **32**, 12346 (1993).
- [24] J. Käs, H. Strey, J. X. Tang, D. Finger, R. Ezzel, E. Sackmann and P. A. Janmey: *F-Actin, a Model Polymer for Semiflexible Chains in Dilute, Semidilute and Liquid Crystalline Solutions*, *Biophys. J.* **70**, 609 (1996).
- [25] P. G. de Gennes and J. Prost: *The Physics of Liquid Crystals*, Clarendon Press, Oxford (1993).
- [26] L. Onsager: *The Effects of Shape on the Interaction of Colloidal Particles*, *Ann. N.Y. Acad. Sci.* **51**, 627 (1949).
- [27] J. P. Straley: *Third Virial Coefficient for the Gas of Long Rods*, *Mol. Cryst. & Liq. Cryst.* **24**, 7 (1973).

- [28] Z. Y. Chen: *Nematic Ordering in Semiflexible Polymer Chains*, *Macromolecules* **26**, 3419 (1993).
- [29] F. Ziebert and W. Zimmermann: *Pattern formation driven by nematic ordering of assembling biopolymers*, *Phys. Rev. E* **70**, 022902 (2004).
- [30] A. B. Verkhovsky, T. M. Svitkina and G. G. Borisy: *Self-polarization and directional motility of cytoplasm*, *Curr. Bio.* **9**, 11 (1999).
- [31] F. J. Nédélec, T. Surrey, A. C. Maggs and S. Leibler: *Self-organization of microtubules and motors*, *Nature* **389**, 305 (1997).
- [32] T. Surrey, M. B. Elowitz, P. E. Wolf, F. Yang, F. Nédélec, K. Shokat and S. Leibler: *Chromophore-assisted light inactivation and self-organization of microtubules and motors*, *Proc. Natl. Acad. Sci. USA* **95**, 4293 (1998).
- [33] T. Surrey, F. Nédélec, S. Leibler and E. Karsenti: *Physical Properties Determining Self-Organization of Motors and Microtubules*, *Science* **292**, 116 (2001).
- [34] O. Thoumine and A. Ott: *Time scale dependent viscoelastic and contractile regimes in fibroblasts probed by microplate manipulation*, *J. Cell Sci.* **110**, 2109 (1997).
- [35] L. LeGoff, F. Amblard and E. Furst: *Motor-Driven Dynamics in Actin-Myosin Networks*, *Phys. Rev. Lett.* **88**, 018101 (2002).
- [36] D. Humphrey, C. Duggan, D. Saha, D. Smith and J. Käs: *Active fluidization of polymer networks through molecular motors*, *Nature* **416**, 413 (2002).
- [37] R. Urrutia, M. A. McNiven, J. P. Albanesi, D. B. Murphy and B. Kachar: *Purified kinesin promotes vesicle motility and induces active sliding between microtubules in vitro*, *Proc. Natl. Acad. Sci. USA* **88**, 6701 (1991).
- [38] D. Smith, F. Ziebert, D. Humphrey, C. Duggan, W. Zimmermann and J. Käs: *Molecular motor-induced instabilities and crosslinkers determine biopolymer organization*, submitted (2006).
- [39] M. Doi and S. F. Edwards: *The Theory of Polymer Dynamics*, Clarendon Press, Oxford (1986).
- [40] T. B. Liverpool and M. C. Marchetti: *Instabilities of Isotropic Solutions of Active Polar Filaments*, *Phys. Rev. Lett.* **90**, 138102 (2003).
- [41] K. Kruse and F. Jülicher: *Actively contracting bundles of polar filaments*, *Phys. Rev. Lett.* **85**, 1778 (2000).
- [42] M. C. Cross and P. C. Hohenberg: *Pattern Formation outside of equilibrium*, *Rev. Mod. Phys.* **65**, 851 (1993).

- [43] A. C. Newell, T. Passot and J. Lega: *Order parameter equations for patterns*, *Ann. Rev. Fluid Mech.* **25**, 399 (1992).
- [44] P. Manneville: *Dissipative Structures and Weak Turbulence*, Academic Press, London (1990).
- [45] F. Ziebert and W. Zimmermann: *Nonlinear competition between asters and stripes in filament-motor systems*, *Eur. Phys. J. E* **18**, 41 (2005).
- [46] F. Ziebert and W. Zimmermann: *comment on "Instabilities of Isotropic Solutions of Active Polar Filaments"*, *Phys. Rev. Lett.* **93**, 159801 (2004).
- [47] J. Howard: *Molecular motors: structural adaptations to cellular functions*, *Nature* **389**, 561 (1997).
- [48] R. Vale and R. Milligan: *The Way Things Move: Looking Under the Hood of Molecular Motor Proteins*, *Science* **288**, 88 (2000).
- [49] P. Janmey, J. Tang and C. Schmidt: *Actin filaments*, Biophysics Textbook Online/Biophysical Society.
- [50] M. Schliwa and G. Woehlke: *Molecular motors*, *Nature* **422**, 759 (2003).
- [51] T. Pollard: *The cytoskeleton, cellular motility and the reductionist agenda*, *Nature* **422**, 741 (2003).
- [52] T. Pollard: *Rate constants for the reactions of ATP- and ADP-actin with the ends of actin filaments*, *J. Cell Biol.* **103**, 2747 (1986).
- [53] B. Soltys and G. Borisy: *Polymerization of tubulin in vitro: Direct evidence for assembly onto microtubule ends and from centrosomes*, *J. Cell Biol.* **100**, 1682 (1985).
- [54] H. Yin and T. Stossel: *Control of cytoplasmic actin gel-sol transformation by gelsolin, a calcium-dependent regulatory protein*, *Nature* **281**, 583 (1979).
- [55] F. McNally and R. Vale: *Identification of katanin, an ATPase that severs and disassembles stable microtubules*, *Cell* **75**, 419 (1993).
- [56] T. Kreis, B. Geiger and J. Schlessinger: *Mobility of microinjected rhodamine actin within living chicken gizzard cells determined by fluorescence photobleaching recovery*, *Cell* **29**, 835 (1982).
- [57] W. Saxton, D. Stemple, R. Leslie, E. Salmon, M. Zavortink and J. McIntosh: *Tubulin dynamics in cultured mammalian cells*, *J. Cell Biol.* **99**, 2175 (1984).
- [58] A. Marx and E. Mandelkow: *A model of microtubule oscillations*, *Eur. Biophys. J.* **22**, 405 (1994).

- [59] M. Hammele and W. Zimmermann: *Modeling oscillatory microtubule polymerization*, *Phys. Rev. E* **67**, 021903 (2003).
- [60] J. Theriot, T. Mitchison, L. Tilney and D. Portnoy: *The rate of actin-based motility of intracellular *Listeria monocytogenes* equals the rate of actin polymerization*, *Nature* **357**, 257 (1992).
- [61] H. Huxley: *The double array of filaments in cross-striated muscle*, *J. Biophys. Biochem. Cytol.* **3**, 631 (1957).
- [62] L. Bourdieu, T. Duke, M. B. Elowitz, D. A. Winkelmann, S. Leibler and A. Libchaber: *Spiral Defects in Motility Assays: A Measure of Motor Protein Force*, *Phys. Rev. Lett.* **75**, 176 (1995).
- [63] T. Duke, T. Holy and S. Leibler: *"Gliding Assays" for Motor Proteins: A Theoretical Analysis*, *Phys. Rev. Lett.* **74**, 330 (1995).
- [64] T. Funatsu, Y. Harada, M. Tokunaga, K. Saito and T. Yanagida: *Imaging of single fluorescent molecules and individual ATP turnovers by single myosin molecules in aqueous solution*, *Nature* **374**, 555 (1995).
- [65] S. Ray, E. Meyrhofer, R. Milligan and J. Howard: *Kinesin follows the microtubule's protofilament axis*, *J. Cell Biol.* **121**, 1083 (1993).
- [66] J. Molley, J. Burns, J. Sparrow, R. Tregear, J. Kendrick-Jones and D. White: *Single-molecule mechanics of heavy meromyosin and S1 interacting with rabbit or *Drosophila* actins using optical tweezers*, *Biophys. J.* **68**, 298s (1995).
- [67] F. Lipmann: *Metabolic generation and utilization of phosphate bond energy*, *Adv. Enz.* **1**, 99 (1941).
- [68] W. Schief and J. Howard: *Conformational changes during kinesin motility*, *Curr. Opin. Cell Biol.* **13**, 19 (2001).
- [69] P. Das, J. Xu, J. Roy and N. Chakrabarti: *Liquid crystal polymorphism in F-actin: Optical microscopic and rotatory dispersion studies*, *J. Chem. Phys.* **111**, 8240 (1999).
- [70] P. Chaikin and T. Lubensky: *Principles of condensed matter physics*, Cambridge University Press, Cambridge (2000).
- [71] L. Landau and E. Lifschitz: *Lehrbuch der Theoretischen Physik, Band 5*, Akademie-Verlag, Berlin (1975).
- [72] H. N. W. Lekkerkerker, P. Coulon, R. VanDerHaegen and R. Deblieck: *On the isotropic-liquid crystal phase separation in a solution of rodlike particles of different lengths*, *J. Chem. Phys.* **80**, 3427 (1984).

- [73] R. F. Kayser and H. J. Raveche: *Bifurcation in Onsager's model of the isotropic-nematic transition*, *Phys. Rev. A* **17**, 2067 (1977).
- [74] H. Zocher: *Über freiwillige Strukturbildung in Solen. (Eine neue Art anisotrop flüssiger Medien.)*, *Z. Anorg. Chem.* **147**, 91 (1925).
- [75] G. Oster: *Two-phase formation in solutions of tobacco mosaic virus and the problem of long-range forces.*, *J. Gen. Physiol.* **33**, 445 (1950).
- [76] P. Sollich: *Predicting phase equilibria in polydisperse systems*, *J. Phys.: Cond. Mat.* **14**, R79 (2002).
- [77] T. Odijk and H. N. W. Lekkerkerker: *Theory of the Isotropic-Liquid Crystal Phase Separation for a Solution of Bidisperse Rodlike Macromolecules*, *J. Phys. Chem.* **89**, 2090 (1985).
- [78] J. P. Straley: *Liquid Crystals in Two Dimensions*, *Phys. Rev. A* **4**, 675 (1971).
- [79] D. Frenkel and R. Eppenga: *Evidence for algebraic orientational order in a 2-dimensional hard-core nematic*, *Phys. Rev. A* **31**, 1776 (1985).
- [80] M. Bates and D. Frenkel: *Phase behavior of two-dimensional hard rod fluids*, *J. Chem. Phys.* **112**, 10034 (2000).
- [81] J. P. Straley: *The Gas of Long Rods as a Model for Lyotropic Liquid Crystals*, *Mol. Cryst. & Liq. Cryst.* **22**, 333 (1973).
- [82] J. K. G. Dhont and W. J. Briels: *Isotropic-nematic spinodal decomposition kinetics*, *Phys. Rev. E* **72**, 031404 (2005).
- [83] J. P. Straley: *Frank Elastic Constants of the Hard-Rod Liquid Crystal*, *Phys. Rev. A* **8**, 2181 (1973).
- [84] T. Shimada, M. Doi and K. Okano: *Concentration fluctuation of stiff polymers. III. Spinodal decomposition.*, *J. Chem. Phys.* **88**, 7181 (1988).
- [85] F. Ziebert: *Über räumlich periodische Koexistenz von isotroper und nematischer Phase*, Diploma thesis, University of the Saarland, Saarbrücken (2002).
- [86] J. Langer: *Theory of Spinodal Decomposition in Alloys*, *Ann. Phys. (N.Y.)* **65**, 53 (1971).
- [87] J. W. Cahn and J. E. Hilliard: *Free Energy of a Nonuniform System. I. Interfacial Free Energy*, *J. Chem. Phys.* **28**, 258 (1958).
- [88] A. Bray: *Theory of phase-ordering kinetics*, *Adv. Phys.* **51**, 481 (2002).

- [89] S. C. Glotzer, D. Stauffer and N. Jan: *Monte Carlo Simulations of Phase Separation in Chemically Reactive Binary Mixtures*, *Phys. Rev. Lett.* **72**, 4109 (1994).
- [90] S. C. Glotzer, E. A. DiMarzio and M. Muthukumar: *Reaction-Controlled Morphology of Phase-Separating Mixtures*, *Phys. Rev. Lett.* **74**, 2034 (1995).
- [91] A. J. Liu and G. H. Fredrickson: *Phase Separation Kinetics of Rod/Coil Mixtures*, *Macromolecules* **29**, 8000 (1996).
- [92] T. Odijk: *Theory of Lyotropic Polymer Liquid Crystals*, *Macromolecules* **19**, 2313 (1986).
- [93] J. K. G. Dhont: *Rotational Brownian Motion of Colloidal Rods*, in *Soft Matter, Complex Materials on Mesoscopic Scales, 33th IFF course*, edited by J. K. G. Dhont, G. Gompper, and D. Richter (2002).
- [94] T. A. J. Lenstra, Z. Dogic and J. K. G. Dhont: *Shear-induced displacement of isotropic-nematic spinodals*, *J. Chem. Phys.* **114**, 10151 (2001).
- [95] W. Maier and A. Saupe: *Eine einfache molekulare Theorie des nematischen kristallinflüssigen Zustandes*, *Z. Naturforsch. A* **13**, 564 (1958).
- [96] P. Ilg, I. V. Karlin and H. C. Öttinger: *Generating moment equations in the Doi model of liquid-crystalline polymers*, *Phys. Rev. E* **60**, 5783 (1999).
- [97] L. E. Reichl: *A Modern Course in Statistical Physics*, Wiley-VCH, Weinheim (2004).
- [98] E. Hinch and L. Leal: *Constitutive equations in suspension mechanics. 2. Approximate forms for a suspension of rigid particles affected by brownian rotations*, *J. Fluid Mech.* **76**, 4269 (1976).
- [99] H. Pleiner and H. R. Brand, *Hydrodynamics and Electrohydrodynamics of Liquid Crystals*, in *Pattern Formation in Liquid Crystals*, edited by A. Buka and L. Kramer (Springer, New York, 1996).
- [100] P. Hohenberg and B. Halperin: *Theory of dynamic critical phenomena*, *Rev. Mod. Phys.* **49**, 435 (1977).
- [101] T. M. Svitkina, A. B. Verkhovskiy, K. M. McQuade and G. G. Borisy: *Analysis of the Actin-Myosin II System in Fish Epidermal Keratocytes: Mechanism of Cell Body Translocation*, *J. Cell Biol.* **139**, 397 (1997).
- [102] T. Wakatsuki, R. Wysolmerski and E. Elson: *Mechanics of cell spreading: role of myosin II*, *J. Cell Sci.* **116**, 1617 (2003).
- [103] C. M. Marques, M. S. Turner and M. E. Cates: *End-evaporation kinetics in living-polymer systems*, *J. Chem. Phys.* **99**, 7260 (1993).

- [104] K. Takiguchi: *Heavy Meromyosin Induces Sliding Movements between Antiparallel Actin filaments*, *J. Biochem.* **109**, 520 (1991).
- [105] K. Kruse, S. Camalet and F. Jülicher: *Self-propagating patterns in active filament bundles*, *Phys. Rev. Lett.* **87**, 138101 (2001).
- [106] A. Benedix: *Strukturbildungsvorgänge in zellulären Motor-Filament-Systemen mit Reaktionskinetik*, Diploma thesis, University of the Saarland, Saarbrücken (2004).
- [107] B. Gentry and J. Käs: unpublished.
- [108] R. Heald, R. Tournebise, T. Blank, R. Sandaltzopoulos, P. Becker, A. Hyman and E. Karsenti: *Self-organization of microtubules into bipolar spindles around artificial chromosomes in Xenopus egg extracts*, *Nature* **382**, 420 (1996).
- [109] B. Bassetti, M. C. Lagomarsino and P. Jona: *A model for the self-organization of microtubules driven by molecular motors*, *Eur. Phys. J. B* **15**, 483 (2000).
- [110] H. Y. Lee and M. Kardar: *Macroscopic equations for pattern formation in mixtures of microtubules and molecular motors*, *Phys. Rev. E* **64**, 056113 (2001).
- [111] J. Kim, Y. Park, B. Kahng and H. Y. Lee: *Self-organized patterns in mixtures of microtubules and motor proteins*, *J. Korean Phys. Soc.* **42**, 162 (2003).
- [112] S. Sankararaman, G. Menon and P. Kumar: *Self-organized Pattern formation in Motor-Microtubule Mixtures*, *Phys. Rev. E* **70**, 031905 (2004).
- [113] Y. Tanaka-Takiguchi, T. Kakei, A. Tanimura, A. Takagi, M. Honda, H. Hotani and K. Takiguchi: *The Elongation and Contraction of Actin Bundles are Induced by Double-headed Myosins in a Motor Concentration-dependent Manner*, *J. Mol. Biol.* **341**, 467 (2004).
- [114] H. Nakazawa and K. Sekimoto: *Polarity Sorting in a Bundle of Actin filaments by Two-Headed Myosins*, *J. Phys. Soc. Japan* **65**, 2404 (1996).
- [115] K. Kruse, A. Zumdick and F. Jülicher: *Continuum theory of contractile fibres*, *Europhys. Lett.* **64**, 716 (2003).
- [116] K. Kruse and F. Jülicher: *Self-organization and mechanical properties of active filament bundles*, *Phys. Rev. E* **67**, 051913 (2003).
- [117] R. A. Simha and S. Ramaswamy: *Hydrodynamic Fluctuations and Instabilities in Ordered Suspensions of Self-Propelled Particles*, *Phys. Rev. Lett.* **89**, 058101 (2002).
- [118] Y. Hatwalne, S. Ramaswamy, M. Rao and R. A. Simha: *Rheology of Active-Particle Suspensions*, *Phys. Rev. Lett.* **92**, 118101 (2004).

- [119] I. S. Aranson and L. S. Tsimring: *Pattern formation of microtubules and motors: Inelastic interaction of polar rods*, *Phys. Rev. E* **71**, 050901 (2005).
- [120] T. B. Liverpool and M. C. Marchetti: *Bridging the microscopic and the hydrodynamic in active filament solutions*, *Europhys. Lett.* **69**, 846 (2005).
- [121] F. Nédélec: *Auto-organisation d'un Mélange de Microtubules et de Moteurs*, Thesis, University Paris XI, Paris (1998).
- [122] F. Nédélec and T. Surrey: *Dynamics of microtubule aster formation by motor complexes*, *C. R. Acad. Sci. Paris S. IV* **6**, 841 (2001).
- [123] A. Ahmadi, T. B. Liverpool and M. C. Marchetti: *Nematic and polar order in active filament solutions*, *Phys. Rev. E* **72**, 060901 (2005).
- [124] V. Rühle, F. Ziebert and W. Zimmermann: unpublished.
- [125] I. Teraoka, N. Ookubo and R. Hayakawa: *Molecular theory on the entanglement effect of rodlike polymers*, *Phys. Rev. Lett.* **55**, 2712 (1985).
- [126] I. Teraoka and R. Hayakawa: *Theory of dynamics of entangled rod-like polymers by use of a mean-field Green-function formulation. I. Transverse diffusion*, *J. Chem. Phys.* **89**, 6989 (1988).
- [127] K. Kruse, J. F. Joanny, F. Jülicher, J. Prost and K. Sekimoto: *Asters, Vortices, and Rotating Spirals in Active Gels of Polar Filaments*, *Phys. Rev. Lett.* **92**, 078101 (2004).
- [128] K. Kruse, J. F. Joanny, F. Jülicher, J. Prost and K. Sekimoto: *Generic theory of active polar gels: a paradigm for cytoskeletal dynamics*, *Eur. Phys. J. E* **16**, 5 (2005).
- [129] A. B. Verkhovskiy, T. M. Svitkina and G. G. Borisy: *Polarity sorting of actin filaments in cytochalasin-treated fibroblasts*, *J. Cell Sci.* **110**, 1693 (1997).
- [130] I. S. Aranson and L. S. Tsimring: *Theory of self-assembly of microtubules and motors*, to appear in *Phys. Rev. E*, 2006.
- [131] S. Ciliberto, P. Coulet, J. Lega, E. Pampaloni and C. Perez-Garcia: *Defects in Roll-Hexagon Competition*, *Phys. Rev. Lett.* **65**, 2370 (1990).
- [132] L. A. Segel: *The non-linear interaction of a finite number of disturbances to a layer of fluid heated from below*, *J. Fluid Mech.* **21**, 359 (1965).
- [133] I. Teraoka and R. Hayakawa: *Theory of dynamics of entangled rod-like polymers by use of a mean-field Green function formulation. II. Rotational diffusion*, *J. Chem. Phys.* **91**, 2643 (1989).

- [134] S. M. Cox and P. C. Matthews: *Instability and localisation of patterns due to a conserved quantity*, *Physica D* **175**, 196 (2003).
- [135] P. C. Matthews and S. M. Cox: *Pattern formation with a conservation law*, *Nonlinearity* **13**, 1293 (2000).
- [136] A. Roxin and H. Riecke: *Destabilization and localization of traveling waves by an advected field*, *Physica D* **156**, 19 (2001).
- [137] R. Peter and W. Zimmermann: *Traveling ion channel density waves affected by a conservation law*, to appear in *Phys. Rev. E*, 2006.
- [138] F. Nédélec, T. Surrey and A. C. Maggs: *Dynamic concentration of motors in microtubule arrays*, *Phys. Rev. Lett.* **86**, 3192 (2001).
- [139] I. S. Aranson and L. Kramer: *The world of the complex Ginzburg-Landau equation*, *Rev. Mod. Phys.* **74**, 99 (2002).
- [140] W. Zimmermann, in *Defects, Singularities and Patterns in Nematic Liquid Crystals: Mathematical and Physical Aspects*, Vol. 332 of *NATO Advanced Study Institute, Series C*, edited by J. M. Coron, J. M. Ghidaglia, and F. Helein (Kluwer, Dordrecht, 1991).
- [141] M. Silber and E. Knobloch: *Hopf bifurcation on a square lattice*, *Nonlinearity* **4**, 1063 (1991).
- [142] M. Silber, H. Riecke and L. Kramer: *Symmetry-breaking Hopf bifurcation in anisotropic systems*, *Physica D* **61**, 260 (1992).
- [143] H. Riecke, M. Silber and L. Kramer: *Temporal forcing of small-amplitude waves in anisotropic systems*, *Phys. Rev. E* **49**, 4100 (1994).
- [144] K. Yasuda, Y. Shindo and S. Ishiwata: *Synchronous behavior of spontaneous oscillations of sarcomeres in skeletal myofibrils under isotonic conditions*, *Biophys. J.* **70**, 1823 (1996).
- [145] H. Fujita and S. Ishiwata: *Spontaneous Oscillatory Contraction without Regulatory Proteins in Actin Filament-Reconstituted Fibers*, *Biophys. J.* **75**, 1439 (1998).
- [146] J. Quaas and C. Wylie: *Surface Contraction Waves (SCWs) in the Xenopus Egg Are Required for the Localization of the Germ Plasm and Are Dependent upon Maternal Stores of the Kinesin-like Protein Xklp1*, *Developmental Biology* **243**, 272 (2002).
- [147] H.-G. Döbereiner, B. Dubin-Thaler, G. Giannone, H. S. Xenias and M. P. Sheetz: *Dynamic Phase Transitions in Cell Spreading*, *Phys. Rev. Lett.* **93**, 108105 (2004).

- [148] G. Giannone, B. J. Dubin-Thaler, H.-G. Döbereiner, N. Kieffer, A. R. Bresnick and M. P. Sheetz: *Periodic Lamellopodial Contractions Correlate with Rearward Actin Waves*, *Cell* **116**, 431 (2004).
- [149] W. Zimmermann, M. Sesselberg and F. Petruccione: *Effects of disorder in Pattern-Formation*, *Phys. Rev. E* **48**, 2699 (1993).
- [150] M. Hammele, S. Schuler and W. Zimmermann: *Effects of parametric disorder on a stationary bifurcation*, *Physica D* **218**, 105 (2006).
- [151] W. Zimmermann, B. Painter and R. Behringer: *Pattern formation in inhomogeneous convective systems*, *Eur. Phys. J. B* **5**, 575 (1998).
- [152] M. P. Sheetz, R. Chasan and J. Spudich: *ATP-dependent movement of myosin in vitro - characterization of a quantitative assay*, *J. Cell Biol.* **99**, 1867 (1984).
- [153] J. Uhde, M. Keller, E. Sackmann, A. Parmeggiani and E. Frey: *Internal Motility in Stiffening Actin-Myosin Networks*, *Phys. Rev. Lett.* **93**, 268101 (2004).
- [154] T. Nishizaka, R. Seo, H. Tadakuma, K. Kinoshita and S. Ishiwata: *Characterization of single actomyosin rigor bonds: Load dependence of lifetime and mechanical properties*, *Biophys. J.* **79**, 962 (2000).
- [155] M. Gardel, F. Nakamura, J. Hartwig, T. Stossel and D. Weitz: *Prestressed F-actin networks cross-linked by hinged filamins replicate mechanical properties of cells*, *Proc. Natl. Acad. Sci. USA* **103**, 1762 (2006).
- [156] R. Schmitz and W. Zimmermann: *Spatially periodic modulated Rayleigh-Bénard convection*, *Phys. Rev. E* **53**, 5993 (1996).
- [157] A. Sanz-Anchelergues, A. M. Zhabotinsky, I. R. Epstein and A. P. Munuzuri: *Turing pattern formation induced by spatially correlated noise*, *Phys. Rev. E* **63**, 056124 (2001).
- [158] R. Peter, M. Hilt, F. Ziebert, J. Bammert, C. Erlenkämper, N. Lorscheid, C. Weitenberg, A. Winter, M. Hammele and W. Zimmermann: *Stripe-hexagon competition in forced pattern-forming systems with broken up-down symmetry*, *Phys. Rev. E* **71**, 046212 (2005).
- [159] F. Ziebert, M. Hammele and W. Zimmermann: *On cytoskeletal patterns and intrinsic disorder effects*, to appear in *Nonlinear Phenomena in Complex Systems (Minsk)*, 2006.
- [160] P. Hotulainen and P. Lappalainen: *Stress fibers are generated by two distinct actin assembly mechanisms in motile cells*, *J. Cell Biol.* **173**, 383 (2006).

- [161] F. Wottawah, S. Schinkinger, B. Lincoln, R. Ananthakrishnan, M. Romeyke, J. Guck and J. Käs: *Optical Rheology of Biological Cells*, *Phys. Rev. Lett.* **94**, 098103 (2005).
- [162] P. Janmey, S. Hvidt, J. Käs, D. Lerche, A. Maggs, E. Sackmann, M. Schliwa and T. Stossel: *The Mechanical Properties of Actin Gels*, *J. Biol. Chem.* **269**, 32503 (1994).

Ich erkläre hiermit an Eides Statt, daß ich diese Arbeit selbst angefertigt und nur die in der Arbeit angegebenen Hilfsmittel verwendet habe.

Bayreuth, den

Falko Ziebert